Equilibrium and kinetics studies of hydrogen storage onto hybrid activated carbon-metal organic framework adsorbents produced by mild syntheses

Zhewei Yu

Thèse de Doctorat

Zhewei YU

Mémoire présenté en vue de l'obtention du

grade de Docteur de l'École des Mines de Nantes

sous le label de L'Université Nantes Angers Le Mans

École doctorale : *Sciences Pour l'Ingénieur, Géosciences, Architecture (ED 498)*

Discipline : *Energétique, Génie des Procédés*

Unités de recherche :
UMR CNRS 6144 GEPEA Génie des Procédés de l'Environnement et de l'Agro-alimentaire
Unité Chimie et Procédés, Ecole Nationale Supérieure de Techniques Avancées (ENSTA ParisTech), Université Paris Saclay

Soutenue : *le 10 Février 2016*

NNT : *2016EMNA0236*

EQUILIBRIUM AND KINETICS STUDIES OF HYDROGEN STORAGE ONTO

HYBRID ACTIVATED CARBON-METAL ORGANIC FRAMEWORK

ADSORBENTS PRODUCED BY MILD SYNTHESES

JURY

Rapporteurs :	**Pierre MILLET**	Professeur	Université Paris-Sud 11
	Khashayar SALEH	Professeur	Université de Technologie de Compiègne
Examinateurs :	**Walter FURST**	Professeur	ENSTA ParisTech
	Laurence FOURNAISON	Directrice de Recherche	IRSTEA
Directeur :	**Pascaline PRE**	Professeur	Ecole des Mines de Nantes
Co-encadrant :	**Johnny DESCHAMPS**	Enseignant-Chercheur HDR	ENSTA ParisTech
Invités :	**Olivier BAUDOUIN**	Ingénieur de Recherche	ProSim
	Didier DALMAZZONE (co-directeur)	Professeur	ENSTA ParisTech
	Lomig HAMON (co-encadrant)	Maitre-assistant	Ecole des Mines de Nantes

Thèse de Doctorat

Zhewei YU

Mémoire présenté en vue de l'obtention du

grade de Docteur de l'École des Mines de Nantes

sous le label de L'Université Nantes Angers Le Mans

École doctorale : *Sciences Pour l'Ingénieur, Géosciences, Architecture (ED 498)*

Discipline : *Energétique, Génie des Procédés*

Unités de recherche :
UMR CNRS 6144 GEPEA Génie des Procédés de l'Environnement et de l'Agro-alimentaire
Unité Chimie et Procédés, Ecole Nationale Supérieure de Techniques Avancées (ENSTA ParisTech), Université Paris Saclay
Soutenue : *le 10 Février 2016*

EQUILIBRIUM AND KINETICS STUDIES OF HYDROGEN STORAGE ONTO

HYBRID ACTIVATED CARBON-METAL ORGANIC FRAMEWORK

ADSORBENTS PRODUCED BY MILD SYNTHESES

JURY

Rapporteurs :	**Pierre MILLET**	Professeur	Université Paris-Sud 11
	Khashayar SALEH	Professeur	Université de Technologie de Compiègne
Examinateurs :	**Walter FURST**	Professeur	ENSTA ParisTech
	Laurence FOURNAISON	Directrice de Recherche	IRSTEA
Directeur :	**Pascaline PRE**	Professeur	Ecole des Mines de Nantes
Co-encadrant :	**Johnny DESCHAMPS**	Enseignant-Chercheur HDR	ENSTA ParisTech
Invités :	**Olivier BAUDOUIN**	Ingénieur de Recherche	ProSim
	Didier DALMAZZONE (co-directeur)	Professeur	ENSTA ParisTech
	Lomig HAMON (co-encadrant)	Maitre-assistant	Ecole des Mines de Nantes

This dissertation is dedicated to my wife and my parents.

Acknowledgements

Foremost, I would like to express the sincerest gratitude to my supervisor, Prof. Pascaline Pré for her continuous support of my Ph.D. study and related research, for her patience, motivation and immense knowledge as well as her kind and helpful guidance during the three years.

My co-supervisor, Prof. Didier Dalmazzone was very kind and patient with me. He helped me through these three years' work. I'm deeply grateful to him.

I would like also to thank the other members of my thesis committee: Dr. Johnny Deschamps and Dr. Lomig Hamon for their insightful comments and encouragement. They were always there for helping whenever needed. The discussions with them were always meaningful and opened new perspectives of the work.

I'm grateful to Prof. Pierre Millet, Prof. Khashayar Saleh, Dr. Laurence Fournaison, Mr. Olivier Baudouin who accepted to participate in my defence committee.

I would like to thank Dr. Karikkethu Prabhakaran Prasanth for his kind help in the lab work. He was a good teacher and his explanations were very detailed and helpful.

I would give my thanks to all staffs of ENSTA ParisTech and Ecole des Mines de Nantes, especially Prof. Laurent Catoire, Prof. Walter Fürst, Dr. Patrice Paricaud, Dr. Félicie Theron, Dr. Eric Dumont. My memory of these three years is plenty of laughter and happiness.

I thank my labmates for the fancy environment they have created. In particular, I am glad to have friends like Mr. Aurélien Demenay, Dr. Julien Glorian, Dr. Mickael Matrat, Dr. Shunyi Li, Mr. Kévin Morisseau and Ms. Mouna Ben Jaber during the three years.

I am also grateful to all my friends who have helped me stay sane through these difficult years. Their support and care helped me overcome setbacks and stay focused on my study. I greatly value their friendship and I deeply appreciate their belief in me.

Most importantly, none of this would have been possible without the love and the patience of my family, especially my wife and my parents whom this dissertation is dedicated to.

Résumé et mots-clés

Résumé

Depuis une quinzaine d'années, les matériaux poreux de type Metal Organic Frameworks (MOFs) offrent de nouvelles perspectives dans le cadre du stockage d'hydrogène par adsorption. Ces matériaux possèdent une structure et un réseau de pores particulièrement adaptés à l'adsorption des gaz. Ainsi, le téréphtalate de Chrome (III) (MIL-101(Cr)), composé chimiquement très stable, possède une grande capacité de stockage de l'hydrogène, du dioxyde de carbone et du méthane. Afin de renforcer sa capacité de stockage d'hydrogène, un dopage au charbon actif (AC) du matériau a été envisagé.

Les synthèses des matériaux dopés et non-dopés ont été réalisées et, pour cela, différents agents minéralisants (acide fluorhydrique, acide acétique et acétate de sodium) ont été testés. Les matériaux synthétisés ont été caractérisés par diffraction des rayons X (DRX), par microscopie électronique à balayage (MEB), par analyses thermogravimétriques (ATG) et par adsorption d'azote à 77K.

Les capacités de stockage d'hydrogène de ces matériaux à 77 K et 100 bar ont été évaluées par mesures des isothermes d'adsorption de l'hydrogène réalisées par méthodes volumétrique et gravimétrique. Les résultats obtenus par ces deux méthodes sont en parfait accord et le matériau composite affiche une capacité d'adsorption de 13.5 wt%, supérieure à celle du matériau non dopé, égale à 8.2 wt % dans les mêmes conditions expérimentales.

Finalement, afin d'évaluer les vitesses d'adsorption et de désorption de l'hydrogène sur le MIL-101(Cr) et le MIL-101(Cr) dopé au charbon actif, les cinétiques d'adsorption ont été mesurées à 77 K par méthode volumétrique. Les résultats obtenus ont été comparés au modèle de la force motrice linéaire, Linear Driving Force (LDF). Un modèle de diffusion dépendant de la température a été développé afin de tenir compte des variations de températures qui se produisent durant le processus d'adsorption.

Mots clés

MOF /MIL-101(Cr) /Charbon actif /Stockage d'hydrogène /Synthèse /Adsorption /Cinétique /Expérimental /Modélisation

Abstract and keywords

Abstract

Since the last 15 years, porous solids such as Metal-Organic Frameworks (MOFs) have opened new perspectives for the development of adsorbents for hydrogen storage. The structure and the pore networks of these materials are especially adapted to the adsorption of gases. The chromium (III) terephthalate-based MIL-101(Cr) is a very stable material which exhibits good adsorption uptakes for hydrogen (H_2), carbon dioxide (CO_2) and methane (CH_4).

In this study, syntheses were carried out by different ways and several mineralizing agents such as hydrofluoric acid (HF), acetic acid (CH_3COOH) and sodium acetate (CH_3COONa) have been tested. Moreover, Activated Carbon (AC) has been introduced in the framework to create an AC incorporated composite material with an enhanced specific surface area. Conventional techniques such as powder X-ray diffraction (PXRD), scanning electron microscopy (SEM), thermogravimetric analysis (TGA) and nitrogen (N_2) adsorption isotherms at 77 K were used for materials characterizations.

In the aim to evaluate hydrogen storage capacities of these materials, hydrogen adsorption isotherms were measured at 77 K *via* both volumetric and gravimetric methods, and the obtained results are in good agreement. A hydrogen uptake value of 13.5 wt% has been measured at 77 K and 100 bar for the composite material which shows a great improvement of hydrogen capacity compared to the pristine MIL-101(Cr) (8.2 wt%).

Finally, hydrogen adsorption kinetics has been measured at 77 K by using volumetric method. The obtained results were compared to the Linear Driving Force (LDF) model and a temperature dependent diffusion model was also considered to take into account the temperature variation which occurs during the adsorption process.

Mots-clés

MOF /MIL-101(Cr) /Charbon actif /Stockage d'hydrogène /Synthèse /Adsorption /Cinétique /Expérimental /Modélisation

Résumé

La demande croissante en énergie ainsi que l'aggravation de la pollution liée aux émissions de dioxyde de carbone CO_2, imposent à ce jour la mise en place de nouvelles sources d'énergie renouvelables et surtout non polluantes. Dans ce contexte, les énergies photovoltaïques, éoliennes ou géothermiques représentent des solutions alternatives. Sources d'énergie primaires, elles permettent de produire de l'électricité et de la chaleur pouvant être ensuite utilisées dans différentes conditions, pour répondre aux besoins et à la demande. Pour des applications stationnaires, les technologies qui doivent être mises en œuvre pour stocker et convertir l'énergie produite par ces sources intermittentes sur des installations stationnaires apparaissent aujourd'hui plus matures que celles requises en vue d'une utilisation mobile. Pour pallier l'épuisement des ressources énergétiques fossiles et répondre aux problématiques environnementales qui leur sont associées, l'hydrogène apparait alors comme une solution alternative à une nouvelle économie de l'énergie.

L'hydrogène est un vecteur énergétique qui contient une énergie massique trois fois plus grande que l'essence. Il peut être produit à partir de sources renouvelables ou fossiles, et utilisé en combustion directe ou dans des piles à combustibles. Le stockage d'hydrogène demeure néanmoins un verrou majeur de la filière, qui s'avère encore plus difficile à résoudre dans le cas d'applications embarquées. Les technologies actuelles permettent un stockage sous forme gazeuse à haute pression, un stockage liquide à très basse température et un stockage chimique ou physique. Ces technologies sont envisageables sur des installations stationnaires opérant à plus ou moins grande échelle, par contre, leurs performances technico-économiques sont à ce jour insuffisantes pour servir des applications mobiles. Or, la levée de ce verrou s'avère incontournable dans le cadre du développement d'une économie de l'énergie incluant l'hydrogène. Bien que les stockages gazeux et liquide apparaissent comme les techniques les plus matures, ces dernières font appel à des conditions extrêmes de température et de pression qui ne permettent pas de satisfaire aux spécifications requises pour des applications mobiles, telles que fixées par le Department of Energy (DOE) américain. Afin de répondre aux contraintes de poids, d'encombrement et de sûreté du procédé, le stockage physique par adsorption dans un matériau poreux semble être une solution prometteuse car elle met en œuvre une cinétique rapide et réversible, dans des conditions de température et de pression modérées.

Ainsi, le développement de procédés de stockage d'hydrogène suffisamment performants et acceptables d'un point de vue coûts et sécurité représente un défi actuel majeur. Cette thèse a pour objectif de proposer un procédé de stockage de l'hydrogène par adsorption qui soit extrapolable à grande échelle. Cette méthode requiert l'utilisation d'un matériau qui associe à la fois légèreté, stabilité et grande capacité de stockage. Ce matériau doit aussi pouvoir être produit en quantités industrielles, à partir de substances chimiques disponibles et dont l'utilisation est autorisée par la réglementation REACh (Registration, Evaluation, Autorisation of Chemical products). Après une étude bibliographique préliminaire, un type de matériau à structure mésoporeuse, MIL-101(Cr) faisant parti de la famille des réseaux organo-métalliques (''Metal Organic Frameworks'', MOF) a été sélectionné, en considérant d'une part la possibilité d'adapter les conditions de synthèse aux

contraintes de production industrielle, et d'autre part la stabilité chimique ainsi que les grandes surfaces spécifiques pouvant être développées. Afin d'accroître encore les capacités d'adsorption en hydrogène de ce type d'adsorbant, l'adjonction d'un agent dopant microporeux sous forme de poudre de carbone activé a par ailleurs été envisagée.

Dans un premier temps, les synthèses des matériaux MIL-101(Cr) et MIL-101(Cr) dopés au charbon actif ont été réalisées. La synthèse, telle que décrite dans la littérature, fait appel à l'acide fluorhydrique en tant qu'agent minéralisant. Or ce composé est fortement toxique et, pour des raisons de sécurité, il n'est pas judicieux de l'utiliser à l'échelle industrielle. Ainsi différents agents minéralisants tels l'acide acétique ou l'acétate de sodium ont été mis en œuvre pour tenter de produire le MIL-101(Cr) par différentes voies de synthèse, c'est-à-dire en utilisant différentes méthodes de chauffage et solutions de lavage, et en faisant varier la concentration de charbon actif introduit comme agent dopant. Les produits synthétisés bruts obtenus ont ensuite été lavés à l'éthanol, au diméthylformamide (DMF) ou avec une solution de fluorure d'ammonium (NH_4F) afin d'éliminer les résidus tels que l'acide benzenedicarboxylique restant dans les pores. Les matériaux obtenus ont ensuite été dégazés sous vide afin d'éliminer l'eau et le solvant résiduels.

Les matériaux synthétisés ont alors été caractérisés par diffraction de rayon X afin d'examiner leurs structures cristallines, par microscopie électronique à balayage pour étudier les morphologies de leurs cristaux et par thermogravimétrie pour évaluer la stabilité thermique. Les résultats montrent que le MIL-101(Cr) synthétisé par utilisation de l'acide acétique comme agent minéralisant a une structure cristalline similaire à celle théorique. Le matériau produit présente une taille moyenne de cristaux de 120 nm. Les MIL-101(Cr) dopés au charbon actif présentent des taux de cristallinité inférieurs par rapport à leurs homologues non dopées, ce qui montre l'influence de l'incorporation du charbon actif sur la germination et la croissance des cristaux. Ainsi la taille moyenne d'un cristal de MIL-101(Cr) dopé avec 5 wt% de charbon actif diminue jusqu'à 80 nm. Quant à la morphologie des cristaux, elle semble moins régulière que celle observées pour le MIL-101(Cr) pur. L'analyse thermogravimétrique montre que ces matériaux sont thermiquement stables jusqu'à 200°C. Au-delà de 200°C, le cristal se décompose avec la disparition dans un premier temps des molécules d'eau terminales de la structure, puis, dans un second temps, des composés organiques liants les clusters métalliques du MOF.

La porosité des matériaux adsorbants a été étudiée à partir de la mesure des isothermes d'adsorption d'azote à 77 K. Les surfaces spécifiques développées, ainsi que les distributions de tailles des pores ont été évaluées. Les isothermes d'adsorption obtenues, décrivant des quantités adsorbées à l'équilibre en fonction de la pression relative d'azote, sont de type IV : une hystérèse à la désorption est observée pour une pression relative de l'ordre de p/p^0=1 ce qui témoigne de la mésoporosité de ces matériaux. Par ailleurs, la présence de deux échelons sur les isothermes pour une pression relative p/p^0 de l'ordre de 0,15 et 0.25 peut être associée aux ouvertures des deux catégories des faces (pentagonales et hexagonales) qui délimitent les cages du matériau. Les surfaces spécifiques de ces adsorbants ont été calculées en considérant le modèle de Langmuir et la théorie BET. Le modèle de Langmuir est basé sur la formation d'une phase adsorbée constituée d'une monocouche moléculaire, alors que la théorie BET suppose une adsorption multicouche. Les résultats de ces modélisations montrent que les matériaux synthétisés possèdent de grandes surfaces spécifiques. Le MIL-101(Cr) pur synthétisé à partir d'acide acétique a une surface spécifique de Langmuir de 4668 $m^2.g^{-1}$ et une surface BET de 3223 $m^2.g^{-1}$. Un dopage au charbon actif correspondant à une concentration massique de 5 % augmente les surfaces spécifiques de Langmuir et BET, qui

atteignent respectivement 4951 m².g⁻¹ et 3542 m².g⁻¹. Un maximum de la surface spécifique est obtenu par l'adjonction de charbon actif, et au-delà d'une certaine concentration en charbon actif, une perte de porosité qui se traduit par une diminution de la surface spécifique est observée. Les distributions de taille des pores ont été calculées suivant deux méthodes : à partir du modèle de Barrett, Joyner et Halenda (BJH) et à partir de la théorie de la densité fonctionnelle non locale (Non Local Density Functional Theory NLDFT). La méthode BJH considère que seuls des mésopores sont présents dans le matériau adsorbant et que l'équation de Kelvin décrivant la condensation capillaire est applicable sur l'ensemble du domaine mésoporeux. Néanmoins, pour des pores de taille inférieure à 7,5 nm, différentes corrections ont été considérées, ainsi que différentes équations permettant de tenir compte de l'épaisseur de la couche adsorbée. Les résultats obtenus à partir des différents calculs des corrections ont été comparés et il a été montré que la correction et l'équation de calcul de l'épaisseur de la couche adsorbée proposée par Kruk-Jaroniec-Sayari (KJS) aboutissent à une distribution de tailles de pores dont les valeurs centrées sur 26 et 31 Ǻ sont très proches des tailles de pores théoriques. La méthode NLDFT tenant compte des interactions fluide-fluide et fluide-solide nécessite de disposer d'un champ de force décrivant les interactions atomiques des éléments présents dans le MIL-101(Cr). Cette méthode a été appliquée en se basant sur un champ de potentiel chimique issu de la littérature. Elle a permis d'obtenir des résultats similaires à ceux obtenus via la méthode BJH dans le domaine mésoporeux, et a étendu la mesure de distribution de taille des pores dans le domaine microporeux, correspondant à des tailles inférieures à 20 Ǻ. La présence de pores de l'ordre de 1 nm a été ainsi établie, supposés formés par le super tétraèdre de la structure de MIL-101(Cr). Les volumes des pores ont été déduits soit à partir de l'intégration de la distribution de la taille de pores obtenue par la méthode BJH, soit à partir des quantités adsorbées d'azote à la pression relative p/p^0=0,98. Le volume de pore calculé pour les adsorbants est de l'ordre de 2 cm³.g⁻¹ ; le MIL-101(Cr) dopé à une concentration massique de 5% de charbon actif développe un volume total de pore de 2,65 cm³.g⁻¹.

Les performances de stockage de l'hydrogène ont été évaluées sur le panel de matériaux adsorbants synthétisés, incluant les échantillons MIL-101(Cr) purs obtenus par différentes voies de synthèse et dopés au charbon actif. Les capacités d'adsorption ont été déterminées à partir de la mesure d'isothermes d'équilibre sur deux appareillages différents, opérant d'une part par volumétrie et d'autre part par gravimétrie. La méthode de mesure volumétrique implique la mesure directe de la température et de la pression dans la chambre d'adsorption, remplie avec une quantité connue d'hydrogène présent en phase adsorbée et en phase gazeuse. Les quantités adsorbées en excès sont déduites à partir de l'équation de conservation de masse et de l'équation d'état du gaz. Les mesures ayant été effectuées jusqu'à 50 bar, à la température de 77 K, la méthode dite du « double volume imaginaire » a été appliquée afin de rendre compte des gradients de température entre le réservoir à l'ambiante et la chambre d'adsorption immergée dans l'azote liquide. La méthode gravimétrique repose sur la mesure du changement de la masse de d'échantillon exposé à la phase gazeuse. Pour effectuer cette mesure, une microbalance à suspension magnétique est employée. La masse d'hydrogène adsorbé en excès est calculée à partir d'un bilan de forces qui prend en compte l'effet de poussée d'Archimède. Les mesures ont été réalisées suivant cette méthode jusqu'à 100 bar, aux températures de 77 et 298 K. Les isothermes mesurées par les deux méthodes en conditions cryogéniques ont été comparés entre elles, et un bon accord a été trouvé. Les capacités de stockage des matériaux ont été déduites et exprimées par unité de masse et de volume d'adsorbant. A 100 bar et 77 K, les capacités massiques rapportées aux quantités absolues d'hydrogène adsorbé ont

été évaluées au maximum à 14.8 % pour le MIL-101(Cr) pur et à 19.8 % pour les matériaux dopés au charbon actif, correspondant à des capacités volumiques respectivement de 27.1 et 37.7 g.L^{-1}. Cette amélioration des capacités de stockage sur les matériaux dopés a été attribuée à l'augmentation de la fraction de volume microporeux créé par la présence de charbon active dans le réseau cristallin. Comparées aux capacités de stockage reportées dans la littérature pour d'autres types d'adsorbants, notamment MOF ou MOF-composites, les valeurs obtenues avec les matériaux MIL-101(Cr) dopés au charbon actif sont sensiblement supérieures.

L'étude des performances de stockage mesurées dans des conditions d'équilibre a été complétée par une analyse cinétique du phénomène d'adsorption de l'hydrogène. Celle-ci a été conduite à partir de la mesure par la méthode volumétrique, de la variation temporelle des quantités d'hydrogène adsorbées en excès, déduites de l'acquisition des données de pression et température à chaque instant dans la chambre d'adsorption. Ces mesures ont été réalisées dans une gamme pression basse, entre 0.2 et 5 bar, dans le but de déterminer les coefficients de diffusion intra-particulaires à faible taux de recouvrement. Les courbes cinétiques obtenues pour les différents matériaux testés MIL-101(Cr) purs et dopés, montrent des allures similaires. Ces courbes ont été dans un premier temps modélisées à partir du modèle de la force motrice linéaire (LinearDriving Force LDF), en prenant en compte l'effet des variations de température induites par l'exothermicité du phénomène. Néanmoins, le modèle LDF bien que couramment utilisé, a été développé pour décrire des vitesses dans des conditions où le système est proche de l'équilibre. Cette hypothèse n'est cependant pas vérifiée aux conditions de pression les plus élevées appliquées dans cette étude, si bien que le modèle ne permet pas de décrire convenablement les courbes cinétiques aux pressions de 1 et 5 bar. Afin de mieux décrire les courbes cinétiques expérimentales, un modèle prenant en compte la variation radiale de la concentration adsorbée dans la particule assimilée à une sphère homogène est considéré. Le transfert de matière est alors supposé mettre en jeu une résistance partielle externe, créée par le film entourant la particule, et une résistance diffusionnelle de surface à l'intérieur de la particule. Afin de simplifier le problème, le profil expérimental de température est modélisé par une fonction gaussienne asymétrique. L'emploi de ce modèle permet d'obtenir un bon accord avec les courbes de prises de masses expérimentales mesurées sur toute la gamme de pression considérée dans ce travail. Les diffusivités de surface à concentration quasi nulle sont déduites par ajustement du modèle avec les données expérimentales, moyennant la prise en compte de la correction de Darken. Les valeurs de diffusivité de surface ainsi obtenues dans les conditions de référence à la température de 77K pour le MIL-101(Cr) pur synthétisé d'acide acétique, et dopé à 5 % de charbon actif apparaissent du même ordre de grandeur, respectivement égales à 1.6. 10^{-16} et 0.8.10^{-16} m^2.s^{-1}. Les coefficients de transfert externe k_{ex} dans les conditions expérimentales testées varient en fonction de la pression entre 0.3.10^{-10} m.s^{-1} à 0.2 bar, et 7.4.10^{-10} m.s^{-1} à 5 bar.

Les travaux réalisés ont ainsi permis de démontrer la possibilité de synthétiser des matériaux organo-métalliques de type MIL-101(Cr) purs et dopés avec du charbon actif suivant un protocole simple, ne nécessitant pas d'agent minéralisant toxique, donc aisément extrapolable à l'échelle industrielle. Les résultats expérimentaux montrent un gain sensible des performances de stockage à 77K d'hydrogène sur les matériaux MIL-101(Cr) dopés par l'adjonction de concentrations modérées de charbon actif. Par rapport au matériau non dopé, le gain de capacité d'adsorption en valeur absolue a été ici évalué à 37% en volume et 34% en masse. Les approches de modélisation des courbes expérimentales de prise de masse ont permis la détermination de grandeurs diffusionnelles intra-particulaires de référence, indépendante de la pression. Les diffusivités

intraparticulaires apparaissent peu modifiées par le dopage mais diminuent avec l'augmentation de la fraction de microporosité. Ces données cinétiques couplées celles d'équilibres pourront être utilisées pour prédire par simulation le comportement d'un réservoir de stockage d'hydrogène opérant par modulation de pression dans des conditions cryogéniques. Les performances montrées par les matériaux MIL-101(Cr) dopés au charbon actif encouragent à poursuivre les recherches vers une meilleure compréhension de ces structures et le développement de nouveaux matériaux hybrides comme candidats potentiels au stockage d'hydrogène pour les applications mobiles dans le futur.

Table of Contents

List of Tables

22

23

List of Figures

General Introduction

La demande croissante en énergie ainsi que l'aggravation de la pollution liée aux émissions de dioxyde de carbone CO_2, imposent à ce jour la mise en place de nouvelles sources d'énergie renouvelables et surtout non polluantes. Dans ce contexte, les énergies photovoltaïques, éoliennes ou géothermiques représentent des solutions alternatives. Sources d'énergie primaires, elles permettent de produire de l'électricité et de la chaleur pouvant être ensuite utilisées dans différentes conditions, pour répondre aux besoins et à la demande. Pour des applications stationnaires, les technologies qui doivent être mises en œuvre pour stocker et convertir l'énergie produite par ces sources intermittentes sur des installations stationnaires apparaissent aujourd'hui plus matures que celles requises en vue d'une utilisation mobile. Pour pallier l'épuisement des ressources énergétiques fossiles et répondre aux problématiques environnementales qui leur sont associées, l'hydrogène apparait alors comme une solution alternative à une nouvelle économie de l'énergie. L'hydrogène est un vecteur énergétique qui contient une énergie massique trois fois plus grande que l'essence. Il peut être produit à partir de sources renouvelables ou fossiles, et utilisé en combustion directe ou dans des piles à combustibles. Le stockage d'hydrogène demeure néanmoins un verrou majeur de la filière, qui s'avère encore plus difficile à résoudre dans le cas d'applications embarquées. Les technologies actuelles permettent un stockage sous forme gazeuse à haute pression, un stockage liquide à très basse température et un stockage chimique ou physique. Ces technologies sont envisageables sur des installations stationnaires opérant à plus ou moins grande échelle, par contre, leurs performances technico-économiques sont à ce jour insuffisantes pour servir des applications mobiles. Or, la levée de ce verrou s'avère incontournable dans le cadre du développement d'une économie de l'énergie incluant l'hydrogène. Bien que les stockages gazeux et liquide apparaissent comme les techniques les plus matures, ces dernières font appel à des conditions extrêmes de température et de pression qui ne permettent pas de satisfaire aux spécifications requises pour des applications mobiles, telles que fixées par le Department of Energy (DOE) américain. Afin de répondre aux contraintes de poids, d'encombrement et de sûreté du procédé, le stockage physique par adsorption dans un matériau poreux semble être une solution prometteuse car elle met en œuvre une cinétique rapide et réversible, dans des conditions de température et de pression modérées.

Ainsi, le développement de procédés de stockage d'hydrogène suffisamment performants et acceptables d'un point de vue coûts et sécurité représente un défi actuel majeur. Cette thèse a pour objectif de proposer un procédé de stockage de l'hydrogène par adsorption qui soit extrapolable à grande échelle. Cette méthode requiert l'utilisation d'un matériau qui associe à la fois légèreté, stabilité et grande capacité de stockage. Ce matériau doit aussi pouvoir être produit en quantités industrielles, à partir de substances chimiques disponibles et dont l'utilisation est autorisée par la réglementation REACH. Après une étude bibliographique préliminaire, un type de matériau à structure mésoporeuse, MIL-101(Cr) faisant parti de la famille des réseaux organo-métalliques (''Metal Organic Frameworks'', MOF) a été sélectionné, en considérant d'une part la possibilité d'adapter les conditions de synthèse aux contraintes de production industrielle, et d'autre part la stabilité chimique ainsi que les grandes surfaces spécifiques pouvant être développées. Afin d'accroître encore les capacités d'adsorption en hydrogène de ce type d'adsorbant, l'adjonction d'un agent dopant microporeux sous forme de poudre de carbone activé a par ailleurs été envisagée.

I.   Context and applications

The energy demand grows with global population and economic development because the consumption is related to every domain of human activities such as residential, commercial, industrial as well as transportation (IEA, 2015a).

Among all types of fuels for primary energy production, the fossil fuels take major part with a percentage which is always above 80% for the past decades (The World Bank Databank, 2015). While global population densities keep growing, the worldwide reserves of energy as a form of fossil fuels are depleting. Therefore, it is crucial to develop alternative energy sources and carriers in order to sustain the global demand.

Apart from the fossil fuel limitations and demand, another important issue related to our energy supply is environmental pollution. Scientists have observed that carbon dioxide (CO_2) or so-called greenhouse gases (GHG) concentrations in the atmosphere have been increasing steadily over the past century, compared to the pre-industrial era. The concentration of CO_2 in the air in 2013 was about 40% higher than that in the mid-1800s (Stocker et al., 2013). The rise of CO_2 concentration causes anthropogenic warming and sea level rise which can further induce polar ice melting, permafrost defrosting and the increase of extreme weather phenomena.

The rise of global consumption of energy and the CO_2 emissions are presented by continent in Figure I.1. Clearly, the global demand for energy has nearly doubled from the year 1980 to 2012 as well as the CO_2 emissions and this trend will not be changed by decency according to IEA (2014).
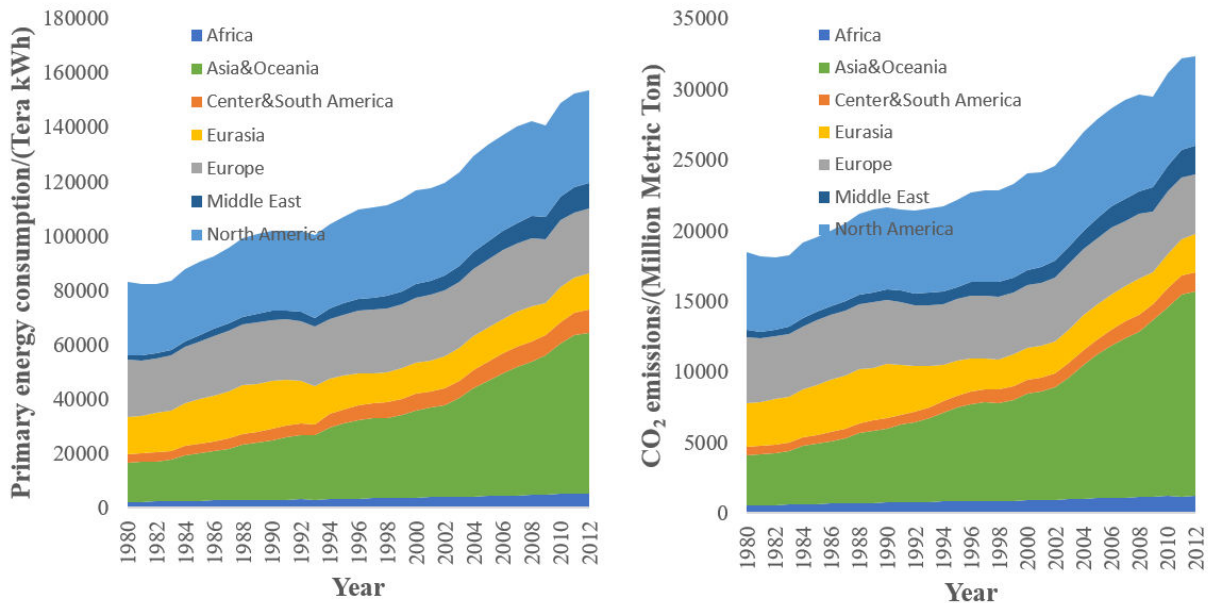
Figure I.1: World energy consumption and CO₂ emissions from 1980 to 2012, presented by continent (IEA, 2015b).

In this scope, all countries are responsible for minimizing their CO_2 emissions and improving the share of clean energy consumption in total energy consumption. According to the United Nations Framework convention on Climate Change (UNFCCC) and Kyoto Protocol (KP), it has set binding obligations on the industrialized countries to reduce their emissions of CO_2. According to 21st Conference of Parties (COP 21), all countries are engaged to limit the climate warming by 2°C compared to the pre-industrial era. Hence, the development of renewable energy generation meets to global political targets.

Renewable energy such as the sunlight, the wind, the sea waves and the geothermal heat becomes important in energy generation. The total global renewable power capacity exceeded 1470 GW in 2012, which represents an increase of 8.5 % compared to 2011. Wind power accounted for about 39 % of renewable power capacity added in 2012, followed by hydropower and solar photovoltaic power, each accounting for approximately 26 % (Zervos, 2013). In Europe, the electricity generation using renewable energy sources has been doubled from 2003 to 2013 (Eurostat, 2015). In France, the renewable energy shares in total energy consumption accounted for 20.7 % in 2013 (RTE, 2013). However, these energy sources are intermittent and vary in season or day/night. The produced energy could be stored in an intermediate carrier such that can be released during high energy demand periods for end applications. Electricity, heat as well as solid and liquid fuels can be used as an energy carrier in an energy storage system. The comparison of different types of energy storage systems are presented in Table I.1.

Table I.1: Comparison of different energy storage system, according to Cau et al. (2014).

Technology	Cost/ ($.kWh^{-1})	Durability/ (year)	Power density/ (W.kg^{-1})	Gravimetric energy density/ (Wh.kg^{-1})	Energy Efficiency/ (%)
Li-ion battery	600-2500	5-20	100-5000	75-250	85-90
Super-capacitor	300-2000	20+	500-5000	0.05-30	97
Pumped-hydro	5-100	40-100	-	0.5-1.5	70-87
Hydrogen	2-20	30	-	400-1000	-
Flywheel	1000-5000	15-20	400-1600	5-130	80-99
Pressurized air	2-50	20-100	-	30-60	40-80

From Table I.1, it can be observed that, compared to other energy storage system, hydrogen has a low cost and a high gravimetric density. By using a fuel cell for energy conversion, the energy conversion efficiency can reach 85 % which makes hydrogen a good candidate for energy storage (Mekhilef et al., 2012).

In fact, since 1990s a strong interest of international scientific and industrial community has been addressed for the possibility of developing a global 'hydrogen economy' (see Figure I.2) based on the hypothesis that hydrogen could be used as a future energy carrier (CEA, 2004; Deschamps et al., 2015; Hetland and Mulder, 2007; McDowall and Eames, 2006).
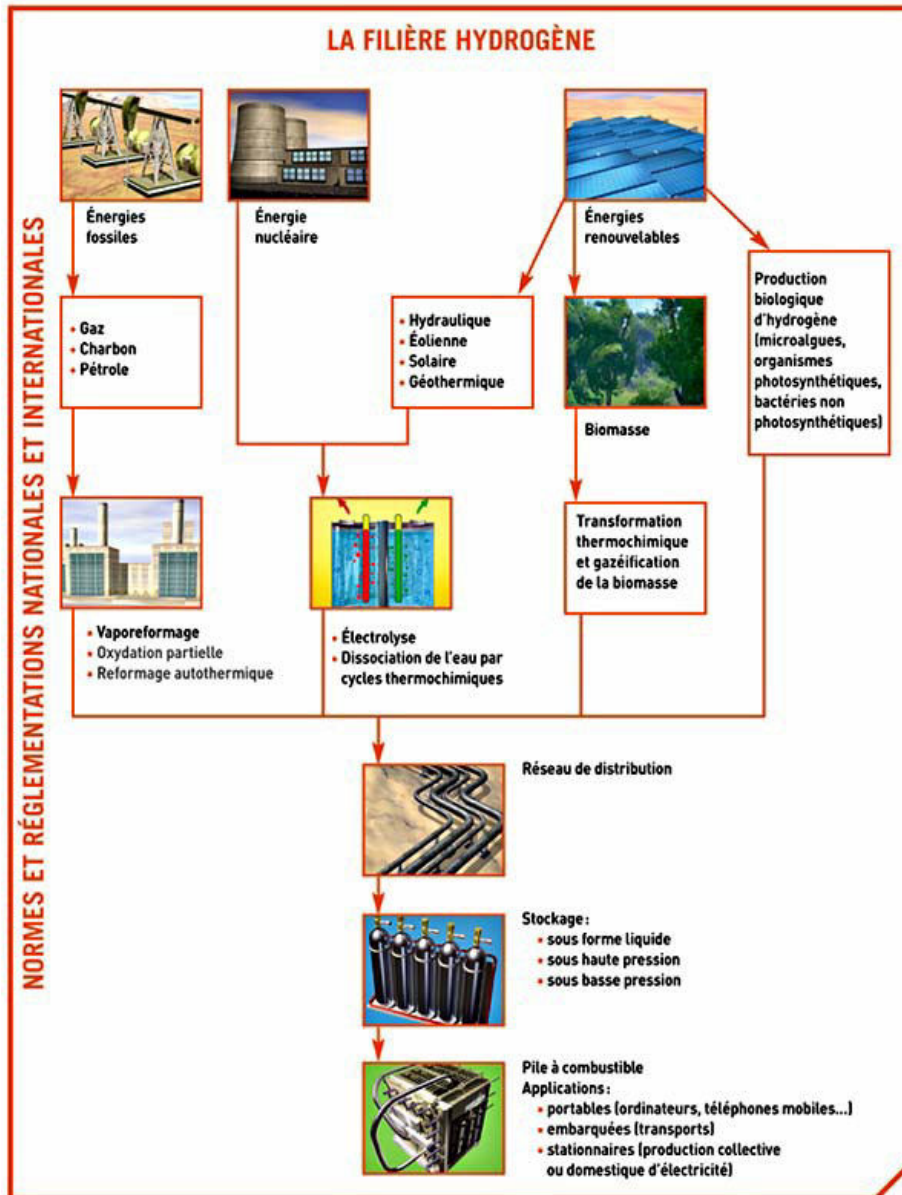
Figure I.2: Hydrogen economy with production, distribution, storage and utilization of hydrogen, according to CEA (2004).

In Europe, different stationary hydrogen projects have been developed, for instance, MYRTE, GRHYD and Hybridkraftwerk projects: (i) The Mission hYdrogène Renouvelable pour l'inTégration au réseau Electrique (MYRTE) platform consists of a solar photovoltaic (PV) array, a Proton Exchanged Membrane (PEM) fuel cell rated at 210 kW, an electrolyser, several storage tanks (hydrogen, oxygen, and water), a thermal management system, and an electricity conversion associated with various subsystems for the purpose of stabilizing the electrical network of Corsia ("MYRTE hydrogen energy storage test powers up in Corsica," 2014). (ii) The Gestion des Réseau par l'injection d'Hydrogène pour Décarboner les énergies (GRHYD) project, led by GDF-Suez (Engie) and different partners, aims to transform electricity from renewable energy produced

35

outside peak periods into hydrogen and also to use this hydrogen in combination with natural gas for heating, hot water production and as a fuel for buses ("GDF Suez, McPhy in French GRHYD project on methane, hydrogen," 2012). Two demonstration projects have been launched, one is an industrial scale Hythane® fuel (hydrogen + methane) project where a natural gas vehicle fueling station will be adapted to a hydrogen/natural gas mixture of 6% hydrogen at first then 20% to fill natural gas-fuelled buses; the other project involves the injection of hydrogen into the natural gas distribution network. A residential neighbourhood (in Dunkerque) of some 200 housing units will be heated using a mixture of hydrogen and natural gas, with the hydrogen content varying up to a maximum volume of 20 %. (iii) The Hybridkraftwerk project, which is led by Enertrag, a German company specialized in energy production by renewable energy source and Total, combines grid-connected wind turbines, two biogas plants and an electrolyzer (500 kW) which can produce and store 1350 kg of hydrogen by using 5 storage tanks at 30 bar. The hydrogen will be mixed with biogas for energy conversion, either to produce electricity or to produce heat for residential usage (ENERTRAG, 2015).

The choice of hydrogen as one of the main future energy carrier has important advantages related to its fundamental properties. Gaseous hydrogen is colorless, odorless, tasteless and nontoxic, and it is a strong reducing agent even at room temperature. Its physical properties are listed in Table I.2. Hydrogen is very energetic and contents a big amount of energy per unit of mass (gravimetric energy density). Compared to gasoline, its energy density per unit of mass is three times higher. This comparison is shown in Table I.3.

Table I.2: Physical properties of hydrogen, adapted from Gupta and Pant (2008).

Property	Value
Molecular weight	2.01594 g.mol^{-1}
Density of gas (at 0°C and 1 atm)	0.308987 kg.m^{-3}
Density of solid at -259°C	85.8 kg.m^{-3}
Density of liquid at -253°C	70.8 kg.m^{-3}
Melting point temperature (at 1 atm)	-259 °C
Boiling point temperature (at 1 atm)	-253 °C
Critical temperature	-240 °C
Critical pressure	12.8 atm
Critical density	31.2 kg.m^{-3}
Heat capacity of gaseous hydrogen (at 1 atm)	14.4 kJ.kg^{-1}.K^{-1}
Flammability	4-75 vol%, with ignition energy 0.02 mJ

Table I.3: Gravimetric and volumetric energy density comparisons between hydrogen, methane, propane, gasoline and diesel, calculated based on lower heating value (LHV), according to Gupta and Pant (2008).

Fuel	Energy density per unit of mass/ $(MJ.kg^{-1})$	Energy density per unit of volume (gas)/ $(MJ.m^{-3}$ at 1 atm, 15°C)	Energy density per unit of volume (gas)/ $(MJ.m^{-3}$ at 200 atm, 15°C)	Energy density per unit of volume (gas)/ $(MJ.m^{-3}$ at 690 atm, 15°C)	Energy density per unit of volume (liquid)/ $(MJ.m^{-3})$
Hydrogen	140.4	10	1825	4500	8491
Methane	43.6	32.6	6860	-	20920
Propane	28.3	86.7	-	-	23488
Gasoline	48.6	-	-	-	31150
Diesel	33.8	-	-	-	31435

In our environment, hydrogen exists almost under the elemental form and is associated with oxygen or carbon atoms. Therefore, pure hydrogen (H_2) which is an energetic vector has to be produced to be used as an energy carrier.

I.1. Hydrogen production

Hydrogen is the most abundant element in the universe, however, less than 1% of hydrogen on earth exists in dihydrogen form but in compounds like water (H_2O) or hydrocarbons.

The mature technologies for hydrogen production are steam reforming of natural gas, partial oxidation of hydrocarbons or cracking of hydrocarbons, gasification of coal, electrolysis of water (Board on Energy and Environmental Systems National Research Council et al., 2004). It is reported that hydrocarbons (natural gas and petroleum) account for 78% of the world's hydrogen production (Gupta and Pant, 2008) which produce greenhouse gases. The energy requirement for electrolysis of water can be supplied by renewable energy sources like wind or sunshine which are carbon dioxide emission free. Besides, biological production of hydrogen from biomass is also an option for hydrogen production.

Hydrogen can be produced from hydrocarbons by means of steam reforming of natural gas (steam methane reforming-SMR) or partial oxidation (PO_X) (Muradov, 2008).

The steam reforming of natural gas or other light hydrocarbons for hydrogen production involves two chemical reactions:

$$CH_4 + H_2O \xrightarrow{350\,°C} 3H_2 + CO$$

$$CO + H_2O \xrightarrow{200\,°C} H_2 + CO_2$$
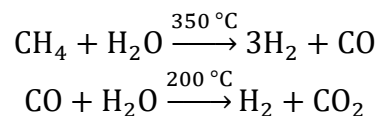
This process is inexpensive and efficient, with an efficiency of about 70% based on the lower heating value of hydrogen (Department of Energy, 2015). The steam reforming of such primary fuels (water gas shift) releases CO_2 to atmosphere although the CO_2 can be removed through carbon sequestration. Meanwhile, the natural gas is non-renewable and cannot hold for a sustainable hydrogen economy. Hence, it can be a transitional solution only.

Partial oxidation of natural gas is the process where hydrogen is produced through the partial combustion of methane with oxygen to yield carbon monoxide and hydrogen.

Coal is the most plentiful fuel on earth and is expected to be an important energy source for the next hundreds of years. The coal can be converted into syngas in a gasifier (*e.g.*, fixed bed, fluidized bed or entrained flow) (Lin, 2008). The gas-phase water-gas shift reaction is important which controls the equilibrium of CO, H_2, CO_2 and H_2O (Fisher-Tropsch process).

Water is extremely abundant on earth. The decomposition of water to produce hydrogen requires energy input which can combine to a renewable energy source (Rozain and Millet, 2014). Different types of water electrolysis cells have been developed, namely, alkaline water electrolyser, proton exchange membrane (PEM) water electrolyser, high temperature water electrolyser based on solid oxide fuel cell (Millet, 2012). Current low temperature hydrogen electrolysis can offer a conversion efficiency about 62%, based on its lower heating value (Holladay et al., 2009).

Most of the biomass sources contain a large amount of hydrogen. The conversion of biomass to hydrogen is similar to that of coal. Gasification of biomass results in a syngas which consists of carbon monoxide, carbon dioxide and hydrogen. Compared to coal, biomass is a renewable energy resource which has less impact on the environment. However, the Department of Energy (2015) reported that the cost of direct gasification of lignocellulosic biomass is about 3 times larger than using steam reforming of natural gas (Spath et al., 2000). A lower conversion efficiency (35%) was also reported (Department of Energy, 2015). Other biological hydrogen productions involving, *e.g.* fermentation and photosynthesis suffers also the drawback of low efficiency.

I.2.   Hydrogen distribution

Hydrogen distribution can be achieved over the road and the sea in cryogenic liquid tankers or *via* gaseous tube trailers. Nevertheless, gas grids are considered to be the main option for distribution of large amounts of hydrogen. Gaseous hydrogen can then be distributed to the point of use after injection and transportation in pipelines. This mode of distribution dated back to 70 years ago and several thousand kilometres of hydrogen pipelines have been constructed globally (IEA, 2007). In France, Air Liquide constructed several hydrogen pipelines between the northern France and Belgium (650 km) and in the region of Lyon (50 km).

Four major issues for gaseous hydrogen delivery *via* pipelines are analysed and they are listed as following:

- *High initial capital investment costs*. Even though transporting gaseous hydrogen *via* the existing pipelines is a low-cost option by mixing hydrogen with natural gas (hydrogen volume percentage < 20 %). However, substantial modifications may be required for delivering pure hydrogen (Department of Energy, 2015).
- *Hydrogen embrittlement of steel pipelines and alternative*. Current welding technology for pipeline impacts the steel microstructure the can exacerbate hydrogen embrittlement issues.

Eliminations or mitigation of hydrogen embrittlement is the key to ensuring the safe, cost-effective and long-term reliability of hydrogen delivery pipeline infrastructure (Feng, 2006).

- *Hydrogen leakage and integrity monitoring sensors*. The hydrogen molecule is very small and diffuses rapidly compared with other gases such as natural gas. Hence, low-cost leak detection sensors are needed to protect against third-party damage-related and other mechanical failures (Department of Energy, 2015).

- *Hydrogen compression*. Gaseous hydrogen contains only one-third of the energy of natural gas by volume (see Table I.2). The output of hydrogen needs to be under higher pressure to make sure of energy content per volume. Current technologies of compressors need to be enhanced for large-scale hydrogen delivery (Leighty et al., 2006).

I.3. Hydrogen conversion

Hydrogen is an energy vector that can be directly used as a fuel for internal combustion engines (ICEs) or as a chemical carrier for electric power storage and generation in fuel cells.

Combustion of hydrogen in the presence of oxygen only forms water. However, in real combustion conditions, the gaseous reactants are not pure and unwanted by-products such as carbon monoxide (CO) or carbon dioxide (CO_2) as well as nitrous oxides (NO_X) are produced. Hydrogen internal combustion engine (HICE) has been developed for nearly 40 years. Tokyo City university developed one of the first HICE for automotive usage (Furuhama et al., 1978). Nowadays, current petrol engines can be converted to run on hydrogen by injecting hydrogen through a specialized spark plug. In 2005, BMW has developed a bifueled HICE functioning with both hydrogen and gasoline. However, the control of NO_X emission requires being improved. Moreover, the energy conversion efficiency of such engines is limited by the Carnot cycle efficiency ($\eta_{carnot}=1-T_c/T_h$ with T_c and T_h the temperature of the cold reservoir and the hot reservoir, respectively) (Schlapbach and Züttel, 2001). Finally, HICE is not deemed to be a sustainable solution due to the energy efficiencies associated with the current petrol engines (Schlapbach, 2009).

Another alternative is fuel cell which combines hydrogen with oxygen from air with the only by-product being water. In a fuel cell, positively charged hydrogen ions formed at the cathode react with oxygen at the anode through an electrolyte. Different types of fuel cells have been developed depending on the nature of electrolyte: potassium hydroxide, polymer membrane, immobilized liquid molten carbonate, immobilized liquid phosphoric acid, ion exchange membrane or ceramic (Hess et al., 1995). For on-board vehicular use, Proton Exchange Membrane (PEM) fuel cells have undergone significant developments in recent years. The membrane then most often composed of a polymeric membrane, such as Nafion®, whereas metal catalysts such as Platinum or Iridium, are deposited on the electrodes. Both these two specificities make PEM fuel cells very costly today, but improvements of their performances are expected to increase the current density so that better capacities should be obtained with the same amount of material. An advantage of the PEM

technology is its capacity, but PEM fuel cells are easily poisoned by impurities such as CO. Cost reduction, reliability and poison resistance are still obstacles for their wide range applications.

A schematic representation of a PEM fuel cell is shown in Figure I.3. PEMs have a relatively low operating temperature ranging between 50 and 80 °C with an energy conversion efficiency about 60 % (Schlapbach, 2009). If some of the waste heat is reused, then the efficiency can reach 80 % (Barbir, 2012).
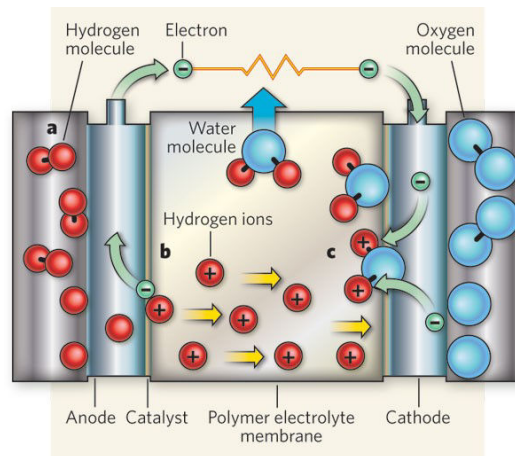
Figure I.3: Proton Exchange Membrane (PEM) fuel cell structure, according to Schlapbach (2009)

I.4. Hydrogen storage

The storage of hydrogen represents the crucial problem of the hydrogen network. Considering its volumetric energy density (see Table I.3), hydrogen appears by far less advantageous than other fuels. Moreover, its high flammability implies additional constraints for its storage which can be achieved only by 3 ways, including gas compression, liquefaction or storage within solid-state materials. The latter technique involves the hydrogen storage by chemical or physical interactions with a solid material.

Hydrogen storage is considered for both stationary and mobile applications. As shown previously, it is not really difficult to implement hydrogen in stationary applications (MYRTE, GRHYD, Hybridkraftwrekproject). However, the storage for mobile uses is associated with a lot of constraints, *i.e.* the mass, the volume, the filling time, the security. Considering this challenge and the constraints associated, the aim of this thesis concerns the study of hydrogen storage for mobile applications. Moreover, a pre-study of a scaling up system combining hydrogen production, storage and utilization will be performed. To reach these objectives it is then necessary to study the criteria, the objectives and the different technologies associated with the onboard storage.

II. Scientific and strategic approaches

II.1. Hydrogen storage: criteria and objectives

The criteria need to assess and to compare different hydrogen storage solutions are the volume, the weight, the cost of entire equipment, its safety, the energy requirements as well as the reversibility and charging/release rate of hydrogen to and from the reservoir. However, the storage system specifications vary and depend on hydrogen uses. In a stationary storage situation such as gas station, the weight and the volume of the system becomes less important while for mobile storage, the weight and the volume of storage system become more important issues.

Certain early markets of hydrogen usage which require stationary hydrogen storage are today considered as mature. These include: (i) stationary power such as backup power for telecommunications towers, emergency services, and basic infrastructure (*e.g.*, water and sewage pumps); (ii) portable power such as personal laptop battery chargers, portable generator sets (gen-sets), or mobile lighting; (iii) material handling equipment such as forklift trucks, pallet jacks, and airport baggage and pushback tractors, according to Department of Energy (2015).

Hydrogen storage systems for automotive applications mobilize a lot of research efforts. The American Department of Energy (DOE) places this application as a priority and has set since 2005 some technical milestones to be achieved to develop a storage technology viable for onboard light-duty fuel cells enabling vehicle transportation over 300 miles (483 km). These specified targets have been recently modified, in May 2015, to match more realistically the current results of worldwide scientific research (Table II.1).

Table II.1: Technical system targets for onboard hydrogen storage for light-duty vehicles (Department of Energy, 2015)

Target	2010 (new)	2010 (old)	2015 (new)	2015 (old)	Ultimate
System Gravimetric Density	[4.5]	[6]	[5.5]	[9]	[7.5]
[wt%] or (kWh.kg^{-1})	(1.5)	(2.0)	(1.8)	(3)	(2.5)
System Volumetric Density	[28]	[45]	[40]	[81]	[70]
[g.L^{-1}] or (kWh.L^{-1})	(0.9)	(1.5)	(1.3)	(2.7)	(2.3)
System Fill Time of 5 kg hydrogen	[4.2]	[3]	[3.3]	[2.5]	[2.5]
[min] or (kg.min^{-1})	(1.2)	(1.67)	(1.5)	(2.0)	(2.0)
Storage System Cost	-	[133]	-	[67]	-
[\$.kg^{-1} H$_2$] or (\$.kWh$_{net}^{-1}$)	-	4	-	2	-
Delivery pressure (bar), Fuel Cell/Internal Combustion Engine	(4/35)	(4/35)	(3/35)	(3/35)	(3/35)

II.2. Hydrogen storage: comparison of different methods

Hydrogen may be stored in physical form under high pressure at ambient or sub-ambient temperatures, or as a cryogenic liquid near its normal boiling point of 20 K. However, these traditional mechanical means of hydrogen storage (compression or liquefaction) are energetically and financially expensive. An alternative storage method such as cryocompression of hydrogen has been developed. Additionally, hydrogen may be stored as a solution in metals, bonded to other elements as hydrogen compounds or adsorbed as a diatomic molecule in porous solid (Durbin and Malardier-Jugroot, 2013; Harris et al., 2004; Züttel, 2004).

II.2.1. Mechanical storage of hydrogen

Hydrogen storage by compression

Typically, an efficient compressed hydrogen storage system requires a working pressure of 700 bar and a volume of 220 L to store 5 kg hydrogen gas (Walker, 2008). The mass of the cylinder usually made of steel represents an important constraint. To avoid this, composite cylinders have been developed so that operating pressures and reservoir masses have been then considerably reduced (Gao and Krishnamurthy, 2008). A type IV vessel which is a composite lightweight cylinder with a polymer liner-like high density polyethylene HDPE, to prevent gas diffusion and load-bearing composite overwrap was so designed, as illustrated in Figure II.1. This system reaches a gravimetric hydrogen uptake capacity of 1.7 kWh.kg^{-1} and a volumetric hydrogen uptake capacity of 0.9 kWh.L^{-1} (Department of Energy, 2015). This storage method is used in the forthcoming Toyota Mihai hydrogen fuel cell vehicle (Bimbo et al., 2015). However, the volume of the storage tank remains large for onboard use whilst the high pressure represents an important safety problem.
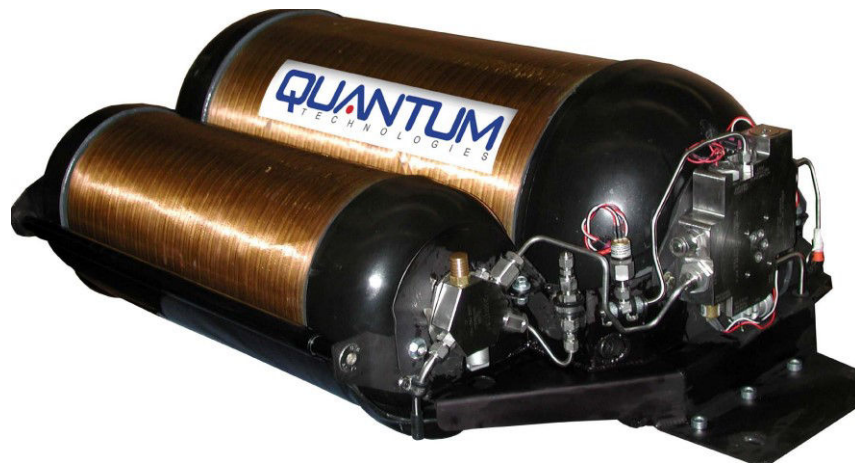
Figure II.1: GM HydroGen3 "Compressed 700" 10,000-psi (70 MPa) Hydrogen Fuel Storage System (Quantum technologies)

Hydrogen storage by liquefaction

In view of a vast hydrogen infrastructure, very large quantities of hydrogen may be distributed and stored as a liquid at about 20 K (-253°C). Today hydrogen liquefiers are a mature technology for capacities up to 30 ton.day[-1] and with energy requirements of 30 to 45 MJ per kilogram of liquefied hydrogen while the world's capacity today is around 350 ton.day[-1], which is lower than the required capacity for fuelling a mobility largely based on hydrogen (Valenti, 2016). Diverse investigations indicate though that liquefier capacity as high as 900 ton.day[-1] as well as energy requirements as low as 18-25 MJ.kg^{-1} may be achieved (Valenti, 2016).

Liquid hydrogen has the advantage to offer high volumetric storage capacity. The volumetric energy density of liquid hydrogen is far higher than compressed gas and reaches 70.8 g.L^{-1} at -253 °C and 1 atm. However, the liquefaction of hydrogen consumes a lot of energy and is very costly. The cost of hydrogen liquefaction was estimated to be 1-1.5 \$.kg^{-1}, compared to 0.15-0.6 \$.kg^{-1} for compressions at 700 bar (Ekins and Bellaby, 2008). Liquid hydrogen can be stored in a cryostat, or a double walled container. However, the problem is the boil-off effect which causes leakages. The boil-off effect happens because liquid hydrogen evaporates easily during delivery and refuelling or when it adsorbs heat from the environment. The tank must be vented every 3-5 days during inactivity to prevent dangerous and costly boil-off lost. Meanwhile, the container cannot be stored in a confined area during several days. For instance, a full 5 kg tank affected by a 1 W heat would lose all its hydrogen in approximately 3 weeks (Aceves et al., 2006).

Hydrogen storage by cryocompression

The newest hydrogen storage technologies combine compression and cryogenic storage of hydrogen. Liquid hydrogen vessels can be pressurized and create a combination of liquid hydrogen and high pressure hydrogen in the head space (Satyapal et al., 2007). The density of liquid hydrogen increases from 70 g.L^{-1} at 1 atm to 87 g.L^{-1} at 237 atm (Ahluwalia et al., 2010). According to these authors, cryocompressed vessels are able to withstand heat since hydrogen within the vessel can be vented at a higher temperature. Venting stops when the tank reaches ambient temperature and the pressure within the vessel is maintained so that the hydrogen density remains at 30% of the initial liquid hydrogen density. This is better for storage and makes the tanks safer during dormant periods. Moreover, pressurized hydrogen becomes a supercritical fluid at a pressure higher than 13 atm and this can eliminate unused space in the container which increases the volumetric energy density.

Otherwise, cooling compressed hydrogen gas is another option to enhance hydrogen storage performance. Compressed hydrogen gas tanks are often cooled to liquid nitrogen temperature which can increase the volumetric capacity by three times when comparing to non-cooled hydrogen. It has been found that 740 atm is required to store 4.1 kg of hydrogen in 100 L at room temperature but only 148 atm is required to store the same volume at 77 K (Paggiaro et al., 2010).

II.2.2. Chemical storage of hydrogen

Hydrogen storage by chemical reaction with water

Hydrogen can be generated through a chemical reaction of water and other chemical compounds, *e.g.* sodium metal, which can be produced by reducing NaOH in a solar furnace. By calculation, the storage of hydrogen by using sodium has a gravimetric density of 3.0 wt% and if lithium is used to replace of sodium, the gravimetric density increases to 6.3 wt% (Züttel, 2004). This storage method suffers different problems, especially the controlling of the reduction of the chemical compounds to produce original metal (Züttel, 2003) and is nowadays not adopted for on-board hydrogen storage applications.

Hydrogen storage in Metal hydrides

Typical case of chemically bonded hydrogen is metal hydrides, where metals and metal alloys react with hydrogen (Schlapbach and Züttel, 2001) according to the following reaction:

$$M + H_2 \underset{\longleftarrow}{\overset{reversible}{\longrightarrow}} MH_x$$
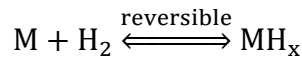
Molecular hydrogen is initially physisorbed onto the surface of the metal. The molecular hydrogen splits into atomic hydrogen which migrates across the surface. The diffusion of atomic hydrogen into local interstitial sites creates a solid-solution, which is called the α-phase. The α-phase where hydrogen atoms locate randomly in the metal will transform into an energetically favorable β-phase by concentrating locally hydrogen. This transformation is illustrated in Figure II. 2.
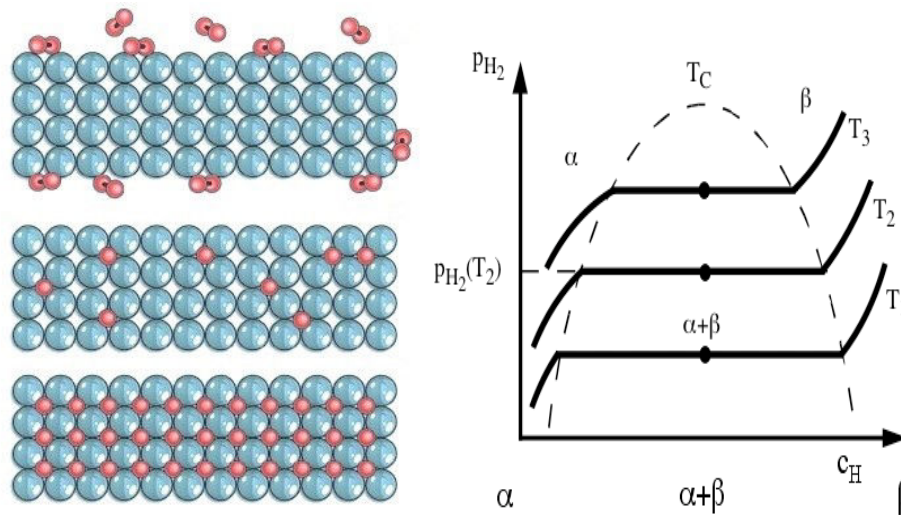
Figure II. 2: Illustration of the interaction of hydrogen gas with a metal at different stages to form a metal hydride: adsorbed on surface (top-left), α-phase (middle-left) and β-phase (bottom-left) and the pressure-composition-temperature (PCT) phase diagram (Dornheim, 2011; Schlapbach, 2009)

For metal hydrides constituted of alloy, usually there exists one element (A) with high affinity for hydrogen and one element (B) with low affinity of hydrogen. The latter, which is not used for hydrogen storage, is helpful for the dissociation of hydrogen (Züttel, 2003). Element A is typically

a transition, rare earth or alkaline metal such as La, Ti, Zr and Mg with B element such as Ni, V, Cr, Mn and Fe.

Mg_2Ni is the first hydrogen storage material found in the 1960s, which can reversibly react with H_2 to form Mg_2NiH_4 which has a hydrogen uptake capacity of 3.6 wt% (Reilly and Wiswall, 1968). Later, hydrogen storage in $LaNi_5$ (Van Vucht et al., 1970) was discovered and have relatively large volumetric storage capacity and other hydrogen storage alloys, such as FeTi (Reilly and Wiswall, 1974), $ZrCr_2$ and V based solid solution alloy (Wiswall and Reilly, 1972) were discovered. The electrochemical performance of $RENi_5$ (RE-Rare Earth metals) based metal hydrides promoted the invention of Ni-MH battery in the 1980s (Cuevas et al., 2001). Recent research found that RE-Mg-Ni based AB_3 type alloy (Young and Nei, 2013) can meet the demands of pursuing higher energy density of Ni-MH battery. However, metal hydrides have low gravimetric capacities for the usage of heavy metal elements which appears to not be suitable for mobile applications (vehicles) (Reilly and Sandrock, 1980). Nevertheless, they can be used for stationary and marine applications such as boats and submarines (Dantzer, 2002).

In general, light elements, namely Li, B, C, N, Na, Mg, Al and Si should be the components of high capacity hydrogen storage materials because their hydrides have high gravimetric and volumetric densities. However, the light-weight hydrides generally suffer from poor reversibility under moderate temperature and pressure conditions due to over high thermodynamic stability and/or slow kinetics (Wang et al., 2016). Mg shows a theoretical gravimetric storage capacity of 7.66 wt% and its hydride formation has a low plateau pressure around 1 bar (Sakintuna et al., 2007) for MgH_2 metal hydride. Various Mg-based alloys have been investigated for reversible hydrogen storage, and the alloying elements include rare earth metals RE (Darriet et al., 1980; Kamegawa et al., 2006; Ouyang et al., 2007; Pezat et al., 1980), transition metals TM (Bobet et al., 2001; Liang et al., 1999; Pozzo and Alfe, 2009) and other metals such as Al, Sn, In and Pd (Zaluski et al., 1995; Zhong et al., 2011a, 2011b). The H in MgH_2 has partial ionic bonding with Mg and the formation enthalpy of MgH_2 reaches 75 kJ.mol^{-1} (Stampfer et al., 1960). This is the intrinsic reason which explains that the alloying elements would be expelled from MgH_2 when Mg-based alloys are hydrogenated, which makes the thermodynamic tuning of MgH_2 difficult by alloying. The development of novel Mg-based hydrides is intended to change the binding energy of Mg with H by partial substitution with the elements having weak bond with H such as TMs (Fe, Co, Ni) (Bobet et al., 2000; Cui et al., 2013; Didisheim et al., 1984; Dong et al., 2015) and non-TMs (Al, Ag, Cd, In) (Si et al., 2013; Skripnyuk and Rabkin, 2012; Zhong et al., 2011a, 2011b). Recent studies also focused on the kinetics of absorption in Mg-hydride. By introducing catalysts like V_2O_5 (Khrussanova et al., 1989) or NbO_5 (Dornheim et al., 2007), the charging time can be less than two minutes at 250 °C, which achieved the charging time target set by DOE (see Table II.1).

Complex hydrides use light-weight elements to form tetrahedral complex anions such as borates $-BH_4^-$ and metal alanates $-AlH_4^-$. Their formation and release of hydrogen consist of a series of decomposition and recombination reactions. High volumetric and gravimetric hydrogen density has been found for $LiBH_4$ (18.5 wt%) (Eberle et al., 2009). However, during hydrogen regeneration, only three-quarter of the hydrogen can be released upon melting temperature of 280°C (Harris et al., 2004). Moreover, their formation requires high temperature (600°C) and high pressure (350

bar) (Orimo et al., 2005)). In the past two decades, effective strategies such as adding a catalyst, nanoscaling and destabilization have been successfully developed to improve hydrogen storage properties of complex hydrides.

Hydrogen storage in covalent hydrides

Hydrides such as organic hydrocarbons and ammonia are also studied. Researchers have concentrated on the development of organic chemical hydrides consisting of reversible catalysis pairs such as decalin dehydrogenation/naphthalene hydrogenation, methylcyclohexane dehydrogenation/toluene hydrogenation and tetralin dehydrogenation/naphthalene hydrogenation (Hodoshima and Saito, 2008). The crucial point of non-metallic hydrides is the process of dehydrogenation. For example, the dehydrogenation of cyclohexane requires a temperature of 300°C to form benzene (Biniwale et al., 2005) and ammonia requires more than 400°C to break down and generate hydrogen with the presence of Ni or Ru catalysts (Li et al., 2005). Despite this high temperature requirement for the formation and regeneration, the absorption/desorption kinetics of hydrides is very slow (Sakintuna et al., 2007).

II.2.3. Physical storage of hydrogen

The volumetric storage density of light gases such as hydrogen can be increased through attractive interactions between hydrogen molecules and the surface of an adsorbent, resulting, at low pressure, in significantly higher uptake over compression at the same thermodynamic conditions. However, high capacity hydrogen storage in porous materials only achieves at very low temperature for physisorption until now, because of the weak interaction between the hydrogen molecule and the adsorbents. The binding energy is usually less than 10 kJ.mol^{-1}, and the hydrogen storage capacity is usually about 1 wt% at ambient temperature (Schlapbach and Züttel, 2001).

Different porous materials such as carbons (carbon nanotubes (CNTs), activated carbons (ACs), templated carbons), zeolites, and Metal Organic Frameworks (MOFs) have been investigated for hydrogen storage. According to the most recent studies (Bimbo et al., 2015), high-surface area materials tailored for hydrogen storage are a promising route for storage in mobile applications and cryocharging is a promising strategy for hydrogen storage system since it increases volumetric densities and avoids energy penalties of operating at high pressure and/or at low temperature.

Hydrogen storage in carbon based adsorbents

Carbon-based structures which have been investigated for hydrogen storage include carbon nanotube-based structures, activated carbons and templated carbon.

Carbon nanotubes consist of rolled up graphite sheets into a cylindrical shape. Single-wall carbon nanotubes (SWCNTs) concerns only one graphite sheet and have an inner diameter from 0.7 to several nanometres. Multi-wall carbon nanotubes (MWCNTs) are made of concentric rolled-up graphite sheets with adjacent distance around 0.3 nm and the number of sheets varies from 2 to more than 100 (Popov, 2004).

A brief summary of hydrogen uptake data reported for carbon nanotubes at 77 K is shown in Table II.2.

Table II.2: Hydrogen uptake capacities reported in the literature, for both SWCNTs and MWCNTs

	Specific surface area $(m^2.g^{-1})$	Condition (bar, K)	Gravimetric capacity (wt%)
SWCNT	780	1, 77	0.8 (Takagi et al., 2004)
	1300	1, 77	1.8 (Takagi et al., 2004)
	285	80, 80	8.25 (Ye et al., 1999)
	-	60, 77	3.94 (Karikkethu Prabhakaran et al., 2011)
MWCNT	1220	1, 77	0.9 (Jordá-Beneyto et al., 2007)
	1220	10, 77	1.5 (Jordá-Beneyto et al., 2007)
	-	1, 300	0.25 (Wu et al., 2000)

Activated carbons can be produced from a variety of natural or synthesized precursors, and develop large specific surface up to 3000 $m^2.g^{-1}$. The activation process can be either physical or chemical. Physical activation consists in heating a carbonized material up to 700°C to 1000°C in the presence of oxidizing gases such as carbon dioxide (CO_2) or water steam. For chemical activation, the carbonaceous precursor is directly heated from 500°C to 800°C in the presence of dehydrating substances such as zinc chloride ($ZnCl_2$), phosphoric acid (H_3PO_4) or potassium hydroxide (KOH). On the opposite of carbon nanotubes, activated carbons are characterized by highly disordered nanostructures, as illustrated in Figure II.3.
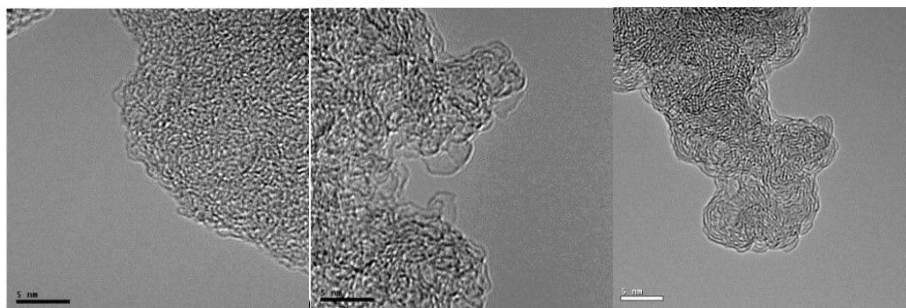
Figure II.3: Transmission electron microscopy (TEM) images of disordered nanostructures of activated carbon (Pré et al., 2013a).

Norit produced a large range of activated carbons, some of them were reported to have a hydrogen uptake as high as 2.14 wt% at 1 bar and 77 K (Nijkamp et al., 2001). Other activated carbon

materials with specific surface area of 2000 $m^2.g^{-1}$ showed a maximum hydrogen uptake nearly 5 wt% at 30 bar and 77 K (Dumont et al., 2006).

Zeolite templated carbon with regular pore geometries can be produced by chemical vapour deposition of carbon over a zeolite structure following by acid washing to remove the zeolite template (Kyotani et al., 1997). Hydrogen storage capacities of 6.0 and 6.9 wt% were reported at 20 bar and 77 K for this type of material which have BET (Brunauer-Emmett-Teller) specific surface area of 3189 and 3150 $m^2.g^{-1}$, respectively. A comparison of different hydrogen storage capacities of activated carbons as well as templated carbons is given in Table II.3.

Table II.3: Hydrogen uptake capacities of different activated carbons and templated carbons

	Specific surface area $(m^2.g^{-1})$	Condition (bar, K)	Gravimetric capacity (wt%)
AC Norit SX 1	922	1, 77	1.5 (Nijkamp et al., 2001)
AC (AX-21)	2421	10, 77	4 (Texier-Mandoki et al., 2004)
	2800	35, 77	5.3 (Benard and Chahine, 2001)
Norit R0.8	1384	20, 77	2.9 (Schmitz et al., 2008)
PICATIF SC	2075	30, 77	5.0 (Dumont et al., 2006)
CA800	2191	20, 77	3.0 (Yang et al., 2007)
CB850h	3150	20, 77	6.9 (Yang et al., 2007)

In carbon-based materials, the main limitation comes from the relatively small binding energy on the graphene surface (4-6 $kJ.mol^{-1}$). For conventional porous carbons, the hydrogen uptake at ambient temperature is proportional to their adsorbing surface. However, according to recent theoretical studies, optimized graphene-based structures containing even infinite slit-shape pores are not able to meet DOE goals, although their H_2 storage at low temperature is very promising (Kuchta et al., 2010).

Hydrogen storage in zeolites

Zeolites can be formed by hydrothermal syntheses. They are largely used as molecular sieves, adsorbents, drying agents, catalysts, ion exchanger and water softeners. They are aluminosilicate materials and their structures are based on assemblies of SiO_4 and AlO_4 tetrahedra. The anionic skeleton of zeolites is penetrated by channels giving a honeycomb-like structure. Zeolites are microporous crystalline aluminosilicates of general formula $M^{n+}_{m/n}[(SiO_2)_p(AlO_2)_m]\cdot xH_2O$, where M is a cation which neutralizes the negative charge on the aluminosilicate framework. Additional

negative charges of aluminium in place of silicon are neutralized by the presence of cations in the centre of the tetrahedral units. Water molecules are often present for coordination.

For hydrogen storage, zeolites are limited by their low specific surface area ($\sim$1000 $m^2.g^{-1}$). For instance, in NaX, the hydrogen adsorption capacity was reported to be 2.55wt% at 77 K under 40 bar (Du and Wu, 2006). Langmi *et al.* (2005) studied hydrogen storage in different ion-exchanged zeolites and the best result was obtained in CaX, where the hydrogen adsorption capacity was reported to be 2.19wt% at 77 K under 15 bar. The theoretical limit of hydrogen uptake capacity is 2.86 wt% calculated by classical atomistic simulations, which implies that zeolites are not qualified candidates for hydrogen storage applications (Vitillo et al., 2005).

Hydrogen storage in Metal Organic Frameworks

Over the past decade, hydrogen storage in metal-organic frameworks (MOFs) received a worldwide attention because they possess versatile structures, high surface areas, large free volumes, high porosities and tunable pore geometries and functionalities. MOFs are porous solids which are structurally similar to zeolites and they show great potential for applications such as heterogeneous catalysis (Lee et al., 2009), gas purification and separation (Li et al., 2009) and gas storage (Suh et al., 2012) . Several categories are often mentioned in literature: isoreticular metal organic framework (IRMOF), metal organic framework (MOF), zeolitic imidazole frameworks (ZIF), porous metal organic framework (PMOF), microporous metal organic framework (MMOF) which are all MOFs (O'Keeffe, 2009). Coordination polymers (CPs) and porous coordination polymers (PCPs) are sometimes used for naming a MOF material as well.

MOFs are formed by coordinate bonds from multidentate linkers to metal or metal cluster centres. Most commonly used metal nodes are transition elements where binding sites are linear, T-shape, tetrahedral, square-planar, square-pyramidal, trigonal-bipyramidal, octahedral, cubic, trigonal-prismatic or pentagonal-bipyramidal. The structure of MOFs are well studied and secondary building units (SBUs) are used to describe both metal nodes and organic linkers (Eddaoudi et al., 2001; O'Keeffe et al., 2000). The coordination between the SBUs makes the framework.

Considering that MOFs are composed of metal nodes and organic linkers, a large variety of materials can be synthesized depending on the nature of these two major components. Changing organic linkers can further tune the pore size of the framework. For instance, the IRMOF series shown in Figure II.4 are based on $[Zn_4O]^{6+}$ SBU with various organic linkers.
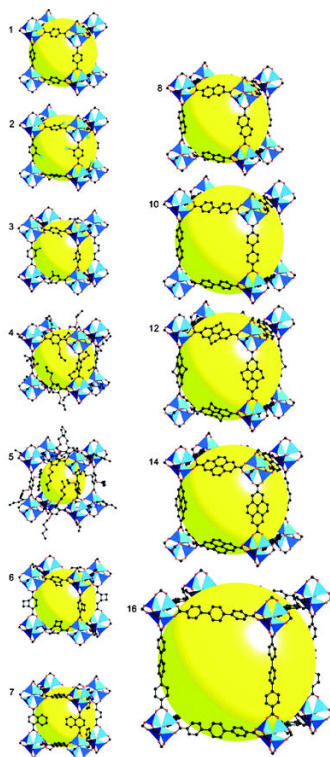
Figure II.4: Structures of IRMOF1, 2, 3, 4, 5, 6, 7, 8, 10, 12, 14, 16 using [Zn₄O]⁶⁺ building blocks and different organic linkers (Eddaoudi, 2002).

Organic linkers are often O-donor type carboxylates or N-heterocyclic based on pyridyl, imidazole and tetrazole groups. Therefore, the MOFs can be divided into subcategories like carboxylate-based MOFs, azolate-based MOFs and mix-linker MOFs (Suh et al., 2012).

- Carboxylate-based MOFs

Carboxylate-based MOFs form the majority of reported synthesized materials (Suh et al., 2012). The advantage of the carboxylic acids is that they have high acidity (pKa about 4) which allows facile *in situ* deprotonation for MOF formation (Murray et al., 2009).

The MOF-5 (IRMOF-1), based on the $[Zn_4O]^{6+}$ tetrahedral metallic clusters connected by terephthalic linkers (benzene dicarboxylic = BDC = $C_8H_4O_4^{2-}$), has undergone extensive research. The structure of MOF-5 is illustrated in Figure II.5. From the literature, its specific surface area ranges from 572 to 3800 $m^2.g^{-1}$ (Kaye et al., 2007; Panella et al., 2006; Sabo et al., 2007; Wong-Foy et al., 2006). Such variations can be attributed to the sample preparation and handling as well as to the partial decomposition of the framework after exposure to air and moisture and possibly to the incomplete activation of the porous framework (Hafizovic et al., 2007). The hydrogen uptake capacity of MOF-5 material rises to 7.1 wt% at 40 bar and 77 K. At room temperature, MOF-5 only holds 1,65 wt% of hydrogen at 48 bar (Pan et al., 2004). Bordiga *et al.* (2005) showed that the adsorptive properties of MOF-5 were mainly related to the dispersive interactions with internal pore walls. Other weak electrostatic interactions of energy of 7.4 $kJ.mol^{-1}$ were also attributed to the cluster Zn_4O_{13}.
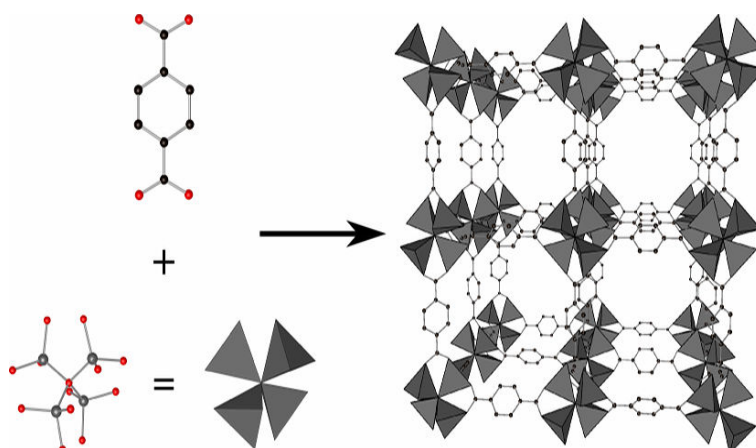
Figure II.5: Structural representation of MOF-5: the $[Zn_4O]^{6+}$ tetrahedral metallic clusters (bottom-left) connected by terephthalic linkers ($C_8H_4O_4^{2-}$) (top-left). Figure adapted from Kaye et al. (2007).

$Zn_4O(BTB)_2$ (BTB = 4,4',4''-benene-1,3,5-triyltribenzoate) or MOF-177 was found to have exceptionally high specific surface area (4750 $m^2.g^{-1}$ BET specific surface area) and its hydrogen uptake capacity was measured at 7.5 wt% at 80 bar and 77 K (Furukawa et al., 2007). In MOF-177, the tetrahedral $Zn_4O_6^-$ SBU is linked *via* large triangular tricarboxylic linker, resulting in particularly large pores which are not favourable for volumetric storage capacity. Hence, the volumetric storage capacity only reached 32 $g.L^{-1}$ due to the large pore size.

Frameworks containing copper metal nodes were also synthesized and tested. The most famous one, $Cu_3(BTC)_2$ (BTC = benzene-1,3,5-tricarboxylate) commonly named HKUST-1 (Hong Kong University of Science and Technology) or Cu-BTC, consists of a $Cu_2(O_2CR)_4$ paddle wheel structure where R is an aromatic ring with dimeric supric tetracarboxylate units (Chui, 1999). Only one coordination site of the Cu^{2+} metal centre is occupied by a carboxylate oxygen atom, whereas the other one is coordinated with a water molecule in axial position. This water molecule can be removed by heating under vacuum so that an open metal site of Cu^{2+} is exposed (Suh et al., 2012). From measurements by variable-temperature infrared spectroscopy and neutron scattering, this open metal site was reported as a hydrogen binding site (Bordiga et al., 2007; Peterson et al., 2006). Hydrogen storage capacities of 2.5 wt% at 1 bar (Rowsell and Yaghi, 2006) and 3.6 wt% at 10 bar and 77 K (Xiao et al., 2007) were measured for this material. Its hydrogen uptake is nevertheless limited by its moderate specific surface area, which is about 1500 $m^2.g^{-1}$ (Rowsell and Yaghi, 2006). Higher hydrogen uptakes were attained with other Cu-based MOF materials, such as Cu_2(qptc) (qptc = quaterphenyl-3,3''',5,5'''-tetracarboxylate) or so-called NOTT-102 (NOTT = Nottingham). This last material is characterized by a paddle wheel structure, with a BET surface area of 2930 $m^2.g^{-1}$. At 20 bar and 77 K, it shows a gravimetric and volumetric hydrogen storage capacity of 6.1 wt% and 41.1 $g.L^{-1}$, respectively (Lin et al., 2006). The hexacarboxylate linker based MOF, NOTT-112, with a significantly larger specific surface area of 3800 $m^2.g^{-1}$ demonstrates a hydrogen uptake capacity of 7.07 wt% between 35-40 bar at 77 K (Yan et al., 2009).

In order to increase the gravimetric hydrogen storage capacity, light metals such as Be, Mg and Al were used as metal nodes in MOFs. $Be_{12}(OH)_{12}(BTB)_4$ was for instance synthesized and tested. It showed a gravimetric capacity of 6.0 wt% at 20 bar , 77 K (Sumida et al., 2009). $Mg_2(dobdc)$ (dobdc = 2,5-dioxido-1,4-benzenedicarboxylate) or MOF-74(Mg) with a BET surface area of only 1510 $m^2.g^{-1}$ shows a hydrogen uptake capacities varying from 2.2 wt% to 3.2 wt% at 1 bar (Sumida et al., 2011). MIL-53(Al), which showed an uptake of 3.8 wt% at 16 bar and 77K, shares the same structure with MIL-53(Cr), Cr(OH)(BDC), which showed an uptake of 3.1 wt% at 16 bar and 77 K (Férey et al., 2003).

The MIL (Material from Institute Lavoisier) series are more often composed of trimeric chromium octahedral cluster. The $Cr_3OF(BDC)_3$ named MIL-101(Cr) is synthesized using chromium salt and terephthalic acid in the presence of hydrofluoric acid as a mineralizing agent under hydrothermal condition (Férey et al., 2005b). It exhibits a BET and Langmuir specific surface area of 4100 and 5900 $m^2.g^{-1}$, respectively. It shows a gravimetric hydrogen storage capacity of 6.1 wt% at 80 bar and 77 K (Latroche et al., 2006) and due to the open chromium metal site, it is also reported to have an isosteric enthalpy of hydrogen adsorption of 10 $kJ.mol^{-1}$ at low coverage.

- Azolate based MOFs

Azolate linkers such as tetrazolate, triazole, pyrazole and imidazole can be used to synthesize MOF materials.

Tetrazolate is a five-membered heterocyclic ring and a functional analogue of the carboxylate group for its acidity and planarity, the linker has a pKa value of 4.4. By replacing carboxylic acid, $Zn_3(BDT)_3$ (BDT = 1,4-benzeneditetrazolate) and $Cu[Cu_4Cl(ttpm)_2]_2$ (ttpm = tetrakis (4-tetrazolyphenyl) methane), structurally equivalent to MOF-5 and $Cd_4(TCPM)_2$ (TCPM= tetrakis (4-carboxyphenyl) methane) were produced (Dincă et al., 2006).

$Mn_3[(Mn_4Cl)_3(BTT)_8(CH_3OH)_{10}]_2$ (BTT = 1,3,5-benzenetristetrazolate) or Mn-BTT was also synthesized and showed a hydrogen uptake of 5.1 wt% at 90 bar and 77K (Dincă et al., 2006).

There exist two types of triazole depending on the position of N on the ring, 1,2,3-triazole and 1,2,4-triazole. Demessence et al. (2009) reported the synthesis of $H_3[(Cu_4Cl)_3(BTTri)_8]$ (BTTri = 1,3,5-tris(1H-1,2,3-trizol-5-yl)benzene) with a BET surface area of 1770 $m^2.g^{-1}$ and a hydrogen uptake capacity of 1.2 wt% at 1.2 bar, 77 K.

Co(BDP) (BDP = 1,4-benzenedi(4'-pyrazolyl) has been synthesized using Co(II) and BDP acid. It shows a high Langmuir specific surface area (2670 $m^2.g^{-1}$) and a hydrogen uptake capacity of 3.1 wt% at 30 bar and 77 K (Choi et al., 2008).

Imidazole molecule can be coordinated with a bond angle of 144°, close to the Si-O-Si bond (Natarajan and Mahata, 2009). Therefore, the imidazole based MOFs are called zeolitic imidazolate frameworks (ZIFs). This type of MOF is very stable up to 350°C (Park et al., 2006). The ZIF-8 ($Zn(MeIM)_2$) (MeIM = 1-methylimidazole) with a BET specific surface area of 1630 $m^2.g^{-1}$ and Langmuir specific surface area 1810 $m^2.g^{-1}$, showed a gravimetric hydrogen uptake of 1.27 wt% at 1 bar and 3.01 wt% at 55 bar and 77 K (Park et al., 2006). The ZIF-11 ($Zn(PhIM)_2$) (PhIM = benzylimidazole) showed a hydrogen uptake of 1.37 wt% at 1 bar and 77 K (Park et al., 2006).

- Mixed-linker MOFs

Porous MOFs that contain two different organic linkers within the same framework can be synthesized. Park and Suh (2008) reported the synthesis of SNU-6 with two types of linkers, $Cu_2(BPnDC)_2(bpy)$ (BPnDC=4,4'-benzophenone dicarboxylate, 4,4'-bpy=4,4'-bipyridine). The resulted framework showed a Langmuir specific surface area of 2910 $m^2.g^{-1}$ and a BET specific surface area of 2590 $m^2.g^{-1}$. Its hydrogen uptake capacity is of 4.87 wt% gravimetrically or 15.4 $g.L^{-1}$ volumetrically at 70 bar and 77 K. Dicarboxylate and tricarboxylate are used for the synthesis of UMCM-1 (University of Michigan Crystalline Material) or $Zn_4O(BDC)(BTB)_{4/3}$ (Koh et al., 2008). On the octahedral building unit of Zn_4O, as illustrated in Figure II.5, two BDC linkers are adjacent and the other four positions are occupied by BTB linkers which construct an octahedral cage. No hydrogen storage data is available for UMCM-1. However, UMCM-2, $Zn_4(T^2DC)(BTB)_{4/3}$ (T^2DC=thieno[3,2-b]thiophene-2,5-dicarboxylate) synthesized using the same principle shows a Langmuir specific surface area of 6060 $m^2.g^{-1}$ and a BET specific surface area of 5200 $m^2.g^{-1}$ (Koh et al., 2009). This MOF can store up to 6.9 wt% hydrogen at 46 bar and 77 K.

- Hydrogen storage enhancement by increasing the specific surface area of MOF

Frost *et al.* (2006) performed Grand Canonical Monte Carlo (GCMC) simulations for hydrogen adsorption in 10 IRMOF adsorbents. The effects of the specific surface area, of the free volume and heat of adsorption on the hydrogen uptake were investigated. The results showed that at low pressure, the hydrogen uptake is controlled by the heat of adsorption; at an intermediate pressure (30 bar), it is correlated with the surface area; and at high pressure (120 bar), the free pore volume is a more influencing factor. To reach the DOE requirements, pressure below 100 bar must be operated, and increasing the specific surface area and the pore volume are then the most important issues.

Figure II.6 shows the correlation between the gravimetric hydrogen uptakes measured at 77 K and the BET specific surface area of a variety of MOFs. The trend observed is linear, demonstrating the interest to develop high surface area to enhance gravimetric hydrogen storage capacities.
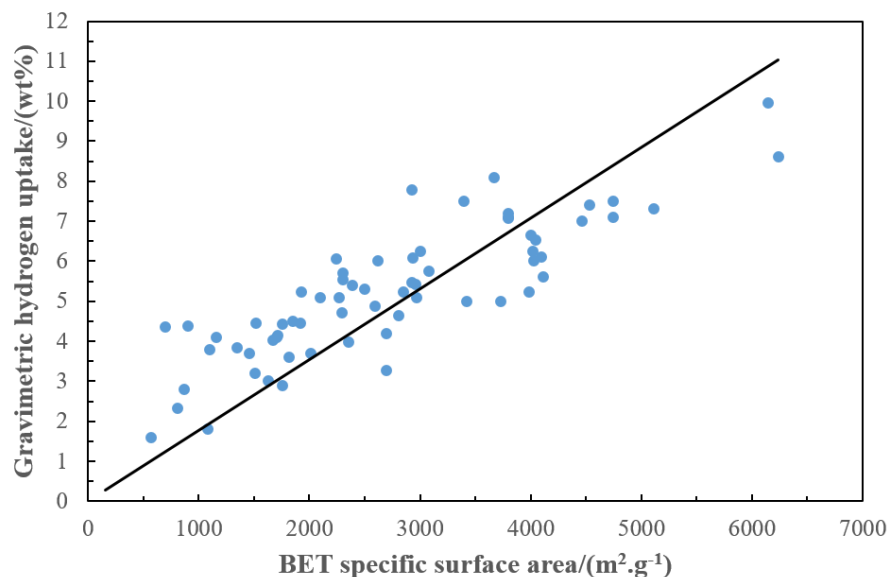
Figure II.6: Gravimetric high pressure hydrogen uptake capacity at 77 K related to the BET specific surface area for different MOF adsorbents, adapted from Suh et al. (2012).

$Zn_4O(BTE)_{4/3}(NDC)$ (BTE = 4,4',4''-[benzene-1,3,5-triyl-tris(ethyne-2,1-diyl)]-tribenzoate and NDC = naphthalenedicarboxylate) or MOF-210 which shows the highest BET specific surface area of 6240 $m^2.g^{-1}$ and also the highest Langmuir specific surface area of 10400 $m^2.g^{-1}$, has a maximal excess gravimetric hydrogen uptake capacity of 8.6 wt% at 80 bar and 77 K, which corresponds a absolute uptake of 17.6 wt% gravimetrically and 44 $g.L^{-3}$ volumetrically (Furukawa et al., 2010). $Cu_3(ttei)$ (ttei = 5,5',5''-(((benzene-1,3,5-triyltris(ethyne-2,1-diyl))tris(benzene-4,1-diyl))tris-(ethyne-2,1-diyl))triisophthalate) or NU-100, with a specific surface area of 6143 $m^2.g^{-1}$ can store up to 9.95 wt% of hydrogen at 56 bar and 77 K in excess, and at 70 bar its absolute uptake reached 16.4 wt% gravimetrically (Farha et al., 2012).

- Hydrogen storage enhancement by MOF doping

Doping MOF by other material to form a composite has been explored for the purpose of improving hydrogen uptake capacity (Zhu and Xu, 2014). Noble metals can be used as doping agents. MOF-5 impregnated with Palladium nanoparticles (Pd NPs) led to an increase of reversible hydrogen storage from 1.15 to 1.86 wt% at 1 bar and 77 K, according to Cheon and Suh (2009) and from 1.03 to 1.48 wt% under the same conditions, according to Sabo *et al.* (2007). The performance of enhancement was attributed to the spillover effect of Pd NPs and the MOFs acting as a spillover receptor (Sabo et al., 2007). MIL-100(Al) was modified with around 2 nm Pd NPs, resulting in a significant change in gas sorption properties (Zlotea et al., 2010). At 77K, Pd doped MIL-100(Al) adsorbed less hydrogen than no doped one (1.3 wt% and 3.1 wt%, respectively). However, at room temperature, the hydrogen uptake capacity of Pd doped MIL-100(Al) can store nearly two times more than no doped one (0.35 wt% and 0.19 wt%, respectively). A platinum doped MOF-177 (Pt@MOF-177) material was investigated (Proch et al., 2008). It showed a hydrogen storage

54

capacity of almost 2.5 wt% in the first cycle at 25°C and 144 bar. This one sharply decreased down to 0.5 wt% in consecutive cycles. The authors suggested that such a loss in hydrogen uptake could be attributed to the formation of palladium hydrides that were not desorbed at room temperature. Suh's group doped Magnesium nanocrystals embedded in SNU-90' structures (MgNC@SNU-90') to form a hybrid hydrogen storage material (Lim et al., 2012). Although the hydrogen storage capacity at 77 K was not significantly enhanced by Mg doping, this material performed physisorption at low temperature but chemisorption at high temperature.

Carbon-MOF composites have been studied (Vilatela and Eder, 2012). CNTs have been considered as useful composite fillers in H_2 storage research, the incorporation of CNTs into MOF was first exploited by Yang *et al.* (2009). The CNT@MOF-5 composite was synthesized by adding acid-treated MWCNTs dispersed in DMF to the MOF-5 synthesis mixture. The obtained composite had the same crystal structure and morphology as those of pristine MOF-5, and the presence of MWCNTs admixed with MOF-5 crystals was confirmed by TEM. Compared to the pristine MOF-5, a higher Langmuir specific surface area was found, which increased from 2160 to 3550 $m^2.g^{-1}$. The prepared sample showed an enhancement of the hydrogen storage capacity from 1.2 to 1.52 wt% at 77 K and 1 bar, and from 0.3 to 0.61 wt% at 298 K and 95 bar. Karikkethu Prabhakaran *et al.* (2011) synthesized single-wall carbon nanotube doped MIL-101 (SWCNT@MIL-101). Hydrogen storage capacities were observed increased from 6.37 to 9.18 wt% at 77 K up to 60 bar and from 0.23 to 0.64 wt% at 298 K and 60 bar, which was ascribed to the decrease in the pore size and enhancement of micropore volume of MIL-101 by nanotube incorporation. The same study has been performed later at 298 K up to 100 bar (Karikkethu Prabhakaran and Deschamps, 2015a). A gravimetric uptake of 1.04 wt% was measured for doped MIL-101(Cr) compared to 0.45 wt% for the pristine one. By using Pt loaded MWCNT incorporating with MOF-5, S.J. Yang *et al.* (2010) found that the hydrogen storage capacity was enhanced 4.2 times with respect MOF-5 and 2.3 times with respect to Pt-MWCNTs. The authors indicated that in the Pt-MWCNT, the substrate, the MWCNT plays a role as an efficient primary spillover receptor which enhanced the hydrogen uptake capacity. MOF-5, which secured the porosity, acted as a secondary H_2 spillover receptor. Hydrogen storage was improved from 1.2 to 1.89 wt% in the composite at 1 bar and 77 K (S. J. Yang et al., 2010).

According to Rao *et al.* (2011), by enhancing electrostatic charge quadrupole and dipole interaction between H_2 and Li coated fullerene doped IRMOF-10, achieved a gravimetric hydrogen uptake of 6.3 wt% and a volumetric uptake of 43 $g.L^{-1}$ at 243 K and 100 bar.

Activated carbon doped MIL-101(Cr) were synthesized (Karikkethu Prabhakaran and Deschamps, 2015b; Somayajulu Rallapalli et al., 2013) by hydrothermal method and adding activated carbon into reactant solution. It was found that the hydrogen adsorption capacity was enhanced by 58 % due to the reduction of pore size and improvement of pore volume additional micropore volume were formed (Somayajulu Rallapalli et al., 2013).

II.3. Conclusion and hydrogen storage method chosen for this work

A summary of different storage methods is presented in Table II.4 to compare the different hydrogen storage methods presented previously.

Table II.4: Comparison of the gravimetric density, volumetric density, operating temperature and pressure for hydrogen storage methods (Durbin and Malardier-Jugroot, 2013; Harris et al., 2004; Züttel, 2004).

Storage method	Gravimetric /(wt%)	Volumetric /(g.L^{-1})	T /(°C)	p /(bar)	Advantage/disadvantage
Compressed hydrogen	13	<40	15	350-700	Extreme pressure
Liquid hydrogen	Tank material dependent	70.8	-252	1	Extreme temperature, very costly and boil-off problem
Compressed liquid hydrogen	Tank material dependent	47.8	25	1	Complicated and expensive
Compressed cryogenic hydrogen	-	~40	-196	<200	Complicated and less effective than adsorption
Metal hydrides	<7	150	<300	1	Low gravimetric values due to heavy metals, slow kinetics
Complex hydrides	<18	150	<650	1 (desorption) 350 (sorption)	Desorption needs elevated temperature. Sorption needs high pressures, slow kinetics
Adsorbed hydrogen	<8	20	-196 or 15 depends on adsorbent	100	Fully reversible but low temperature

It can be deduced from Table II.4 that the physical adsorption method for hydrogen storage requires moderate pressures and temperatures (77 K and about 100 bar) compared to other storage methods. Meanwhile, hydrogen storage and regeneration by physisorption are fully reversible due to the low interaction energy between hydrogen and adsorbents compared to some hydrides. Moreover, the kinetics of adsorption/desorption of hydrogen from adsorbent is good enough to fulfil onboard usage requirements.

Among all adsorbents for physisorption of hydrogen, doped MOF with high surface area and/or with higher hydrogen adsorption heat can provide higher hydrogen uptake capacity which makes it outstanding from other adsorbent materials.

Considering these arguments, the work proposed in this study will use a doped MOF for hydrogen storage. However, economic aspect must be taken into consideration for well choosing the adsorbent for scaling-up synthesis. Two indicators are used here to compare different MOF and

doped MOF adsorbents: the primary ingredient price and the space-time yield (SPY) for their productions.

The prices of primary ingredients required for the syntheses of MOF-5, HKUST-1, MOF-177 and MIL-101(Cr) are specified in Table II.5. These MOFs are the very first developed ones which only require one pot synthesis for their productions. Recent developed MOFs like MOF-210 and NU-100 which need extra complex syntheses of organic linkers are not taken into consideration.

Table II.5: Price comparison for MOFs' syntheses: MOF-5, MOF-177, Cu-BTC (HKUST-1) and MIL-101(Cr). All prices are consulted from Sigma-Aldrich.

	MOF-5	MOF-177	HKUST-1	MIL-101
Metal salt	Zinc nitrate hexahydrate	Zinc nitrate hexahydrate	Copper nitrate hemi(pentahydrate)	Chromium nitrate nonahydrate
Metal salt cost (Euros/500g at 98%)	38.2	38.2	102.5	161.0
Organic linker	H_2BDC	H_3BTB	H_3BTC	H_2BDC
Organic linker cost (Euros/500g)	26.1	226.5 (1 g)	296.0	26.1
Solvent	DEF[*]	DEF[*]	Ethanol/Water	Water
Solvent cost (Euros)	99.8 by 100 g	99.8 by 100 g	32.6 by 1 L/-	-

[*]DEF=N,N-diethylformamide.

Another economic indicator for MOF synthesis is the space-time yield (STY), which shows the yield of production by unit of time and by unit of space (reactor volume) for the synthesis reaction. Stock and Biswas (2012) reviewed the STY of different MOFs and the results are shown in Table II.6.

Table II.6: Comparison of different MOF syntheses' Space-Time Yields (SPYs)

MOF	STY/(kg.m^{-3}.day^{-1})	Ref
MIL-53(Al) or Basolite A100	160	(Czaja et al., 2009)
HKUST-1 or Basolite C300	225	(Czaja et al., 2009)
Fe-BTC or Basolite F300	20	(Czaja et al., 2009)
ZIF-8	100	(Czaja et al., 2009)
$Mg(O_2CH)_2$ or Basosiv M050	>300	(Czaja et al., 2009)
MIL-100(Fe)	>120	(Seo et al., 2012)

Unfortunately, no experimental data of SPY of MIL-101 synthesis is available. However, the reported synthesis method seems to be productive (Férey et al., 2005b) and the price of primary reactants for MIL-101(Cr) synthesis is attractive. Moreover, it has a high hydrogen storage capacity according to Latroche *et al.* (2006).

The prices of doping materials are consulted and only activated carbon shows a high price/quality ratio for doping usage. It is also reported that activated carbon doping increases the hydrogen adsorption capacity of MIL-101(Cr) (Karikkethu Prabhakaran and Deschamps, 2015b; Somayajulu

Rallapalli et al., 2013). Considering all these issues presented, it is economical to use activated carbon doped MIL-101(Cr) as an adsorbent for hydrogen storage.

II.4. Methodology and structure of the thesis

The methodology and the scientific approach of this work are adopted and are presented in Figure II.7.
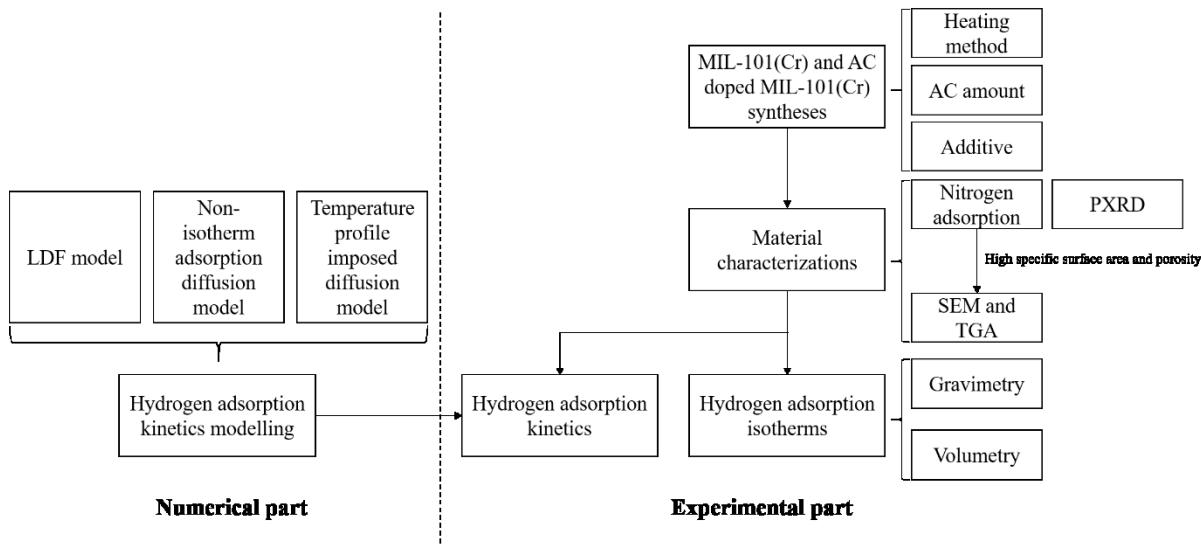
Figure II.7: Methodology and scientific approach of this work.

For high hydrogen uptake capacity, a highly porous adsorbent (AC doped MIL-101(Cr)) needs to be produced. The method of adsorbent synthesis is important and is directly correlated to the porosity of synthesized products, which implies that with different ratio of reactants, mineralizing agents, temperature or heating method, the products of syntheses can have very different properties, especially the porosity (Biemmi et al., 2009; Guo and Chen, 2012). Therefore, the first step of the work concerns the evaluation of several parameters of MIL-101(Cr) and AC doped MIL-101(Cr) syntheses in order to find an appropriate synthesis method. The high porous products are chosen according to their performances during nitrogen adsorption isotherms at 77 K. Other properties such as crystallinity, morphology and thermal stability are also evaluated to further characterize the samples.

After examinations of the properties of synthesized products, the high porous samples are chosen and tested for their hydrogen adsorption performances. The hydrogen adsorption isotherm at room temperature as well as at cryogenic temperature (77K) should be measured in order to evaluate the obtained porous materials. The most appropriate product would be then selected for synthesis scaling-up.

Considering that adsorption isotherms can be measured either by volumetric method or gravimetric method, it is expected to analyse the influences of measure techniques. The hydrogen adsorption isotherms at 77 K then need to be measured on both apparatus and the results will be compared.

The adsorption kinetics needs to be well studied also and up to now, very few researchers are concentrated on this issue (Bimbo et al., 2015; Saha et al., 2009, 2008). Experimentally, the kinetics can be recorded and the data fitting can be made by using well-developed linear driving force model (LDF) (Glueckauf, 1955a). Meanwhile, as the adsorption is an exothermic process, it is interesting to study the effect of temperature during this process. Finally, numerical modelling of hydrogen adsorption kinetics aims to develop models which consider more adsorption parameters (temperature, pressure, inlet gas flow).

This manuscript is spitted up into 5 parts:

- The general introduction is divided into two parts. The first part presents the context and the applications of hydrogen in the energetic mix, the state of the art of hydrogen production, distribution and utilizations at the current stage. In the second part which leads to the problematic of this study and adopted strategy: different hydrogen storage methods are presented and compared.

- Chapter 1 describes the material syntheses and their upscaling, as well as their characterization. MIL-101(Cr) and activated carbon doped MIL-101(Cr) samples are produced by different ways, using different mineralizing agents and heating methods (conventional or microwave). The structural properties of products are characterized by X-Ray Diffraction (XRD). Obtained patterns are compared with theoretically simulated one and their crystallinities are evaluated. The morphologies of products are characterized by Scanning Electron Microscopy (SEM), and the mean crystal sizes of different samples are calculated. Thermogravimetric Analysis (TGA) is used for characterizing the thermal stabilities of samples. Pore volumes and distributions as well as the specific surface areas are assessed by measurement and modelling of nitrogen (N_2) adsorption isotherms at 77 K.

- Chapter 2 focuses on the experimental determination of hydrogen adsorption isotherms measured at ambient and cryogenic temperature, in a large pressure range using both volumetric and gravimetric methods and their comparisons for the different synthesized adsorbents.

- Chapter 3 examines the kinetics of hydrogen adsorption in the produced materials. The measurements of hydrogen adsorption kinetics are carried out by using the volumetric method at different pressures range from 0.2 to 5 bar. Models based on Linear Driving Force (LDF) assumption and numerical solving of the equation of diffusion are developed to interpret the experimental kinetic data.

- Finally, a conclusion resumes the most important results obtained. The principal achievements of this thesis and the perspectives of future works are also presented.

Chapter 1

MOF's syntheses, activations and characterizations

Les synthèses des matériaux MIL-101(Cr) et MIL-101(Cr) dopés au charbon actif ont été réalisées. La synthèse, telle que décrite dans la littérature, fait appel à l'acide fluorhydrique en tant qu'agent minéralisant. Or ce composé est fortement toxique et, pour des raisons de sécurité, il n'est pas judicieux de l'utiliser à l'échelle industrielle. Ainsi différents agents minéralisants tels l'acide acétique ou l'acétate de sodium ont été mis en œuvre pour tenter de produire le MIL-101(Cr) par différentes voies de synthèse, c'est-à-dire en utilisant différentes méthodes de chauffage et solutions de lavage, et en faisant varier la concentration de charbon actif introduit comme agent dopant. Les produits synthétisés bruts obtenus ont ensuite été lavés à l'éthanol, au diméthylformamide (DMF) ou avec une solution de fluorure d'ammonium (NH_4F) afin d'éliminer les résidus tels que l'acide benzenedicarboxylique restant dans les pores.

Les matériaux synthétisés ont ensuite été caractérisées par diffraction de rayon X afin d'examiner les structures cristallines obtenues, par microscopie électronique à balayage pour étudier les morphologies des cristaux et par thermogravimétrie pour en évaluer la stabilité thermique. Les résultats montrent que le MIL-101(Cr) synthétisé par utilisation de l'acide acétique comme agent minéralisant a une structure cristalline similaire à celle théorique et il présente une taille moyenne de cristaux de 120 nm. Les MIL-101(Cr) dopés au charbon actif présentent des taux de cristallinité inférieurs par rapport à leurs homologues non dopés, ce qui montre l'influence de l'incorporation du charbon actif sur la germination et la croissance des cristaux. Ainsi la taille moyenne d'un cristal de MIL-101(Cr) dopé avec 5 wt% de charbon actif diminue jusqu'à 60 nm. L'analyse thermogravimétrique montre que ces matériaux sont thermiquement stables jusqu'à 200°C.

La porosité des matériaux adsorbants a été étudiée à partir de la mesure des isothermes d'adsorption d'azote à 77 K. Les isothermes d'adsorption obtenues, décrivant des quantités adsorbées à l'équilibre en fonction de la pression relative d'azote, sont de type IV : une hystérèse à la désorption est observée pour une pression relative de l'ordre de p/p^0=1 ce qui témoigne de la mésoporosité de ces matériaux. Les surfaces spécifiques de ces adsorbants ont été calculées en considérant le modèle de Langmuir et la théorie BET. Le MIL-101(Cr) pur synthétisé à partir d'acide acétique a une surface spécifique de Langmuir de 4668 $m^2.g^{-1}$ et une surface BET de 3223 $m^2.g^{-1}$. Un dopage au charbon actif correspondant à une concentration massique de 5 % augmente les surfaces spécifiques de Langmuir et BET, qui atteignent respectivement 4951 $m^2.g^{-1}$ et 3542 $m^2.g^{-1}$. Un maximum de la surface spécifique est obtenu par l'adjonction de charbon actif, et au-delà d'une certaine concentration en charbon actif, une perte de porosité qui se traduit par une diminution de la surface spécifique est observée. Les distributions de taille des pores ont été calculées suivant deux méthodes : à partir du modèle de Barrett, Joyner et Halenda (BJH) et à partir de la théorie de la densité fonctionnelle non locale (Non Local Density Functional Theory NLDFT. Les résultats obtenus à partir des différents calculs des corrections ont été comparés et il a été montré que la correction et l'équation de calcul de l'épaisseur de la couche adsorbée proposée par Kruk-Joraniec-Sayari (KJS) aboutissent à une distribution de tailles de pores centrées sur 26 et 31 Å, qui sont des valeurs très proches des tailles de pores théoriques. La méthode NLDFT a permis d'obtenir des résultats similaires à ceux obtenus via la méthode BJH dans le domaine mésoporeux, et a étendu la mesure de distribution de taille des pores dans le domaine microporeux, correspondant à des tailles inférieures à 20 Å. La présence de pores de l'ordre de 1 nm a été ainsi établie, supposés formés par le super tétraèdre de la structure de MIL-101(Cr). Les volumes des pores ont été déduits soit à partir de l'intégration de la distribution de la taille de pores obtenue par la méthode BJH, soit à partir des quantités adsorbées d'azote à la pression relative p/p^0=0,98. Le volume de pore calculé pour les adsorbants est de l'ordre de 2 $cm^3.g^{-1}$; le MIL-101(Cr) dopé à une concentration massique de 5% de charbon actif développe un volume total de pore de 2,65 $cm^3.g^{-1}$.

1. MOFs' syntheses, activations and characterizations

1.1. Introduction: MIL-101(Cr) and Activated Carbon doped MIL-101(Cr)

MIL-101(Cr) where MIL stands for "Material Institute Lavoisier" was firstly produced by Férey *et al.* (2005b). The chemical formula of the material is $Cr_3F(H_2O)_2O[(O_2C)C_6H_4(CO_2)]_3 \cdot nH_2O$ (where n ~ 25) according to original research.

Its building block, computationally designed as a Super Tetrahedron (ST) is made from the linkage of 1, 4-benzene dicarboxylic anions (BDC) and inorganic trimers that consist of three chromium atoms in an octahedral environment with four oxygen atoms of the bidentate dicarboxylates, one μ_3-oxocentered atom, and one oxygen atom from the terminal water or fluorine group. Octahedral are related through the μ_3-oxocentered atom to form the trimeric building unit. The four vertices of the ST are occupied by the trimers, and the organic linkers are located at the six edges of the ST. This computational design is represented in Figure 1.1.
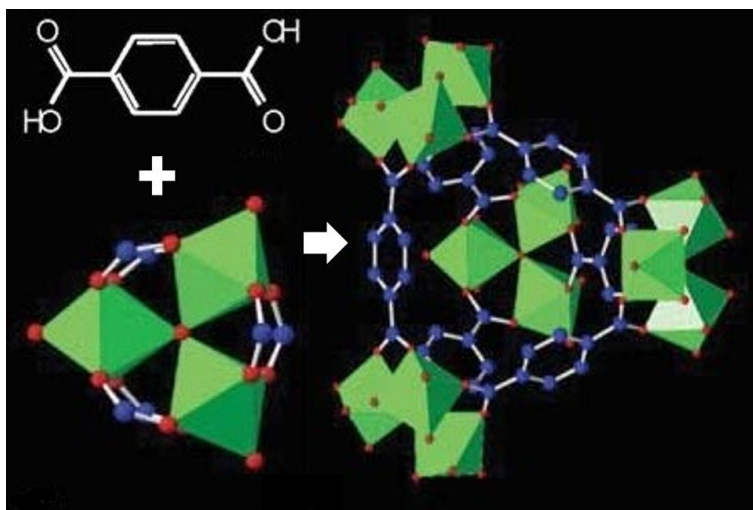
Figure 1.1: Chromium octahedral related by μ_3-O atom (red dot) and the 1,4-BDC anions structure combined (blue dots stand for carbon atoms and hydrogen atoms are omitted) to form the trimeric building unit (Figure adapted from Férey et al. (2005b)). Chromium atoms are located in the centres of the octahedral (green).

The STs are microporous with a free aperture about 8.6 Å and these building blocks were then assembled and the connection between the ST was established through vertices to ensure a 3D network of 'corner-sharing' super tetrahedral. The resulting framework delimits two types of mesoporous cages which are present in a 2:1 ratio, with pore diameters of 29 Å and 34 Å, respectively. The smaller cages show pentagonal windows with an opening of 12 Å while the larger cages possess both pentagonal and larger hexagonal windows with 14.5 and 16 Å free apertures, respectively (Férey et al., 2005a, 2005b; Mellot-Draznieks and Férey, 2005).

Powder X-Ray Diffraction (PXRD) data reveal a face centre cubic (*fcc*) cell with edge length about 89 Å (space group $Fd\text{-}\bar{3}m$) (Lebedev et al., 2005) and it showed apparently a zeolite-type architecture named Mobil Thirty-Nine (MTN) according to the Reticular Chemistry Structure Resource (RSCR) database. This structure is illustrated by Figure 1.2.
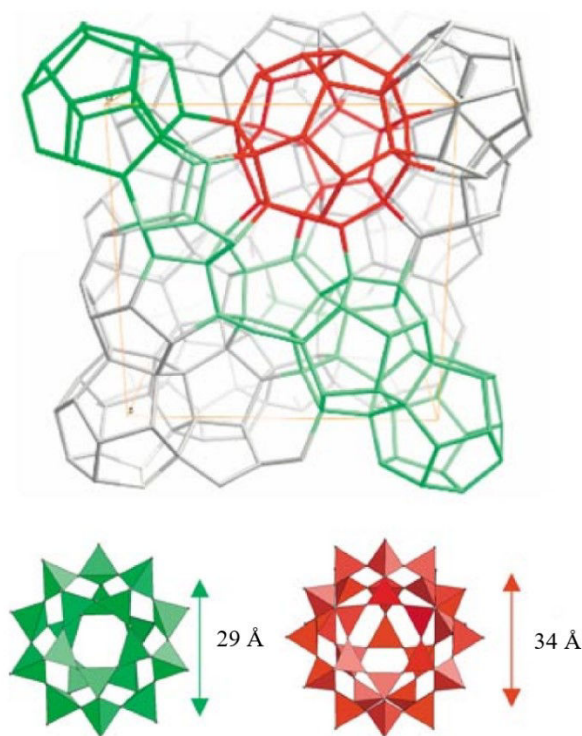
Figure 1.2: The assembling of large cage (34 Å in diameter) with pentagonal windows with 12 Å aperture and hexagonal windows with 14.5 and 16 Å free apertures and small cage (29 Å in diameter) with only pentagonal window with 12 Å aperture yields MIL-101(Cr)'s MTN type structure (Figure adapted from Férey et al. (2004))

MIL-101(Cr) has high thermal stability up to 275 °C in air and the guest molecules in pores can be removed without framework collapsing. It is also very stable in a humid atmosphere unlike its counterparts such as MOF-5 and MOF-177 (Férey et al., 2005b) and is then suitable for applications in moisture (Akiyama et al., 2012; Huo and Yan, 2012). MIL-101(Cr) has a high Langmuir specific surface area of 5900 $m^2.g^{-1}$ and a BET (Brunauner Emmett and Teller) specific surface area of 4100 $m^2.g^{-1}$ (Férey et al., 2005b). The synthesis has been repeated according to the same procedure described in the literature (Cao et al., 2014; Henschel et al., 2008; Khutia et al., 2013; Kim et al., 2012; Li and Yang, 2008; Pires et al., 2014; Salomon et al., 2014; Senkovska and Kaskel, 2008; Szilágyi et al., 2014; Wee et al., 2014) and the BET specific surface area measured is about 3000 $m^2.g^{-1}$.

The activated carbon doped MIL-101(Cr) was reported (Karikkethu Prabhakaran and Deschamps, 2015b; Somayajulu Rallapalli et al., 2013). Different concentrations of activated carbon were tested to enhance the porosity and the hydrogen uptake capacity of the synthesized composites

(Somayajulu Rallapalli et al., 2013). Among all doped samples with different amount of activated carbon, 10 mg AC of type WS-480 (0.68 wt%) doped MIL-101(Cr) showed highest specific surface area (BET specific surface area = 3556 $m^2.g^{-1}$) and a 58% of increase in hydrogen uptake capacity (10.1 wt%) at 77 K and 60 bar (Somayajulu Rallapalli et al., 2013). According to these authors, the high surface area and high hydrogen uptake capacity are presumably due to the increase of the micropores within the framework and the exposure of chromium (Cr) metal site by adding activated carbon. The activated carbon incorporated in MIL-101(Cr) is also mentioned by Karikkethu Prabhakaran and Deschamps (2015b), where a larger BET specific surface area was found, 3458 $m^2.g^{-1}$ compared to the pristine MIL-101(Cr) (3148 $m^2.g^{-1}$). A higher hydrogen uptake capacity is also reported for AC doped MIL-101(Cr) (11.7 wt%), compared to the pristine MIL-101(Cr) (7.3 wt%).

1.2. MIL-101(Cr) and AC doped MIL-101(Cr) syntheses

1.2.1. Hydrothermal syntheses of MIL-101(Cr)

The original synthesis of MIL-101 (Cr) (Férey et al., 2005b) consists of hydrothermal reaction of terephthalic acid or so-called benzene dicarboxylic acid (H_2BDC) with chromium nitrate nonahydrate ($Cr(NO_3)_3 \cdot 9H_2O$), hydrofluoric acid (HF), and water (H_2O) at 210°C with auto-generated pressure, which yields a green powder like product (MIL-101(Cr)) according to the following scheme:

$$Cr(NO_3)_3 \cdot 9H_2O + H_2BDC + HF + H_2O \xrightarrow{250\,°C} Cr_3F(H_2O)_2O[(O_2C)C_6H_4(CO_2)]_3 \cdot nH_2O$$
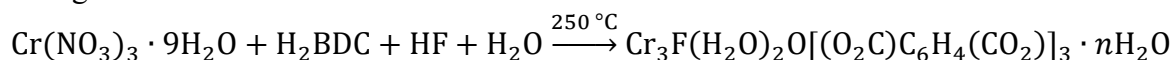
with $n{\sim}25$ according to Férey *et al.* (2005b).

In this method, HF was used as a mineralizing agent and also it is part of the synthesized product. However, it is not the only one mineralizing agent suitable for this synthesis. Besides, HF is a chemical toxicant: it is highly corrosive and also contact poison. HF is able to penetrate tissue, life-threatening poisoning can occur readily through exposure of skin or eyes, and more readily when inhaled or even swallowed (Yamashita et al., 2001). Hence, HF must be handled using protective equipment and safety precautions. Apart from HF, it is reported that acetic acid (CH_3COOH) (Huang et al., 2011), alkaline acetates (CH_3COOLi, K, Na) (Guo and Chen, 2012; C. Zhou et al., 2013), sodium hydroxide (NaOH) (Khan et al., 2011), tetramethyl ammonium hydroxide (TMAOH) (J. Yang et al., 2010) as well as nitric acid (HNO_3) (Zhao et al., 2015) can be used as mineralizing agents for the syntheses and provide MIL-101(Cr) compound with good porous quality.

The hydrothermal syntheses of MIL-101(Cr) performed in this work always involve the mixture of $Cr(NO_3)_3 \cdot 9H_2O$, H_2BDC in distillate water. The molar ratio between the two reactants is always 1:1, and the molar ratio between chromium salt, benzene dicarboxylic acid and water has been kept as about 1:1:278 (Khan et al., 2011). HF and two other different suitable mineralizing agents (CH_3COOH and CH_3COONa) have been tested. The amounts of the different reactants used for the different syntheses are listed in Table 1.2.

The experimental procedure is quite easy. $Cr(NO_3)_3 \cdot 9H_2O$, H_2BDC, mineralizing agent (HF, CH_3COOH or CH_3COONa) are mixed with water in a 75 mL Teflon-lined stainless steel autoclave built in the laboratory and represented in Figure 1.3. The mixture is then ultrasonicated for 15 minutes to have a better mix of different reactants and the autoclave is placed in a preheated oven. Since benzene dicarboxylic acid is not soluble in atmospheric conditions, the synthesis needs to be performed at high temperature and thus in an autoclave to manage the auto-generated pressure. The experimental conditions such as temperature and heating duration of the different syntheses are listed in Table 1.2. It needs to point out that the Teflon container can't suffer high temperature (210 °C) and the highest temperature applied is 200 °C. After completion of the reaction, the autoclave is removed from the oven and allowed to cool down to room temperature. The reaction mass is then filtered using a glass filter with pore size 2 (pore size range from 40 to 100 μm) to remove the residual H_2BDC present as white needle-like crystals in the crude product and again filtered using a glass filter with pore size 5 (pore size range from 1 to 1.6 μm) to separate product, which is as-synthesized MIL-101(Cr). The filtered product is washed with hot water for several times and dried at 80 °C in the oven.

Figure 1.3: Teflon-lined stainless steel autoclave built for MIL-101(Cr) synthesis

1.2.2. Microwave-assisted syntheses of MIL-101(Cr)

The hydrothermal synthesis is not the only one method used to get MIL-101(Cr) and this compound can be obtained using different methods of heating such as microwave and ultrasound assisted syntheses (Stock and Biswas, 2012). MIL-101(Cr) synthesized *via* microwave-assisted method was reported (Khan et al., 2011). Compare to the conventional heating method by the oven, microwave propagates through the solution and affords homogeneous heat. The faster rate of synthesis by using microwave heating is due to the rapid dissolution of the terephthalic acid precursor (Jhung et al., 2007), which is believed to be the effect of microwave irradiation, and this leads to a reduction of the induction period for crystal nucleation (Hong et al., 2009).
Experimentally, three different syntheses of MIL-101 (Cr) using microwave-assisted method were carried out. The experimental conditions of the different syntheses are described in Table 1.2.

1.2.3. Activated carbon doped MIL-101(Cr) syntheses

Activated carbon NORIT- RB3 is particularly interesting for the doping of MOF materials. This compound is ultra-microporous and shows a quite significant BET specific surface area of 900 $m^2.g^{-1}$ (Rufford et al., 2013). Moreover, it is much cheaper and easily available compared with other potential doping materials, such as standard single-walled carbon nanotubes (price about 5700 times lower according to Sigma Aldrich, where 1 g of SWCNT costs about several hundred euros depending on the product quality).

Before the synthesis, NORIT-RB3 supplied by Sigma Aldrich is treated with nitric acid (HNO_3:H_2O=1:1 *v/v*) for purification and functionalization. Quantitative analysis of hydrogen, oxygen and carbon content of carbon samples was performed by microcombustion analysis on a Thermo Finnigan Flash EA1112 CHNS-O elemental analyser. The method involves the complete and instantaneous oxidation of the sample by "flash combustion". The combustion products are separated by a chromatographic column and detected by the thermal conductivity detector, which gives an output signal proportional to the concentration of the individual components of the mixture. The obtained results are given in Table 1.1.

Table 1.1: Elemental analysis results of activated carbon NORIT-RB3.

Experiment	% N	% C	% H	% S	%O
1	0.26	78.06	0.39	-	13.94
2	0.28	78.42	0.91	-	13.96
3	0.28	78.07	0.49	-	13.42
Mean	0.27	78.18	0.60	-	13.77

After nitric acid treatment, it is grinded in a mortar to obtain a regular powder form which increases the contact with the reactants during the synthesis. The size of grinded activated carbon was not controlled during grinding and the size distribution is not evaluated.

The activated carbon doped MIL-101(Cr) (AC-MIL-101(Cr)) samples have been synthesised using the hydrothermal method. Similar to the synthesis of the pristine MIL-101 (Cr), the Teflon-lined stainless steel autoclave is charged with same reactants such as $Cr(NO_3)_3 \cdot 9H_2O$, H_2BDC, distilled water and mineralizing agent (CH_3COOH). A specific amount of well grinded activated carbon, corresponding to a mass ratio of activated carbon to final yielded product of about 2 to 10 wt%, is then added. The mixture is ultrasonicated for 15 minutes for a better mixture of reactants before being heated in the oven in the same conditions of temperature and time of the pristine sample synthesis. The experimental conditions and the different syntheses are described in Table 1.2.

Table 1.2: Reactants, mineralizing agents, doping materials, heating methods, heating duration for different MIL-101(Cr) and activated carbon doped MIL-101(Cr) syntheses.

Group number		1	2	3	4	5	6	7	8	9	10
Reactants	$Cr(NO_3)_3 \cdot 9H_2O$	4 g 0.01 mol	4 g 0.01 mol	4 g 0.01 mol	6 g 0.015 mol	6 g 0.015 mol	6 g 0.015 mol	4 g 0.01 mol	4 g 0.01 mol	4 g 0.01 mol	4 g 0.01 mol
	H_2BDC	1.66 g 0.01 mol	1.66 g 0.01 mol	1.66 g 0.01 mol	2.49 g 0.015 mol	2.49 g 0.015 mol	2.49 g 0.015 mol	1.66 g 0.01 mol	1.66 g 0.01 mol	1.66 g 0.01 mol	1.66 g 0.01 mol
	H_2O	50 mL 2.78 mol	50 mL 2.78 mol	50 mL 2.78 mol	75 mL 4.17 mol	75 mL 4.17 mol	75 mL 4.17 mol	50 mL 2.78 mol	50 mL 2.78 mol	50 mL 2.78 mol	50 mL 2.78 mol
Mineralizing agent		HF 2 mL 0.01 mol	CH_3COOH 570 µL 0.01 mol	CH_3COONa 0.8 g 0.01 mol	-	CH_3COOH 855 µL 0.015 mol	CH_3COONa 1.2 g 0.015 mol	CH_3COOH 570 µL 0.01 mol	CH_3COOH 570 µL 0.01 mol	CH_3COOH 570 µL 0.01 mol	CH_3COOH 570µL 0.01 mol
Doping material		-	-	-	-	-	-	AC 0.02 g	AC 0.05 g	AC 0.08 g	AC 0.10 g
Heating method		conventional	conventional	conventional	microwave	microwave	microwave	conventional	conventional	conventional	conventional
Synthesis temperature (°C)		200	200	180	210	210	210	200	200	200	200
Synthesis duration (hour)		8	8	20	1	1	1	8	8	8	8

1.2.4. Activation of as-synthesized products

After synthesized reactions, impurities such as solvent or unreacted reactants stay inside the pores and block them partially or totally (Férey et al., 2005b). Therefore, it is necessary to perform the activation of the material which consists of eliminating these impurities and obtaining a porous framework. Some specific precautions are required during the activation: some impurities can be part of the porous structure and their elimination can cause the collapsing of the framework.

Different activation ways of as-synthesized MIL-101(Cr) have been mentioned in the literature (Férey et al., 2005b; Hong et al., 2009; Hwang et al., 2008; Llewellyn et al., 2008). The essential point of the activation process concerns the elimination of the unreacted benzene dicarboxylic acid particles within the pores.

In the first reported activation of MIL-101(Cr), ethanol (CH_3CH_2OH) was used to wash as-synthesized product (Férey et al., 2005b) for the purpose of removing unreacted residuals in pores. Another method uses dimethylformamide (DMF) and ethanol as the solvent to wash as-synthesized MIL-101(Cr) (at 70°C), since H_2BDC is more soluble in DMF than in water. Then ethanol is used to exchange with DMF solvent as it is easier to be removed (Hong et al., 2009).

The third method consists of washing as-synthesized product with ammonium fluoride solution (NH_4F) (30 mmol NH_4F dissolved in 500 ml H_2O) at 70°C, during 12 hours. The objective is also to remove by dissolution the H_2BDC particles present within the pores. After this treatment the product is filtered to remove the solution and the filtered material is then washed several times with hot water (70°C) (Llewellyn et al., 2008).

The solvent-exchanged as-synthesized products are then heated to 130 °C in primary vacuum for the purpose of removing guest molecules, especially the terminal water molecules connected to the octahedral trinuclear $Cr(III)_3O$ building units and creating potential Lewis acid sites (Hong et al., 2009).

1.3. Characterizations of synthesized materials: Methods

The synthesized materials have been characterized to know their physical or chemical properties such as the structure, the crystallinity, the morphology, the thermal stability and the porosity. The characterizations of these properties were achieved using Powder X-Ray Diffraction (PXRD), Scanning Electron Microscopy (SEM), Thermogravimetric Analysis (TGA) and nitrogen (N_2) adsorption at 77 K. The results of these analyses allow us to compare the different ways of syntheses, the effect of the doping as well as the prediction of the hydrogen adsorption behaviours.

1.3.1. Powder X-Ray Diffraction analyses

Powder X-ray diffraction measurements have been performed at ambient temperature in a Bruker AXS D8 Advance system in the 2θ range 5° to 15° at a scan speed of 0.1° sec^{-1} using Cu$_{K\alpha}$

(λ=1.54056 Å) radiation to determine the framework crystallinity. The diffraction pattern is expressed as intensity measured as a function of the scattering angle, multiplied by 2. Diffraction occurs when Bragg's law is satisfied:

$$2d \sin \theta = n\lambda \qquad (1.1)$$

where θ is the scattering angle, n is an integer representing the order of the diffraction peak and λ is the wavelength of the X-ray beam, d is the inter-planar distance between adjacent planes (h,k,l) defined as:

$$d = \frac{a}{\sqrt{h^2 + k^2 + l^2}} \qquad (1.2)$$

where (h,k,l) is the Miller indices defining the family of planes in a crystal structure and a is the lattice constant.

1.3.2. Scanning Electron Microscopy analyses

The morphology and the crystal size of MIL-101(Cr) and AC doped MIL-101(Cr) samples can be studied using Scanning Electron Microscope (Lin et al., 2014; Ren et al., 2014). In this technique electrons are excited and accelerated to several keV (1 to 10 KeV) and then sent to the surface of a sample. A part of the electrons passes through the sample without any interactions and others are scattered by the atoms and they are then detected and monitored. The images could be created by analysis of the secondary and backscattered electrons as the electron-sample interactions reveal information regarding the morphology of the surface of the sample. Compared to light microscopes, SEM allows a higher resolution (at 10-100 nm scale) which is of main interest for sample morphology characterizations. In this work, the morphologies of samples are studied by using JEOL 7600F Scanning Electron Microscope.

1.3.3. Thermogravimetric Analyses

Thermogravimetric analysis (TGA) characterises the mass change of a sample as a function of temperature, under controlled atmosphere. It provides a quantitative measurement of the mass changes of a material associated with both thermodynamic transitions and thermal degradation. This technique can be used also to investigate the thermal stability and the decomposition products of a material. The measurements were performed using a Setaram LabSysevo TGA-DTA apparatus at a heating rate of 5 K.min^{-1} starting from 300 K to 1000 K.

1.3.4. Pore analyses of MIL-101(Cr) and activated carbon doped MIL-101(Cr)

1.3.4.1. Experimental method for pore analyses

The porosity is a crucial property of MIL-101(Cr) and its activated carbon doped counterparts. It characterises the adsorption behaviour of the material and it is directly related to the hydrogen adsorption capacity.

Experimentally, a volumetric method is used to perform the measurements. In this method the sample is outgassed under primary vacuum and is immersed into liquid nitrogen Dewar to maintain the temperature at 77 K (nitrogen normal ebullition temperature). The probe nitrogen is then dosed at several pressures; at each pressure, equilibrium of adsorption/desorption is reached and the amount of adsorbed/desorbed gas is calculated using p-V-T (pressure, volume and temperature) measurements performed before and after dosing. Nitrogen is an inert gas and its small size allows to fill the pores. It is needed to mention that different gases at different pressure-temperature conditions can also be used for measurements. Alternative probe gases can be krypton (at 77K) for low specific surface area measurement), argon (at 87K) and carbon dioxide (at 273 K) for ultramicropore analyses. In this case, nitrogen is a good probe gas for porosity analysis. Moreover, under subcritical conditions, capillary condensation becomes important and the textural properties of the porous sample such as pore-size can be highlighted. A supercritical phase of test gas can be used to measure the nature of the surface and the adsorption potential of gases. As pore size distribution represents an important information for this work, subcritical nitrogen at sub-atmospheric pressure is used.

None of the gases cited above can explore exactly the porous structure. They have their proper form and physical/chemical properties and they are not well adaptable for different shapes of pores which are theoretically described to be well packed by layers of spherical atoms or even sometimes described to have a flat surface. Similarly, the probe gases are also described to have a spherical form because only the covolume is considered. Finally, the porosity measured by gas adsorption isotherm can only provide some general information about the porous structure of the material.

1.3.4.2. *Isotherm and hysteresis loop patterns*

The measurement results in an isotherm of adsorption which is a set of point of adsorbed amount versus the pressure applied. The shape of the isotherm curve and its hysteresis pattern (if exists) provides information about the physisorption mechanism in pores, the solid and gas interactions and can be used to qualitatively predict the types of pores present in the adsorbent.

IUPAC (Internationa Union of Pure and Applied Chemistry) (Sing, 1985) classified the adsorption isotherms into six types (Type I to VI) with four hysteresis pattern types (H1 to H4). A recent and more detailed classification of isotherm types and hysteresis loops is given (Thommes et al., 2015) and graphically illustrated in Figure 1.4.
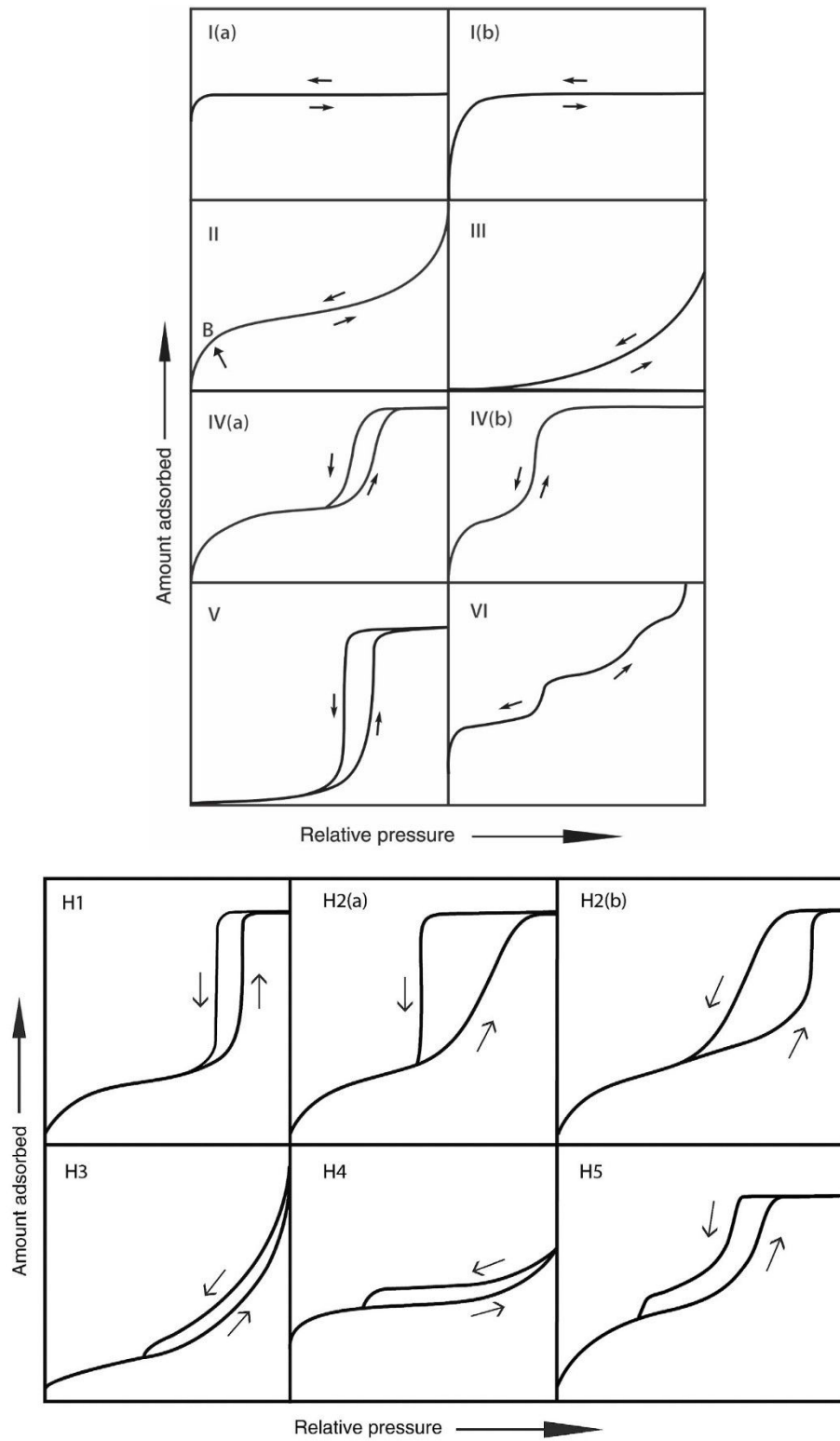
Figure 1.4: Six types of isotherms and five types of hysteresis loops classified according to Thommes et al. (2015).

Type I isotherm reflects an adsorption in a purely microporous adsorbent with very high adsorption at low relative pressure ($p/p^0 < 0.2$), followed by a linear region and finally a convex shape at higher relative pressure. The lower relative pressure adsorption corresponds to the mechanism of the enhanced adsorbent-adsorptive interactions in narrow micropores and monolayer coverage. Type I(a) isotherms are measured when materials have mainly very narrow micropores (diameter< 1 nm) and Type I(b) isotherms are measured when materials have a broader pore size distribution but always in micropore region (diameter<2.5 nm).

Type II isotherm often refers to nonporous or macroporous adsorbents. Type III isotherm is also observed for those nonporous or macroporous solid showing very weak adsorbent-adsorptive interaction which explains the mere increase of adsorbed amount in the low relative pressure region. Type IV isotherm characterizes a mesoporous adsorbent which shows a hysteresis loop associated to capillary condensation and evaporation taking place in mesopores. Type IV(a) isotherms occur when the pore width exceeds a certain critical width, depending on the adsorption system and temperature. Type IV(b) isotherms are related to adsorbents which have smaller mesopores or conical and cylindrical mesopores that are closed at the tapered end.

Type V isotherm is observed when adsorbent-adsorptive interactions are weak and adsorptive-adsorptive interactions are strong. Type VI isotherm represents a layer-by-layer adsorption on a highly uniform nonporous surface.

Concerning the hysteresis loops, the original IUPAC classification (Sing, 1985) identified four types (H1 to H4) which are now extended to six (Thommes et al., 2015). The H1 hysteresis shows a minimal and a steep, narrow loop which is due to the narrow range of uniform mesopores. Type H2 are related to more complex pore structures where network effects are more accentuated (pore blocking or percolation). The distinction between H2(a) and H2(b) relies on the distribution of pore size and H2(b) hysteresis happens with a larger distribution of pore size. Type H3 loop is given by non-rigid aggregates of plate-like particles and pore network consists of macropores which are not completely filled by pore condensate. H4 loop is similar to Type I/II isotherm and is often found with aggregated crystals of zeolites, mesoporous zeolites and micro-mesoporous carbons. Finally, type H5 hysteresis can be associated to pore structures containing both open and partially blocked mesopores.

1.3.4.3. *Specific surface area calculations*

Langmuir's monolayer adsorption model (Langmuir, 1918) is used to calculate the specific surface area created by the pore networks. In his theory of adsorption mechanism, several hypotheses are made:

- All of the adsorption sites are energetically equivalent and each site can only accommodate one molecule.
- The surface is energetically homogeneous and adsorbed molecules do not interact between them.
- There are no phase transitions.
- At the maximum adsorption, only one monolayer is formed (see Figure 1.5)

- The gas phase is perfect, the adsorbed phase is ideal
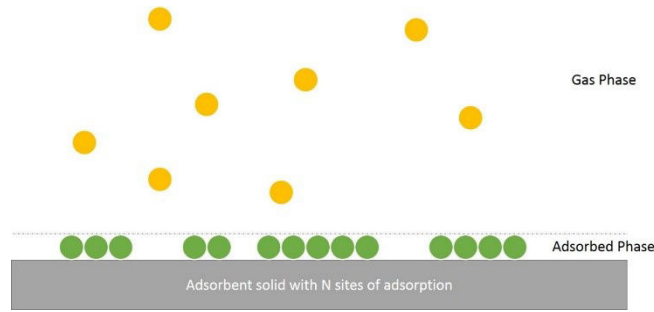
Figure 1.5: Langmuir's monolayer adsorption model

The function of fractionally occupied sites θ can be expressed as:

$$\theta = \frac{n}{n_m} = \frac{bp}{1 + bp} \qquad (1.3)$$

where the coefficient b (bar^{-1}) is the affinity constant of Langmuir isotherm which depends on temperature. n is the number of sites occupied and n_m the total number of sites which can be occupied in the monolayer.

Equation 1.3 can be then written as:

$$\frac{p}{n} = \frac{1}{n_m b} + \frac{p}{n_m} \qquad (1.4)$$

where p/n is a function of $1/b$ with a slope of $1/n_m$ and an intersection of p/n_m. By applying this method for a nitrogen adsorption isotherm, n_m can be deduced.

The Langmuir specific surface area (A) is then expressed as the following equation:

$$A = N_A n_m A_{N_2} \qquad (1.5)$$

where N_A is the Avogadro number (6.02×10^{23} mol^{-1}) and A_{N_2} is the cross section area of the probe nitrogen molecule (0.162 nm^2).

Brunauer, Emmett and Teller (BET) model can be applied for specific surface area calculation as well (Brunauer et al., 1938). This model illustrated by Figure 1.6 uses a multiple layer adsorption mechanism and the layer formed by adsorbate can be used as a new surface to adsorb other adsorbates and finally the number of layers can be infinite.
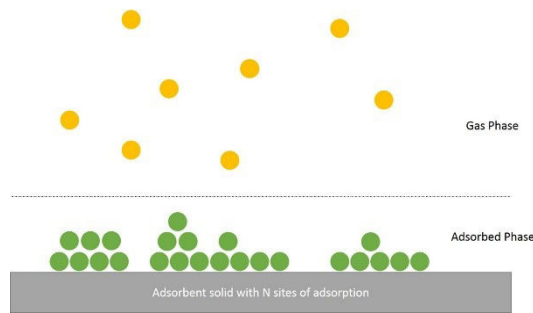
Figure 1.6: BET's multilayer adsorption model

For specific surface area calculation in BET theory, an equation alike Equation 1.5 is used:

$$\frac{p}{n(p^0 - p)} = \frac{1}{n_m C} + \frac{C - 1}{n_m} \frac{p}{p^0}$$

(1.6)

where p^0 is the reference pressure (bar), normally atmospheric pressure and C a positive constant which depends on the energy of adsorption. By applying this equation to fit experimental data, the monolayer capacity n_m can be calculated which can be further interpreted to the BET specific surface area by multiplying the cross section area of probe nitrogen molecule (0.162 nm^2).

Extreme caution is needed for application of BET method, especially with the presence of micropores and main criteria of its application are given (Rouquerol et al., 2007):

- The fitted linear trend should have a positive intercept (quantity C). A negative intercept on the ordinate of the BET plot indicates an inappropriate pressure range.
- The term $n(1-p/p^0)$ should increase continuously as a function of p/p^0.
- The relative pressure where monolayer completion is formed should be included in the calculation.

Comparing the two models, it can be deduced that Langmuir specific surface area calculated should be always higher than BET specific surface area calculated, which is caused by the differences in their assumptions. During the adsorbing of the same amount of adsorptive, Langmuir theory implies that all adsorbates are in a monolayer while BET theory suggests that there exist several layers. Therefore, calculated Langmuir specific surface area is always larger.

1.3.4.4. Total pore volume calculations

The total specific pore volume measured by N$_2$ adsorption technique can be obtained by application of Gurvich rule (Sing et al., 2014c). The specific pore volume is calculated by using liquid molar volume adsorbed at the relative pressure (p/p^0) of 0.980. This pressure corresponds to a pore size of 129.1 nm and hence the total specific pore volume is evaluated including all pores smaller than 129.1 nm. Otherwise, this volume can be computed by integration of pore size distributions represented as a function of pore radius.

1.3.4.5. Pore size distribution analyses by BJH method

Pores are classified into three types according to IUPAC classification (Rouquerol et al., 1994): micropore (pore of internal width less than 2 nm), mesopore (pore of internal width between 2 and 50 nm) and macropore (pore of an internal width greater than 50nm). As reported, MIL-101(Cr) contains two types of pores with diameters larger than 2 nm which are in mesopore range (Férey et al., 2005b). Hence, it is reasonable to apply mesopore size analysis for the synthesized adsorbents. Nitrogen adsorption is accepted as a standard method for mesopore size analysis and the sorption data can be interpreted to reveal the pore structure information. The pore size distribution (PSD) is calculated using the BJH (Barret, Joyner and Halenda) method (Barrett et al., 1951). The core of this method is based on the formation of capillary layer governed by Kelvin equation (Thomson, 1871) which describes the effect of surface curvature of the liquid-vapour meniscus on the vapour pressure and relates the pore diameter with the relative pressure:

$$\ln \frac{p}{p^0} = -\frac{2\gamma}{r_k RT} \tag{1.7}$$

where p/p^0 is the relative vapour pressure, γ is the surface tension (N.m^{-1}), r_k is the curvature of the meniscus (m), R is the gas constant (8.314 J.K^{-1}.mol^{-1}) and T is the temperature (K). This surface curvature of the liquid-vapour meniscus is illustrated in Figure 1.7.
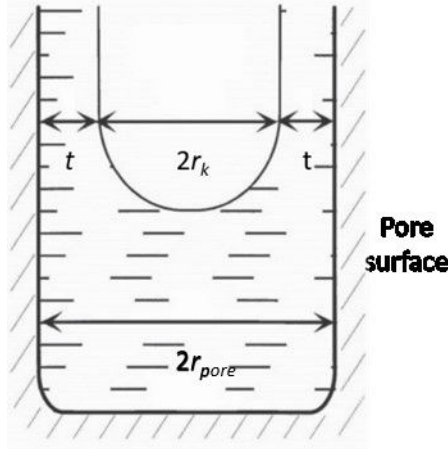
Figure 1.7: Relation between the Kelvin radius r_k and the pore radius r_{pore} in a cylindrical mesopore, figure adapted from Sing et al. (2014c).

The radius calculated r_k by Kelvin equation is the mean radius of curvature of the meniscus, which is not equal to the pore radius, as illustrated in Figure 1.7. The capillary condensation does not occur against directly with the pore surface but with several layers of adsorbates. The thickness of adsorbed layer t depends upon p/p^0. The exact pore radius can be calculated by Equation 1.8:

$$r_{pore} = r_k \cos\theta + t \tag{1.8}$$

where θ is the contact angle between the capillary condensate and the adsorbed layer. It is often assumed to be zero for practical reasons.

However, Kelvin equation fails to calculate the pore size distribution in the range of the narrow mesopores (Foster, 1932), as it neglects the fluid-fluid and fluid-solid interactions. It can underestimate the pore size and the pore size distribution is doubtful beyond 7.5 nm (Lastoskie et al., 1993). Faas (1981) and Kruk *et al.* (1997) used empirical relations to correct Equation 1.8 in order to approach the real pore size distributions.

The thickness equation which quantifies the thickness of the adsorbed layer on the pore surface is useful in the absence of experimental data concerning the thickness layer of adsorbed nitrogen in MIL-101(Cr). Different thickness equations have been developed:

- Harkins and Jura thickness equation (Harkins and Jura, 1944)

$$t = \left(\frac{13.99}{0.034 - \ln \frac{p}{p^0}} \right)^{0.5} \tag{1.9}$$

- Halsey thickness equation (Halsey, 1948)

$$t = 3.54 \left(-\frac{5}{\ln \frac{p}{p^0}} \right)^{0.333} \tag{1.10}$$

- Kruk-Jaroniec-Sayari (KJS) thickness equation (Kruk et al., 1997)

$$t = \left(\frac{60.65}{0.0371 - \ln \frac{p}{p^0}} \right)^{0.3968} \tag{1.11}$$

- Broekhoff de Boer (BdB) thickness equation (De Boer et al., 1966)

$$\ln \frac{p}{p^0} = -\frac{16.11}{t^2} + 0.1682 \exp(-0.1137t) \tag{1.12}$$

Different corrections, as well as original Kelvin equation, are applied to compute the pore size distribution combining the different thickness calculation methods presented above.

It should be noted that the real pore structures are much more complex than the models taken and the resulted pore size distribution should be interpreted as an equivalent cylindrical pore size distribution.

Theoretically, the BJH theory is a desorptive method used (from high relative pressure to lower relative pressure) for the purpose of emptying the condensed adsorptive. It can be also applied to adsorption branch of the isotherm (Sing et al., 2014c). Meanwhile, in the case of a broad distribution of pore size the desorption branch is particularly sensitive to the tensile strength effect (TSE) phenomenon which limits the applicability of Kelvin equation beyond a critical diameter of 4 nm (Groen et al., 2003).

1.3.4.6. *Pore size distribution analyses by NLDFT method*

Another efficient method to evaluate the mesopores of an adsorbent is the non-localized density functional theory (NLDFT) (Sing et al., 2014c), developed from the density functional theory

(DFT). Macroscopic thermodynamic methods such as Dubinin-Raduskevich (DR) and related method (Dubinin-Astakhov or DA), Horvath-Kawazoe (HK), Satio-Foley (SF) and BJH methods assume that pores are filled with a liquid adsorptive with bulk-like properties. However, fluid confined in narrow meso- or micropores changes the properties based on the principle of statistical mechanics. Density functional methods are based on the idea that the free energy of an inhomogeneous fluid can be expressed as a functional of $\rho(r)$ which represents the density profile in the function of spatial location (Seaton and Walton, 1989). Once this functional is known, all the relevant thermodynamic functions can be calculated. In a DFT treatment, the statistical mechanical Grand Canonical ensemble is considered. The appropriate free energy quantity is the Helmholtz free energy, or grand potential functional $\Omega[\rho(r)]$. This free energy functional is expressed in terms of the density profile, $\rho(r)$. Therefore, by minimising the free energy at constant chemical potential μ, volume V and temperature T, it is theoretically possible to deduce the equilibrium density profile.

For a one-component fluid, which is under the influence of a spatially varying external potential, the grand potential functional becomes:

$$\Omega[\rho(r)] = F[\rho(r)] + \int dr \rho(r)[U_{ext}(r) - \mu] \tag{1.13}$$

where $F[\rho(r)]$ is the intrinsic Helmholtz free energy functional, $U_{ext}(r)$ is the external interaction energy and the integration is performed over the pore volume, V.

The $F[\rho(r)]$ functional can be separated into an ideal gas term and contributions from the repulsive and attractive forces between the adsorbent molecules (*i.e.* the fluid-fluid interactions). Hard-sphere repulsion and pairwise Lennard-Jones potential are usually considered, and a mean field treatment is generally applied to the long-range attraction. However, the evaluation of the density profile of an inhomogeneous hard sphere fluid near a solid surface presents a special problem for localized density functional theory: the mean field approach provides an unrealistic picture of the density profile in this region. This is because short-range correlations near such walls are not allowed for the local density approximation. For this reason, a non-localized density functions have been developed.

The NLDFT approach involves the incorporation of short-range smoothing approximation of the fluid density and weighting functions. Various procedures such as the smoothed density (Tarazona, 1985) have been reported and are discussed by Ravikovitch and Neimark (2001a, 2001b). An improved description is obtained for the uniform fluid over a wide range of densities in the confined state. In this manner, it has been possible to obtain a good agreement with the density profiles determined by Monte Carlo molecular simulation (Cracknell et al., 1995; Lastoskie et al., 1993; Neimark et al., 2003).

NLDFT appears to give a satisfactory description of adsorption and phase transitions in slit-shaped and cylindrical pores. However, this approach has limitations. It fails for very narrow pores and also cannot predict the solid-liquid adsorbate transitions. The adsorbent surface is assumed to be smooth but experimentally, this particularity is observed only for graphitic carbon or some types of boron nitride. Moreover, if layering is also predicted for other systems, anomalies are obtained in the derived pore size distribution.

In practice, NLDFT can be used to generate a series of hypothetical individual pore isotherms for a range of pore sizes and wall potentials. It is also possible to construct such kernel by another theoretical approach or by molecular simulation (*e.g.* Grand Canonical Monte Carlo (GCMC) simulation).

The pore size distribution is obtained by solving the generalised adsorption isotherm integral equation expressed by Equation 1.14, which correlates the kernel of the theoretical isotherms with the experimental isotherm:

$$N_{exp}\left(\frac{p}{p^0}\right) = \int_{w_{min}}^{w_{max}} N_{theo}\left(\frac{p}{p^0}, w\right) f(w)\,dw \tag{1.14}$$

This equation is based on the assumption that the measured isotherm is composed of a number of individual single pore isotherms and is dependent on their distribution, *f(w)* over a finite range of pore size *w*.

During NLDFT application, firstly, the kernel which corresponds well to the adsorbent sample (*i.e.* between pore shape, pore chemistry, temperature and probe molecule) should be chosen. The pore size distribution can be extracted once the regression fit and the experimental isotherm are in good agreement, as shown in Figure 1.8.
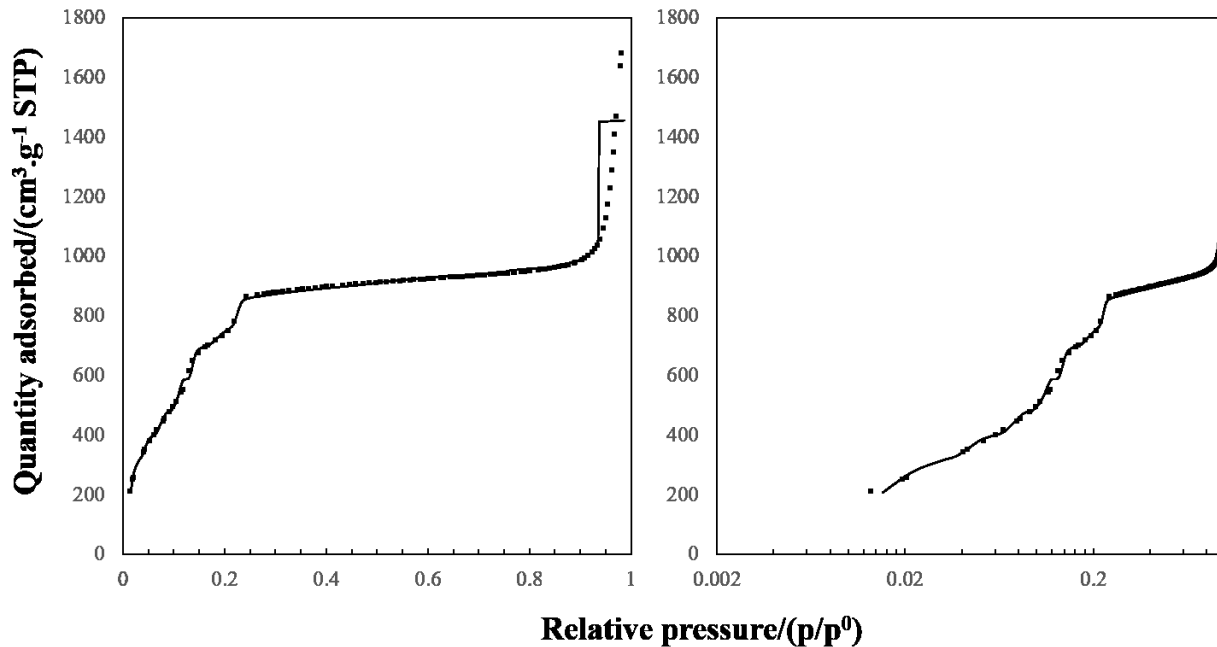
Figure 1.8: Goodness of fit by NLDFT method using the model developed by Tarazona (1985) and Tarazona et al. (1987) for nitrogen adsorption isotherm measured at 77 K for MIL-101(Cr) sample. Experimental data in black dots and NLDFT curve in black solid lines. On the left the relative pressure is linear and on the right it is logarithmic.

1.4. Results and discussion

1.4.1. Powder X-ray diffraction patterns of synthesized MIL-101(Cr) and AC doped MIL-101(Cr) composites

The structure of activated carbon (AC) NORIT-RB3 is analysed by using powder X-ray diffraction (PXRD) and the result is shown in Figure 1.9.
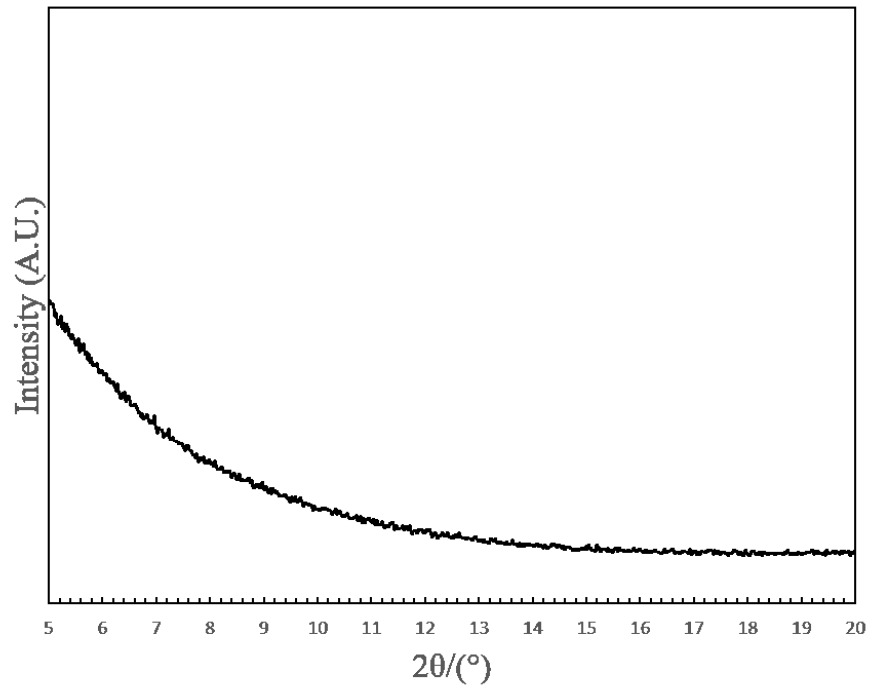
Figure 1.9: PXRD pattern of AC NORIT-RB3.

The PXRD pattern shows very well that the AC is totally amorphous without any crystal structure (Pré et al., 2013b).

The PXRD patterns of the samples synthesized according to the Table 1.2 are shown and compared with literature data (Lebedev et al., 2005) in Figure 1.10. The scattering angle is limited to 5° with the apparent peaks which correspond to the lattice plan (Miller indices: *h,k,l*) showed in Table 1.3.
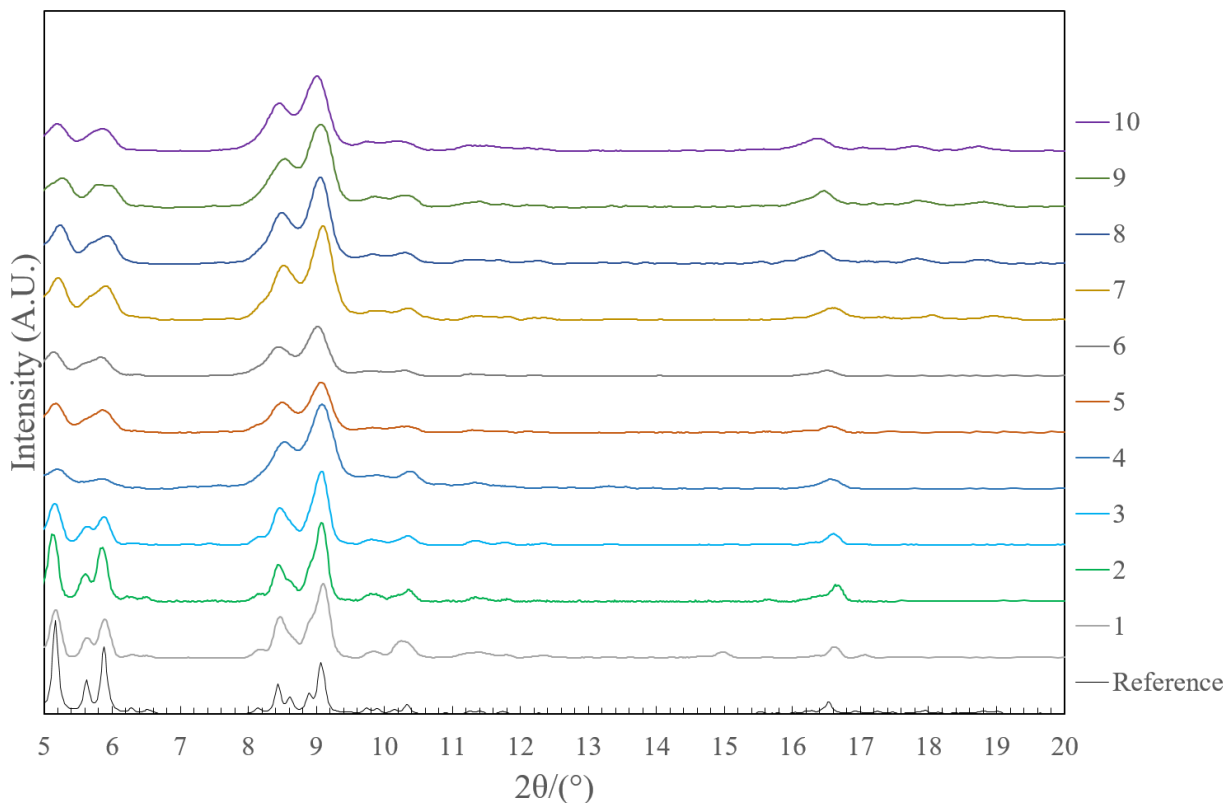
Figure 1.10: PXRD patterns of samples synthesized according to Table 1.2 (see page 68), reference pattern generated by the Mercury software using the information given by Lebedev et al. (2005).

Table 1.3: Scattering angle (2θ) with d-space and the Miller index of the lattice plans (Férey et al., 2005b; Lebedev et al., 2005; J. Yang et al., 2010).

2θ/(°)	d/(Å)	(h,k,l)
5.16	17.103	1,1,5/3,3,3
5.88	15.022	1,3,5
8.44	10.473	2,2,8
9.06	9.755	1,1,9/3,5,7
10.34	8.551	2,2,10
11,26	7.855	0,8,8
16.53	5.359	5,9,13
16.92	5.237	4,4,16
17.27	5.131	10,10,10

The patterns of different samples are represented with the simulated XRD pattern of pristine MIL-101(Cr) which was generated from the literature (Lebedev et al., 2005) using the program Mercury. It was shown a good resolution of a centric *fcc* structure like MIL-101(Cr) with cell volume 706 000 Å^3 is not possible, even with the use of synchrotron radiation powder diffraction (Férey et al., 2005b). This property explains well that the peaks can only have a high order of Miller indices.

81

By comparing different patterns, the MIL-101(Cr) synthesized using acetic acid (CH₃COOH) and using hydrofluoric acid (HF) seem to have a better crystallinity (see pattern 1 and 2 in Figure 1.10), since it has a better intensity height/width ratio. The MIL-101(Cr) synthesized using sodium acetate (CH₃COONa) (pattern 3) showed less crystallinity in this way. This phenomenon can be explained by the effect of the addition of different modulating linkers (mineralizing agent) during MIL-101(Cr) syntheses. It is reported that typical modulating linkers such as monocarboxylate molecules can be used to control crystal size and shape (acetic, benzoic or formic acid) (Diring et al., 2010; Tsuruoka et al., 2009; Umemura et al., 2011). The presence of modulating monocarboxylate agents might influence the structure of the framework. In some case the modulator is effectively incorporated into the network structure through replacement of the framework linkers, which creates connectivity defects in the structure (Wu et al., 2013).

The MIL-101(Cr) prepared by using microwave assisted method showed significantly broader peaks with identical peak positions. The results are in agreement with the literature (Bromberg et al., 2012; Khan et al., 2011), in which it was explained that the broader peaks are due to the smaller size of the synthesized particles.

The peak positions in the PXRD pattern of AC doped MIL-101(Cr) are not modified after carbon incorporation and are in good agreement with pristine MIL-101(Cr), which implies that the doping does not change the lattice structure of MIL-101(Cr). However, the doping affects the crystallinities of the synthesized composites since AC is amorphous. This conclusion is confirmed by the broader peaks localised in PXRD patterns of AC doped MIL-101(Cr) samples. Comparing patterns of sample 6 and 10 (20 mg AC doped MIL-101(Cr) and 100 mg AC doped MIL-101(Cr)), it can be observed that the peaks in pattern 10 seem to be broader. This observation can imply that the loading of AC doesn't affect the *fcc* structure of the MOF. However, a larger amount AC added reduces the crystallinity of the product (Somayajulu Rallapalli et al., 2013).

1.4.2. Microscopic studies of synthesized MIL-101(Cr) and AC doped MIL-101(Cr)

Four samples, namely, MIL-101(Cr) synthesized using acetic acid (CH₃COOH), MIL-101(Cr) synthesized using sodium acetate (CH₃COONa), 20 mg AC (2 wt%) doped MIL-101(Cr) and 50 mg (5 wt%) AC doped MIL-101(Cr) have been studied using Scanning Electron Microscopy (SEM) analyses. The choice of these samples is based on their porosity and their potential hydrogen uptake capacities which make them more interesting to be studied. In order to distinguish these samples from others, MIL-101(Cr) synthesized using acetic acid will be denoted as MIL-101(Cr)-a; MIL-101(Cr) synthesized using sodium acetate will be denoted as MIL-101(Cr)-b; 20 mg AC doped MIL-101(Cr) will be denoted as AC-MIL-101(Cr)-a and 50 mg AC doped MIL-101(Cr) will be denoted as AC-MIL-101(Cr)-b. The SEM images of these compounds are shown in Figure 1.11:
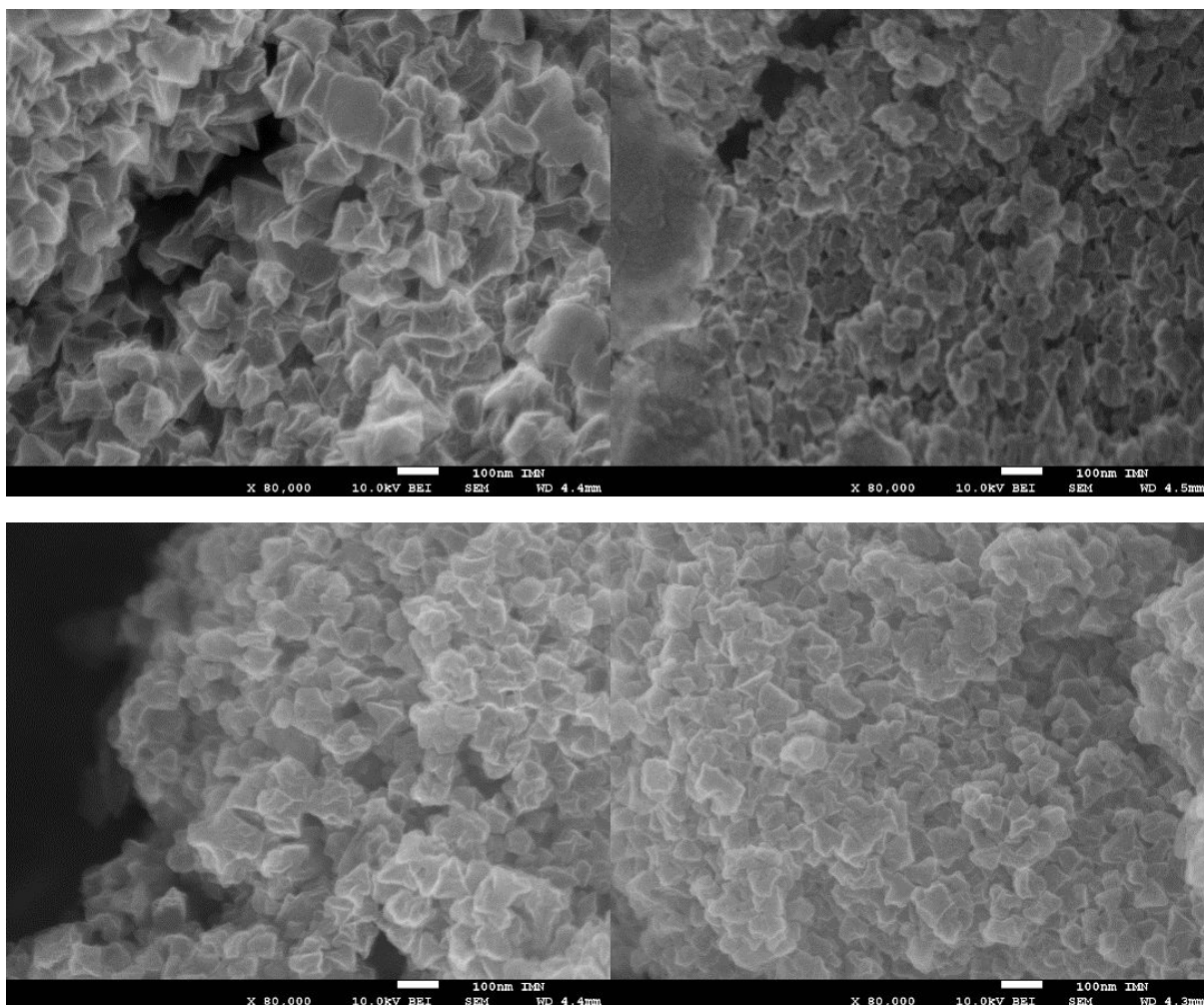
Figure 1.11: Images of crystals of MIL-101(Cr) and AC doped MIL-101(Cr) samples observed by SEM. Top left: MIL-101(Cr) synthesized using acetic acid (MIL-101(Cr)-a). Top right: MIL-101(Cr) synthesized using sodium acetate (MIL-101(Cr)-b). Bottom left: 20 mg AC doped MIL-101(Cr) (AC-MIL-101(Cr)-a). Bottom right: 50 mg AC doped MIL-101(Cr) (AC-MIL-101(Cr)-b)

The MIL-101(Cr)-b sample possess smaller crystals with an average size down to *ca* 50 nm whereas the MIL-101(Cr)-a sample shows larger crystals with an average size up to *ca* 120 nm. However, the distribution of crystal size is not very homogeneous and the smallest particles can be down to 50 nm whereas the largest ones can reach to 200 nm. The heterogeneity of the acetic acid assisted MIL-101(Cr) crystal size can be also observed in literature (Ren et al., 2014). It was reported also that the synthesis of MIL-101(Cr) with HF resulted in heterogeneous crystal size of the product (J. Yang et al., 2010). This heterogeneity of the crystal size can be related to the non-uniform heat diffusion inside the reaction cell. The heating rate directly induces the quality of the nucleation which influenced the size of the crystal. Basically an important heating rate allows a faster nucleation which produces larger crystals size. This behaviour is confirmed by the results obtained by Férey *et al.* (2005b). The smallest crystal size of MIL-101(Cr) synthesized using sodium acetate could be explained by the effect of a higher pH value of the initial solution used for

the synthesis. It is reported that higher pH promotes the dissolution of the BDC molecules (J. Yang et al., 2010; J.-J. Zhou et al., 2013). It can be assumed then the nucleation rate may be accelerated at a higher pH. Hence, the increased concentrations of both chromium trimers and benzenedicarboxylate will lead to the decrease of the size of the synthesized product. This phenomenon has also been observed for an aluminophosphate molecular sieve (Jhung et al., 2004) and confirmed for MIL-101(Cr) synthesis (Bromberg et al., 2012; Khan et al., 2011). The crystal sizes measured by SEM images are in good agreement with the PXRD patterns given previously in Figure 1.10, which show broader peaks than simulated one due to the smaller size of the synthesized crystals.

The AC incorporated MIL-101(Cr) crystals have less regular forms which might be caused by the growth of MIL-101 on the surface of the AC, which leads to a polycrystalline MOF layer, as confirmed by literature (Somayajulu Rallapalli et al., 2013). The size of 20 mg and 50 mg AC doped MIL-101(Cr) (AC-MIL-101(Cr)-a and b) are about 80, 60 nm, respectively. The smaller sizes of AC doped MIL-101(Cr) samples are also confirmed with their PXRD patterns with broader peaks, as illustrated in Figure 1.10.

1.4.3. Thermal stabilities of synthesized MIL-101(Cr) and AC doped MIL-101(Cr)

The thermal stabilities of MIL-101(Cr) synthesized using acetic acid (MIL-101(Cr)-a), sodium acetate (MIL-101(Cr)-b) and 50 mg AC doped MIL-101(Cr) (AC-MIL-101(Cr)-b) samples are investigated from 300 K to 1000 K. During analyses the samples were kept under constant argon flow. The results of thermal stabilities are shown in Figure 1.12.
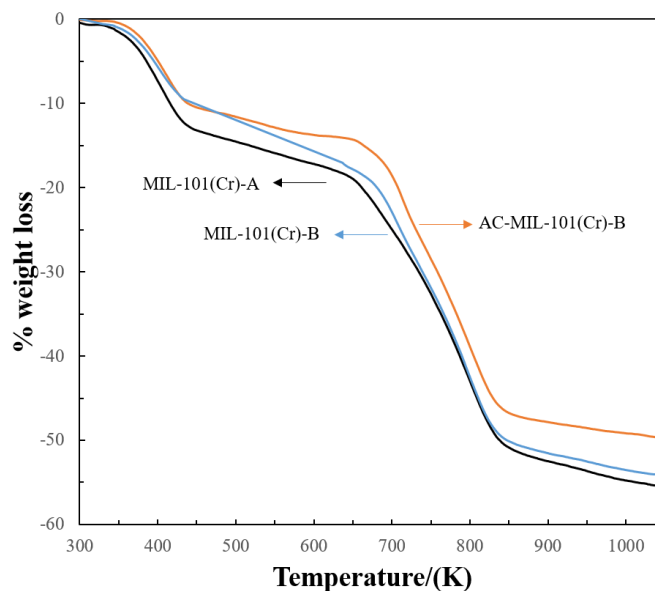
Figure 1.12: TGA plots of MIL-101(Cr) synthesized using acetic acid (green line), MIL-101(Cr) synthesized using sodium acetate (light blue line) and 50 mg AC doped MIL-101(Cr) (dark blue line) samples.

84

The weight loss of the different samples shows three weight loss steps. The first weight loss step from 300 K to 473 K is attributed to the loss of guest water molecules from the large cages (d=34 Å) (Férey et al., 2005b). The second weight loss step from 473 K to 623 K is attributed to the loss of water molecules from the small cages (d=29 Å) and the last weight loss step above 623 K is attributed to the elimination of –OH and other coordinated groups (Férey et al., 2005b). The framework is decomposed at a temperature above 623 K. MIL-101(Cr) doped with 50 mg AC shows less weight loss because activated carbon has a higher thermal stability than MIL-101(Cr), which is in good agreement with Karrikkethu Prabhakaran and Deschamps (2015b) and Somayajulu Rallapalli *et al.* (2013).

1.4.4. Pore analyses of synthesized MIL-101(Cr) and AC doped MIL-101(Cr)

1.4.4.1. Nitrogen adsorption/desorption isotherms

Nitrogen adsorption/desorption isotherm of the AC NORIT-RB3 was measured at 77 K and is presented in Figure 1.13.
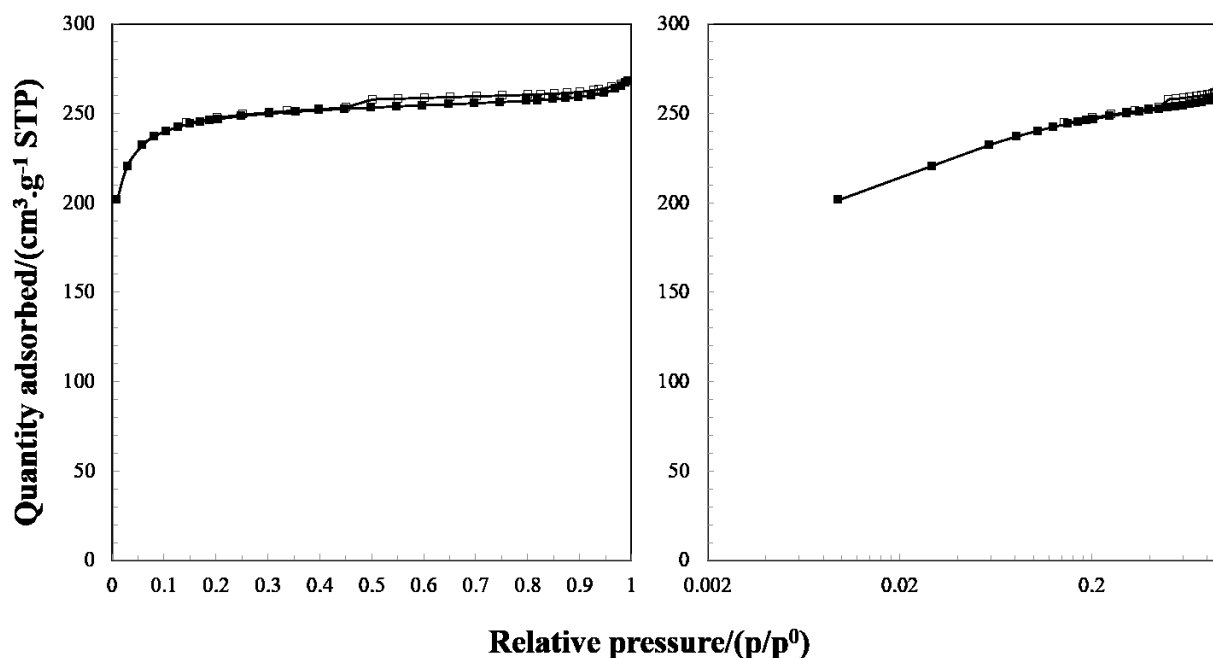
Figure 1.13: Nitrogen (N₂) adsorption isotherm curve of AC NORIT-RB3. On the left the relative pressure is linear and it is logarithmic on the right.

Nitrogen adsorption/desorption isotherm of AC shows well type I isotherm according to the IUPAC classification (Sing, 1985) which proves its microporosity. It shows also a hysteresis loop which can be classified as type H4, which confirms also its mesoporosity (Thommes et al., 2015). Nitrogen adsorption/desorption isotherms of the different MIL-101(Cr) (pristine samples as well as AC doped ones) were measured at 77 K and are represented in Figure 1.14.

85
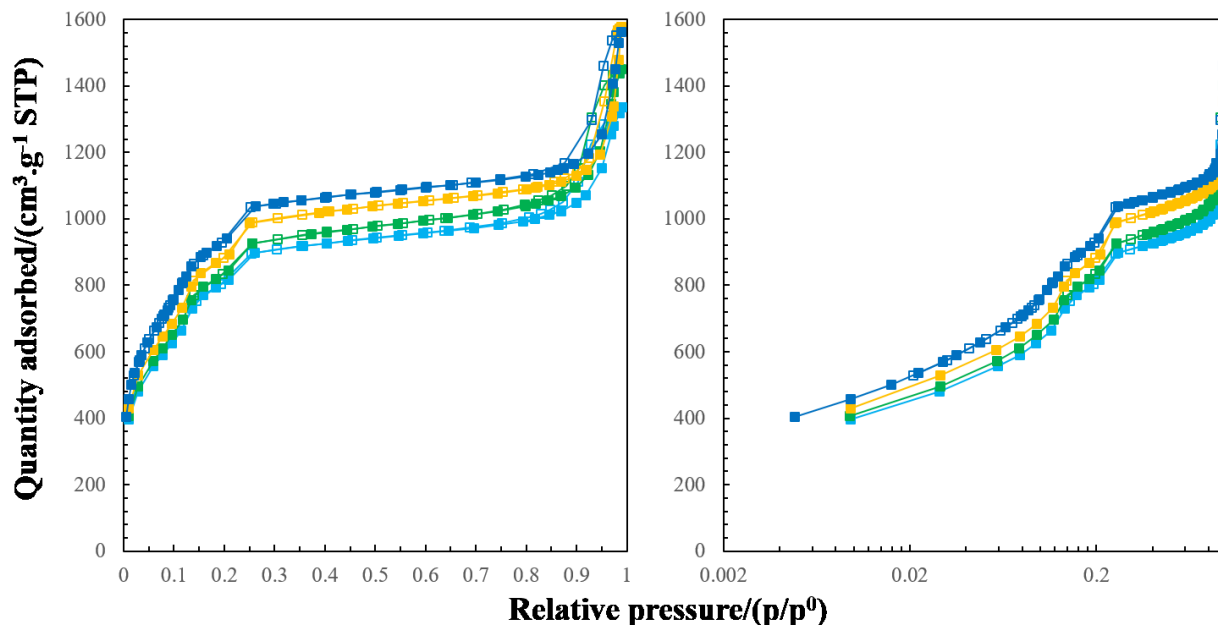
Figure 1.14: Nitrogen (N₂) adsorption isotherms for pore characterizations of (1) MIL-101(Cr)-a in green, (2) MIL-101(Cr)-b in light blue (3) AC-MIL-101(Cr)-a in yellow and (4) AC-MIL-101(Cr)-b in dark blue. On the left the scale of the relative pressure is linear; it is logarithmic on the right.

According to the IUPAC classification (Sing, 1985) and recent classification proposed by Thommes *et al.* (2015), these isotherms belong to a type IV with a type H1 hysteresis and are in very good agreement with the literature (Férey et al., 2005b).

The MIL-101(Cr) material contains two types of cages limited by 12 pentagonal faces for the smaller and by 16 faces (12 pentagonal and 4 hexagonal) for the larger. The smaller cage (29 Å in diameter) exhibit pentagonal windows with a free aperture of about 12 Å, while the larger cages (34 Å in diameter) possess both pentagonal and hexagonal window with a *ca* 14.5 Å by 16 Å free aperture (Férey et al., 2005b; Hong et al., 2009). Considering this, the N_2 adsorption/desorption isotherm of the MIL-101(Cr) at 77 K exhibits two secondary uptakes near 0.15 and 0.25 p/p^0 (Figure 1.14), indicating the presence of the two nanoporous windows in the framework (Férey et al., 2005b). Compared to the pristine sample, the activated carbon doped MIL-101(Cr) shows a more important adsorption of nitrogen at low relative pressure area, which can suggest that the incorporation of carbon particles with MIL-101(Cr) facilitates the formation of micropores in the framework (Sing et al., 2014a).

1.4.4.2. Langmuir and BET specific surface areas

The specific surface area (Langmuir and BET) of AC and the different MIL-101(Cr) materials as well as AC incorporated counterparts synthesized are listed in Table 1.4.

86

Table 1.4: Langmuir and BET specific surface area of AC and samples synthesized and activated listed in Table 1.2, page 68.

Sample	Langmuir ssa*/(m^2.g^{-1})	BET ssa*/(m^2.g^{-1})
AC	1076	956
1	3699	2638
2 or MIL-101(Cr)-a	4668	3223
3 or MIL-101(Cr)-b	4549	3131
4	3411	2457
5	3676	2629
6	1026	749
7 or AC-MIL-101(Cr)-a	4905	3407
8 or AC-MIL-101(Cr)-b	4951	3542
9	4276	2968
10	4003	2785

*ssa stands for specific surface area.

From Table 1.4, it can be observed that the microwave-assisted syntheses yield low-quality porous MIL-101(Cr) compared to conventional heating syntheses and the mineralizing agents affect the porosity of synthesized products. Meanwhile, it can be clearly observed that AC incorporation increases considerably the specific surface area of the MIL-101(Cr) material and this increase depends on the concentration of AC. The evolution of the specific surface area as a function of the amount of doping is illustrated in Figure 1.15.
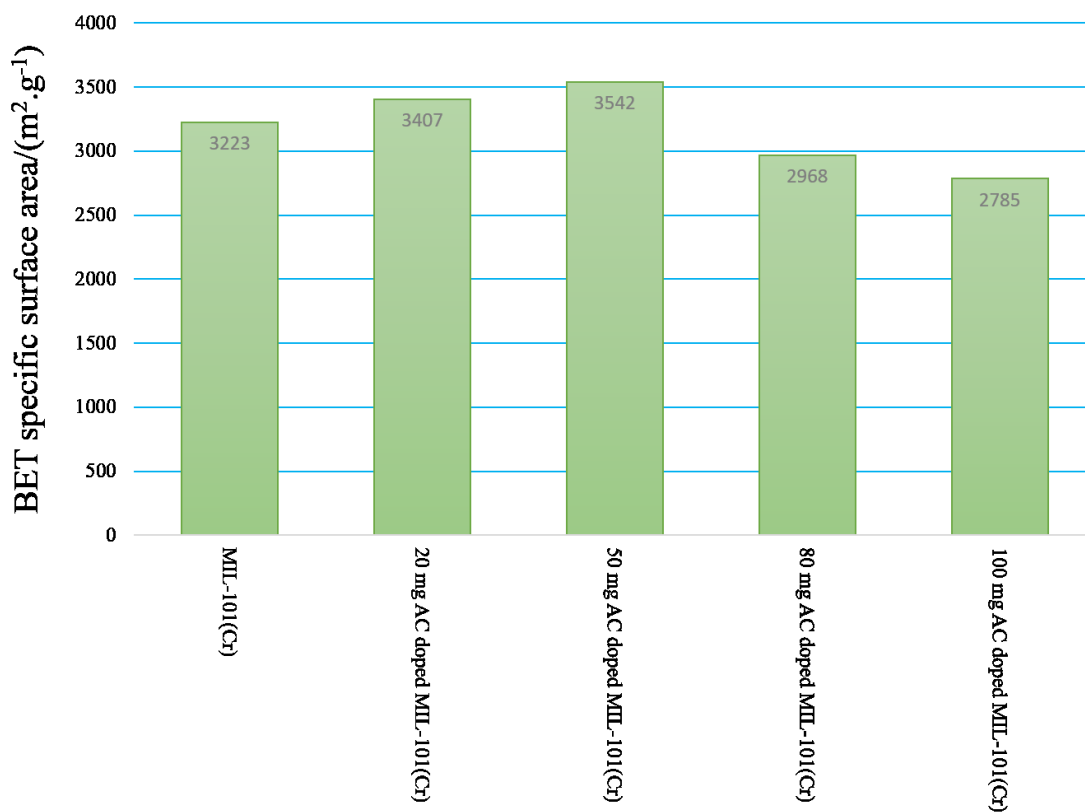
Figure 1.15: Effect of AC doping on the BET specific surface area of synthesized composites.

50 mg AC (5 wt%) doped MIL-101(Cr) material (AC-MIL-101(Cr)-b) shows the highest specific surface area, which implies that this doping amount is optimized for high specific surface area MIL-101(Cr) composite synthesis (Somayajulu Rallapalli et al., 2013).

Compared to the literature, the synthesized MIL-101(Cr) samples have relatively high specific surface area. This comparison is shown in Table 1.5.

Table 1.5: Summary of surface areas of reported MIL-101(Cr) and their synthesis conditions in order to compare with this work.

Mineralizing agent	Time/(h)	Temperature/(°C)	$S_{BET}/(m^2.g^{-1})$	Reference
HF	8	200	2638	This work
CH$_3$COOH	8	200	3223	
CH$_3$COONa	18	180	3131	
HF	8	220	4100	(Férey et al., 2005b)
HF	8	220	2231	(Szilágyi et al., 2014)
HF	8	220	2233	(Cao et al., 2014)
HF	8	220	2651	(Zhou et al., 2014)
HF	8	220	2846	(Pires et al., 2014)
HF	8	220	2931	(Li and Yang, 2008)
HF	8	220	2995	(Wee et al., 2014)
HF	8	220	3007	(Salomon et al., 2014)
NaOH	24	210	3200	(Khan et al., 2011)
-	18	218	3460	(Bromberg et al., 2012)
TMAOH	24	180	3197	(J. Yang et al., 2010)
HNO$_3$	8	220	3450	(Zhao et al., 2015)
CH$_3$COOH	8	220	2660	
HF	8	220	3620	
-	8	220	2410	
HCl	8	220	1560	
H$_2$SO$_4$	8	220	1750	
HF	8	220	2887	(Somayajulu Rallapalli et al., 2013)
CH$_3$COOH	8	220	3148	(Karikkethu Prabhakaran and Deschamps, 2015b)
HF	8	220	2887	(Karikkethu Prabhakaran et al., 2011)
HF	8	220	1270	(Anbia and Hoseini, 2012)
CH$_3$COOLi	12	200	3401	(J.-J. Zhou et al., 2013)
CH$_3$COOK	12	200	3398	

The enhancements of specific surface area of doped MIL-101(Cr) composites are also compared with other carbon adsorbent doped MOFs, as shown in Table 1.6.

Table 1.6: Comparison between AC doped MIL-101(Cr) and other carbon adsorbent doped MOFs.

MOF	Doping agent	$S_{BET}/(m^2.g^{-1})$	Enhancement in S_{BET}	Reference
MIL-101(Cr)	AC	3407	5.7%	This work
MIL-101(Cr)	AC	3542	9.8%	
MIL-101(Cr)	AC	2968	-7,9%	
MIL-101(Cr)	AC	2785	-13.6%	
MIL-101(Cr)	AC	3556	23.2%	(Somayajulu Rallapalli et al., 2013)
MIL-101(Cr)	AC	3458	9.8%	(Karikkethu Prabhakaran and Deschamps, 2015b)
MIL-101(Cr)	SWCNT	2998	3.8%	(Karikkethu Prabhakaran et al., 2011)
MIL-101(Cr)	MWCNT	1243	-2.1%	(Anbia and Hoseini, 2012)
MIL-101(Cr)	graphene oxide	2928	9.4%	(Zhou et al., 2014)
Cu(BTC)	MWCNT	1458	-8.1%	(Xiang et al., 2011)
Cu(BTC)	graphene oxide	1002	10.2%	(Petit et al., 2011)
Cu(BTC)	hierarchical porous carbon monolith (HCM)	516	-64.4%	(Qian et al., 2012)
CU(BTC)	vertically-aligned carbon nanotube	767	-54.8%	(Ge et al., 2013)
MOF-5	MWCNT	2900	60.2%	(Yang et al., 2009)
MOF-5	graphite oxide	806	14.2%	(Petit and Bandosz, 2009)
ZIF-8	carbon nanotube	1650	10.3%	(Dumée et al., 2013)

The properties of resulted doping composite, especially the specific surface area vary according to both doping agent and MOF, as can be observed from Table 1.6. This variation might be related to the nature of MOF and the doping agent, the doping concentration as well as the synthesis/activation method.

1.4.4.3. Total pore volumes of MIL-101(Cr) and AC doped MIL-101(Cr) composites

The total pore volume calculated by Gurvich rule and BJH adsorption data is presented in Table 1.7. The pore volume calculated by Gurvich rule depends on the relative pressure used (with corresponding pore width) and here it is limited at p/p^0=0.98 with pore width 129.1 nm. The pore volume calculated by BJH adsorption data is an integral of pore volume with pore diameter larger than 1.7 nm, which represents the lowest limit of BJH method (Barrett et al., 1951).

Table 1.7: Pore volume of MIL-101(Cr)-a, MIL-101(Cr)-b, AC-MIL-101(Cr)-a and AC-MIL-101(Cr)-b calculated by applying Gurvich rule of single point pore volume or BJH method using nitrogen adsorption data.

Sample	Pore volume/($cm^3.g^{-1}$) Single point	Pore volume/($cm^3.g^{-1}$) BJH adsorption
MIL-101(Cr)-a	1.94	2.02
MIL-101(Cr)-b	1.92	1.94
AC-MIL-101(Cr)-a	2.02	2.50
AC-MIL-101(Cr)-b	2.04	2.65

Differences can be observed from pore volume calculations. It is also interesting to remark that AC doped MIL-101(Cr)s show larger pore volume.

1.4.4.4. *Pore size distributions of MIL-101(Cr) and AC doped MIL-101(Cr) composites*

Different correction of Kelvin equation and thickness equations are used firstly in BJH method to calculated the pore size distribution (PSD) according to the adsorption/desorption branches of N_2 adsorption measurements of MIL-101(Cr) (MIL-101(Cr)-a) and AC doped MIL-101(Cr) (AC-MIL-101(Cr)-b). The results are illustrated in Figure 1.16 and Figure 1.17 respectively.
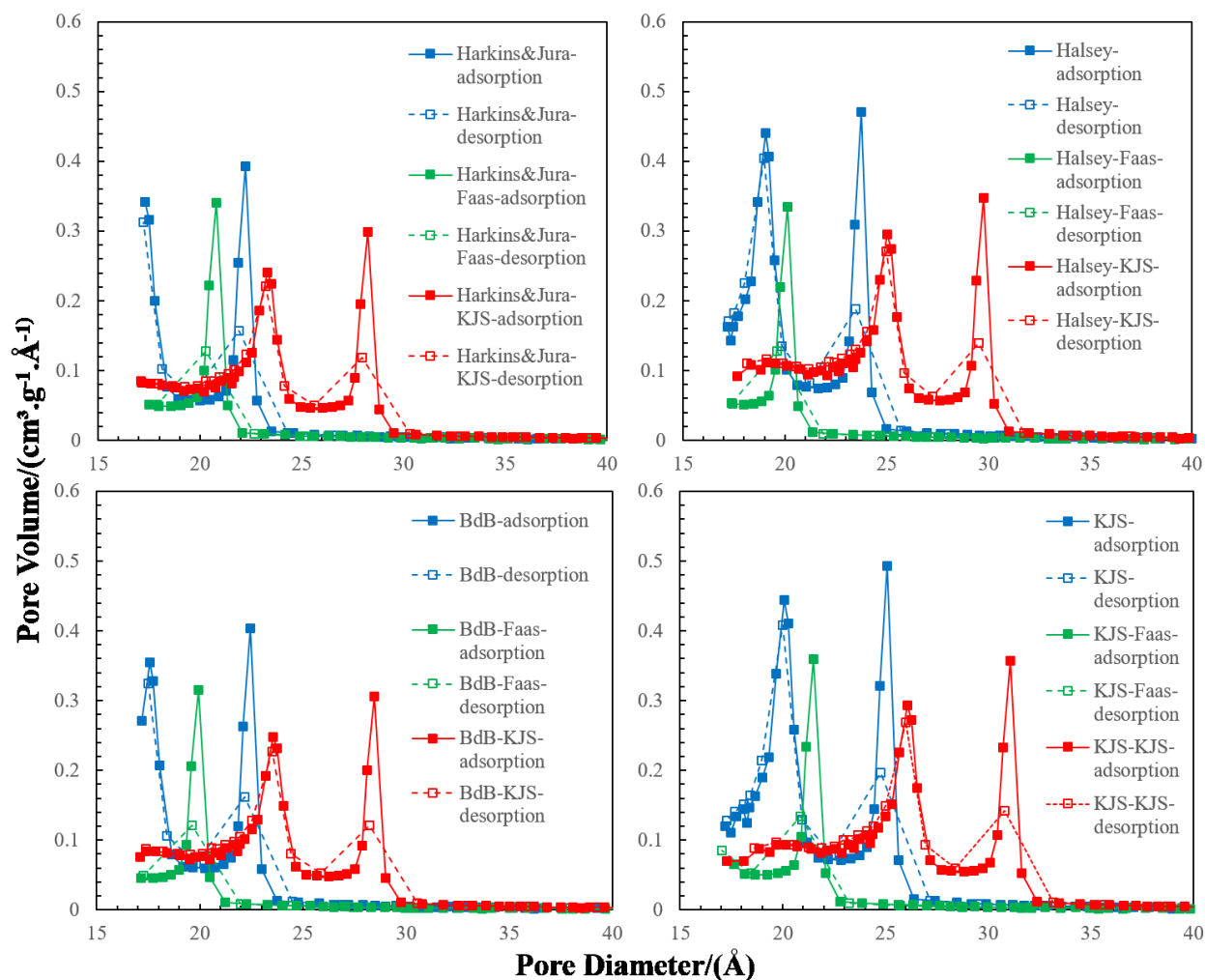
Figure 1.16: Pore size distribution of MIL-101(Cr) (MIL-101(Cr)-a) sample calculated by using original Kelvin equation or with Faas/Kruk-Jaroniec-Sayari correction. The thickness equation applied are, namely, Harkins-Jura thickness equation (top-left), Halsey equation (top-right), Broekhoff de Boer equation (bottom-left) and Kruk-Jaroniec-Sayari equation (bottom-right). The pore size distribution calculated based on adsorption (solid lines) and desorption (dashed lines) branches are both presented.
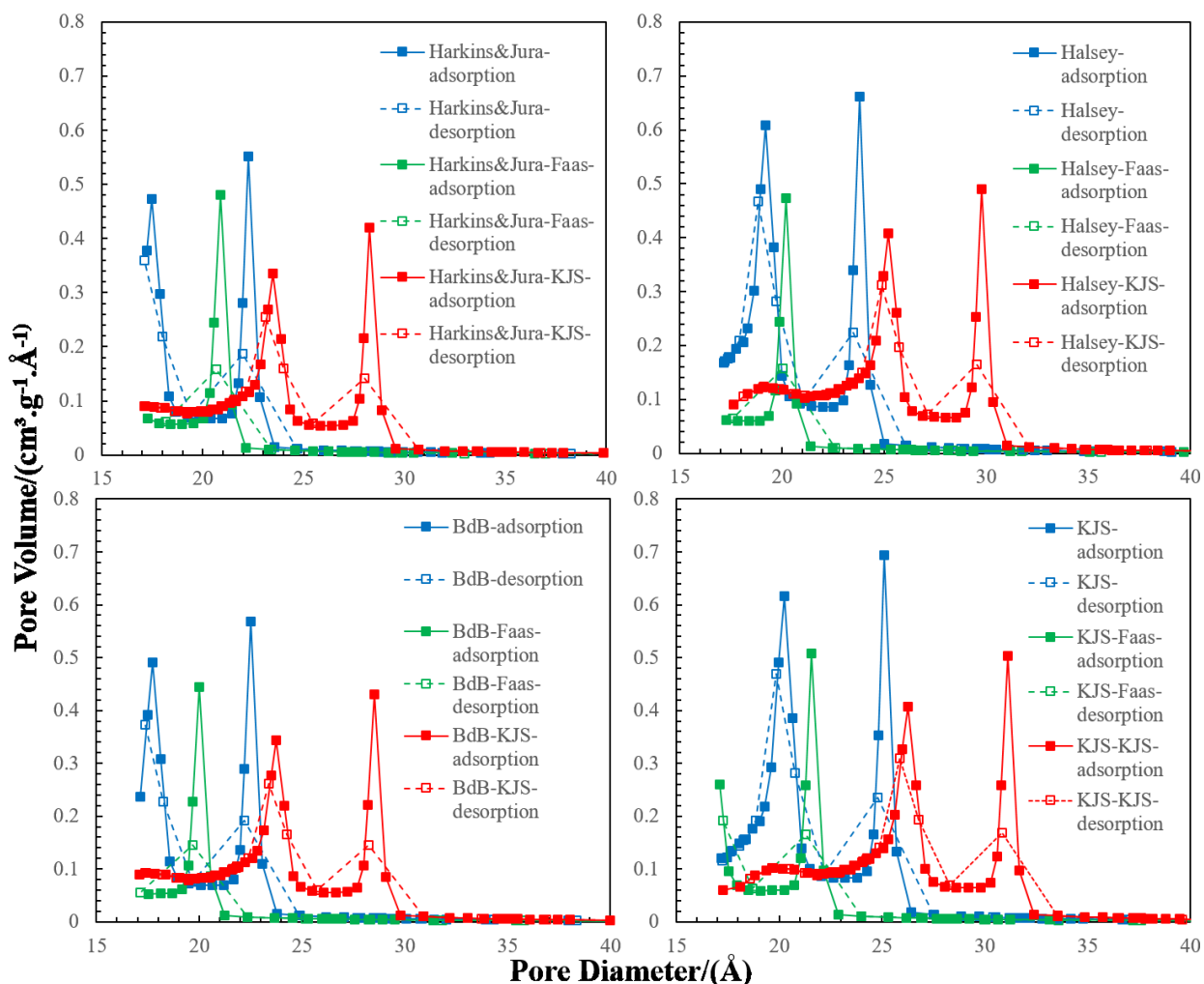
Figure 1.17: Pore size distribution of AC doped MIL-101(Cr) (AC-MIL-101(Cr)-b) sample calculated by using original Kelvin equation or with Faas/Kruk-Jaroniec-Sayari correction. The thickness equation applied are, namely, Harkins-Jura thickness equation (top-left), Halsey equation (top-right), Broekhoff de Boer equation (bottom-left) and Kruk-Jaroniec-Sayari equation (bottom-right). The pore size distribution calculated based on adsorption (solid lines) and desorption (dashed lines) branches are both presented.

It can be observed from the results shown in Figure 1.16 and Figure 1.17 that the smallest pore diameter measurable by BJH method is 1.7 nm. Generally, all methods show PSDs with two peaks (for Faas correction, the other peak is in micropore region which cannot be calculated by BJH method, see bottom-right of Figure 1.17) and the sharpness of the differential peak indicates that the distribution is narrow.

It can be also observed from Figure 1.16 and Figure 1.17 that the influence of thickness equation is less than the correction methods for Kelvin equation. The Faas correction gives a negative translation of the PSD while the KJS correction gives a positive translation of the PSD.

In KJS method, the relation between the pore diameter and the relative equilibrium pressure was empirically derived from adsorption data of ordered mesoporous materials such as MCM-41, which

possessed open-ended cylindrical pores of controlled size (Kruk et al., 1997). It can be observed from Figure 1.16 that the PSD calculated using Kruk-Jaroniec-Sayari (KJS) correction and KJS thickness equation (26 and 31 Å) shows the best agreement with the theoretical pore size of MIL-101(Cr) (29 and 34 Å) (Férey et al., 2005b). In the BJH method, it is supposed that the pores are cylindrical which is geometrically different from the reality. Hence, the difference in pore size is acceptable.

The PSDs of the adsorption branch and the desorption branch have the same peak which means no tensile strength effect (TSE) has been shown during the measurements. Knowing that the TSE often happens for the adsorbents showing a broad range of mesopores (Groen et al., 2003), it is reasonable to admit that MIL-101(Cr) which only has two types of mesopores does not show this effect. As the number of points in desorption branch is less than that of adsorption branch, the PSD diagram represented using differential form (dV/dr) shows broader distribution.

NLDFT method is firstly applied to compute the PSD of the activated carbon Norit RB3. The kernel chosen is the 2 dimensional NLDFT with carbon finite slit pores (pore diameter to width aspect ratio of 6) (Jagiello and Olivier, 2009). The result is presented in Figure 1.18.
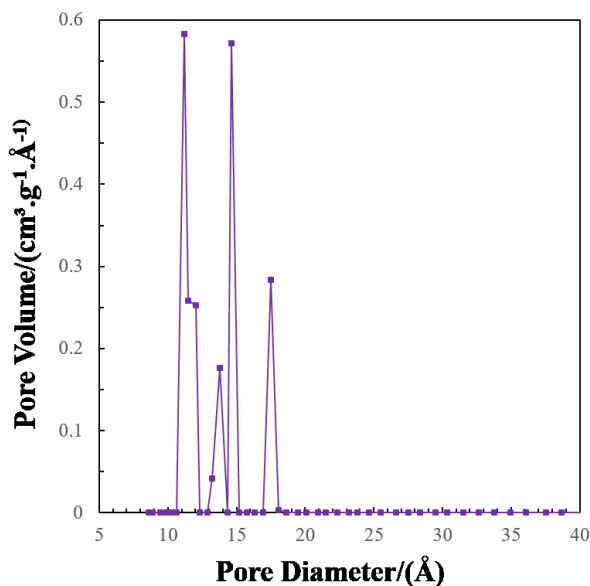
Figure 1.18: Pore size distribution calculated for AC Norit RB3.

The PSD of the AC shows well its microporosity where all pore diameters range from 10 to 20 Å. NLDFT method is also used to evaluate the pore size distribution of MIL-101(Cr) in literature (Sonnauer et al., 2009). It was said that compared to BJH method, microscopic methods based on statistical mechanics such as NLDFT are more accurate. Conventional BJH method assumes only bulk-fluid behaviour and neglects details concerning the fluid-wall interactions. Therefore, this method could easily underestimate the pore size up to 25% for narrow mesopores (pore size smaller than 100 Å). On the contrary, with the application of adsorption potential (N_2-oxidic/siliceous

surface) and the geometry (cylindrical) simulated in NLDFT method, a more precise PSD with a real adsorbent situation is observed.

In this work the NLDFT kernel chosen is based on Tarazona's smoothed density approximation with weighting function corresponding to a cylindrical geometry, developed by Tarazona (1985; 1987). The choice of this kernel is based on the good agreement of regression fit generated by NLDFT and the experimental isotherm. A comparison between BJH method and NLDFT method is illustrated in Figure 1.19.
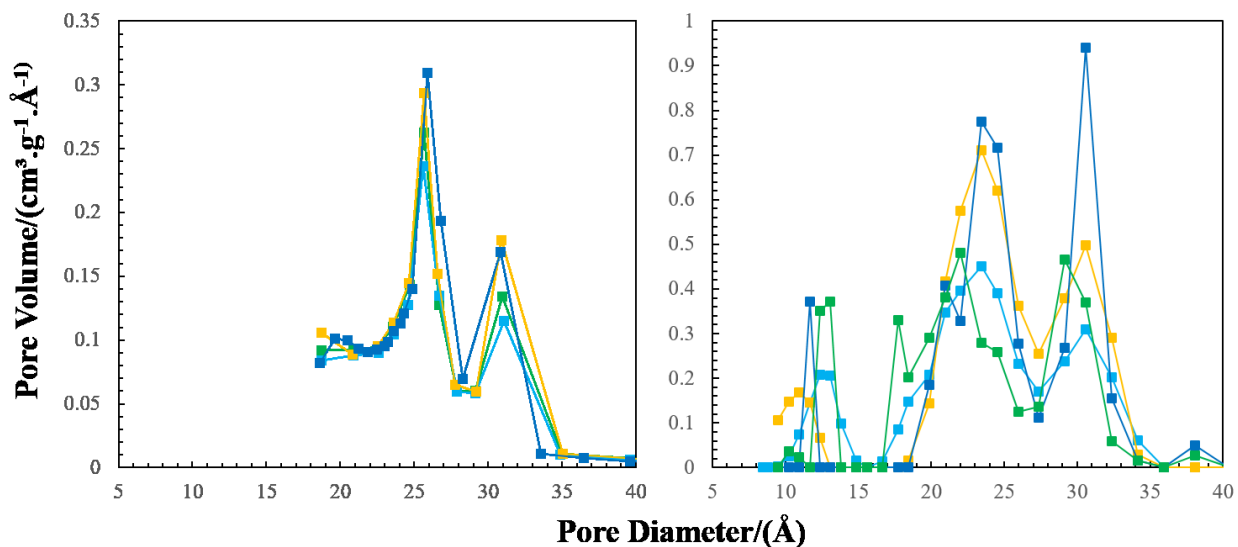
Figure 1.19: Pore size distribution calculated by BJH method (left) and NLDFT method (right) for MIL-101(Cr) and AC doped MIL-101(Cr) composite samples: MIL-101(Cr) synthesized using acetic acid in green, MIL-101(Cr) synthesized using sodium acetate in light blue, 2 wt% AC doped MIL-101(Cr) in yellow and 5wt% AC doped MIL-101(Cr) in dark blue.

As illustrated in Figure 1.19, it can be observed that all samples have nearly the same distribution of the pores and the values of 26 and 31 Å pore diameters are very close to the theoretical results of 29 and 34 Å (Férey et al., 2005b). Moreover, AC doped MIL-101(Cr)s show higher porosity than non-doped ones and these results are in good agreement with the data of (Somayajulu Rallapalli et al., 2013). In PSD calculated by NLDFT method, a peak around 10 Å appears and the latter can be attributed to the 8.6 Å aperture of the Super Tetrahedron (ST) formed by chromium trimers.

Considering the applicability of NLDFT to the whole range of pores, it can be observed that results given by NLDFT can be extended to micropore range, due to its applicability to the whole range of pores. However, the calculated PSDs shows broader peaks compared to BJH method and the pore volume is larger. This phenomenon can be a consequence of the choice of the kernel used for the calculations (more appropriate for zeolites (Tarazona, 1985; Tarazona et al., 1987)).

1.4.5. Effect of washing process

The as-synthesized products need to be washed in order to remove the residual molecules, especially the unreacted BDC molecules trapped in the pores.

Washing solutions for as-synthesized MIL-101(Cr) purification mentioned in the literature include ethanol (Férey et al., 2005b), DMF and ethanol (Chowdhury et al., 2009), NH_4F solution (Karikkethu Prabhakaran and Deschamps, 2015b), ethanol and NH_4F solution (Jiang et al., 2011). Three of these methods have been tested for washing the as synthesized products and the results are shown in Table 1.8, since the effect of only ethanol wash is not good as ethanol and NH_4F solution wash.

Table 1.8: Comparison of different activation method for MIL-101(Cr) as-synthesized products.

As-synthesized product	Wash method	S_{BET} before wash /(m².g⁻¹)	S_{BET} after wash /(m².g⁻¹)
MIL-101(Cr)-a	NH_4F	2597	3171
MIL-101(Cr)-a	Ethanol and NH_4F	2597	3223
MIL-101(Cr)-b	NH_4F	2608	3015
MIL-101(Cr)-b	Ethanol and NH_4F	2608	3131
MIL-101(Cr)-c*	NH_4F	1855	2069
MIL-101(Cr)-c*	DMF and ethanol	1855	2638

*MIL-101(Cr)-c refers to MIL-101(Cr) synthesized using HF.

The results show that the washing by using ethanol following by NH_4F solution treatment gives a final product more porous. Purification with DMF and ethanol can also easily remove the residuals in pores and produce highly porous adsorbent. However, the manipulation of DMF is difficult and costly, as this work is about to scale-up the synthesis, the purification using ethanol and NH_4F solution seems to be a good solution.

1.4.6. Effect of different synthesis parameters

Concerning the synthesis of MIL-101 using HF as the mineralizing agent, the risks associated with the safety are very important and the obtained product is not highly porous as expected. Synthesis of MIL-101(Cr) with acetic acid as mineralizing agent seems to provide better results than the synthesis using HF and the obtained BET surface area value reaches more than 3000 m².g⁻¹.

The synthesis of MIL-101 consists essentially of the formation of chromium trimers and the deprotonation of H_2BDC. Therefore, adding CH_3COONa instead of CH_3COOH or HF increases the pH value of the solution, and this rise is helpful to deprotonate H_2BDC into benzenedicarboxylate in water. Huang *et al.* (2011) reported that H_2BDC molecules become soluble in water when pH=6 and this phenomenon greatly enhances the formation of nuclei of MIL-101(Cr). Moreover, the improvement of the solubility of H_2BDC molecules is advantageous because no extra activation process is needed and after the synthesis (J.-J. Zhou et al., 2013), no white needle-like H_2BDC molecules are observed in the autoclave.

The solvent is crucial in MIL-101(Cr) synthesis. Solvent effects concerning MOF synthesis are already well discussed in the literature. Diao *et al.* (2011) reported that the dimensional framework of Cadmium-4,4′-oxybis(benzoic acid)-4,4′-bipyridine (Cd(OBA)(bipy)) depends on the solvent used for the synthesis (dimethylformamide (DMF) or water). It was also reported that the addition of acetone in the reaction mixture during the synthesis of MIL-100(Fe), produces the MIL-45(Fe) material with smaller pores (Birsa Čelič et al., 2012). The H_2O/acetone molar ratio in the reaction mixture reveals the controlling role of acetone in the formation of MIL-45(Fe) and MIL-100(Fe) structures through oxidation-reduction and material-solvent interaction processes. Goesten *et al.* (2013) investigated the formation of NH_2-MIL-53(Al) and NH_2-MIL-101(Al) using *in-situ* WAXS and SAXS (Wide and Small-angle X-ray Scattering). It was suggested that NH_2-MIL-53(Al) is formed through hydrolysis of aluminium chloride hexahydrate ($AlCl_3 \cdot 6H_2O$) and if DMF is added the intermediate phase NH_2-MOF-253 (Al) is then transformed into NH_2-MIL-101(Al). Khan *et al.* (2011) used only chromium metal salt and H_2BDC for their synthesis and they concluded that higher water concentration can prevent Cr(III) transformation into Cr(II) during the synthesis and the formation of Cr trimers is preferred. Similarly, the synthesis of MIL-53 material is nearly stopped at higher reactant:water molar ratio (1:500). However, with the presence of the mineralizing agent, this ratio can be reduced to *ca* 1:260. Hence, the solvent used for MIL-101(Cr) and AC doped MIL-101(Cr) syntheses is water with a fixed molar ratio at 1:268 in this work. The results showed that the crystallinities and porosities of synthesized products are in good agreement with literature (Férey et al., 2005b; Guo and Chen, 2012; Huang et al., 2011; Karikkethu Prabhakaran and Deschamps, 2015b; Somayajulu Rallapalli et al., 2013; J.-J. Zhou et al., 2013) and imply that this molar ratio (1:268) of solvent is proper for MIL-101(Cr) and AC doped MIL-101(Cr) syntheses.

1.5. Conclusion

Pristine MIL-101(Cr) and AC incorporated MIL-101(Cr) were synthesized. Different synthesis methods and parameters, such as mineralizing agents (hydrofluoric acid (HF), acetic acid (CH_3COOH) and sodium acetate (CH_3COONa)) and heating temperature (180 and 200°C) were tested. Conventional heating and microwave-assisted heating methods were also applied. The tested doping concentrations of AC varied between 20 mg and 100 mg, which correspond to a mass ratio of yielded pristine MIL-101(Cr) between 2 and 10 wt%.

The as-synthesized products were washed by using different washing methods (ethanol (CH_3CH_2OH), dimethylformamide (DMF), ammonium fluoride (NH_4F) solution) to remove guest molecules trapped within the pores and the obtained compounds were characterized by using conventional techniques.

It was shown that both crystal size and crystallinity influence the quality of powder X-ray diffraction (PXRD) patterns. The crystal size and the crystallinity can be modified by the mineralizing agent and doping during syntheses. Pristine MIL-101(Cr) synthesized using

CH₃COOH appears to have the best crystallinity as well as the pristine sample synthesized using HF.

Scanning electron microscopy (SEM) images were performed and the morphologies of different samples were studied. The images showed that MIL-101(Cr) synthesized using CH₃COOH possesses the largest mean crystal size (120 nm) among all samples tested whereas MIL-101(Cr) synthesized with CH₃COONa has the smallest mean crystal size (50 nm). The smaller size of the latter could be due to the mineralizing agent effect which increases the pH of the solution and therefore accelerates the nucleation rate. The AC doped samples have smaller crystal sizes down to 60 or 80 nm (for 2 or 5 wt% AC doped MIL-101(Cr)). The less regular crystal forms of AC doped samples could be caused by the growth of MIL-101(Cr) on the surface of the AC and this phenomenon leads to a polycrystalline MOF layer.

The TGA studies showed that MIL-101(Cr) as well as AC doped MIL-101(Cr) are stable up to 200°C (473 K) and they decompose at the temperature above.

The pore structures and specific surface area of samples were analysed by nitrogen (N₂) adsorption technique at 77 K. All samples show a type IV nitrogen adsorption isotherm with type H1 hysteresis which confirms the mesoporosity of synthesized products. The specific surface areas of samples were calculated using the Langmuir monolayer adsorption model and the BET (Brunauer-Emmett-Teller) multilayer adsorption model. Apparently, AC doping at low concentration increases the porosity of MIL-101(Cr) while exhaustive doping decreases the porosity of the framework. Highest Langmuir specific surface area of 4951 $m^2.g^{-1}$ and BET specific surface area of 3542 $m^2.g^{-1}$ were measured for the 5 wt% AC doped MIL-101(Cr) compound. The pristine MIL-101(Cr) synthesized using HF shows a Langmuir specific surface area of 3699 $m^2.g^{-1}$ and a BET specific surface area of 2638 $m^2.g^{-1}$. The MIL-101(Cr) synthesized using CH₃COOH and CH₃COONa show enhanced specific surface area and MIL-101(Cr) synthesized using CH3COOH reaches a Langmuir specific surface area of 4668 $m^2.g^{-1}$ and a BET specific surface area of 3223 $m^2.g^{-1}$.

Pore size distributions were calculated using both BJH (Barret-Joyner-Halenda) and non-localized density functional theory (NLDFT) methods. In BJH method, Faas and KJS (Kruk-Jaroniec-Sayari) corrections are applied to correct the original Kelvin equation used for the calculation of the capillary condensation. Different equations were used to calculate the thickness of adsorbed nitrogen layer. The results showed that the KJS correction and the thickness equation seems to correctly compute the pore size distribution of the samples and the values of the calculated pore diameters are 26 and 31 Å, which are very close to the theoretical ones. NLDFT using kernel developed by Tarazona can also achieve this pore size distribution. Moreover, with this method, micropores formed by the super tetrahedrons (STs) can be evaluated (aperture of 8.6 Å).

Chapter 2
Hydrogen Adsorption Isotherms

Les performances de stockage de l'hydrogène ont été évaluées sur le panel de matériaux adsorbants synthétisés, incluant les échantillons MIL-101(Cr) purs obtenus par différentes voies de synthèse et dopés au charbon activé. Les capacités d'adsorption ont été déterminées à partir de la mesure d'isothermes d'équilibre sur deux appareillages différents, opérant d'une part par volumétrie et d'autre part par gravimétrie. La méthode de mesure volumétrique implique la mesure directe de la température et de la pression dans la chambre d'adsorption, remplie avec une quantité connue d'hydrogène présent en phase adsorbée et en phase gazeuse. Les quantités adsorbées en excès sont déduites à partir de l'équation de conservation de masse et de l'équation d'état du gaz. Les mesures ayant été effectuées jusqu'à 50 bar, à la température de 77 K, la méthode dite du « double volume imaginaire » a été appliquée afin de rendre compte des gradients de température entre le réservoir à l'ambiante et la chambre d'adsorption immergée dans l'azote liquide. La méthode gravimétrique repose sur la mesure du changement de la masse de d'échantillon exposé à la phase gazeuse. Pour effectuer cette mesure, une microbalance à suspension magnétique est employée. La masse d'hydrogène adsorbé en excès est calculée à partir d'un bilan de forces qui prend en compte l'effet de poussée d'Archimède. Les mesures ont été réalisées suivant cette méthode jusqu'à 100 bar, aux températures de 77 et 298 K. Les isothermes mesurées par les deux méthodes en conditions cryogéniques ont été comparés entre elles, et un bon accord a été trouvé. Les capacités de stockage des matériaux ont été déduites et exprimées par unité de masse et de volume d'adsorbant. A 100 bar et 77 K, les capacités massiques rapportées aux quantités absolues d'hydrogène adsorbé ont été évaluées au maximum à 14.8 % pour le MIL-101(Cr) pur et à 19.8 % pour les matériaux dopés au charbon actif, correspondant à des capacités volumiques respectivement de 27.1 et 37.7 g.L^{-1}. Cette amélioration des capacités de stockage sur les matériaux dopés a été attribuée à l'augmentation de la fraction de volume microporeux créé par la présence de charbon active dans le réseau cristallin. Comparées aux capacités de stockage reportées dans la littérature pour d'autres types d'adsorbants, notamment MOF ou MOF-composites, les valeurs obtenues avec les matériaux MIL-101(Cr) dopés au charbon actif sont sensiblement supérieures.

2. Hydrogen adsorption isotherms

2.1. Physical adsorption: theory

2.1.1. Description of the process

To discuss the adsorption process, three terms have to be preliminarily defined:
- Adsorbent: solid with surface available for binding molecules.
- Adsorptive: fluid (gas or liquid) molecules in both adsorbed and bulk phases.
- Adsorbate: molecules adsorbed on solid surface

The physical adsorption or so-called physisorption phenomenon describes an increase of density of an adsorbate at the surface of an adsorbent.

In physisorption, the interactions between molecules are governed by van der Waals forces (dispersion-repulsion) and electrostatic interactions.

The van der Waals forces arise from instantaneous induced dipoles (London Dispersion Force) (London, 1937), induced dipole-induced quadrupole and induced quadrupole-induced quadrupole interactions (Ruthven, 1984). The calculation of such potential is difficult, but this potential is usually approximated by using the Lennard-Jones potential function graphically represented in Figure 2.1. This potential function is usually used to approximately represent the dispersion-repulsion interaction (Jones, 1924):

$$\phi = 4\varepsilon \left[\left(\frac{\sigma}{r_{ij}} \right)^{12} - \left(\frac{\sigma}{r_{ij}} \right)^{6} \right] \qquad (2.1)$$

where ε and σ are characteristics of the molecules: ε represents energetically the depth of potential well and σ is the finite distance where the inter-particle potential is zero; r_{ij} is the distance between two atoms.
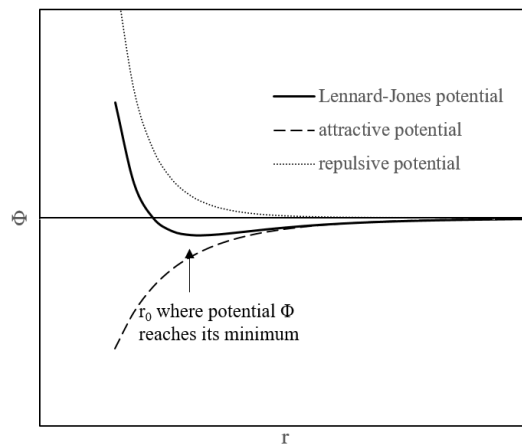
Figure 2.1: Lennard-Jones potential as a function of distance r_{ij} separating the adsorptive molecule from the adsorbent surface.

The r_{ij}^{-12} term represents the repulsive part of the potential and describes the Pauli repulsion at short ranges due to the overlapping electron orbitals. The r_{ij}^{-6} term characterises the attractive part and describes attractions at long ranges (dispersion force).

Because of strong repulsive interactions, the Lenard-Jones potential increases rapidly when the distance r_{ij} is close to zero. It increases after reaching a minimum at $r_{ij}=r_0$, when the attractive interaction becomes larger than the repulsive contribution. r_0 is the equilibrium position of the two molecules, for instance, the distance between two hydrogen atoms in a dihydrogen molecule is 0.74 Å (DeKock and Gray, 1989). At large distance, the contribution of the attractive forces becomes less and less intense until being nil.

The electrostatic force is important while there is a significant electric field in the region of the surface and additional adsorption energy arises from polarization, field-dipole and field gradient-quadrupole interactions (Ruthven, 1984). Thus, for adsorbents such as zeolites (Auerbach et al., 2003) or MOFs with open metal sites (He and Chen, 2014), the electrostatic contribution for adsorption energy cannot be neglected.

The surface of the solid contains a lot of adsorbent atoms or molecules which have their potential overlaid and superimposed. A potential energy landscape is then formed and a low potential position corresponds to a binding site for adsorbate. This phenomenon is illustrated in Figure 2.2.
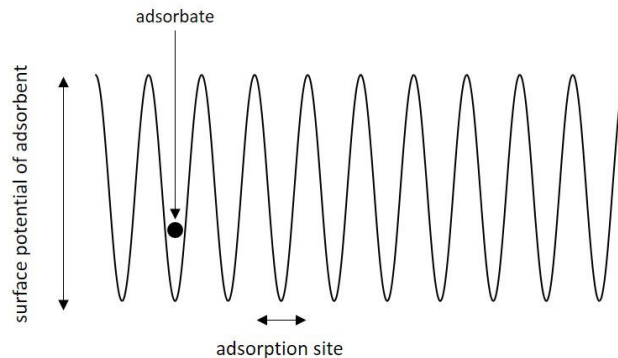
Figure 2.2: Surface potential of adsorbent and the binding sites formed for adsorbate.

If one adsorptive molecule is close enough to the surface of the adsorbent, it can drop into the surface potential well and fall into adsorbed phase (Figure 2.2). Otherwise, a local thermal agitation can cause a jumping out of the adsorbed molecule from the potential, inducing desorption from the surface of the adsorbent.

2.1.2. Gas-solid interface: adsorption in excess

The total amount of adsorbable compound in the system is divided into two parts, the adsorbed phase and the gas phase. The exact evaluation of the adsorbed amount (*i.e.*, the adsorbed phase) requires a good knowledge of either the exact volume of gas or the variation of the local concentration of gas. In practice, it is impossible to reach these requirements. To overcome this problem, Gibbs (1878) proposed an alternative approach which uses the concept of "surface excess"

to quantify the adsorbed amount. According to this concept, the total volume of gas adsorbed is divided into two parts by an imaginary line called "the Gibbs dividing surface" (GDS) and placed parallel to the surface of the adsorbent. One of these two parts is filled with the gaseous adsorptive at a density equal to the bulk gas density, whereas the other fraction is occupied by the amount of gas condensed in excess, with a density larger than the bulk gas. This description is illustrated in Figure 2.3.
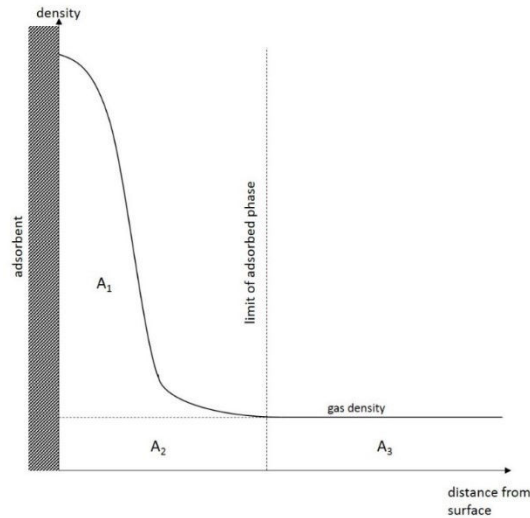
Figure 2.3: Gibbs representation of adsorbed phase: density of fluid phase as a function of the distance from the adsorbent. The y-axis is the density and the x-axis is the distance from the surface. Section A_1 represents the amount adsorbed in excess. Section A_2 represents the equivalent amount of gas occupying the volume of the condensed phase. Section A_3 represents the amount of the gas phase adsorptive in the pores.

In Figure 2.3, three zones are distinguished: adsorbent, adsorbate (adsorbed layer) and the adsorptive in the gas phase. The amount adsorbed in excess at the pore surface represented by section A_1 which is defined as the difference between the total amount of adsorptive ($A_1+A_2+A_3$) and the amount which would be present in the gas volume assuming a constant gas density up to GDS (A_2+A_3). The absolute adsorbed amount corresponds to the sum of sections A_1 and A_2 (Rouquerol et al., 2014).

It is impossible to experimentally determine the volume of the adsorbed phase V_a. However V_a can be evaluated using methods like the theory of the functional density (Murata et al., 2002). The potential theory developed by Polanyi (1932, 1916, 1914) and micropore filling theory developed by Dubinin (1967) can also be applied to evaluate the volume of adsorbed phase (Hamon et al., 2014). The correlation between the energetic distribution function and the pore size distribution function, the theory of integral heat of adsorption were applied for adsorbed phase determination as well (De Weireld, 2000; Jagiello et al., 1994; Jagiello and Schwarz, 1993).

Alternative simplified method can also be implemented to calculated the absolute adsorbed amount:

The density of the adsorbed phase ρ_{ad} can be considered as constant (Lewis et al., 1950; Reich et al., 1980). It can be then assimilated to the value of the liquid density of hydrogen (70.85 kg.m^{-3} at 20.37 K) (Lemmon et al., 2010). The mass of the adsorbed phase is then expressed as:

$$m^a = m_{GE}^a + \rho_{H_2}(p,T)\frac{m^a}{\rho_{ad}} \tag{2.2}$$

where m^a is the absolute adsorbed mass and m_{GE}^a the mass adsorbed in excess, ρ_{H_2} is the hydrogen gas density and ρ_{ad} the density of the adsorbed phase.

Otherwise, it can be assumed that the volume of the adsorbed phase is considered as constant (Payne et al., 1968; Quirke and Tennison, 1996). It can then be assimilated, either to the monolayer volume ($V_a=\sigma S$, where σ is the diameter of the adsorptive molecule (m) and S is the specific surface area (m^2.g^{-1})) or to the total pore volume V_{pore} (cm^3.g^{-1}). The absolute mass of the adsorbed phase can then be expressed as:

$$m^a = m_{GE}^a + \rho_{H_2}(p,T)V_{ad} \tag{2.3}$$

where $V_{ad}=V_a$ or V_{pore}.

2.1.3. Adsorption isotherms modelling

According to Gibbs phase law, three variables are needed to characterize the system which consists of gas-adsorbed phase: the temperature (T), the pressure (p) and the adsorbed quantity (q). The relationship between the adsorbed amount and the equilibrium pressure at a given temperature is called the adsorption isotherm (Sing et al., 2014b). Usually, an adsorption isotherm of a gas in an adsorbent is expressed in the following form:

$$q = f(p) \tag{2.4}$$

where q is the adsorbed amount per unit of mass of adsorbent and p is the applied pressure.

Different adsorption isotherm equations have been developed, based on either theoretical or empirical considerations. A brief review of the most conventional isotherm equations applicable for the computation of the equilibrium adsorbed quantities is given below:

2.1.3.1. Henry's model: linear adsorption relationship

For an ideal surface at infinite dilution (low surface coverage), where every adsorbed molecule is well isolated, the relationship between the adsorbed amount and the applied pressure is linear. By analogy with the gases dissolved in solutions, this relationship is referred as Henry's law (Henry, 1803) and it is expressed as following:

$$q = k_H p \tag{2.5}$$

where q is the amount adsorbed (mol.kg^{-1}), k_H the Henry's constant (mol.kg^{-1}.bar^{-1}) and p the pressure applied (bar). Henry's law only applies at a very low coverage of the adsorbent surface.

2.1.3.2. Langmuir's model: monolayer adsorption

Langmuir (1918) proposed one adsorption mechanism based on several hypotheses:

(i) all adsorption sites are energetically equivalent and no interaction exists between adsorbed molecules, (ii) each adsorption site can only hold one adsorbate, (iii) only one layer of adsorbate can be formed. The relationship between the quantity of adsorbate and the pressure is then:

$$q = q_0 \frac{bp}{1 + bp} \tag{2.6}$$

where q_0 is the monolayer adsorption capacity (mol.kg^{-1}) and b is the Langmuir adsorption affinity (bar^{-1}).

At low pressure, Equation 2.6 reduces to Henry's law and at high pressure q approaches to q_0 which implies the formation of the monolayer.

2.1.3.3. *Brunauer-Emmett-Teller's model: multilayer adsorption*

Brunauer *et al.* (1938) extended the Langmuir's monolayer adsorption model to multilayer adsorption with certain assumptions: (i) each molecule in the first adsorbed layer serves as one site for the second and subsequent layer, (ii) the molecules in the second and subsequent layers are considered to behave as the saturated liquid while the equilibrium constant for the first layer of molecules in contact with the surface of the adsorbent is different, and the adsorption isotherm derived is:

$$q = \frac{q_0 C \left(\frac{p}{p^0}\right)}{\left(1 - \frac{p}{p^0}\right)\left(1 - \frac{p}{p^0} + C\left(\frac{p}{p^0}\right)\right)} \tag{2.7}$$

with p^0 the saturation vapour pressure (bar) and C a constant which depends on the heat of adsorption (Lamb and Coolidge, 1920).

2.1.3.4. *Dubinin's model: micropore filling*

Polanyi (1932, 1916, 1914) assumed that the molecules near a surface move according to a potential and the change in this potential can be expressed as a difference of chemical potential between the adsorbed phase and the bulk phase:

$$E = RT\ln\left(\frac{p^0}{p}\right) \tag{2.8}$$

The equation above implies that large variations of the chemical potential should be obtained in the high pressure range and therefore adsorptive molecules should be located closer to the surface. Based on the theory of Polanyi, Dubinin used the idea of micropore filling instead of layer by layer deposition of adsorbate. In this theory, the ratio of adsorption potentials, $\beta = E/E_0$, is constant if they fill the same volume in pores for a given adsorbent. β is defined as the affinity coefficient and E_0 is a reference adsorption potential.

Dubinin and Raduchkevich (1947) used this approach and by assuming that the micropore size distribution is Gaussian, the characteristic curve of adsorption is obtained and can be then expressed as:

$$q = q_0 \exp\left[-\left(\frac{RT}{\beta E} \ln \frac{p^0}{p}\right)^2\right] \qquad (2.9)$$

The Dubinin-Radushkevich (DR) model have three major disadvantages according to Ruthven (1984): (i) the equation doesn't reduce to Henry's law at low coverage, (ii) the estimation of q_0 gives uncertainty, (iii) the assumption of temperature-independent characteristic curve is not suitable for many systems. However, it was very useful to interpret adsorption data in activated carbon (Chen and Yang, 1994).

2.1.3.5. *Empirical isotherm equations*

In order to fit the experimental adsorption isotherm data, empirical isotherm equations have also been derived. Some of these empirical equations are given in Table 2.1.

Table 2.1: Examples of empirical isotherm equations.

Name of isotherm	Equation
Freundlich	$q = kp^{1/m}$
Sips	$q = q_0 \dfrac{kp^{1/m}}{1 + kp^{1/m}}$
Toth	$q = q_0 \dfrac{p}{(b + p^m)^{1/m}}$
Dubinin-Astakhov	$q = q_0 \exp\left[-\left(\dfrac{RT}{\beta E} \ln \dfrac{p^0}{p}\right)^N\right]$

where q stands for the quantity adsorbed, q_0 is the maximum quantity that can be adsorbed by the material at a certain temperature, p is the pressure and b, k, m and N are empirical parameters.

The Freundlich equation is the earliest empirical isotherm equation. Meanwhile, it can be also obtained by assuming that the surface is heterogeneous in the sense that the adsorption energy is distributed following an exponential decay function. By integrating local isotherm equation which follows Langmuir isotherm equation and with further approximation, Zeldowitsch (1935) found the Freundlich equation can be derived. In the same way, the Sips equation can also be derived by just changing the energy distribution function (Sips, 1948). Moreover, the Sips equation is also called Langmuir-Freundlich equation since it's a combination of the two equations.

The Freundlich equation and the Sips equation both suffer from the disadvantage that they don't reduce to Henry's law at low pressure range. Moreover, the Freundlich equation is not valid at high pressure range since it diverges when applied pressure increases.

The Toth isotherm equation reduces to Henry's law at low pressure and it converges at high pressure. Moreover, it reduces to Langmuir isotherm when the empirical parameter $m=1$, and when m is different from 1, it describes the heterogeneous adsorption.

2.1.4. Adsorption thermodynamics

Adsorption is an exothermal process and it can be characterized by a decrease of the total free energy of the system, G, for a system with constant temperature and pressure. This decrease is described in Equation 2.10:

$$\Delta G^{ads} = \Delta H^{ads} - T\Delta S^{ads} < 0 \tag{2.10}$$

The chemical potentials of the gas phase and the adsorbed phase are defined separately as:

$$\mu^{ads} = \left(\frac{\partial G^{ads}}{\partial n^{ads}}\right)_{T,p}$$

$$\mu^{gas} = \left(\frac{\partial G^{gas}}{\partial n^{gas}}\right)_{T,p} \tag{2.11}$$

If the adsorption system is at equilibrium, then the chemical potentials of the two phases are equal:

$$\mu^{ads} = \mu^{gas} \tag{2.12}$$

By deriving the two sides of Equation 2.12, the classic Clausius-Clapeyron relation is obtained:

$$-s^{ads}dT + v^{ads}dp = -s^{gas}dT + v^{gas}dp \tag{2.13}$$

$$\frac{dp}{dT} = \frac{s^{ads} - s^{gas}}{v^{ads} - v^{gas}} \tag{2.14}$$

with $s^i = \left(\frac{\partial s^i}{\partial n^i}\right)_{T,p}$ and $v^i = \left(\frac{\partial v^i}{\partial n^i}\right)_{T,p}$, respectively.

By admitting that the specific volume of the gas is much greater than that of the adsorbed phase, Equation 2.14 becomes:

$$\frac{dp}{dT} = \frac{s^{ads} - s^{gas}}{-v^{gas}} = -(s^{ads} - s^{gas})\rho^{gas} \tag{2.15}$$

The change in entropy upon adsorption is then:

$$\Delta S^{ads} = -\frac{1}{\rho^{gas}}\left(\frac{dp}{dT}\right)_{n^{ads}} \tag{2.16}$$

At equilibrium, the change of enthalpy can be calculated by combining Equation 2.10 and 2.16:

$$\Delta H^{ads} = -\frac{T}{\rho^{gas}}\left(\frac{dp}{dT}\right)_{n^{ads}} \tag{2.17}$$

This important physical quantity in called the isosteric heat, which characterizes the ratio between the infinitesimal in the adsorbate enthalpy and the infinitesimal change in the adsorbed amount (Do, 1998).

By using equation of state for ideal gas, Equation 2.17 can be further written as van't Hoff equation:

$$\Delta H^{ads} = -RT^2 \left(\frac{d\ln p}{dT}\right)_{n^{ads}} \tag{2.18}$$

In practice, the calculation of isosteric enthalpy of adsorption is to plot $\ln p$ for a given adsorbed amount as a function of $1/T$ from different series of adsorption isotherm. However, the application

of this method relies on the principle that ΔH^{ads} doesn't vary with the temperature and the pressure. Therefore, a temperature difference of 10 K between two isotherms is often considered to be a good compromise to calculate the isosteric heat of adsorption (Rouquerol et al., 2014).

2.2. Experimental methods for isotherm measurements

The techniques such as volumetry, gravimetry, inverse chromatography, oscillometry, impedance spectroscopy (Keller and Staudt, 2005; Rouquerol and Rouquerol, 2014) can be used to perform adsorption isotherms measurements.

The volumetry, or the volumetric method or the Sieverts method (a reference to Sieverts' law) (Sieverts, 1929) is the very earliest way to investigate gas sorption (Gregg and Sing, 1982). According to this method, the adsorptive in the gas phase expands into a vessel where the adsorbent is placed, and the pressure and the temperature are measured throughout the time of the experiment performed in this calibrated, constant volume (Rouquerol and Rouquerol, 2014). By a mass balance equation which involves the equation of state of the gas, the adsorbed amount can be computed. The advantages of using volumetry are: (i) it doesn't require sophisticated high tech equipment, (ii) only temperature and pressure needs to be measured. Meanwhile, the drawbacks of this method are: (i) amount of adsorbent needs to make significant pressure changes for measurements, (ii) difficulty in equilibrium judgements, (iii) adsorptive gas might be adsorbed by vessel instead of adsorbent, (iv) accumulative uncertainties in a step-by-step adsorption isotherm measurement, (v) the measurement of mass-loss during *in-situ* activation.

The gravimetry, or gravimetric method was first applied for adsorption measurement by McBain and Bakr (1926) who used a spring balance during the measurement. In this method, the weight changes of adsorbent in the sample cell during the adsorption are directly monitored and this value can be easily interpreted for adsorption isotherms. However, this technique requires high resolution of the balance (1 µg) and until recent years, the development of electromagnetically compensated beam microbalance and the magnetic suspension balance make this method feasible for most gas adsorption measurements (Keller and Staudt, 2005). The principal advantages of gravimetry are: (i) the accuracy of measurement, (ii) for highly sensitive balances, the amount of sorbent material required is small, (iii) equilibrium of adsorption directly monitored by the balance, (iv) walls of tubes and vessels' adsorption do not interfere the results, (v) extreme pressure can be applied, (vi) the sample mass can be weighed after *in-situ* activation. The disadvantages of gravimetry are: (i) the complexity of the system, compared to volumetric equipment, (ii) preparative measurements required in order to correct the mass measured including the buoyancy, (iii) test gas purity is important. For instance, if a same amount of water is adsorbed instead of hydrogen, the mass accounted is nine times more than that of hydrogen.

The inverse gas chromatography uses a chromatographic equipment to measure adsorption isotherms, however, the adsorbent's nature is unknown instead of the gas mixture (Rouquerol and Rouquerol, 2014). It can be operated in two ways: (i) by injecting continuously the adsorptive gas and recording the breakthrough curve, or (ii) by pulse chromatography, by injecting a minute

amount of adsorptive, which still allows determining the retention time. It is used especially for studying catalyst support adsorbents such as silica, alumina or activated carbon (Kiselev and Yashin, 1969).

Oscillometry is another technique for adsorption isotherm measurements. During gas adsorption measurement, the mass as well as the moment of inertia of the sample will be changed due to the adsorption/desorption of gas molecules, and the viscosity of the gas changes when the applied pressure changes. The two elements will cause the damping of the sample's motion and by recording these motions, the adsorbed amount can be finally computed (Keller and Staudt, 2005).

In the impedance spectroscopy, an electric field is introduced on the adsorbent/adsorbate system and as a result, the polarization of the system is changed due to the electric field. By measuring the physical quantities like the capacitance of a capacitor filled with adsorbent/adsorbate or the permittivity, the adsorbed amount can be deduced (Keller and Staudt, 2005).

Despite all these methods mentioned above, the volumetry and the gravimetry are the mostly used because of the robustness of the system and the simple calculations for interpreting the results (Keller and Staudt, 2005). These two methods were chosen to perform hydrogen adsorption in MIL-101(Cr) and its doped counterparts in this work.

2.3. Volumetric method for adsorption isotherm measurements

2.3.1. Volumetric method: theory

As presented in Section 2.2, in the volumetric method, the temperature and the pressure are the two physical quantities to be measured to calculate the adsorbed amount. A simplified system is illustrated in Figure 2.4.
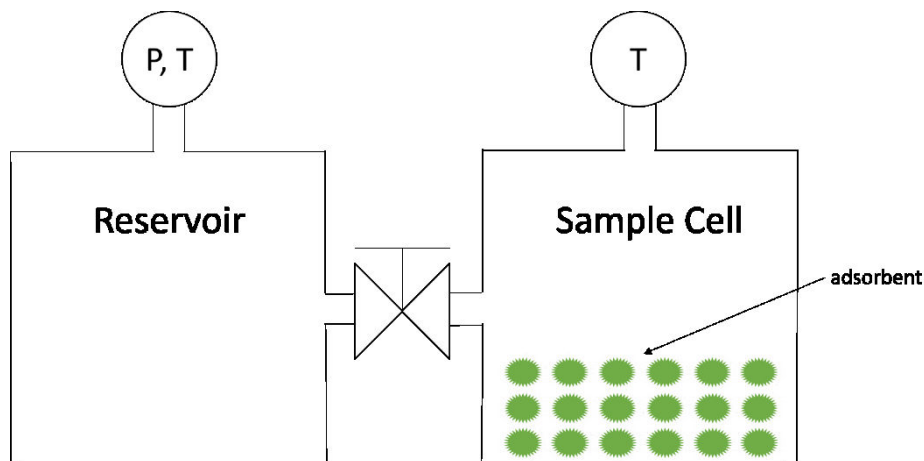
Figure 2.4: Simplified system. The left part is the reservoir where the test gas is firstly dosed. The right part if the sample cell where the adsorbent is filled. The two parts are separated by a valve controlled by the monitoring system.

To determine the absolute mass (m^a) adsorbed during volumetric experiment, the mass balance equation of sorptive gas is considered:

$$m^* = m^g + m^a \qquad (2.19)$$

Here $m^* = m^*(p, T_r, V_r)$ is the mass of the gas initially prepared in the reservoir, m^g is the mass of the sorptive gas contained in the adsorption equilibrium state considered, in both the reservoir and the dead volume of the adsorption chamber (sample cell), The dead volume in the sample cell includes the granular sample external voidage as well as the internal particular porosity which is not filled with adsorbate (Keller and Staudt, 2005). The determination of this dead volume is particularly difficult as the reservoir and the sample cell may work at different temperatures during the experiment.

2.3.1.1. Calibration of the volumes

The determination of the dead volume requires the use of a direct calibration method accounting for the temperature gradient between the reservoir maintained at a reference temperature T_r and the sample cell immersed in liquid nitrogen (T_s=77 K). Helium is used to perform the calibration measurements as it is considered to be a non-adsorbable gas at ambient temperature (Rouquerol and Rouquerol, 2014). The experimental procedure is described in three phases as following:

i. Determination of the volume V_e of helium gas contained at temperature T_r in the system composed of the reservoir connected to the empty adsorption chamber.

ii. Determination of the volume V_f of helium gas contained at temperature T_r in the system composed of the reservoir connected to the adsorption chamber containing the sample. Helium is then assumed to not adsorb in the material.

iii. Determination of the apparent volume V_a of helium gas which at ambient temperature and under the same pressure would enclose the same amount of helium as the one contained in the system composed of the reservoir at temperature T_r and of the empty adsorption chamber at temperature T_s.

Using the thermal equation of state, the initial mass of gas i (helium or hydrogen) prepared in the reservoir can be computed from the measurements of the initial pressure and temperature (P_r, T_r), knowing the volume V_r of the reservoir:

$$m_i^* = \frac{p_r V_r M_i}{R T_r Z_i(p_r, T_r)} \qquad (2.20)$$

The total volume of the empty system V_e is deduced from the measurement of the mass of gas required to achieve pressure p after gas expansion in experiment phase i:

$$V_e = \frac{m_{He}^{*,1}}{M_{He}} \frac{R T_r Z_{He}(p, T_r)}{p} \qquad (2.21)$$

The volume occupied by the solid phase in the adsorption chamber V_{sk} is derived from the determination of the volume V_f in experiment phase ii:

$$V_f = \frac{m_{He}^{*,2}}{M_{He}} \frac{R T_r Z_{He}(p, T_r)}{p} \qquad (2.22)$$

$$V_{sk} = V_e - V_f \qquad (2.23)$$

From the determination of V_a in experiment phase iii (Equation 2.24), two imaginary volumes can be obtained, V_{up} and V_{down} making up V_e, as illustrated in Figure 2.5. It can be seen V_{up} as a volume totally at reference temperature T_r and V_{down} as a volume totally immersed in liquid nitrogen. In this representation, there is no transition volume with temperature gradients, but V_{up} (at T_r) and V_{down} (at T_s) are such to accommodate exactly the same amount of gas as the empty system with the adsorption chamber immersed in liquid nitrogen, so inducing a reproducible temperature gradient. V_{up} does not depend on the presence or the absence of the sample, but V_{down} is modified with the presence of the adsorbent.

$$V_a = \frac{m_{He}^{*,3}}{M_{He}} \frac{RT_r Z_{He}(p, T_r)}{p} \tag{2.24}$$

$$\begin{cases} \dfrac{V_a}{T_r Z_{H_2}(p, T_r)} = \dfrac{V_{up}}{T_r Z_{H_2}(p, T_r)} + \dfrac{V_{down}}{T_s Z_{H_2}(p, T_s)} \\ V_e = V_{up} + V_{down} \end{cases} \tag{2.25}$$
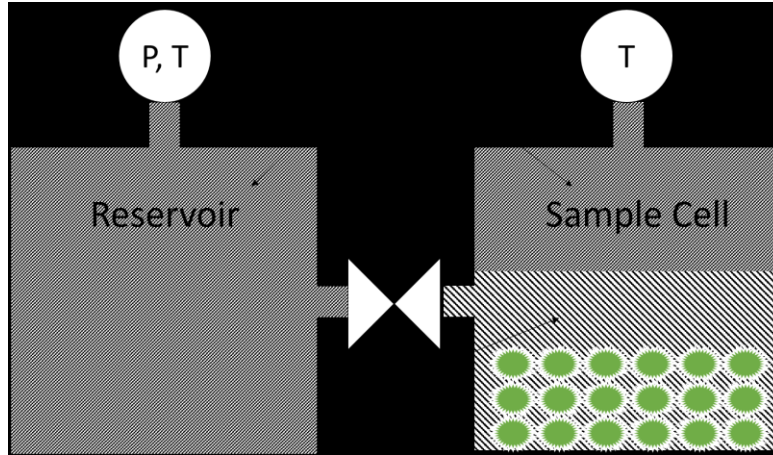
Figure 2.5: Volume calibrated by dividing the sample cell into two parts, namely, V_{up} and V_{down} makes up the volume V_e.

2.3.1.2. Determination of the Gibbs surface excess mass of hydrogen adsorbed

The Gibbs surface excess mass of hydrogen adsorbed m_{GE}^a does not account for the demarcation between the gas and the adsorbed phases filling the internal porosity of the adsorbent particles. It can be determined from the measurement of the mass of hydrogen $m_{H_2}^*$ required to fill the system when the adsorption chamber contains the sample and is immerged in liquid nitrogen and is containing the sample:

$$m_{GE}^a = m_{H_2}^* - \frac{pM_{H_2}}{R}\left[\frac{V_{up}}{T_r Z_{H_2}(p, T_r)} + \frac{(V_{down} - V_{sk})}{T_s Z_{H_2}(p, T_s)}\right] \tag{2.26}$$

2.3.1.3. Estimation of the absolute mass of hydrogen adsorbed

The absolute mass of hydrogen adsorbed m^a accounts for the reduction of V_{lo} caused by the partial filling of the adsorbent porosity with the adsorbed phase can be calculated by using the method presented in Section 2.1.2.

2.3.2. Apparatus and experimental procedure presentation

The measurements have been performed using a Setaram PCTPro apparatus schematically represented in Figure 2.6.
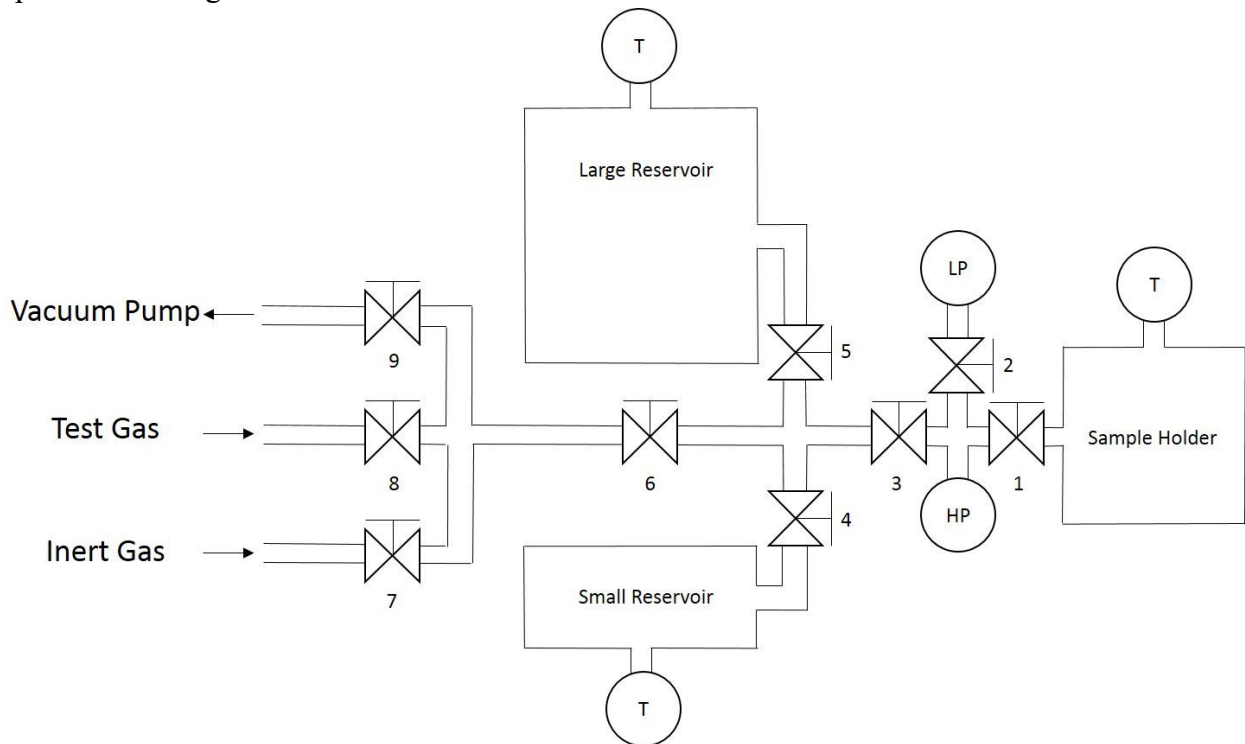
Figure 2.6: Representation of Setaram PCTPro for hydrogen adsorption isotherm measurements. The valves are numerated from 1 to 9. Transducers and thermocouples are marked as LP/HP and T, respectively. LP stands for low pressure transducer and HP stands for the high pressure transducer.

The system is equipped with pneumatic valves and their opening and closing are commanded either automatically or manually by software. The tubing system allows the inlet and the outlet of the gas from the system. The volumes of different parts of tubing, valves, transducers, reservoirs and sample cell are calibrated and given by the producer.

In order to adjust the temperature of the sample cell, it can be either heated by using a heating element equipped with a thermocouple and a PID controller or cooled by immersing in nitrogen liquid.

The samples placed in sample cell for its hydrogen adsorption capacity measurement are previously outgassed for 72 hours at 120 °C in order to eliminate impurities in pores.

The calibration of the volumes was done before the adsorption isotherm measurements, following the procedure presented in Section 3.3.1. The precision of the calibrated volumes was estimated by repeating ten times the calibration procedure (with less than 2% uncertainty).

The experimental procedure that was run for an adsorption isotherm measurement can be described as following:

- The reservoir and the sample cell are firstly pumped under primary vacuum. The reservoir is at reference temperature while the sample cell is at the experimental temperature (here immersed in liquid nitrogen and kept at 77 K).
- The reservoir and the sample cell are then filled with test gas to a given pressure as defined separately as the valve 1, 3, 4, 5 are partially closed in order to isolate the two bulbs.
- The valves between the sample cell and the reservoir are opened (the valves 1, 3, 4, 5 depending on the reservoir) and the test gas (hydrogen here) fills the sample cell and adsorption/desorption takes place.
- After equilibrium is reached, when the pressure and temperature are stable, the valves are closed and the equilibrium temperature and pressure are recorded. Then the reservoir is filled with gas at another given pressure with the increment of pressure pre-defined.
- The adsorption measurement stops once the pressure reaches the upper limit pre-defined and then the desorption measurement will be performed by applying a negative increment of pressure.

The reservoir served during the experiment can be either the larger reservoir, the small reservoir, the tubing system or the combinations of them.

The result of such measurements is supposed to be a set of data with the initial pressures and temperatures of gas prepared in the reservoir, the equilibrium pressure and temperatures. The calculations of adsorbed amount will involve the method previously presented in Section 2.3.1. The final results will show the amounts of adsorbed gas (mol.kg^{-1}) as a function of the equilibrium pressures (bar).

2.4. Gravimetric method for adsorption isotherm measurements

2.4.1. Gravimetric method: theory

During the experiment, adsorptive gas is inserted into the adsorption chamber where is placed the adsorbent in a crucible. During this procedure, the mass is monitored by a magnetic suspension balance (MSB). The mass weighed by MSB can be schematically presented in Figure 2.7.
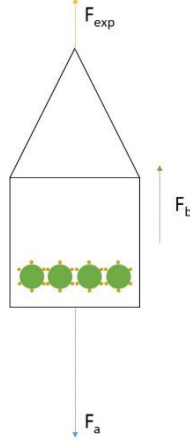
Figure 2.7: Forces applied on the crucible for placing adsorbent: F_{exp} is the force measured experimentally, F_b is the buoyancy force and F_a, the weight. Green dots represent the adsorbent while orange dots represent the adsorbate.

The mass measured by the balance denoted as m^{meas}, accounts for the absolute adsorbed mass m^a and for the mass of the gas displaced due to the Archimedes' principle, also known as the buoyancy effect. Thus, the measured mass can be written as:

$$m^{meas} = m^a - V^{syst}\rho_{gas,H_2} \tag{2.27}$$

The volume of the system V^{syst} is composed of the volumes of the solid phase (adsorbent skeleton), of the adsorbed phase and of the apparatus parts measurable (the crucible which contains the adsorbent, the permanent magnet and the rod between the crucible and the permanent magnet). V^{syst} can be then separated into two parts: V^{nv} which contains the volume of the adsorbent skeleton and the volume of the crucible, the permanent magnet and the rod, $V^{\varphi\,ads}$ the volume of adsorbed phase:

$$V^{syst} = V^{nv} + V^{\varphi\,ads} \tag{2.28}$$

The surface excess amount adsorbed is then:

$$m_{GE}^a = m^{meas} + V^{nv}\rho_{gas,H_2} \tag{2.29}$$

To determine V^{nv}, the simplest way is to measure the mass variation as a function of the gas density when the system is submitted in the presence of a non-adsorbable fluid.

Assuming that Helium cannot be adsorbed at ambient temperature, the plot of the mass measured as a function of Helium density variations is a line with a slope proportional to V^{nv}:

$$V^{nv} = \frac{\Delta m^{meas}}{\Delta \rho_{He}} \tag{2.30}$$

The absolute adsorbed amount can be derived by using methods presented in Section 2.1.2.

2.4.2. Apparatus features

The apparatus used for our hydrogen adsorption studies, schematically illustrated in Figure 2.8, is a Gravimetric sorption Analyzer (Rubotherm IsoSORP GmbH, Germany) equipped with a magnetic suspension balance (MSB).
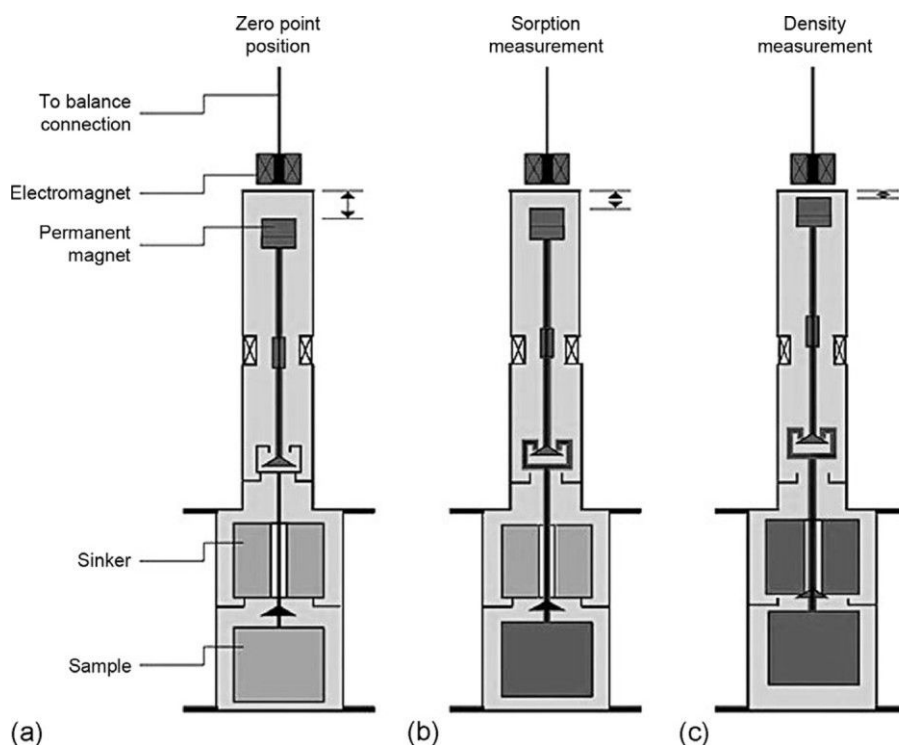
Figure 2.8: Description of the Rubotherm Gravimetric sorption Analyzer–IsoSORP with the successive weighing of (a) tare along, (b) tare+sample and (c) tare+sample+sinker, according to Dreisbach et al. (1996).

The MSB is equipped with an electromagnet in order to transmit the force applied in the sample tube which is connected to a permanent magnetic. Three different positions for the MSB operate on the system which is illustrated in Figure 2.8: tare, tare + sample cell, tare + sample cell + sinker. Firstly, the mass is tared, in the second step MSB records the mass changes and the third measurement position is about to measure the *in situ* density of the high pressure gas.

The solid sample (adsorbent) is placed in a crucible which can be connected to the permanent magnetic by adjustment of its height. The height adjustment is monitored by a position sensor located in the upper part of the sample tube. Furthermore, a 'sinker' is used here in order to measure the buoyancy effect due to the test gas. The sinker can be connected to the permanent magnetic as well as the sample cell by adjusting the position.

The temperature is directly measured in the cell using a PT-100 sensor. The pressure is measured with two pressure transducers PIRC-1 and PIRC-2 depending on the pressure inside the system. In a pressure range higher than 34 bar the pressure transducer PIRC-1 is used and for pressure below 34 bar a more sensitive PIRC-2 is used to visualize the pressure inside the system.

The temperature of the system can be kept at 77 K which was performed by immersing the measuring cell in a liquid nitrogen bath equipped with an automatic level controller which constantly maintains the level of liquid nitrogen. For ambient temperature (298 K), it is achieved by using a Julabo CF-41 temperature controller.

The mass is given with a precision of ± 1µg. The temperature is directly measured in the cell using a PT-100 sensor with a precision of ± 0.1 °C. The cryogenic temperature is well defined by boiling

115

temperature of the liquid nitrogen. The room temperature is regulated using the Julabo cryostat with a precision better than 1 °C.

2.4.3. Experimental procedure in gravimetry

Ultrahigh pure hydrogen (99.9999% vol) supplied by Air Liquide was used for the high pressure adsorption measurements in gravimetry. Hydrogen adsorption/desorption isotherms were performed at 77 and 298 K up to 100 bar.

In a typical hydrogen adsorption measurement, a blank measurement was initially performed with Helium without the sample to measure the empty weight and volume of the crucible.

During the blank measurement, the weight read by the balance can be expressed as following:

$$m^{meas} = m^{sc} - \rho_{gas\,He}(P,T)V^{sc} \tag{2.31}$$

Assuming that the volume of the crucible does not change with applied pressure, the mass measured during such a blank experiment is presented by a straight line as a function of the helium density. The mass of the sample cell corresponds then to the y-intercept and the volume to the crucible is the slope of the line. The graphical representation of the measured mass variation during the blank measurements with respect to Helium density is illustrated in Figure 2.9.
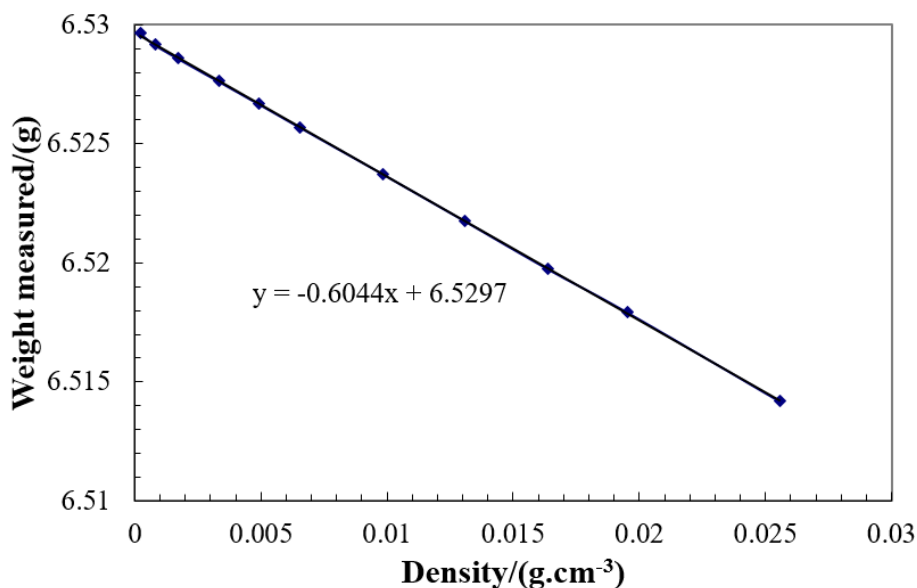
Figure 2.9: Linear relationship between mass measurements and helium density used for measurement of crucible's mass.

The adsorbent was afterwards loaded into the crucible and outgassed at 423 K under vacuum for 72 hours to remove any pre-adsorbed gases and solvents.

A buoyancy measurement was performed at 298 K using helium gas to measure the volume of the skeleton of adsorbent sample loaded for hydrogen adsorption (Murata et al., 2000). An example of buoyancy measurement is illustrated in Figure 2.10. The linearity of the measured points shows

that there is no adsorption during the measurement. Similarly, the y-intercept of the line is the total mass of the crucible containing the sample whereas the slope represents its total volume.
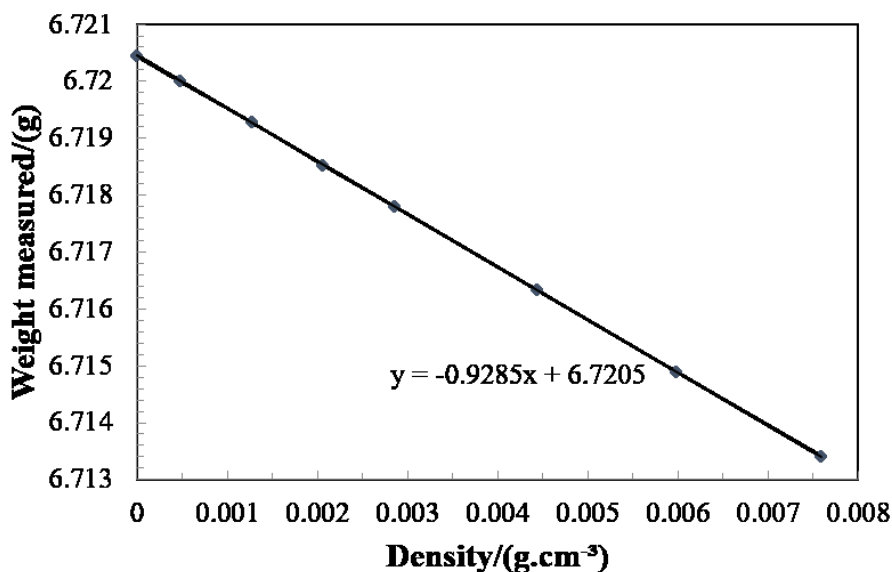
Figure 2.10: Example of Helium adsorption isotherm for buoyancy correction, which shows a linear relationship.

During hydrogen sorption measurements, hydrogen gas at elevated pressure was added incrementally and data points were recorded when the mass stability was reached.

2.5. Samples studied

The different samples studied have been selected as a function of their porosity (BET specific surface area). MOF-5 compound, synthesized according to the method given by Biemmi *et al.* (2009) was considered also to validate the experimental method used with MOF and to make comparisons with MIL-101(Cr) type samples. Activated carbon for doping was also tested for its hydrogen adsorption performance.

The samples presented are:
- MIL-101(Cr) synthesized using CH_3COOH or MIL-101(Cr)-a
- MIL-101(Cr) synthesized using CH_3COONa or MIL-101(Cr)-b
- 2% activated carbon doped MIL-101(Cr) synthesized using CH_3COOH or AC-MIL-101(Cr)-a
- 5% activated carbon doped MIL-101(Cr) synthesized using CH_3COOH or AC-MIL-101(Cr)-b
- MOF-5
- Activated carbon or AC type Norit RB3

The characterizations of the compounds studied expressed in terms of specific surface area (BET), pore volume and bulk density are presented in Table 3.2. The specific surface area and pore volume of MOF-5 and AC are calculated based on the same principle presented in Section 1.3.4.3 and 1.3.4.4.

Table 2.2: BET specific surface areas, pore volume and bulk densities of different compounds studied.

Samples	BET specific surface area /$(m^2 \cdot g^{-1})$	Pore volume (BJH) /$(cm^3 \cdot g^{-1})$	Pore volume (Gurvich) /$(cm^3 \cdot g^{-1})$	Bulk density /$(g \cdot cm^{-3})$
MIL-101(Cr)-a	3223	2.02	1.94	0.20
MIL-101(Cr)-b	3131	1.94	1.92	0.19
AC-MIL-101(Cr)-a	3407	2.50	2.02	0.19
AC-MIL-101(Cr)-b	3542	2.65	2.04	0.19
MOF-5	2473	1.40	1.03	-
AC	956	-	0.41	-

2.6. Results and discussion

2.6.1. The effect of using different reservoirs in volumetric method

The hydrogen adsorption isotherms measurements using volumetric technique entail the use of the double imaginary volume method. It is then essential to evaluate the influence of using different reservoir sizes for the adsorption measurement to ensure that the results are not affected. Considering this, three hydrogen adsorption isotherm measurements at 77 K using the three types of reservoirs mentioned in Section 2.3.2 were performed (large reservoir, small reservoir and tubing).

This test has been done with the MIL-101(Cr)-b sample. The result obtained are represented and compared in Figure 2.11. The good accordance among these three results indicates clearly that the volume of reservoirs used for measurements does not influence the results of hydrogen adsorption isotherms.
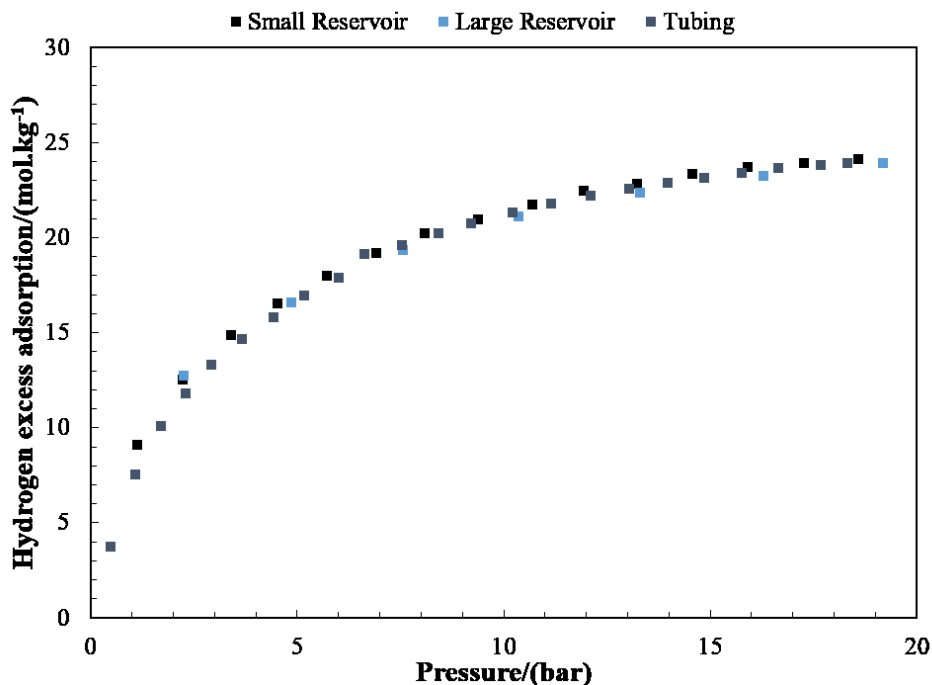
Figure 2.11: Hydrogen excess adsorption measured for MIL-101(Cr) synthesized using CH₃COONa (MIL-101(Cr)-b), the effect of using different reservoir is tested: tubing system served as the reservoir, small reservoir and large reservoir are presented respectively. The volume of tubing system served as the reservoir is 12.39 cm³, the volume of the small reservoir is 162.89 cm³ and the volume of the large reservoir is 1051.26 cm³.

2.6.2. Hydrogen adsorption isotherm measured by volumetric method at cryogenic temperature

In terms of performed experiments, the excess uptake capacities of the compounds listed in Section 2.5 were measured at 77 K up to 50 bar.

The excess adsorption capacities of the different samples at 77 K up to 50 bar are listed in Table 2.3. Both adsorption and desorption isotherm were measured to understand the behaviour of materials under such conditions. The results are presented in Figure 2.12 and indicate that the 5 wt% AC doped MIL-101(Cr) sample can store more hydrogen than the other samples at 77 K. Its capacity reaches 46.1 mol.kg^{-1} at 77 K under 51.2 bar. The results show that at 77 K and 50 bar, the hydrogen uptake is positively correlated to the BET specific surface area and the porosity of the materials.

119
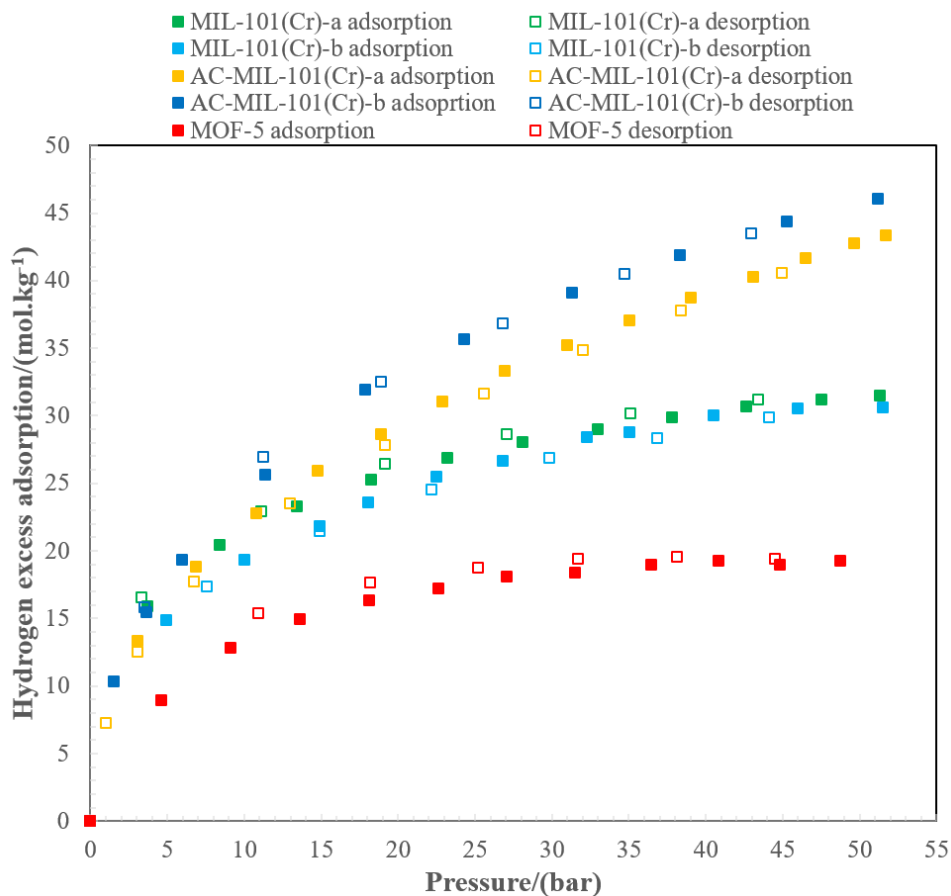
Figure 2.12: Hydrogen adsorption isotherm measured at 77 K up to 50 bar using the volumetric method.

Table 2.3: Hydrogen excess adsorption capacities of the different samples at 77 K measured by volumetry.

Samples	Hydrogen uptake /(mol.kg⁻¹)	Hydrogen uptake /(wt%)	Pressure applied /(bar)
MIL-101(Cr)-a	31.5	6.3	51.3
MIL-101(Cr)-b	30.6	6.1	51.5
AC-MIL-101(Cr)-a	43.3	8.7	51.7
AC-MIL-101(Cr)-b	46.1	9.2	51.2
MOF-5	19.3	3.7	48.7

As it can be observed, the MIL-101(Cr)-a and MIL-101(Cr)-b samples have nearly the same performance in terms of hydrogen adsorption and the AC doped MIL-101(Cr) compounds show higher hydrogen uptake capacity than non-doped MIL-101(Cr) samples.

2.6.3. Hydrogen adsorption isotherm measured using gravimetric method at cryogenic temperature

The hydrogen adsorption isotherms of the same compounds listed in Section 2.5 have been measured at 77 up to 100 bar, using the gravimetric technique. Activated carbon for MIL-101(Cr) doping was also tested for comparison. These isotherms are presented in Figure 2.13.

The hydrogen adsorption capacities of the different materials at 77 K up to 100 bar are listed in Table 2.4. The absolute adsorption capacities are calculated by using Equation 2.3 with the pore volume listed in Table 2.2 calculated by Gurvich rule. The volumetric adsorption capacities are calculated based on the bulk densities presented in Table 2.2.
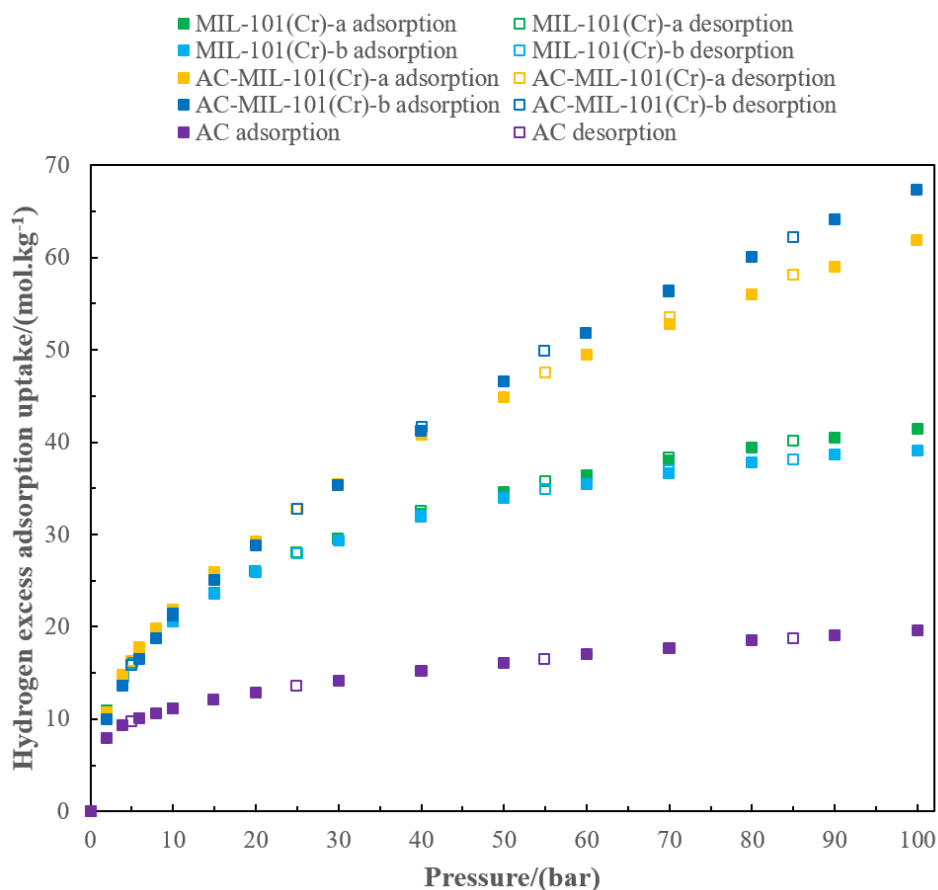
Figure 2.13: Hydrogen adsorption isotherms measured at 77 K up to 100 bar using the gravimetric method.

Table 2.4: Hydrogen excess and absolute adsorption capacities of the different samples at 77 K measured by gravimetry.

Samples	Excess hydrogen uptake /(mol.kg^{-1})	Excess hydrogen uptake /(wt%)	Absolute hydrogen uptake /(mol.kg^{-1})	Absolute hydrogen uptake /(wt%)	Pressure applied /(bar)
MIL-101(Cr)-a	41.1	8.2	71.4	14.8	100
MIL-101(Cr)-b	39.1	7.8	69.1	13.8	100
AC-MIL-101(Cr)-a	61.9	12.3	93.5	18.7	100
AC-MIL-101(Cr)-b	67.4	13.5	99.2	19.8	100
AC	19.6	3.9	26.1	5.2	100

In Figure 2.13, the isotherms of adsorption measured represent the data of excess adsorption which increases continuously when the pressure increases. No hysteresis phenomenon is observed during desorption measurements which means that hydrogen adsorption is fully reversible in all these adsorbents. Among all the samples considered in this study, activated carbon has the lowest hydrogen adsorption uptake since it has the lowest specific surface area and pore volume as well. The amount adsorbed shows a rapid increase at low pressure region, which corresponds to the microporosity of the material (Sing et al., 2014b).

2.6.4. Hydrogen adsorption isotherm measurement using gravimetric method at room temperature

The precision and the resolution of the micro balance (MSB) make it then possible to measure the hydrogen adsorption in MOF materials at room temperature (25 °C, 298 K). Therefore, the hydrogen adsorption isotherms of the five compounds studied previously have been measured at 298 K up to 100 bar. The results obtained are represented in Figure 2.14.
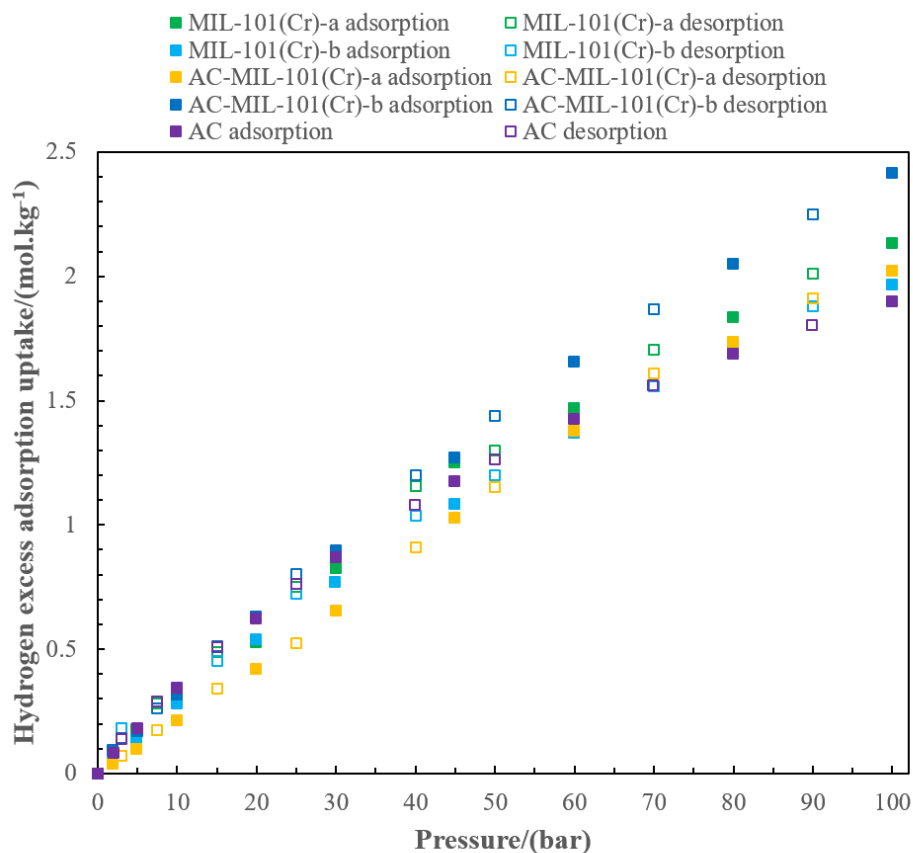
Figure 2.14: Hydrogen adsorption isotherms measured at 298K up to 100 bar using the gravimetric method.

At room temperature, the hydrogen uptake capacities measured are weak (around 0.4 wt%). The obtained results for MIL-101(Cr) and its doped counterparts are comparable with those in literature (Karikkethu Prabhakaran and Deschamps, 2015b; Latroche et al., 2006).

2.6.5. Comparison of results: volumetric method and gravimetric method at cryogenic temperature (77 K)

The hydrogen adsorption performances measured by the volumetric and the gravimetric method at 77 K are compared and illustrated in Figure 2.15.
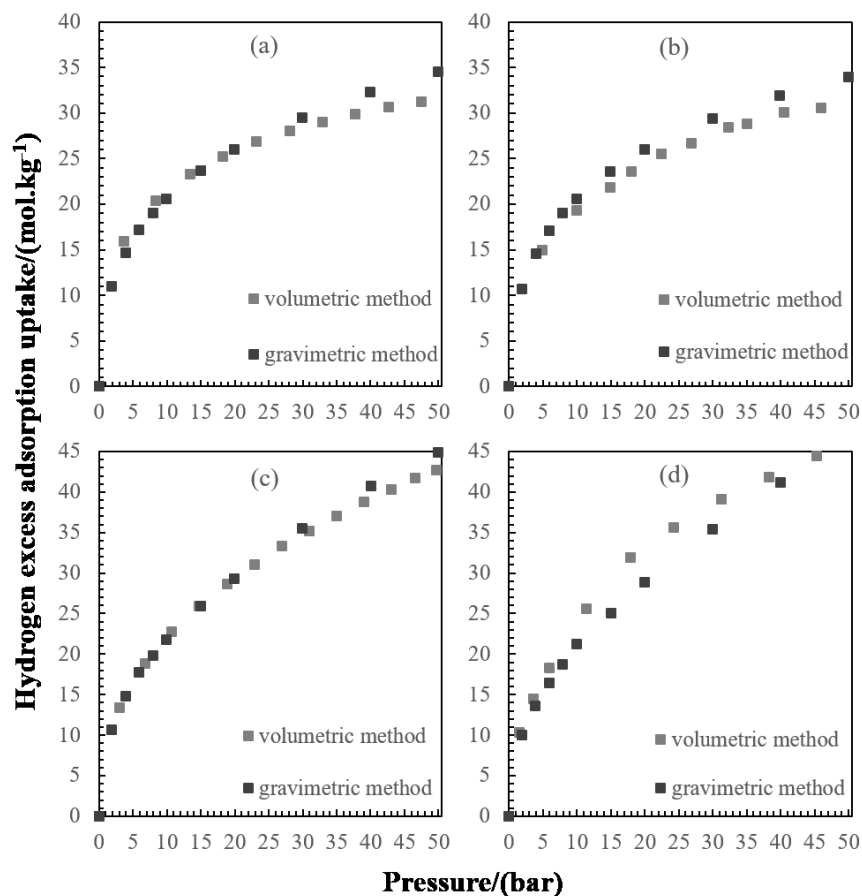
Figure 2.15: Comparison of hydrogen adsorption isotherms measured by volumetric and gravimetric methods: (a) MIL-101(Cr)-a, (b) MIL-101(Cr)-b, (c) AC-MIL-101(Cr)-a and (d) AC-MIL-101(Cr)-b

Good agreements are found between results measured using the volumetric method and those measured using the gravimetric method for all samples. Meanwhile, the small differences shown in Figure 2.15 can be attributed to:

- *activation duration/method*: the samples presented for the gravimetric method measurement can be previously outgassed in Micromeritics VacPrep for its small amount adsorbent requirement (about 0.1 g) compared to the volumetric method (about 1 g) (Keller and Staudt, 2005).
- *adsorbent mass measurement*: the mass of adsorbent is difficult to be weighed after *in situ* outgassing in the volumetry (Keller and Staudt, 2005).
- *volume calibration*: both double imaginary volume method for volumetry and buoyancy correction for gravimetry require volume calibration using Helium as probe gas which may introduce inaccuracies in final results (Furukawa et al., 2007; Rouquerol and Rouquerol, 2014).

2.6.6. Adsorption isotherm approached by theoretical modelling

The results of adsorption isotherms show well the hydrogen molecules form a monolayer on the surface of adsorbents which can be described as a type I isotherm according to the IUPAC classification or Langmuir isotherms. Hence, the isotherms of adsorption measured have been fitted using the Langmuir model. The obtained results are shown in Figure 2.16. The fitting parameters of the model (b and q_0) are listed in Table 2.5.
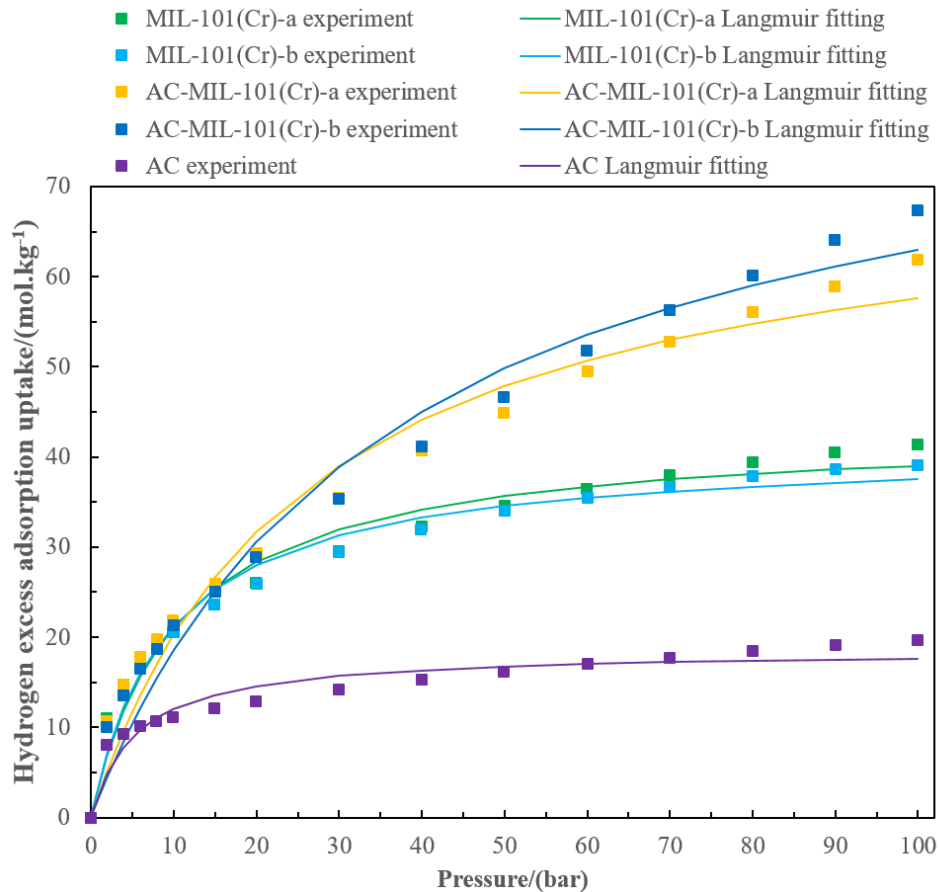
Figure 2.16: Gravimetric adsorption isotherm measurement results fitted by Langmuir model: AC, MIL-101(Cr)-a, MIL-101(Cr)-b, AC-MIL-101(Cr)-a and AC-MIL-101(Cr)-b.

Table 2.5: Coefficients of Langmuir model fitted for each sample studied using the gravimetric method and fitting goodness represented by R^2.

adsorbent	b/(bar^{-1})	q_0/(mol.kg^{-1})	Fitting goodness R^2
AC	0.183	18.6	0.923
MIL-101(Cr)-a	0.096	43.1	0.981
MIL-101(Cr)-b	0.107	41.0	0.974
AC-MIL-101(Cr)-a	0.039	72.4	0.976
AC-MIL-101(Cr)-b	0.028	85.6	0.979

According to literature, the heat of adsorption of hydrogen in MIL-101(Cr) varies from 10 kJ.mol^{-1} at low coverage (Latroche et al., 2006) to 4.3 kJ.mol^{-1} (Schmitz et al., 2008), this great variation is also proved by Berdonosova *et al.* (2015). This fact implies that the hydrogen adsorption in MIL-101(Cr) is heterogeneous. Hence, Freundlich adsorption model (see Section 2.1.3.5) is proposed to fit the experimental data and the results are shown in Figure 2.17. The parameters (*k* and *m*) of Freundlich adsorption model are listed in Table 2.6.
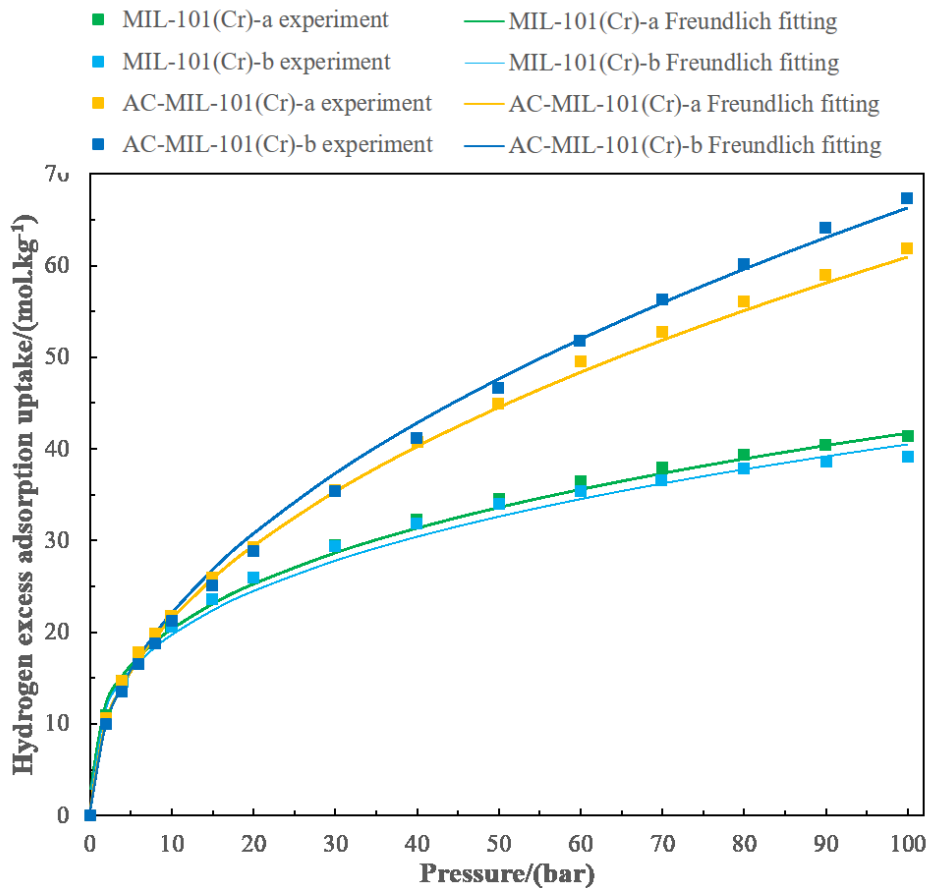
Figure 2.17: Gravimetric adsorption isotherm measurement results fitted by Freundlich model:MIL-101(Cr)-a, MIL-101(Cr)-b, AC-MIL-101(Cr)-a and AC-MIL-101(Cr)-b.

Table 2.6: Coefficients of Freundlich model fitted for each sample studied using the gravimetric method and fitting goodness represented by R^2.

adsorbent	m	k	Fitting goodness R^2
MIL-101(Cr)-a	3.20	9.95	0.996
MIL-101(Cr)-b	3.20	9.61	0.989
AC-MIL-101(Cr)-a	2.21	7.58	0.999
AC-MIL-101(Cr)-b	2.10	7.39	0.998

It can be noticed that the adsorption isotherms at room temperature (298 K) follow a Henry's law, which describes an ideal surface (flat, rigid, perfectly smooth, chemically homogeneous, and zero contact angle hysteresis) within an infinitely diluted adsorptive (Do, 1998).

The adsorption isotherms measured for activated carbon and in MIL-101(Cr) samples at 298 K are fitted by using Henry's linear relationship and it is graphically presented in Figure 2.18. The Henry's constant calculated at 298 K are repertories in Table 2.7.
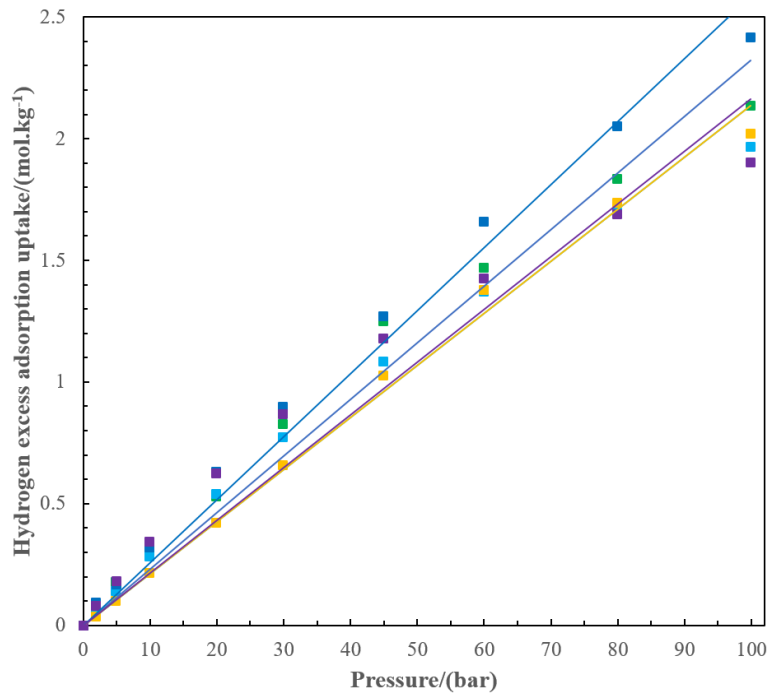
Figure 2.18: : Gravimetric adsorption isotherm measurement results fitted by Henry's model: AC (purple),MIL-101(Cr)-a (green), MIL-101(Cr)-b (light blue), AC-MIL-101(Cr)-a (yellow) and AC-MIL-101(Cr)-b (dark blue).

Table 2.7: Henry's constant calculated at 298K for hydrogen adsorption in AC, MIL-101(Cr)-a, MIL-101(Cr)-b, AC-MIL-101(Cr)-a and AC-MIL-101(Cr)-b.

	AC	MIL-101(Cr)-a	MIL-101(Cr)-b	AC-MIL-101(Cr)-a	AC-MIL-101(Cr)-b
k_H /(mol.kg^{-1}.bar^{-1})	0.22	0.25	0.22	0.22	0.26
Fitting goodness R^2	0.944	0.978	0.994	0.980	0.986

2.6.7. Hydrogen uptake at cryogenic temperature (77 K)

The hydrogen adsorption isotherm measured in MIL-101(Cr) using volumetric method has a good agreement with results reported by Latroche *et al.* (2006). This comparison is illustrated in Figure 2.19.
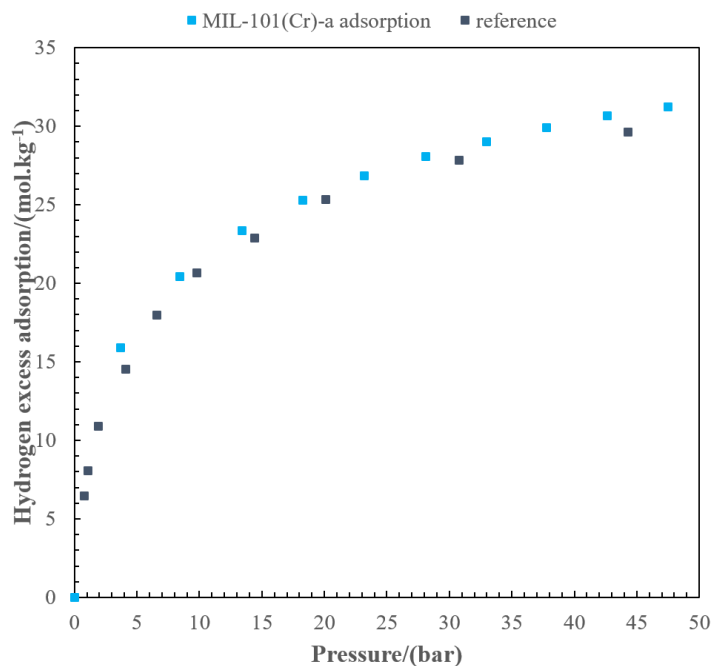
Figure 2.19: Hydrogen adsorption isotherm of MIL-101(Cr)-a (pure MIL-101(Cr) sample) compared with literature (Latroche et al., 2006).

Meanwhile, the results given are higher than those given by Bimbo *et al.* (2015). This difference can be explained by the differences between the methods of syntheses and activations.

Hydrogen adsorption isotherms measured in activated carbon doped MIL-101(Cr) using volumetry were reported by Somalyjulu Rallapalli *et al.* (2013). Their results showed that AC (WS-480) doped MIL-101(Cr) reached 10.1 wt% hydrogen uptake at 77 K under 60 bar (50.1 mol.kg^{-1}) which is comparable to results showed in Figure 2.12. This comparison is illustrated in Figure 2.20.
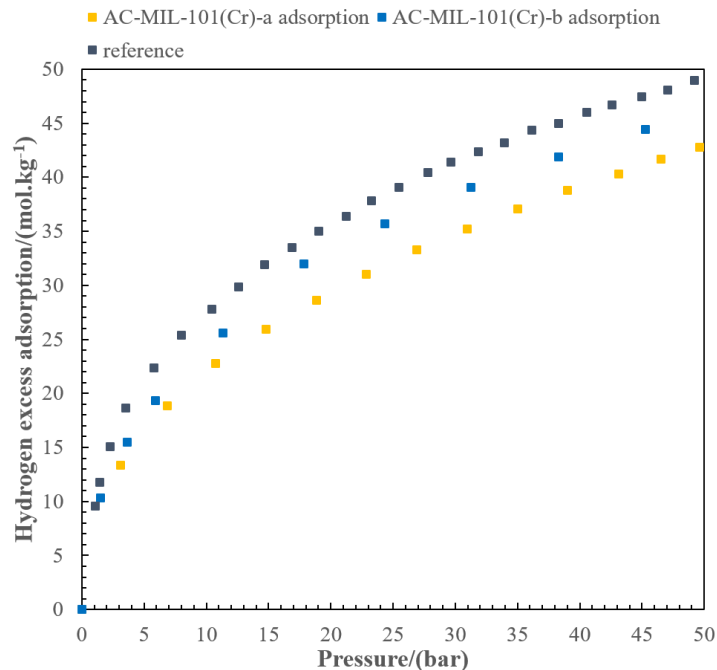
Figure 2.20: Hydrogen adsorption isotherm of AC-MIL-101(Cr)-a (2 wt% AC doped MIL-101(Cr)), AC-MIL-101(Cr)-b (5 wt% AC doped MIL-101(Cr)) compared with results given in literature (Somayajulu Rallapalli et al., 2013)

Hydrogen adsorption isotherms measured with gravimetry are also compared with literature and this comparison is illustrated in Figure 2.21. It is reported by Karikkethu Prabhakaran and Deschamps (2015b) that pristine MIL-101(Cr) can adsorb up to 36.3 mol.kg^{-1} hydrogen at 100 bar and activated carbon doped MIL-101(Cr) can reach to 58.4 mol.kg^{-1} at 100 bar and 77 K. The obtained result for pristine MIL-101(Cr) is also very approached to the simulated one (Ghoufi et al., 2012) where an uptake about 9 wt% (45 mol.kg^{-1}) is obtained.
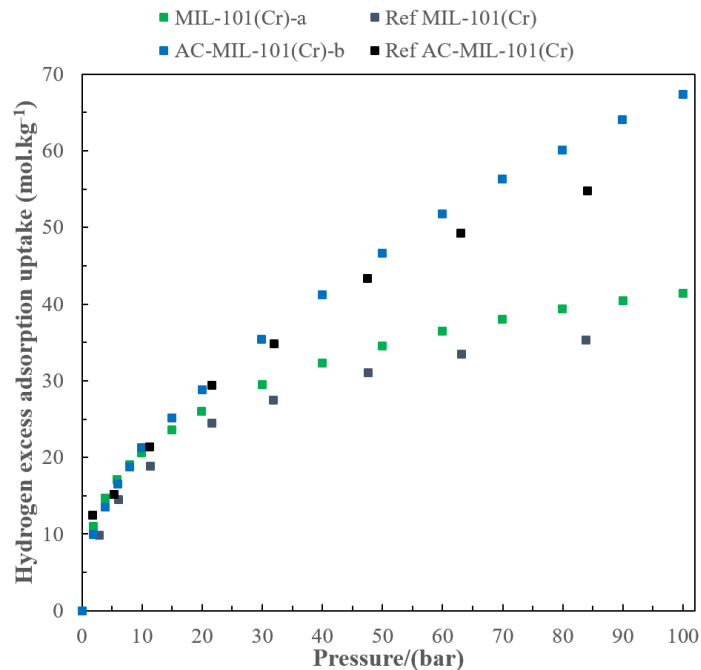
Figure 2.21: Hydrogen adsorption isotherms of MIL-101(Cr)-a and AC-MIL-101(Cr)-b (5% activated carbon doped MIL-101(Cr) sample) compared with literature (Karikkethu Prabhakaran and Deschamps, 2015b)

Hydrogen molecules at 77 K, above its critical temperature (33 K), are only able to form a monolayer on the surface of adsorbent during adsorption. Therefore, the hydrogen uptake capacity is positively correlated to the specific surface area of the adsorbent. Meanwhile, the pore size as well as the existence of open metal sites in adsorbents can affect the hydrogen adsorption capacities (Suh et al., 2012). The results from this study are compared with other MOF or MOF composite adsorbents in Table 2.8.

Table 2.8: Hydrogen adsorption uptake at 77 K and the specific surface area for different adsorbents (MOFs and doped MOFs).

Adsorbent	Surface area/(m².g⁻¹)		Pore volume/ (cm³.g⁻¹)	Hydrogen uptake capacity			Reference
	BET	Langmuir		p/(bar)	Gravimetric/ (wt%)	Volumetric/ (g.L⁻¹)	
AC-MIL-101(Cr)-b	3542	4951	2.04	100	13.5	37.7	This work
AC-MIL-101(Cr)-a	3407	4905	2.02	100	12.3	35.3	This work
MIL-101(Cr)-a	3223	4668	1.94	100	8.2	27.1	This work
MIL-101(Cr)-b	3131	4549	1.92	100	7.8	26.3	This work
MIL-101(Cr)	-	5500	1.90	80	6.1	-	(Latroche et al., 2006)
MIL-101(Cr)	3148	-	2.10	100	7.3	-	(Karikkethu Prabhakaran and Deschamps, 2015b)
AC-MIL-101(Cr)	3458	-	2.04	100	11.7	-	(Karikkethu Prabhakaran and Deschamps, 2015b)
AC@MIL-101(Cr)	3555	-	1.75	60	10.1	-	(Somayajulu Rallapalli et al., 2013)
SWCNT@MIL-101(Cr)	2998	3989	1.32	60	9.2	-	(Karikkethu Prabhakaran et al., 2011)
MOF-5	3800	4400		40	7.1	42.1	(Kaye et al., 2007)
MOF-177	4750	5640	1,59	70-80	7.5	49	(Wong-Foy et al., 2006)
MOF-210	6240	10400	3.6	80	8.6	-	(Furukawa et al., 2010)
NU-100	6143	-	2.82	70	9.95	-	(Farha et al., 2010)

Among all these adsorbents, AC-MIL-101(Cr)-b sample has the highest gravimetric hydrogen uptake capacity since it has a high specific surface area value as well as a large pore volume.

For MIL-101(Cr), it is reported that the microporous super-tetrahedron (ST) and unsaturated metal sites are generally responsible for hydrogen adsorption (Latroche et al., 2006). However, for pristine MIL-101(Cr) samples, the open chromium metal sites are often contaminated by unremoved benzene dicarboxylic acid (H_2BDC) particles which prevent hydrogen adsorption. The doping of AC which remains in the MIL-101(Cr) framework prevents the coordination of unreacted H_2BDC with the chromium metal sites.

Moreover, the AC introduces more micropores in synthesized AC doped MIL-101(Cr) composite samples (Somayajulu Rallapalli et al., 2013). Micropore filling of supercritical H_2 depends on the interaction of hydrogen with the adsorbent pore walls. The interactions will be maximum if the pore diameter is slightly higher than the kinetic diameter of hydrogen, which is 0.289 nm. The formation of micropores increases the interaction between MOF surface and hydrogen molecules. Generally, it is recognized that ultramicropores of 0.6-0.7 nm in diameter are more effective in high level of hydrogen uptake than the pores having other diameters (Yushin et al., 2006), for instance, the SWCNT created ultramicropores helps hydrogen adsorption in SWCNT doped MIL-101(Cr) sample (Karikkethu Prabhakaran et al., 2011; Karikkethu Prabhakaran and Deschamps, 2015a).

The combined effect of both the formation of additional micropores and the activation of unsaturated metal sites by carbon incorporation was responsible for the higher hydrogen uptake capacity in the AC doped MIL-101(Cr) samples (Somayajulu Rallapalli et al., 2013).

For volumetric storage capacity, AC incorporated MIL-101(Cr) seems to be less advantageous, compared to MOF-5 or MOF-177 (see Table 2.8). This is due to the low bulk density of the adsorbent caused by the large pores present in the framework.

The results from this study are compared with other hydrogen storage methods, which are shown in Table 2.9.

Table 2.9: Hydrogen gravimetric and volumetric uptake capacities, compared with storage by compression, liquefaction and storage in hydrides.

Storage method	Compounds	Gravimetric capacity /(wt%)	Volumetric capacity /(g.L⁻¹)	Reference
Physical	AC-MIL-101(Cr)-b	13.5	37.7	This work
	AC-MIL-101(Cr)-a	12.3	35.3	
	MIL-101(Cr)-a	8.2	27.1	
	MIL-101(Cr)-b	7.8	26.3	
Compression (700 bar)	H_2	-	39.2	(Lemmon et al., 2010)
Liquefaction (30 K)	H_2	-	70.8	(Lemmon et al., 2010)
Chemical	$La_{1.8}Ca_{0.2}Mg_{14}N_{13}$	5	-	(Gao et al., 2005)
	$LiBH_4$	18.5	121	(Soulié et al., 2002)
	$LiBH_4 \cdot 0.5MgH_2$- 2 mol% $TiCl_3$	10	-	(Vajo et al., 2005)
	Na_2LiAlH_6	2.5	-	(Genma et al., 2006)
	NaAlH4	5.0	-	(Zaluska et al., 2000)
	α-$Mg(BH_4)_2$	14.9	117	(Filinchuk et al., 2009)
	β-$Mg(BH_4)_2$	14.9	113	(Her et al., 2007)
	γ-$Mg(BH_4)_2 \cdot 0.8H_2$	17.4	98	(Filinchuk et al., 2011)

Better performances are shown for hydrides concerning gravimetric and volumetric hydrogen uptake capacities, as shown in Table 2.9. However, as mentioned previously, the formation of hydrides requires high temperature and a long time for its high binding energy and slow kinetics.

2.6.8. Hydrogen uptake at room temperature (298 K)

Hydrogen uptakes at room temperature in MIL-101(Cr) and AC doped Mil-101(Cr) are moderate because of the low isosteric heat of adsorption. The results are slightly larger than reported value for MOF-5 and Cu-BTC (HKUST-1) (Panella et al., 2006), which are 0.28 and 0.35 wt%, respectively.

In order to enhance hydrogen uptake at ambient temperature, strong adsorption sites should be incorporated into the pores. In addition, the pore surface/curvatures should be optimized for efficient H_2 packing (Suh et al., 2012). It is reported that although big pore volume and high surface area is the most important factor to achieve high hydrogen adsorption capacity at high pressure, however, this capacity can be significantly increased at room temperature if the MOF has a high isosteric heat of H_2 adsorption (Frost and Snurr, 2007). The thermodynamic studies showed that requirement for an adsorbent capable of storing hydrogen at ambient temperature is that the heat of adsorption of hydrogen is above 15.1 kJ.mol⁻¹ (Bhatia and Myers, 2006). Meanwhile, for most MOFs, this isosteric heat is in the range of 4-9 kJ.mol⁻¹ (Suh et al., 2012) and for MIL-101(Cr), this value at low coverage is about 10 kJ.mol⁻¹ (Latroche et al., 2006) and then drops to an average of 4.3 kJ.mol⁻¹ (Schmitz et al., 2008).

Knowing that the doping of AC cannot increase the heat of adsorption of hydrogen in MIL-101(Cr) (Karikkethu Prabhakaran and Deschamps, 2015b), it is reasonable that at room temperature the hydrogen uptake capacities in all these samples are not high. Experimentally, the high hydrogen uptake at room temperature can be achieved by doping metal or metal clusters in MOF adsorbent.

2.7. Conclusion

Hydrogen adsorption isotherms of the synthesised materials were measured using both volumetric and gravimetric methods at 77 and 298 K up to 100 bar.

The volumetric method involves an adsorption measurement in a calibrated volume. The adsorbed quantity can be computed by using the mass balance before and after adsorption by measuring the pressure and the temperature of the system. At 77 K, a double imaginary method is applied in order to compensate the effect of temperature gradient produced between the reservoir immersed in liquid nitrogen and the sample cell kept at room temperature.

In the gravimetric method, the mass is directly measured by using a Magnetic Suspension Balance (MSB) with high accuracy. The buoyancy effect produced by hydrogen gas is not negligible and is corrected by applying the Archimedes' principle after measuring the net volume of the adsorbent. Both measurements give the adsorption excess uptake, which is the part of the mass of adsorbed phase compensated by the buoyancy effect of the bulk phase on the adsorbed phase. An absolute adsorption is then calculated by considering the volume of the adsorbed phase to the excess uptake mass.

The results of hydrogen adsorption measured at 77 K showed a Type I isotherm according to IUPAC classification and the results measured for the same adsorbents using the two different methods were in good agreement. The difference in measured result by these two methods can be related to the activation process, adsorbent mass measurement or volume calibrations in the volumetric method. The most important uptake result was remarked for the 5 wt% AC doped MIL-101(Cr) material which can store up to 13.5 wt% excess hydrogen at 100 bar and 77 K, corresponding to an absolute uptake of about 20 wt% and a volumetric capacity of 37.7 g.L^{-1}. A pristine MIL-101(Cr) synthesized using acetic acid showed a hydrogen excess uptake of 8.2 wt% at 100 bar and 77 K, while MIL-101(Cr) synthesized using sodium acetate showed a hydrogen excess uptake of 7.8 wt% under the same conditions. Moreover, these results showed that the hydrogen uptakes at 77 K are positively correlated to the specific surface area of the adsorbents. The measured isotherms were fitted using Langmuir adsorption model and Freundlich adsorption model, good fittings were obtained.

Hydrogen adsorption isotherms were measured at 298 K using the gravimetric method. All isotherms presented nearly linear forms which can be described by Henry's law. An uptake of about 0.4 wt% in average was found for all adsorbents tested. This low hydrogen uptake capacity is due to the weak hydrogen bonding energy which can be hardly enhanced by activated carbon doping.

Chapter 3
Kinetic studies of hydrogen adsorption on MOF and Carbon-MOF materials

L'étude des performances de stockage mesurées en conditions d'équilibre a été complétée par une analyse cinétique du phénomène d'adsorption de l'hydrogène. Celle-ci a été conduite à partir de la mesure par la méthode volumétrique et de la variation temporelle des quantités d'hydrogène adsorbées en excès, déduites de l'acquisition des données de pression et température. Ces mesures ont été réalisées dans une gamme pression basse, entre 0.2 et 5 bar, dans le but de déterminer les coefficients de diffusion intra-particulaires à faible taux de recouvrement. Les courbes cinétiques obtenues pour les différents matériaux testés MIL-101(Cr) purs et dopés, montrent des allures similaires. Ces courbes ont été dans un premier temps modélisées au moyen du modèle de la force motrice linéaire (Linear Driving Force LDF), en prenant en compte l'effet des variations de température induites par l'exothermicité du phénomène. Néanmoins, le modèle LDF bien que couramment utilisé, a été développé pour décrire des vitesses dans des conditions où le système est proche de l'équilibre. Cette hypothèse n'est cependant pas vérifiée aux conditions de pression les plus élevées appliquées dans cette étude, si bien que le modèle ne permet pas de décrire convenablement les courbes cinétiques aux pressions de 1 et 5 bar. Afin de mieux décrire les courbes cinétiques expérimentales, un modèle prenant en compte la variation radiale de la concentration adsorbée dans la particule assimilée à une sphère homogène est considéré. Le transfert de matière est alors supposé mettre en jeu une résistance partielle externe, créée par le film entourant la particule, et une résistance diffusionnelle de surface à l'intérieur de la particule. Afin de simplifier le problème, le profil expérimental de température est modélisé par une fonction gaussienne a-symétrique. L'emploi de ce modèle permet d'obtenir un bon accord avec les courbes de prises de masses expérimentales mesurées sur toute la gamme de pression considérée dans ce travail. Les diffusivités de surface à concentration quasi nulle sont déduites par ajustement du modèle avec les données expérimentales, moyennant la prise en compte de la correction de Darken. Les valeurs de diffusivité de surface ainsi obtenues dans les conditions de référence à la température de 77K pour le MIL-101(Cr) pur synthétisé au moyen d'acide acétique, et dopé à 5 % de charbon actif apparaissent du même ordre de grandeur, et sont respectivement égales à $1.6 \cdot 10^{-16}$ et $0.8 \cdot 10^{-16}$ $m^2.s^{-1}$. Les coefficients de transfert externe k_{ex} dans les conditions expérimentales testées varient en fonction de la pression entre $0.3 \cdot 10^{-10}$ $m.s^{-1}$ à 0.2 bar, et $7.4 \cdot 10^{-10}$ $m.s^{-1}$ à 5 bar.

3. Kinetic studies of hydrogen adsorption on MOF and Carbon-MOF materials

3.1. Objective of the study

Kinetics of hydrogen adsorption is as important as its uptake capacity for storage in mobile applications. According to American Department of Energy (2015), the time required to fill 5 kg hydrogen into storage system needs to be less than 2.5 minutes (Table II.1). This criterion implies that adsorption kinetics need to be studied for adsorbent material presented in this work. The diffusion of sorptive fluids in porous materials is well studied for different gases, such as CH_4, CO_2, H_2O and VOCs in MOFs, both computationally and experimentally (Babarao and Jiang, 2008; Canepa et al., 2013; Rosenbach et al., 2008). However, the kinetics properties of MOF material for hydrogen storage are rarely studied (Bimbo et al., 2015; Saha et al., 2009, 2008). Hence, the hydrogen adsorption kinetics properties of pristine MIL-101(Cr) samples and activated carbon (AC) doped MIL-101(Cr) samples need to be studied to test the fulfilment of DOE targets.

3.2. Mass transfer phenomena during gas adsorption in a porous adsorbent

The transport of gas molecules in porous materials is governed by diffusion. The diffusion can be generated with or without a gradient of concentration (diffusive transport and self-diffusion, respectively). Apparently diffusive transport is the key factor playing a role in hydrogen adsorption kinetics measurement and the objective of this study.

In a porous material, the diffusion can be further divided into two steps: external diffusion and internal diffusion, as illustrated in Figure 3.1.
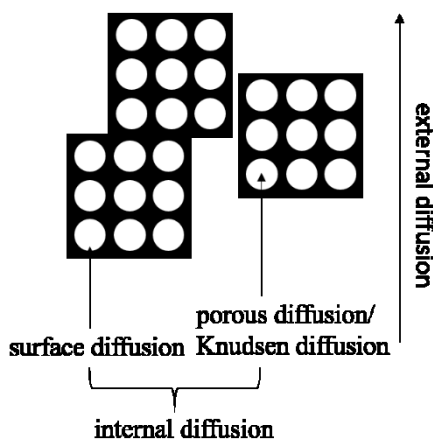
Figure 3.1: Diffusion mechanisms in porous material.

3.2.1. External diffusion

External diffusion takes place outside the adsorbent particle, in the vicinity of its external surface. It is mainly driven by the characteristics of the gas flow surrounding the adsorbent, and most often is dependent on the transport by convection. Each particle is surrounded by a laminar sublayer, through which mass transfer occurs by molecular diffusion. The thickness of the laminar sublayer, and hence the mass transfer coefficient, is determined by the hydrodynamic conditions (Geankoplis, 1983; Perry and Green, 2008; Petrovic and Thodos, 1968; Ruthven, 1984). It can be described according to the film theory with a general transfer coefficient, k_{ex} (m.s^{-1}).
The mass transfer rate is then expressed by:

$$\frac{\partial \bar{q}}{\partial t} = \frac{k_{ex}}{d_p}(q^* - q_s)$$
(3.1)

where:
- $\bar{q}$ is the mean adsorbed quantity in adsorbent particle (mol.m^{-3})
- t is the time (s)
- d_p is the diameter of the adsorbent particle (m)
- q^* is the bulk concentration (mol.m^{-3})
- q_s is the concentration of adsorbed phase at the surface of the adsorbent particle(mol.m^{-3})

Since the transfer is generated by hydrodynamics, the external mass transfer coefficient k_{ex} can be related to dimensionless numbers, such as Reynold, Schmidt and Sherwood numbers (Geankoplis, 1983; Perry and Green, 2008; Petrovic and Thodos, 1968).

$$Re = \frac{ud_p}{v}$$
(3.2)

$$Sc = \frac{v}{D_m}$$
(3.3)

$$Sh = \frac{k_{ex}d_p}{D_m}$$
(3.4)

with
- u the surface velocity (m.s^{-1})
- v the kinematics viscosity of gas (m^2.s^{-1})
- D_m the molecular diffusivity of gas (m^2.s^{-1})

Several empirical relationships have been developed to calculate the external transfer coefficient k_{ex}, which are presented in Table 3.1.

Table 3.1: Semi-empirical relations proposed for the estimation of the external transfer coefficients.

Relation	Range of application	Reference
$k_{ex} = \dfrac{0.357}{\epsilon} Re^{0.64} Sc^{0.33} \dfrac{D_m}{d_p}$	3<Re<2000	(Petrovic and Thodos, 1968)
$Sh = 2 + 0.6 Sc^{1/3} Re^{1/2}$	-	(Ranz and Marshall, 1952)
$Sh = 0.75 Sc^{0.37} Re^{0.4}$	-	(Sandall, 1977)
$Sh = 2 + 1.1 Sc^{\frac{1}{3}} Re^{0.6}$	3<Re<10000	(Wakao and Funazkri, 1978)
$Sh = 1.15 \left(\dfrac{Re}{\epsilon}\right)^{0.5} Sc^{0.33}$	Re>1	(Perry and Green, 2008)
$Sh = \dfrac{1.09}{\epsilon} Re^{0.33} Sc^{0.33}$	0.0015<Re<55	(Wilson and Geankoplis, 1966)
$Sh = \dfrac{0.25}{\epsilon} Re^{0.69} Sc^{0.33}$	55<Re<1050	

It is important to mention that the last two relationships describe the mass transfer from liquid to porous solids which is not the case for this study. Meanwhile, it can be observed that the relation given by Ranz and Marshall (1952) and the relation given by Wakao and Funazkri (1978) imply a minimum Sh=2 which is the lowest mass transfer rate in a quasi-stagnant situation whereas according to other relationships the external mass transfer coefficient is null under such condition.

3.2.2. Internal diffusion

Diffusive transport in pores within adsorbents involves different mechanisms: Poiseuille flow, molecular diffusion, Knudsen diffusion, and surface diffusion (Ruthven, 1984). The resulting diffusion rate is a combination of these different diffusion models and the limiting mechanisms are dependent on the pore structure.

The pore structure parameters which are usually considered are the pore width and the 'tortuosity factor' τ, defined as the ratio of the actual distance between two points and the shortest distance between these two points along the pore (Fogler, 2006).

3.2.2.1. Poiseuille flow

The Poiseuille flow describes a steady laminar flow of incompressible and Newtonian fluid. It is deduced from the Navier-Stokes equations, considering an average velocity u_c in a capillary expressed by:

$$u_c = -\frac{r^2}{8\mu} \frac{dp}{dz_c} \tag{3.5}$$

with

- u_c the average velocity in the capillary of Poiseuille flow (m.s^{-1})
- r the diameter of the capillary (m)
- μ the dynamic viscosity of gas (kg.m^{-1}.s^{-1})
- p the pressure (Pa)

- z_c the capillary length (m)

The velocity is governed by a pressure drop and the interstitial velocity in pores can be calculated accounting to the pore tortuosity (Do, 1998):

$$v = -\frac{r_{pore}^2}{8\mu\tau^2}\frac{dp}{dz} \tag{3.6}$$

with r_{pore} the pore radius (m).

The diffusivity is then expressed by:

$$D_{poiseuille} = -\frac{pr_{pore}^2}{8\mu\tau^2} \tag{3.7}$$

3.2.2.2. Knudsen diffusion

Knudsen diffusion describes the diffusion in pores where collisions between gas molecules and pore walls are frequent (Bird et al., 1960). This means that the mean free path of gas molecules is shorter than the pore diameter, and is characterized by Knudsen constant which is the ratio of mean free path of gas molecule λ (m) and the diameter of pore d_{pore} (m):

$$\lambda = \frac{k_b T}{\pi d_{pore}^2 p\sqrt{2}} \tag{3.8}$$

$$Kn = \frac{\lambda}{d_{pore}} \tag{3.9}$$

where

- k_b is the Boltzmann constant, equals to 1.38×10^{-23} m^2.kg.s^{-2}.K^{-1}
- T is the temperature (K)
- p is the pressure (Pa)

In Knudsen diffusion, it is obviously that $Kn>1$.

The following correlation was proposed by Kennard (1938) to estimate the Knudsen diffusivity

$$D_{kd} = 3.068 r_{pore}\left(\frac{T}{M}\right)^{0.5} \tag{3.10}$$

- D_{kd} is the Knudsen diffusivity (m^2.s^{-1})
- r_{pore} is the mean pore radius (m)
- M is the molar weight of gas (kg.mol^{-1})
- T is the temperature (K)

3.2.2.3. Molecular diffusion

Molecular diffusion characterizes generally the diffusion mode in large size pores. The probability of collisions between gas molecules and pores is very small ($Kn<1$) and the collisions between gas molecules are significant.

According to Bird *et al.* (1960), the molecular diffusion D_{md} in irregular pore geometries can be expressed as a function of the tortuosity factor.

$$D_{md} = \frac{D_m}{\tau}$$
(3.11)

where D_m is the molecular diffusivity in gaseous systems (m^2.s^{-1}).

3.2.2.4. Surface diffusion

The surface diffusion is the most complex transport mechanism occurring in porous materials, as shown in Figure 3.2. Its contribution is especially significant for high surface area adsorbents and at large extents of surface coverage by the adsorbate molecules. Surface diffusion corresponds to the motion of adsorbed molecules jumping from one adsorption site to another vacant site. Therefore, surface diffusion is positively correlated to the surface concentration of adsorbate. As the motion of adsorbed molecules requires thermal agitation, surface diffusion is enhanced by temperature increase. The temperature influence can be described by the Arrhenius law and is represented by an exponential factor depending on the temperature reverse and on the activation energy exp($-E_a/RT$) (Do, 1998) where E_a (J.mol^{-1}) is the activation energy.
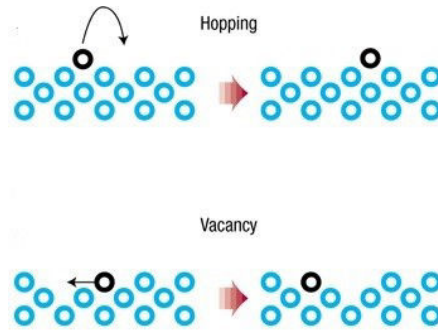
Figure 3.2: Surface diffusion by hopping or jumping to a vacant site, adapted from Tromp (2003).

Darken (1948) studied the diffusion of ions in metallic systems and proposed that the driving force controlling surface diffusion is the gradient of the Gibbs chemical potential $d\mu/dx$ where μ is the chemical potential of the adsorbed phase. If the adsorbed phase and gas phase are in equilibrium, the chemical potentials of these two phases are the same. Assuming the gas as ideal, the gradient of chemical potential can then be expressed as:

$$\frac{d\mu}{dx} = RT\frac{d\ln p}{dx}$$
(3.12)

where R is the ideal gas constant (8.31 J.mol^{-1}.K^{-1}), T is the temperature (K) and p is the pressure (bar).
The surface diffusivity is so derived:

141

$$D_s = D_{s0} \frac{\partial \ln p}{\partial \ln q} \qquad (3.13)$$

where D_{s0} is the diffusivity at zero coverage (m^2.s^{-1}).

For instance, if the adsorption isotherm follows the Langmuir relationship, Equation 3.13 becomes

$$D_s = D_{s0} \frac{1}{1 - \dfrac{q}{q_0}} \qquad (3.14)$$

Higashi *et al.* (1963) used a hopping or the Higashi Ito Oishi (HIO) model, to explain the surface diffusion in which adsorbed molecules migrates from one site to another by hopping movements. According to this model, the number of jumps of adsorbed molecules is proportional to 1/1-θ, where θ is the surface coverage and the diffusivity is derived:

$$D_s = \frac{D_{s0}}{1 - \theta} \qquad (3.15)$$

which is equivalent to Equation 3.13 if Langmuir model is assumed.

However, the HIO model predicts an infinite surface diffusion at full coverage which is not the reality. The working range of HIO model or Darken model using Langmuir adsorption isotherm relation is that monolayer is not formed. Yang *et al.* (1973) modified the HIO model by applying a consolidating second-layer adsorption. In their theory, the average jumps are no longer calculated and the diffusivity D_s (m^2.s^{-1}) is calculated:

$$D_s = \frac{D_{s0}}{(1 - \theta) + \theta \left[\dfrac{\nu_1}{\nu_2} e^{-(\Delta E_1 - \Delta E_2)/RT} \right]} \qquad (3.16)$$

where ν_1 and ν_2 are the vibration frequency of the vacant site and occupied site respectively, and $\Delta E_1 - \Delta E_2$ represents the difference in the heats of adsorption between the first and the second layer.

Suzuki and Fujii suggested a surface diffusion model considering the influence of the surface concentration (Suzuki and Fujii, 1982):

$$D_s = D_{s0}(aq)^n \qquad (3.17)$$

$$Q_s = -Q_0 \ln(aq) \qquad (3.18)$$

$$q = \frac{1}{\dfrac{1}{KC} + \dfrac{1}{kC^{1/n}}} \qquad (3.19)$$

where a (kg.mol^{-1}) is an experimentally fitted parameter for the isosteric heat of adsorption Q_s (J.mol^{-1}), q is the adsorbed quantity (mol.kg^{-1}). The value of k, K and n are determined by experimental equilibrium data fitting. C is gas phase concentration (mol.m^{-3}).

Chen and Yang (1991) proposed a surface diffusion model in which the diffusivity is also dependent on the surface coverage. Rate constants related to the process of adsorption site blockage and to forward migration of the adsorbed molecules were introduced so that the surface diffusivity could be expressed as:

$$\frac{D_s}{D_{s0}} = \frac{1 - \theta + \left(\frac{\lambda}{2}\right)\theta(2 - \theta) + [H(1 - \lambda)](1 - \lambda)\left(\frac{\lambda}{2}\right)\theta^2}{(1 - \theta + \lambda\theta/2)^2} \tag{3.20}$$

Where the parameter λ is the ratio of the rate constants for blockage and for forward migration, and $H(1-\lambda)$ is the Heaviside step function.

In addition to surface diffusion, diffusion in the pores results from two other phenomena, molecular diffusion and Knudsen diffusion. In order to measure the surface diffusivity, the mass transfer mechanisms need to be decoupled. In an attempt to measure the pore diffusivity without the contribution of the surface diffusion, kinetics can be investigated at high temperature, in conditions such that the surface coverage is very low thus the surface diffusion can be neglected. However, the temperature influence on the diffusion coefficients need to be taken into account (Butt and Reed, 1971; Ruthven, 1984; Schneider and Smith, 1968).

3.2.2.5. *Constitutive flux in pores*

The constitutive flux in the pores of the adsorbent material should account for a pore diffusion contribution due to molecular and Knudsen mechanisms, and for the surface diffusion contribution in the adsorbed phase, as illustrated in Figure 3.3. This constitutive flux is calculated by

$$J = -\varepsilon D_p \frac{\partial C}{\partial r} - (1 - \varepsilon)\rho D_s \frac{\partial q}{\partial r} \tag{3.21}$$

where J is the diffusion flux (mol.m^{-2}.s^{-1}), ε is internal particle porosity, D_p is the pore diffusivity (m^2.s^{-1}) and D_s is the surface diffusivity (m^2.s^{-1}), ρ is the bulk density of the adsorbent (kg.m^{-3}), C is the bulk gas concentration (mol.m^{-3}) and q is the adsorbate concentration (mol.kg^{-1}).
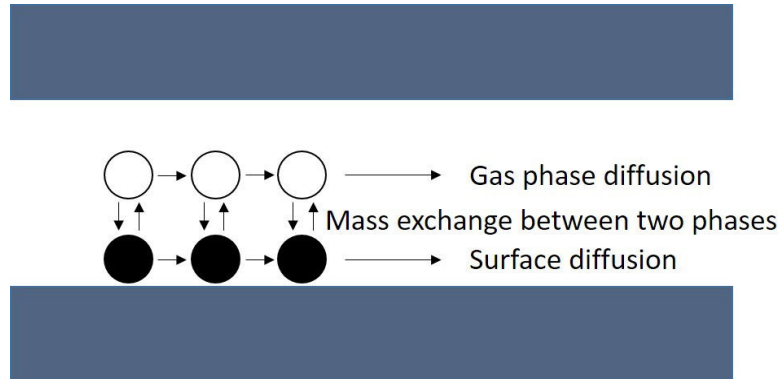
Figure 3.3: Scheme of the gas phase and surface diffusion in pores.

3.2.3. Linear Driving Force model

The different mechanisms of diffusion with different parameters which are difficult to be measured experimentally make it nearly impossible to construct a mathematical model to describe the diffusion. Therefore, the linear driving force (LDF) model was developed by Glueckauf (1955a)

which describes the mass transfer at the adsorbent particle scale by a linear relationship in order to simplify the calculations.

The LDF model was firstly used to model the adsorbed quantity of one adsorbent particle in chromatographic studies (Glueckauf and Coates, 1947) and the proposed relationship is as following:

$$\frac{\partial \bar{q}}{\partial t} = \frac{\Omega D_{eff}}{r_p^2}(q^* - \bar{q}) \tag{3.22}$$

where $\Omega > 1$ and depends on the shape of the particle. This linear relationship implies that the temporal variation of mean adsorbed concentration is proportional to the difference of the bulk concentration and the mean adsorbed concentration in the particle. $\Omega = 14$ has been first recommended for Equation 3.22 by Glueckauf (1955b).

Glueckauf (1955a) demonstrated that this relation can be theoretically deduced from the equation of diffusion for a spherical adsorbent particle surrounded by a continuously increasing pressure environment. The equation of diffusion, according to the second law of Fick, is expressed as:

$$\frac{\partial q}{\partial t} = \frac{1}{r^2}\frac{\partial}{\partial r}\left(r^2 D \frac{\partial q}{\partial r}\right) \qquad 0 \leq r < r_p \tag{3.23}$$

where D (m^2.s^{-1}) is the diffusivity, q is the quantity of adsorbed gas (mol.kg^{-1}), t (s) is the time, r (m) is the distance from the centre of the adsorbent, and r_p the radius of the adsorbent particle.

An analytical solution can be given for a steady-state external condition where the following initial and boundary conditions are used:

$$q(0,r) = 0; q(t,r_p) = q^*; q(t,0) = q_0; \tag{3.24}$$

where q_0 is the constant bulk gas concentration. The solution is given in the following form (Carslaw and Jaeger, 1959):

$$\bar{q} = q_0 + (q^* - q_0)\left\{1 - \frac{6}{\pi^2}\sum_{n=1}^{\infty}\frac{1}{n^2}\exp\left[-(n\pi)^2\frac{Dt}{r_p^2}\right]\right\} \tag{3.25}$$

Instead of a constant external condition, Glueckauf (1955a) supposed a succession of pressure steps to simulate a discrete pressure increase. The boundary condition becomes: $q^* = q_i$ for $t_{i-1} < t < t_i$ with $i > 0$. If dimensionless time variable $\epsilon t = Dt/r_p^2$ is considered, Equation 3.24 develops to:

$$\bar{q} = q_0 + (q_1 - q_0)\left\{1 - \frac{6}{\pi^2}\sum_{n=1}^{\infty}\frac{1}{n^2}exp[-(n\pi)^2\epsilon(t - 0)]\right\}$$

$$+(q_2 - q_1)\left\{1 - \frac{6}{\pi^2}\sum_{n=1}^{\infty}\frac{1}{n^2}exp[-(n\pi)^2\epsilon(t - t_1)]\right\} \tag{3.26}$$

$$+(q_3 - q_2)\left\{1 - \frac{6}{\pi^2}\sum_{n=1}^{\infty}\frac{1}{n^2}exp[-(n\pi)^2\epsilon(t - t_2)]\right\} + \cdots$$

If the pressure varies not in step but continuously, Equation 3.26 becomes

$$\bar{q} = q^* - \frac{6}{\pi^2}\int_{\tau=0}^{\tau=t}\left(\frac{dq}{dt}\right)_\tau \sum_{n=1}^{\infty}\frac{1}{n^2}exp[-(n\pi)^2\epsilon(t - \tau)]d\tau \tag{3.27}$$

By deriving Equation 3.27 by time, then

$$\frac{d\bar{q}}{d\epsilon t} = 6 \int_{\tau=0}^{\tau=t} \left(\frac{dq}{dt}\right)_\tau \sum_{n=1}^{\infty} exp[-(n\pi)^2 \epsilon(t-\tau)]d\tau \tag{3.28}$$

If conditions remain near equilibrium, which implies that ϵt is large, integration by parts of Equation 3.27 and 3.28 gives:

$$\bar{q} = q - \frac{6}{\pi^2}\left\{\frac{dq}{\pi^2 d\epsilon t}A_2 - \frac{d^2 q}{\pi^4 d(\epsilon t)^2}A_3 + \cdots\right\} \tag{3.29}$$

$$\frac{d\bar{q}}{d\epsilon t} = 6\left\{\frac{dq}{\pi^2 d\epsilon t}A_1 - \frac{d^2 q}{\pi^4 d(\epsilon t)^2}A_2 + \cdots\right\} \tag{3.30}$$

where

$$A_i = \sum_{i=1}^{\infty}\frac{1}{n^{2i}} - \sum_{i=1}^{\infty}\frac{exp(-n^2\pi^2\epsilon t)}{n^{2i}} \tag{3.31}$$

From Equation 3.29 and 3.30, it can be derived that:

$$\frac{d\bar{q}}{d\epsilon t} = \pi^2(q^* - \bar{q}) + \frac{6}{\pi^2}\frac{dq}{d\epsilon t}(A_1 - A_2) - \frac{6}{\pi^4}\frac{d^2 q}{d(\epsilon t)^2}(A_2 - A_3) + \cdots \tag{3.32}$$

If the dimensionless time $\epsilon t > 0.1$, the value of A_i-A_{i+1} closely approaches

$$A_i - A_{i+1} = \sum_{i=1}^{\infty}\frac{1}{n^{2i}} - \sum_{i=1}^{\infty}\frac{1}{n^{2i+2}} \tag{3.33}$$

Then Equation 3.32 can be written in the following form:

$$\frac{d\bar{q}}{d\epsilon t} = \pi^2(q^* - \bar{q}) + \left(1 - \frac{\pi^2}{15}\right)\frac{dq}{d\epsilon t} - \left(\frac{1}{15} - \frac{2\pi^2}{315}\right)\frac{d^2 q}{d(\epsilon t)^2} + \cdots \tag{3.34}$$

By neglecting high order terms and replacing $dq/d\epsilon t$ by $d\bar{q}/d\epsilon t$ for thermodynamic equilibrium, Equation 3.34 can be simplified as

$$\frac{d\bar{q}}{d\epsilon t} = 15(q^* - \bar{q}) \tag{3.35}$$

which gives the solution

$$\frac{\bar{q}}{q^*} = 1 - \exp\left(-\frac{15D}{r_p^2}t\right) \tag{3.36}$$

It can be observed that Equation 3.36 is similar to Equation 3.22 with $\Omega=15$. The coefficient $15D/R^2$ is otherwise called global transfer coefficient k_g in LDF model.

It should be noticed that for LDF derivation, assumptions such as quasi-equilibrium system and dimensionless time $\epsilon t > 0.1$ have been set. Therefore, the applicability of Equation 3.36 requires these two conditions which is not always the case in reality.

3.3. Adsorption kinetics measurement

3.3.1. Transport diffusivity measurement techniques

The classical method of measuring internal or macropore diffusivities is Wicke-Kallenbach method (Wicke and Kallenbach, 1941), as illustrated in Figure 3.4.
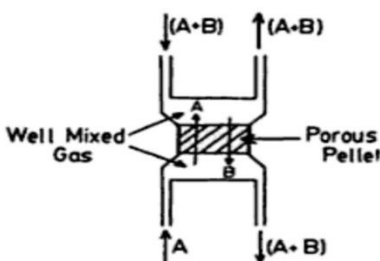
Figure 3.4: The principle of Wicke-Kallenbach apparatus for internal diffusivity measurement (Ruthven, 1984).

By knowing the thickness of the pellet and the concentrations and flow rate of both streams, the fluxes in both directions and hence the effective diffusivity can be calculated. The advantage of using this method is that it depends on a steady-state measurement and it is not affected by finite heat transfer (Ruthven, 1984). However, for micropore diffusivity calculation, this method requires a single crystal with a regular large size which is not applicable in this study.

Inverse chromatography is an alternative way to study sorption kinetics from the dynamic response of a packed column to a change in adsorbate concentration. It can be applied for both macropore and micropore diffusivity measurements. However, it is difficult to separate the effect of diffusion and axial dispersion by involving one experiment (Ruthven, 1984).

Zero length column (ZLC) is introduced by Eic and Ruthven (1988) to measure diffusivities of hydrocarbons in zeolites. This method uses an inert gas purge flow passing through a thin layer of adsorbent already charged with adsorbate. By changing effluent flow concentration, the diffusivity can be computed using the solution of diffusion equation (Equation 3.25).

Otherwise, with uptake rate measurement, the diffusivities of adsorbate in porous solids can be determined. The fractional uptake curve can be approached by the solution of the diffusion equation. However, it is sometimes difficult to find experimental conditions such that the uptake rate is controlled by internal diffusion rather than by heat transfer or other external resistances to mass transfer (Ruthven, 1984).

In this work, the hydrogen diffusivity in MOF and carbon-MOF composite adsorbents is measured by applying uptake rate measurement with the PCT Pro volumetric apparatus (see Section 2.3.2).

3.3.2. Experiment description and calculation method

Hydrogen adsorption kinetics were investigated on the panel of materials synthesized in this study, by using volumetric measurement apparatus described in Section 2.3.2. Three MIL-101(Cr) and doped MIL-101(Cr) samples were chosen to perform the kinetics analyses, namely:

- MIL-101(Cr) synthesized using acetic acid, noted as MIL-101(Cr)-a
- MIL-101(Cr) synthesized using sodium acetate, noted as MIL-101(Cr)-b
- 5 wt% activated carbon doped MIL-101(Cr) synthesized using acetic acid, noted as AC-MIL-101(Cr)-b

MOF-5 was also taken as a reference material to be tested for comparison with kinetics data reported in the literature (Saha et al., 2009).

The adsorption kinetics were measured for a pressure variation between a primary vacuum up to 0.2, 0.5, 1 and 5 bar respectively. The reasons of choosing this panel of pressure are: (i) the low pressure transducer can be used for pressure measurements, which have a higher resolution than the high pressure transducer; (ii) the kinetic studies are for the purpose of measuring uptakes under a constant pressure and temperature. Hence, the volume of the reservoir should be large compared to sample cell and be able to store a big amount of hydrogen for experiments (>> hydrogen adsorbed). Therefore, if high pressure experiments are carried out, which means that a large quantity of hydrogen at room temperature will be inserted into the sample cell and will cause a significant temperature rise and produce difficulties for data interpretations.

The adsorbents were loaded into the sample cell and outgassed at 393 K under vacuum for 72 hours to remove any pre-adsorbed gases and solvents.

After preliminary determination of the dead volumes according to the methods described in Section 2.3.1.1, the procedure applied to carry out the kinetic experiments is as following:

- The hydrogen reservoir is kept at constant temperature 28°C (301 K) and the sample cell is at cryogenic temperature (temperature of liquid nitrogen, 77 K)
- The sample cell and the reservoir are initially closed to each other and pumped under primary vacuum.
- The reservoir is then filled with necessary amount of gas to reach a pre-set value for its initial pressure.
- The reservoir and the sample cell are afterwards connected to each other so that the reservoir is depressurized and the gas is flowing to the sample cell.
- The pressure and the temperature of the system are measured all along the experiment which was conducted over a total duration defined by the operator.

Since the reservoir is not fed with extra gas, the mass balance equations to be used for the determination of the adsorbed quantities with time need to be adapted from those established for equilibrium data measurement.

Using the equation of state of hydrogen, the initial mass prepared in the reservoir is:

$$m_{H_2}^* = \frac{p_r V_r M_{H_2}}{RT_r Z_{H_2}(p_r, T_r)} \tag{3.37}$$

At one instant t after the beginning of the measurement, the mass of gas in bulk can be calculated using double imaginary method presented in the previous chapter and the mass of hydrogen adsorbed in excess m_{GE}^a can be derived:

$$m_{GE}^a(t) = m_{H_2}^* - \frac{p(t)M_{H_2}}{R}\left[\frac{V_{up}}{T_r Z_{H_2}(p(t), T_r)} + \frac{(V_{down} - V_{sk})}{T_s Z_{H_2}(p(t), T_s)}\right] \qquad (3.38)$$

3.3.3. Experimental kinetics curves of hydrogen adsorption

Hydrogen adsorption kinetics curves describe the variation of the fractional uptake q/q_0 (q_0 is the adsorbed quantity at equilibrium) with time as soon as the reservoir and the sample cell were open to each other until equilibrium was established. The uptake fraction gives the ratio of the adsorbed amount in excess over the equilibrium value, corresponding to the conditions of the final reached pressure in the system and to the temperature of liquid nitrogen. This dimensionless variable is helpful to compare the kinetics curves measured at a different pressure (Do, 1998; Ruthven, 1984). The hydrogen kinetic adsorption curves and temperature profiles measured during the experiments conducted at the different pressures on MOF-5 sample are presented in Figure 3.5.
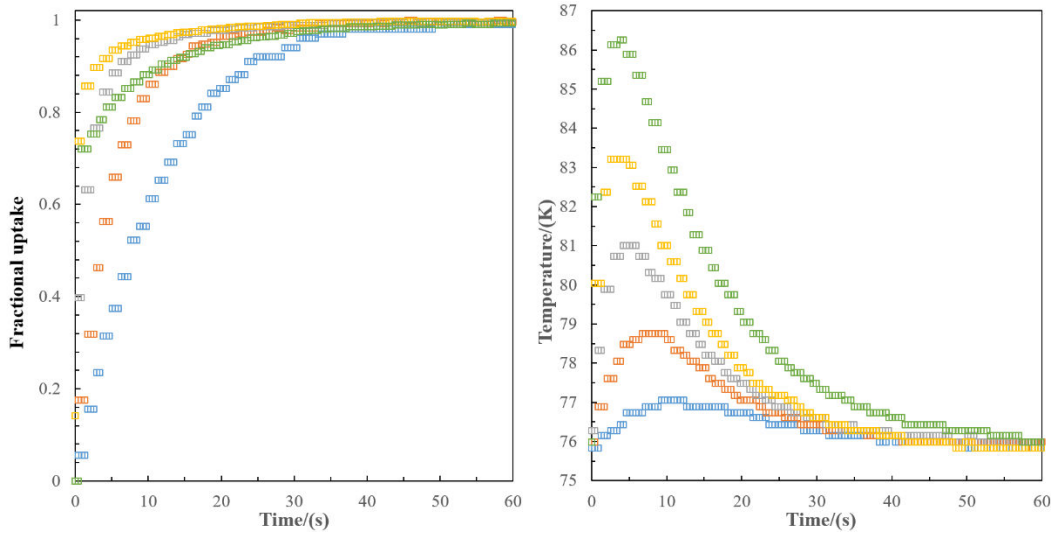
Figure 3.5: Adsorption kinetics of hydrogen in MOF-5 measured at 77 K and 0.2 (blue cubes), 0.5 (red cubes), 1 (grey cubes), 2 (yellow cubes), 5 bar (green cubes) respectively. On the left is the fractional uptake profile as a function of time, on the right is the temperature profile as a function of time.

It can be easily observed that at low final equilibrium pressure such as at 0.2 and 0.5 bar the temperature slightly varies around 77 K. As the pressure increases, the temperature variations become more and more significant and in experiment carried out at 5 bar, the maximal temperature peak is about 10 K. The temperature of the sample cell is measured by using a thermocouple located at the outside wall surface of the sample cell. Therefore, the measured temperature reflects the effects of the adsorbent heating up, caused by the exothermic adsorption process and also by the

introduction of hydrogen initially at the reservoir temperature (28°C), the inertia of the wall material of the sample cell, and the cooling by liquid nitrogen. Note that the wall thickness of the sample cell prevents immediate detection of temperature change inside the sample cell. There is always a delay of time for temperature measurement and heat dissipation by the surrounding of the sample cell.

Regarding the fractional uptake profile, it can be observed that until 2 bar, a higher pressure implies a faster adsorption rate. However, at 5 bar, a longer time is required to achieve equilibrium than at 2 bar. This exception can be explained by a temperature effect. At 5 bar, the temperature rise is higher than at 2 bar and the time required to cool the sample until the equilibrium temperature of 77 K is also longer. The slow temperature decrease when the concentration of the adsorbed hydrogen is close to the equilibrium is then likely to have a limiting effect on the adsorption rate. The hydrogen adsorption kinetic curves measured in the different pressure conditions at 77 K are compared for the different materials in Figure 3.6.
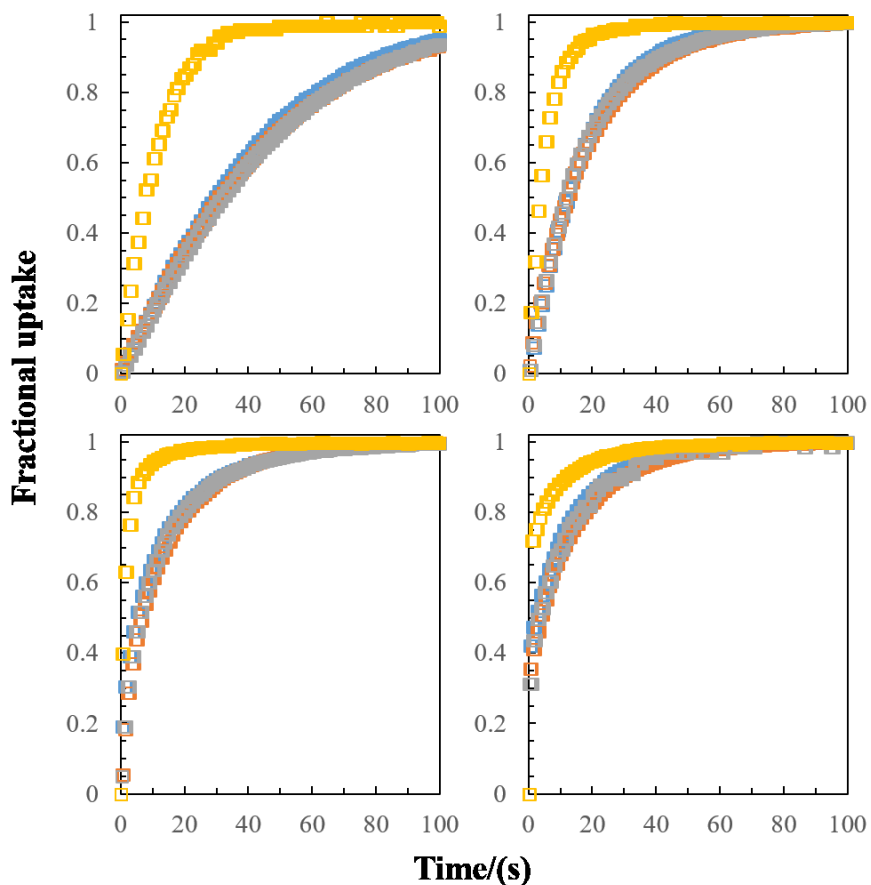
Figure 3.6: Adsorption kinetics measured at 0.2 bar (top left), 0.5 bar (top right), 1 bar (bottom left) and 5 bar (bottom right), respectively. MOF-5 (yellow cubes), MIL-101(Cr)-a (blue cubes), MIL-101(Cr)-b (red cubes) and AC-MIL-101(Cr)-b (grey cubes).

From the results shown above, it can be observed that the adsorption rate on MOF-5 is significantly faster than on MIL-101(Cr) based materials. In addition, the kinetics curves measured for all the three different MIL-101(Cr)s appear to be very close to each other, even quite superimposed, whatever the maximal pressure condition applied. Thus, at 0.5 bar, the equilibrium is reached onto MIL-101(Cr) materials after 100 seconds, while it needs only 30 seconds onto MOF-5. The observed deviation in the adsorption rates between the two types of crystalline structures decreases when the pressure increases: at 1 bar, it takes 80 seconds to reach equilibrium with MIL-101(Cr) and 20 seconds with MOF-5, and at 5 bar 60 seconds and 40 seconds, respectively.

Regarding the pressure effect, it can be observed that higher pressure usually implies faster adsorption rates. This is true for all the tested materials except MOF-5, for which at 5 bar, a longer adsorption rate is required to achieve equilibrium than at 2 bar, as previously noticed.

The obtained results are compared with literature (Bimbo et al., 2015; Saha et al., 2009) and this comparison is illustrated in Figure 3.7.
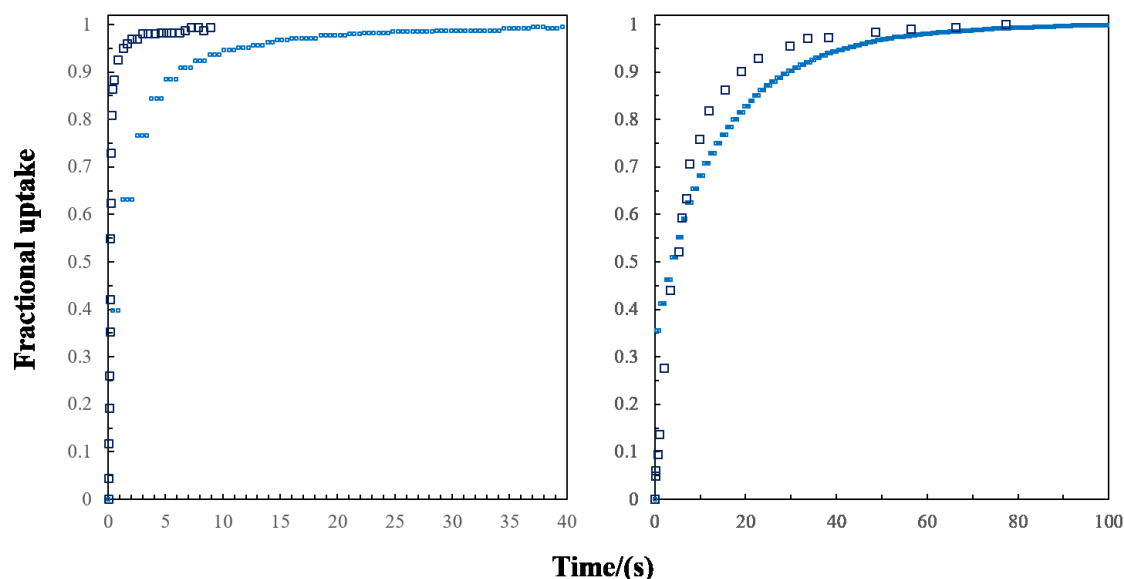
Figure 3.7: Kinetic results compared with literature. On the left, the comparison of hydrogen uptake kinetic is illustrated for MOF-5, with black cubes for data obtained from the literature (Saha et al., 2009) and blue cubes for data obtained from this work (MOF-5 at 1 bar). On the right, the comparison of hydrogen uptake kinetic is illustrated for pristine MIL-101(Cr) adsorbent, with black cubes for data obtained from the literature (Bimbo et al., 2015) and blue cubes for data obtained from this work (MIL-101(Cr)-a at 5 bar).

Good agreements can be observed from the comparison of kinetic data from this study and literature. From Figure 3.7, differences can be noticed for kinetic curves obtained in this study and the literature (Saha et al., 2009) which might be produced by the different experiment condition (temperature change, pressure applied, adsorbent used). In the study of Saha *et al.*, a volumetric apparatus Micromeritics ASAP 2020 was used. For MIL-101(Cr), the kinetic curves obtained from two studies are very similar while it should remark that the pressure applied by Bimbo *et al.* (2015)

is 1.11 MPa (11.1 bar) which is different from the experimental conditions used in this work (kinetic curve presented measured at 5 bar).

3.4. Hydrogen adsorption kinetics fitting by Linear Driving Force model

The experimental hydrogen adsorption kinetics curves are attempted to be described according to the Linear Driving Force (LDF) model, presented in Section 3.2.3.

According to Equation 3.36, if the hydrogen adsorption kinetics follows the LDF model, then a plot of $\ln(1-\bar{q}/q^*)$ versus t should be linear passing through origin with slope $15D/r_p^2$. This is illustrated in Figure 3.8.
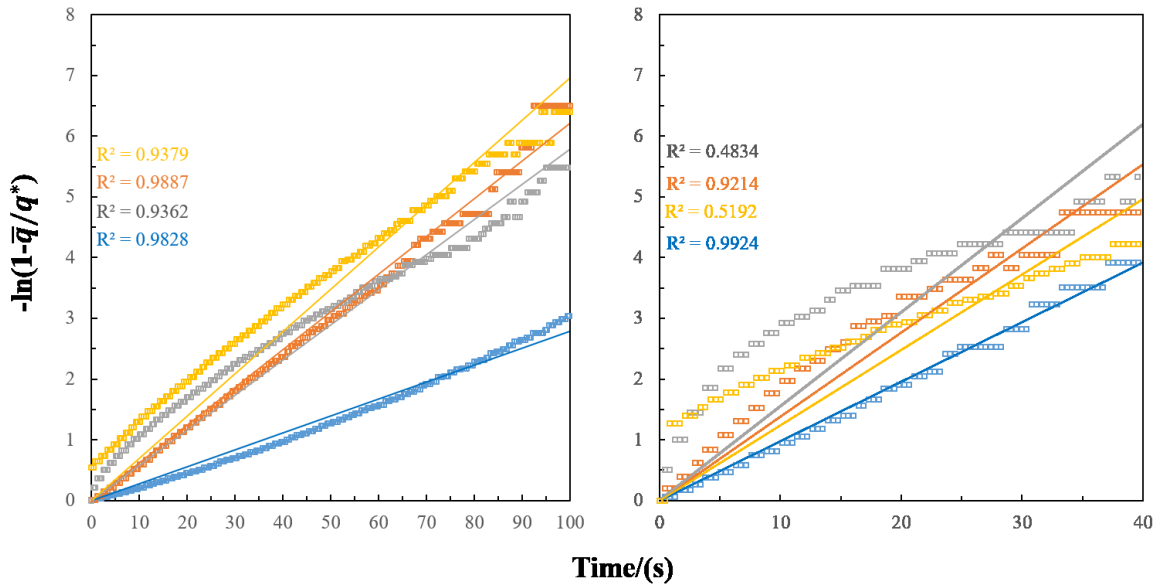
Figure 3.8: -ln(1-q̄/q*) versus t of MIL-101(Cr)-a (left) and MOF-5 (right). Results of different pressures are presented: 0.2 bar (blue), 0.5 bar (orange), 1 bar (grey) and 5 bar (yellow).

It can be observed from Figure 3.8 that good linear relations are shown for kinetic results at 0.2 bar and 0.5 bar which have a high R^2 value. Therefore, at low pressure, *i.e.* 0.2 and 0.5 bar, the LDF model fits well the experimental kinetics data obtained for MIL-101(Cr) type materials, but substantial discrepancies are observed at higher pressure, especially for the experiment carried out for MOF-5 at 5 bar, an offset can be observed. Such offset is due to the high adsorption rate at the beginning of the kinetic uptake measurement (see Figure 3.5). Disagreement between experimental and theoretical data can be attributed to the non-validity of the LDF assumptions in conditions which are too far from the thermodynamical pseudo-equilibrium between the bulk gas and the adsorbed phase. Thus, when the pressure is close or above the atmosphere, the adsorbate concentration increase to reach equilibrium becomes large, so that the thermodynamical pseudo-

equilibrium assumption cannot be applied for large pressure steps. Hence, the LDF model can better fit results of adsorption kinetics measured at 0.2 and 0.5 bar for the adsorbents.

Moreover, according to Glueckauf (1955a), the LDF model is applicable for the dimensionless time variable $\epsilon t > 0.1$, which implies that the data used for diffusivity calculations need to be well chosen, but not from $t=0$. A more practical method for choosing kinetic data proposed by Ruthven (1984) to use the analytical solution of diffusion equation is to determine the fractional uptakes greater than 70%. Under this condition, the analytical solution of the diffusion equation becomes to a similar form of LDF model with a slight difference of coefficient.

The method of least squares is used in order to determine the optimal value of effective diffusion coefficient which minimizes the residuals between experimental and theoretical curves.

The kinetics curves of MIL-101(Cr) type materials are nearly the same, the comparison between the modelling and experimental results is reported in Figure 3.9 for MIL-101(Cr)-a only and the comparison between modelling and experimental results of MOF-5 is presented in Figure 3.10.
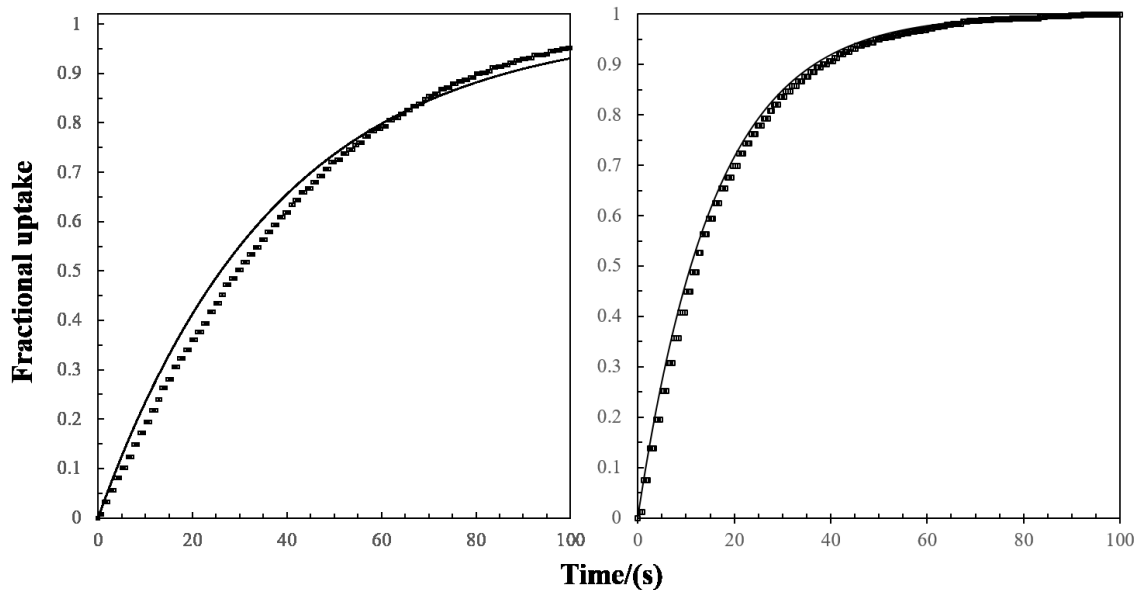
Figure 3.9: Experimental curves of hydrogen adsorption kinetics (black cubes) of MIL-101(Cr)-a at 0.2 bar (left), 0.5 bar (right) fitted by LDF model (black lines).

152
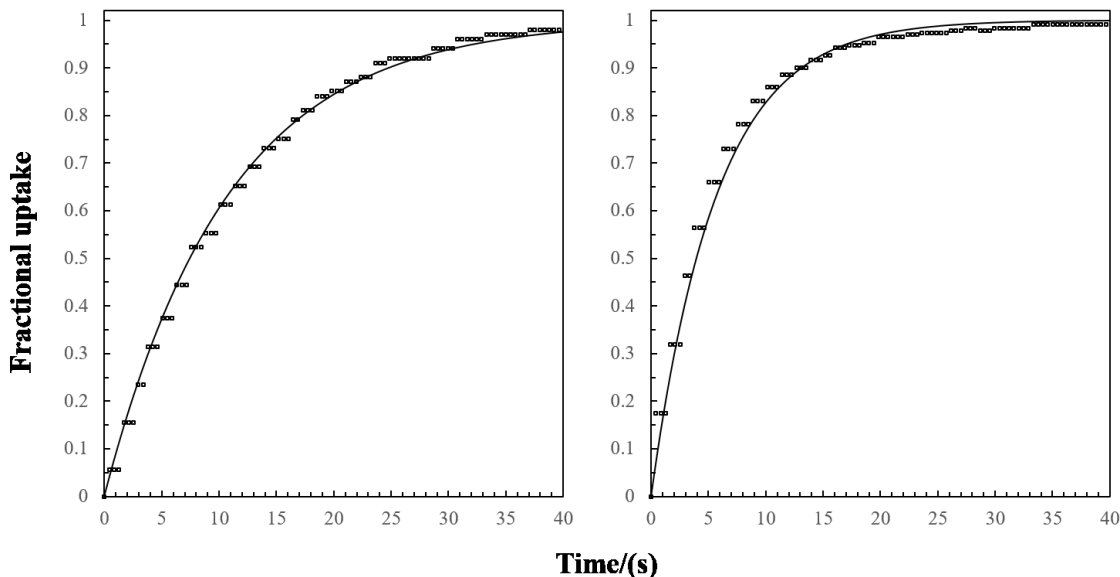
Figure 3.10: Experimental curves of hydrogen adsorption kinetics (black cubes) of MOF-5 at 0.2 bar (left), 0.5 bar (right) fitted by LDF model (black lines).

The effective diffusivities derived from the modelling of the kinetics adsorption curves by the LDF approximation in the low pressure range are specified in Table 3.2.

Table 3.2: Diffusivities modelled at different pressures by the LDF approximation for MIL-101(Cr)-a, MIL-101(Cr)-b, AC-MIL-101(Cr)-b and MOF-5 samples. To calculate the diffusivity of hydrogen in MOF-5, the crystal size measured in literature (Saha et al., 2009) is used (200 µm). Diffusivities are presented in $m^2.s^{-1}$.

Pressure applied/(bar)	MIL-101(Cr)-a	MIL-101(Cr)-b	AC-MIL-101(Cr)-b	MOF-5
0.2	2.9×10^{-17}	0.4×10^{-17}	0.6×10^{-17}	2.5×10^{-10}
0.5	6.1×10^{-17}	1.1×10^{-17}	1.8×10^{-17}	4.7×10^{-10}

The results of experiments show that high pressure makes the adsorption kinetics faster, hence, the diffusivities calculated by applying the LDF model from experimental results grow with the applied pressure. The order -17 makes the computed diffusivities moderate. However, the diffusivities are computed using data measured at the cryogenic condition. Knowing that the diffusivity is temperature dependent according to an Arrhenius relationship ($exp(-E_a/RT)$ where E_a is the activation energy), the diffusivities computed here only reflect the hydrogen diffusion rate at 77 K in these adsorbents.

3.5. The necessity of numerical modelling of hydrogen adsorption kinetics

As the LDF model cannot well be representative of the adsorption kinetics measured in pressure conditions above the atmosphere, a more appropriate model should be established in order to

compute the effective hydrogen diffusivity of hydrogen on MIL-101(Cr) materials and its doped counterparts. Such a model can be derived from the numerical solving of the transient mass balance equation, considering more realistic boundary conditions.

The different influences in a batch system on diffusion is presented (Ruthven, 1984), namely, effect of finite system volume, integral step-variable diffusivity, macropore diffusion and temperature changes due to heat transfer. Concretely in this study, the difficulties related to the application of a numerical method to solve of the transient mass balance equation are listed:

- The gas pressure is not constant during the kinetics experiment, which is contradictory with the assumptions of the LDF model. At the beginning of the experiment, the expansion of the gas from the reservoir is not spontaneously completed and a pressure drop can be observed through the valve.
- The temperature of the bulk gas and that of the adsorbent sample are initially different as the reservoir is kept at a constant temperature of 28 °C, whereas the sample cell is immersed in liquid nitrogen at cryogenic temperature (77 K). Therefore, at the opening of the valve, the gas flow entering the sample cell may cause a temperature rise.
- Response times of the different pressure and temperature transducers are different and may introduce a time delay in the collected data.
- The adsorption process being exothermal, the heat release may induce temperature increases of the adsorbent sample.

3.6. Elaboration of diffusion models

Pore and surface diffusion are concurrently engaged in the hydrogen adsorption process taking place in MIL-101(Cr) type materials.

MIL-101(Cr) adsorbent structures are mesoporous with two pore diameters of 26 and 31 Å according to the result of Section 1.4.4.4. However, the apertures of the pores are much smaller, and it reduces to 12, 14.5 or 16 Å (Lebedev et al., 2005) which is at the micropore level. It is reported that for microporous adsorbent, surface diffusion accounts for over 50% of the total diffusion (Butt and Reed, 1971; Schneider and Smith, 1968) at room temperature. Surface diffusion is also considered to be the major contribution in the hydrogen diffusion in alumina silica (Lange et al., 1995) which possesses mesopores, similar to MIL-101(Cr) for the pore size. Moreover, the surface diffusion is often considered as predominant in large surface area adsorbents, and at low temperature due to large adsorbed quantities (Do, 1998). Hence, it is reasonable to consider that the hydrogen adsorption process on MIL-101(Cr) type materials occurring at a cryogenic temperature is mainly controlled by the surface diffusion. This assumption is so retained in order to simplify the expression of the diffusion flux presented in Equation 3.21.

$$J = \rho D_s \frac{\partial q}{\partial r} \qquad (3.39)$$

3.7. Non-isothermal adsorption approach for hydrogen adsorption kinetics modelling

In a first attempt, the diffusion model was derived by taking into consideration the heat of adsorption, which implies a non-isothermal adsorption model.

3.7.1. Hypotheses and equation system for non-isothermal adsorption model

The non-isothermal adsorption model was applied by retaining the following assumptions:

- The adsorbent particle is considered to be spherical and homogeneous, which means all particles have the same physical and chemical properties so that there is no preferential axis of gas diffusion.
- Hydrogen is considered to be an ideal gas. Despite the effects of its spin at low temperature, its compressibility factor Z is very close to unity and varies by less than 3 % up to 20 bar. The chemical potential of hydrogen at 77 K is so very close to the one of an ideal gas (see Figure 3.11).
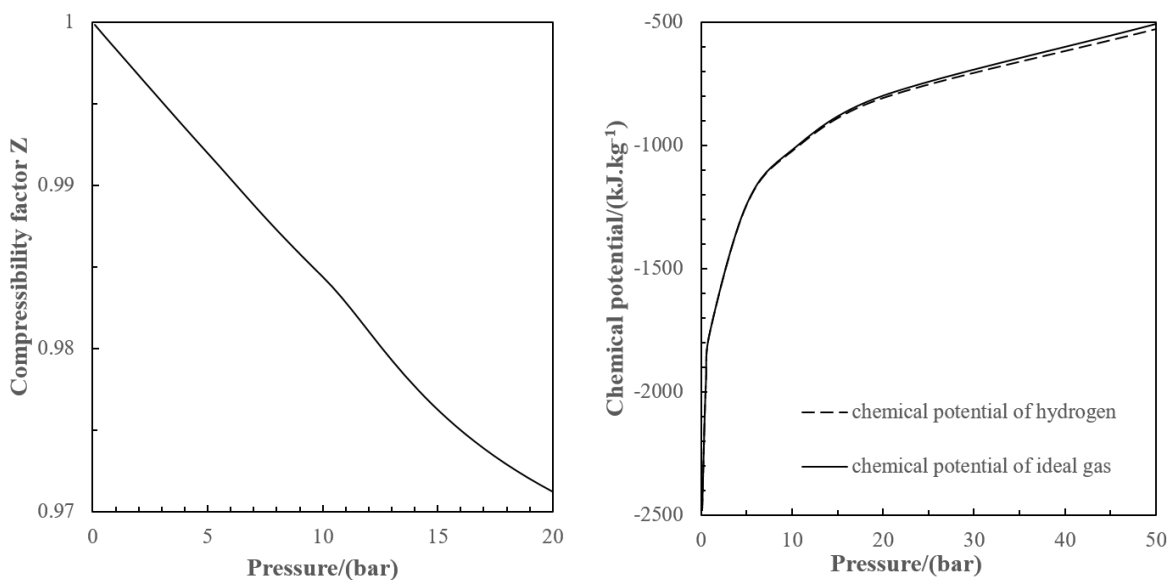
Figure 3.11: Compressibility factor of hydrogen (left) and chemical potential comparison between hydrogen and an ideal gas (right). Data adapted from Lemmon et al. (2010).

- Diffusion at the external surface of the adsorbent particles is supposed to be spontaneously completed, meaning that the external gas film resistance is assumed as negligible.

155

- The concentration of the adsorbate at the external particle surface is the one at the equilibrium with the bulk gas. It is calculated by the Langmuir isotherm model while the affinity constant is temperature-dependent.
- Surface diffusion is considered as the single diffusion process within the particle and this diffusion is governed by the difference of chemical potential in adsorbed phase, which corresponds to Darken's theory.
- The pressure is considered as constant as well as hydrogen bulk concentration throughout the adsorption process.
- The heat of adsorption is assumed to be constant whatever the stage of coverage.
- Heat conduction within the particle is far much faster than heat dissipation at the particle surface, according to Ruthven (1984). Hence, the temperature in the particle is considered to be homogeneous.

As the pressures applied for kinetic measurements do not exceed the saturation pressure which corresponds to the completion of the monolayer in Langmuir isotherm model, Darken's diffusion model (which is equivalent to HIO model) is applicable in this case.

3.7.2. Mass conservation and energy conservation

3.7.2.1. Mass conservation equation

Knowing that the diffusion in pores is governed by surface diffusion and by admitting that the surface diffusion is generated by difference of chemical potential using Darken's theory, the surface diffusion flux in pores can be then derived by combining Equation 3.13 and 3.39:

$$J = -\rho D_s \frac{\partial q}{\partial r} = -\rho D_{s0} \frac{\partial \ln p}{\partial \ln q} \frac{\partial q}{\partial r} \tag{3.40}$$

The mass balance equation is obtained by introducing this flux into the diffusion equation (Equation 3.23), then:

$$\frac{\partial q}{\partial t} = \frac{1}{r^2} \frac{\partial}{\partial r} \left(r^2 D_{s0} \frac{\partial \ln p}{\partial \ln q} \frac{\partial q}{\partial r} \right) \tag{3.41}$$

where the surface diffusivity coefficient D_{s0} depends on temperature:

$$D_{s0} = D_{s0}^{\infty} \exp \left(-\frac{E_a}{RT} \right) = D_{s0}^{0} \exp \left(\frac{E_a}{RT} \left(1 - \frac{T_0}{T} \right) \right) \tag{3.42}$$

where
- D_{s0}^{∞} is the surface diffusivity at zero coverage and infinite temperature (m^2.s^{-1})
- D_{s0}^{0} is the surface diffusivity at zero coverage and reference temperature (m^2.s^{-1})
- T_0 is a reference temperature (K).

3.7.2.2. Heat balance equation:

It is assumed that the temperature in the particle is homogeneous and the heat is exchanged by natural convection with the surroundings at the external surface of the adsorbent particle. Hence, the heat balance equation can be written as:

$$\langle C_p \rangle \frac{dT}{dt} = Q \frac{d\langle q \rangle}{dt} - \frac{a_H h_f}{\rho}(T - T_b) \tag{3.43}$$

where
- $\langle C_p \rangle$ is the mean heat capacity of the adsorbent (J.K⁻¹.kg⁻¹)
- $\langle q \rangle$ is the mean adsorption concentration (mol.kg⁻¹)
- $a_H = 3/r_p$ (m⁻¹) is the surface area per unit of volume of the spherical particle of radius r_p (m)
- h_f is the heat transfer coefficient per unit surface area (W.m⁻².K⁻¹)
- Q is the heat of adsorption (J.mol⁻¹)
- T_b is the bulk phase temperature (K)

The calculation of $\langle q \rangle$ involves the integration of adsorbed concentration in all parts of adsorbent particle:

$$\langle q \rangle = \frac{3}{r_p^{\,3}} \int_0^{r_p} r^2 q \, dr \tag{3.44}$$

3.7.3. Boundary and initial conditions:

As the adsorbent particle is supposed to be spherical and homogeneous without preferential diffusion axis, the symmetry of the particle imposes that in the centre, the first order spatial derivation of adsorbed phase concentration is null, which is a Neumann type boundary condition:

$$r = 0; \quad \frac{\partial q}{\partial r} = 0 \tag{3.45}$$

The external surface of the adsorbent particle is supposed to be in equilibrium with the bulk gas, the concentration distribution is then determined according to the Langmuir isotherm model. Hence, a Dirichlet boundary condition can be used:

$$r = r_p; \quad q_b = f(p_b, T) = q_0 \frac{b(T)p_b}{1 + b(T)p_b} \tag{3.46}$$

and the affinity coefficient b (Pa⁻¹) is related to the temperature according to the following equation:

$$b(T) = b_0 \exp\left(\frac{Q}{RT}\left(1 - \frac{T_0}{T}\right)\right) \tag{3.47}$$

where
- b_0 is Langmuir affinity constant at reference temperature (bar⁻¹)

Initial conditions are set like following:

$$t = 0; \quad q = q_i = 0; \ T = T_i \tag{3.48}$$

3.7.4. Dimensionless forms of the mass and the energy balance equations

The equation system with boundary and initial conditions are changed into a dimensionless one for mathematical simplification. The dimensionless variable of time, distance, concentration and temperatures are defined in Table 3.3 (Do, 1998):

Table 3.3: Dimensionless variables in non-isothermal adsorption equation system.

dimensionless time	$\tau = \dfrac{D_{s0}^0 t}{r_p^{\,2}}$
dimensionless distance	$\eta = \dfrac{r}{r_p}$
dimensionless concentration	$y = \dfrac{q - q_i}{q_b - q_i}$
dimensionless temperature	$\theta = \dfrac{T - T_0}{T_0}$ $\theta_b = \dfrac{T_b - T_0}{T_0}$ $\theta_i = \dfrac{T_i - T_0}{T_0}$

The additional dimensionless parameters are also defined:

$$\varphi(\theta) = \exp\left[\gamma_\mu\left(\frac{\theta}{1+\theta}\right)\right] \tag{3.49}$$

where $\gamma_\mu = E_a/RT_0$.

$$H(y) = \frac{\partial \ln p}{\partial \ln q} = \left\{1 - \left[\frac{\lambda_i}{1+\lambda_i} + \left(\frac{\lambda_b}{1+\lambda_b} - \frac{\lambda_i}{1+\lambda_i}\right)y\right]\right\}^{-1} \tag{3.50}$$

is obtained by introducing Langmuir isotherm, where $\lambda_i = bp_i$ and $\lambda_b = bp_b$.

$$\beta = \frac{Q(q_b - q_i)}{\langle C_p\rangle T_0} \tag{3.51}$$

$$LeBi = \frac{a_H h_f r_p^{\,2}}{\rho D_{s0}^0 \langle C_p\rangle} \tag{3.52}$$

The dimensionless number *LeBi* is related to the heat transfer process and will be further discussed in later section.

The dimensionless system of mass and heat balance equation is then derived.

$$\frac{\partial y}{\partial \tau} = \frac{1}{\eta^2}\frac{\partial}{\partial \eta}\left[\eta^2 \varphi(\theta)H(y)\frac{\partial y}{\partial \eta}\right] \tag{3.53}$$

$$\frac{\partial \theta}{\partial \tau} = \beta \frac{d\langle y \rangle}{d\tau} - LeBi(\theta - \theta_b) \tag{3.54}$$

where for the spherical coordinate system:

$$\langle y \rangle = 3 \int_0^1 \eta^2 y \, d\eta \tag{3.55}$$

The boundary conditions become

$$\eta = 0; \quad \frac{\partial y}{\partial \eta} = 0 \tag{3.56}$$

$$\eta = 1; y = \frac{\dfrac{\lambda_\infty \phi(\theta)}{1 + \lambda_\infty \phi(\theta)} - \dfrac{\lambda_0}{1 + \lambda_0}}{\dfrac{\lambda_\infty}{1 + \lambda_\infty} - \dfrac{\lambda_0}{1 + \lambda_0}} \tag{3.57}$$

where $\lambda_\infty = b_0 p_b$, $\lambda_0 = b_0 p_i$ and

$$\phi(\theta) = \exp\left[-\left(\frac{Q}{RT_0}\right)\left(\frac{\theta}{1+\theta}\right)\right] \tag{3.58}$$

The dimensionless initial condition is:

$$\tau = 0; y = 0, \theta = \theta_i \tag{3.59}$$

Considering the symmetry of adsorbent particle, it is more convenient to rewritten in terms of $u = \eta^2$ where u is defined from 0 to 1 (Villadsen and Michelsen, 1978).

Equation 3.53 is rewritten in the following form:

$$\frac{\partial y}{\partial \tau} = 4\varphi u \frac{\partial H}{\partial u}\frac{\partial y}{\partial u} + 6\varphi H \frac{\partial y}{\partial u} + 4\varphi u H \frac{\partial^2 y}{\partial u^2} \tag{3.60}$$

with the boundary condition:

$$u = 1; \quad y = \frac{\dfrac{\lambda_\infty \phi(\theta)}{1 + \lambda_\infty \phi(\theta)} - \dfrac{\lambda_0}{1 + \lambda_0}}{\dfrac{\lambda_\infty}{1 + \lambda_\infty} - \dfrac{\lambda_0}{1 + \lambda_0}} \tag{3.61}$$

3.7.5. Method for the resolution of the differential equation

The partial differential equation (PDE) system does not have an analytical solution but only a numerical one can be achieved. For spatial differential equation, its resolution can be computed by applying the collocation method. This method is developed by Frazer *et al.* (1937) in order to solve PDE system by reducing the number of dimensions to be able to solve an ordinary differential equation (ODE) system *via* algorithms such as Runge-Kutta method.

In this method, a set of points is chosen within the domain of the variable (*r*) which are called collocation points. In segments separated by collocation points, basis functions are defined, for instance, Lagrange interpolation polynomials (l_i) and the numerical solution of the differential equation is a linear combination of these basis functions. The coefficients of this linear combination

are deduced by minimizing the difference (residual) between exact solution and approximate solution.

Villadsen and Michelsen (1978) found that the residual can be minimized when choosing the collocation points as the zeros of Jacobi polynomial $P_N^{\alpha,\beta}(x)$ where N stands for the order of the polynomial. This polynomial is orthogonal on [-1, 1] and α and β are coefficients defined according to Szegö (1939):

$$\int_{-1}^{1} P_i^{\alpha,\beta}(x)P_j^{\alpha,\beta}(x)(1-x)^{\alpha}x^{\beta}\,dx = \delta_{ij} \tag{3.62}$$

For a spherical adsorption system, $\alpha = 1$ and $\beta = 0.5$ have been proposed by Do (1998) in order to facilitate of mean concentration calculations (Equation 3.55).

In this study, the exact solution of the PDE system is approximated by a sum of basis functions (Lagrange interpolation polynomials).

The zeros of Lagrange interpolation polynomial u_i are located at the roots of Jacobi polynomial of $N+1$ degree $P_{N+1}^{(\alpha,\beta)}(u)$ since it needs to take account of the boundary ($u=1$).

It needs to be noticed that the average dimensionless concentration, $\langle y \rangle$, is expressed by the sum of dimensionless concentration at each collocation points (including the boundary one) times the Radau quadrature weight:

$$\langle y \rangle = \sum_{i=1}^{N} w_i y + w_{N+1}y_{N+1} \tag{3.63}$$

with a vector $\boldsymbol{w} = (w_1, w_2 \dots w_{N+1})^T$ of $N+1$ dimension which is the Radau quadrature weight defined as

$$w_i = \int_0^1 l_i(u)(1-u)^{\alpha}u^{\beta}\,du \tag{3.64}$$

$l_i(u)$ is the Lagrange interpolation polynomial.

Replacing y, the exact solution by a linear combination of Lagrange interpolation polynomials, the equation system becomes to an ODE with dimensionless time variable τ. The resolution of this equation involves the explicit Runge-Kutta method with a moderate accuracy but with rapidness (Ascher and Petzold, 1998; Shampine, 1994).

3.7.6. Parameter sensitivity analysis

A sensitivity analysis was carried out on the two parameters which need to be fitted, namely the dimensionless *LeBi* number, dependent on the heat transfer coefficient, as well as the reference diffusivity D_{s0}^0.

3.7.6.1. *dimensionless number LeBi*

LeBi number has been previously defined in Equation 3.52, and it can be rewritten in the following form:

$$LeBi = \frac{\dfrac{r_p{}^2}{D_{s0}^0}}{\dfrac{\rho\langle C_p\rangle}{a_H h_f}} \tag{3.65}$$

The numerator can be seen as a characteristics time of diffusion. The denominator is the ratio between the specific heat of the adsorbent and the heat dissipation at the particle surface. So the *LeBi* number describes the competition between both the mass and the heat diffusion rates.

In order to test the sensibility of *LeBi* number, other parameters are set and presented in Table 3.4:

Table 3.4: Parameter setting for the test of the sensibility of LeBi number.

radius of particle r_p/(m)	1×10^{-6}
initial gas pressure p_i/(bar)	0
bulk gas pressure p_b/(bar)	5
initial temperature T_i/(K)	77
bulk gas temperature T_b/(K)	77
reference temperature T_0/(K)	77
Langmuir affinity at reference temperature b_0/(bar^{-1})	0.3
maximum adsorption concentration q_0/(mol.kg^{-1})	25
diffusivity at reference temperature D_{s0}^0/(m^2.s^{-1})	5×10^{-12}
heat of adsorption Q/(J.mol^{-1})	4000
activation energy E_a/(J.mol^{-1})	2000
heat capacity $\langle C_p\rangle$/(J.K^{-1}.kg^{-1})	1000
bulk density of adsorbent particle ρ/(kg.m^{-3})	200

The radius of the particle is set here for sensibility test which does not correspond to a certain test material. The heat capacity of MIL-101(Cr) is unknown. However, it is known that specific heat capacity is related to lattice dynamic properties. MOFs have similar structures and they are very close to zeolites. The specific heat of MOFs such as MOF-5, Cu-BTC, MOF-177, *etc.* are reported (Kloutse et al., 2015; Mu and Walton, 2011) and the specific heat for zeolites are also reported (Hemingway and Robie, 1984), it is reasonable to use a specific heat 1000 J.K^{-1}.kg^{-1} with the same magnitude with other MOFs and zeolites.

The variation in the hydrogen fractional uptakes and adsorbent sample temperatures simulated by the non-isothermal adsorption model described above are shown in Figure 3.12, with *LeBi* number varying from 1 to 10.
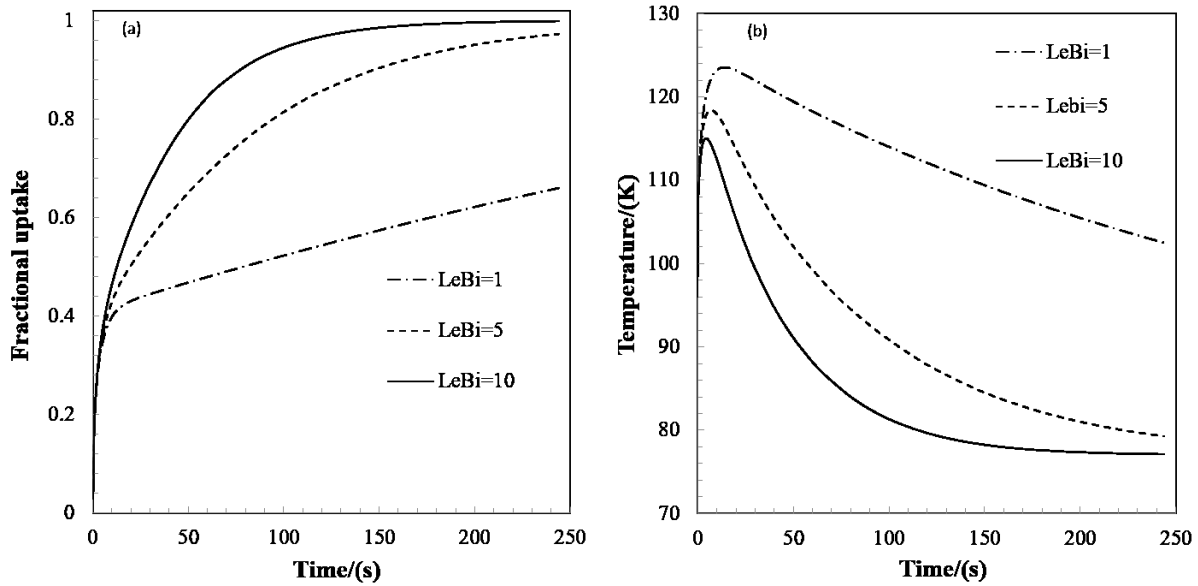
Figure 3.12: Comparison of the effect of the LeBi number on the adsorption kinetics (a) fractional uptake and (b) temperature profiles.

As shown in Figure 3.12 (a), the fractional uptake profile can be divided into two stages. During the first stage, as the fractional uptake is below 0.4, the uptake rate is very high and is marked by a rapid increase of fractional uptake as well as a temperature increase due to the adsorption exothermicity (Figure 3.12 (b)). At this stage, the temperature increase promotes the diffusion. In the second stage, the adsorption rate progressively slows down as equilibrium conditions are approached and the temperature then decreases. The higher the *LeBi* number, the faster the heat dissipation rate and so the temperature drop. At this stage, the temperature drop promotes the uptake capacity of the adsorbent according to temperature dependent isotherm models. Hence, a system with high *LeBi* number can first arrive at adsorption equilibrium.

3.7.6.2. Diffusivity D_{s0}^0

The reference diffusivity D_{s0}^0 determines the adsorption kinetics. Accounting for the influence of the temperature variations, it is interesting to test different scales of diffusivity as well. Excepted D_{s0}^0, which was varied from 10^{-12} to 10^{-8} $m^2.s^{-1}$, all the other model parameters were unchanged, whereas the dimensionless number *LeBi* was set to 10. The simulation results are shown in Figure 3.13.
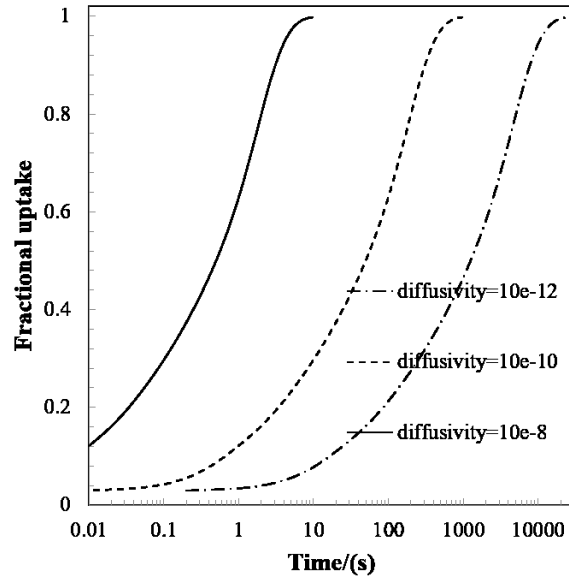
Figure 3.13: Adsorption kinetics simulated with different diffusivities vary from 10^{-12} $m^2.s^{-1}$ to 10^{-8} $m^2.s^{-1}$

By changing the diffusivity, the time scale for the accomplishment of adsorption varies logarithmically and the forms of the curves are not greatly changed.

3.7.7. Model parameter fitting and simulation results

The optimization of the parameters such as the dimensionless *LeBi* number and the reference diffusivity D_{s0}^0 are performed by minimizing the residuals between both the experimental and theoretical curves representative to the fractional uptake profile. The method of the least squares is applied for that purpose. The set of variables which are considered as known and so initially fixed is specified in Table 3.5.

Table 3.5: Parameter settings for non-isothermal adsorption kinetics modelling.

	AC-MIL-101(Cr)-b	MIL-101(Cr)-a	MIL-101(Cr)-b
radius of particle r_p/(nm)	60	120	50
initial gas pressure p_i/(bar)	0	0	0
bulk gas pressure p_b/(bar)	0.2/0.5/1/5	0.2/0.5/1/5	0.2/0.5/1/5
initial temperature T_i/(K)	77	77	77
bulk gas temperature T_b/(K)	77	77	77
reference temperature T_0/(K)	77	77	77
Langmuir affinity at reference temperature b_0/(bar^{-1})	0.028	0.096	0.107
maximum adsorption concentration q_0/(mol.kg^{-1})	85.6	43,1	41.0
heat of adsorption Q/(kJ.mol^{-1})	4	4	4
activation energy E_a/(kJ.mol^{-1})	2	2	2
heat capacity $\langle C_p \rangle$/(J.K^{-1}.kg^{-1})	1000	1000	1000
bulk density ρ/(kg.m^{-3})	190	200	190

It needs to be mentioned that the heat of adsorption is set to 4 kJ.mol^{-1} as this value is fixed during adsorption isotherm measurements according to Schmitz (2008).The activation energy E_a is set to be half of the heat of adsorption (Delage et al., 2000; Giraudet et al., 2009).

From Figure 3.14 to Figure 3.17, the theoretical and experimental fractional uptake and temperature as a function of time, as well as the computed radial profile of the adsorbed amount within the spherical particle at collocation points are presented.

Figure 3.14: Adsorption kinetics: experimental results (black cube) and numerical modelling results (black line) for AC-MIL-101(Cr)-b (a), MIL-101(Cr)-a (b) and MIL-101(Cr)-b (c) respectively. Experiments are carried out at 0.2 bar. From left to right are adsorption kinetics profile (a₁, b₁, c₁), temperature profile (a₂, b₂, c₂) and adsorption kinetics profile modelled at different colocation points (a₃, b₃, c₃), respectively.

165

Figure 3.15: Adsorption kinetics: experimental results (black cube) and numerical modelling results (black line) for AC-MIL-101(Cr)-b (a), MIL-101(Cr)-a (b) and MIL-101(Cr)-b (c) respectively. Experiments are carried out at 0.5 bar. From left to right are adsorption kinetics profile (a_1, b_1, c_1), temperature profile (a_2, b_2, c_2) and adsorption kinetics profile modelled at different colocation points (a_3, b_3, c_3), respectively.

Figure 3.16: Adsorption kinetics: experimental results (black cube) and numerical modelling results (black line) for AC-MIL-101(Cr)-b (a), MIL-101(Cr)-a (b) and MIL-101(Cr)-b (c) respectively. Experiments are carried out at 1 bar. From left to right are adsorption kinetics profile (a_1, b_1, c_1), temperature profile (a_2, b_2, c_2) and adsorption kinetics profile modelled at different colocation points (a_3, b_3, c_3), respectively.

Figure 3.17: Adsorption kinetics: experimental results (black cube) and numerical modelling results (black line) for AC-MIL-101(Cr)-b (a), MIL-101(Cr)-a (b) and MIL-101(Cr)-b (c) respectively. Experiments are carried out at 5 bar. From left to right are adsorption kinetics profile (a₁, b₁, c₁), temperature profile (a₂, b₂, c₂) and adsorption kinetics profile modelled at different colocation points (a₃, b₃, c₃), respectively.

From Figure 3.14 to Figure 3.17, it can be observed that the theoretical uptake profiles match quite well the experimental data, with a better agreement at the highest tested equilibrium pressure, compared to LDF model.

The mismatch observed at the lowest pressure range between experimental and computed uptake profiles may be attributed to the influence of the external surface diffusion resistance which may be actually non negligible when the gas velocity during the sample cell filling is not so fast.

The influence of temperature on adsorptions can be observed from uptake curves, especially the ones describing uptakes at collocation points. In fact, the boundary condition implies at the surface of the adsorbent that the equilibrium is reached spontaneously and the adsorbed quantity at the surface is computed by Langmuir isotherm model. As temperature increases, the Langmuir affinity varies according to an Arrhenius relation. Hence, it can be observed that the concentration at the surface decreases while temperature increases and it returns to the initial value when the temperature drops to the initial temperature. Meanwhile, some deviations are also noted in the temperature profiles, which are significant at 1 and 5 bar. The model then over-estimates the temperature rise caused by adsorption exothermicity. Several explanations can be advanced for these deviations: either the accumulation of heat in the adsorbent has been over-estimated because the computed heat transfer coefficient is too low or the assumed heat of adsorption Q is too high. It has also to be noted that the variation of heat transfer coefficient is not taken into consideration. At the beginning of the experiments, the gas expansion from the reservoir with high velocity will result in forced convection of heat which will further enhance the heat transfer coefficient. Meanwhile, the variation of the heat of adsorption Q with the progressive adsorbent surface coverage is not taken into consideration. Another reason that may explain the overestimation of the temperature rising is related to the estimation of the average adsorbent specific heat capacity considered as constant in the model, but which possibly increases with the adsorbed phase concentration. Finally, it has to be reminded that the temperature is actually measured at the contact of the external wall of the sample cell, and not directly within the material. So that dissipated heat in the sample cell wall may also justify the over-estimation of the temperature rise by this model.

The parameters derived from the non-isothermal adsorption model fitting are reported in Table 3.6.

Table 3.6: Optimal parameters found by fitting the simulation results obtained via the non-isothermal adsorption model with experimental data: LeBi number and reference diffusivity D_{s0}^0.

Parameter	Dimensionless number *LeBi*				Reference diffusivity D_{s0}^0/ $(10^{-17} \text{ m}^2.\text{s}^{-1})$			
Equilibrium pressure /(bar)	0.2	0.5	1	5	0.2	0.5	1	5
MIL-101(Cr)-a	3.0	6.2	2.5	2.0	2.1	4.5	7.7	7.4
MIL-101(Cr)-b	2.2	3.5	3.6	1.9	0.4	0.8	1.4	1.4
AC-MIL-101(Cr)-b	3.3	6.0	3.6	1.8	0.7	1.3	1.9	2.0

By using *LeBi* number, heat transfer coefficients can be further computed and they are in a magnitude of 10^{-2} W.m^{-2}.K^{-1} which are still low compared to heat transfer coefficient of air in free

convection condition. This might imply that the heat transfer is under-estimated during the simulation.

The reference diffusivity data reported for the MIL-101(Cr) type material are in the range $[10^{-17}\text{-}10^{-16}]$ m^2.s^{-1}. The values tend to increase with the pressure, but variations become very small in the highest tested pressure range, *i.e.* between 1 and 5 bar, when the data are also more confident.

In order to improve the model, it appears that external diffusion resistance should be taken into consideration at low pressure. Moreover, a more detailed energy balance accounting for the contribution of the sample cell and of the adsorbed phase on heat dissipation should be used. In order to overcome the difficulties met to compute correctly the temperature profile, another modelling approach is followed, relying on the imposed temperature conditions.

3.8. Imposed temperature adsorption model

According to this model, the adsorbent temperature profiles are no longer calculated, but experimental data are used in order to take into account the thermal effect on the diffusion rates. Moreover, an additional external diffusion resistance is taken into consideration in order to resolve the problem of diffusion at low pressure.

3.8.1. Model assumptions

The assumptions are the same as the ones described previously in the non-isothermal adsorption model in Section 3.7, except that the mass transfer process is then not only dominated by surface diffusion, but also limited by a gas film resistance at the external surface of the particle k_{ex} (m.s^{-1}), which is presented in Section 3.2.1.

3.8.2. Temperature data fitting

The experimental temperature profile is fitted by a skew Gaussian-type function as it results in the best fit of the experimental temperature data, involving the adjustment of 4 parameters (a_0, b_0, c_0, d_0):

$$T = a_0 + b_0\exp\left(-0.5\left(\ln\left(\frac{t}{c_0}\right)\frac{1}{d_0}\right)^2\right) \tag{3.66}$$

3.8.3. Mass conservation equation

The mass balance equation to solve to describe the radial distribution of the adsorbed hydrogen concentration within the internal volume of the adsorbent particle remains unchanged (Equation 3.41), but the boundary condition at the particle surface ($r=r_p$) is modified in order to account for the gas film transfer resistance.

$$r = r_p; \quad q_b = q_0\frac{b(T)p_b}{1 + b(T)p_b}\left(1 - \exp\left(-\frac{k_{ex}}{d_p}t\right)\right) \tag{3.67}$$

The boundary condition at the particle centre (r=0) is unchanged, and the initial conditions also remain the same.

3.8.4. Simulation results

The set of variables used to compute the uptake curves is given in Table 4.6. Both the external mass transfer coefficient k_{ex} and the reference diffusivity D_{s0}^0 are considered as parameters to be fitted in order to minimize the residuals between experimental and computed uptake curves. The simulation results are presented in Figure 3.18 to Figure 3.21.
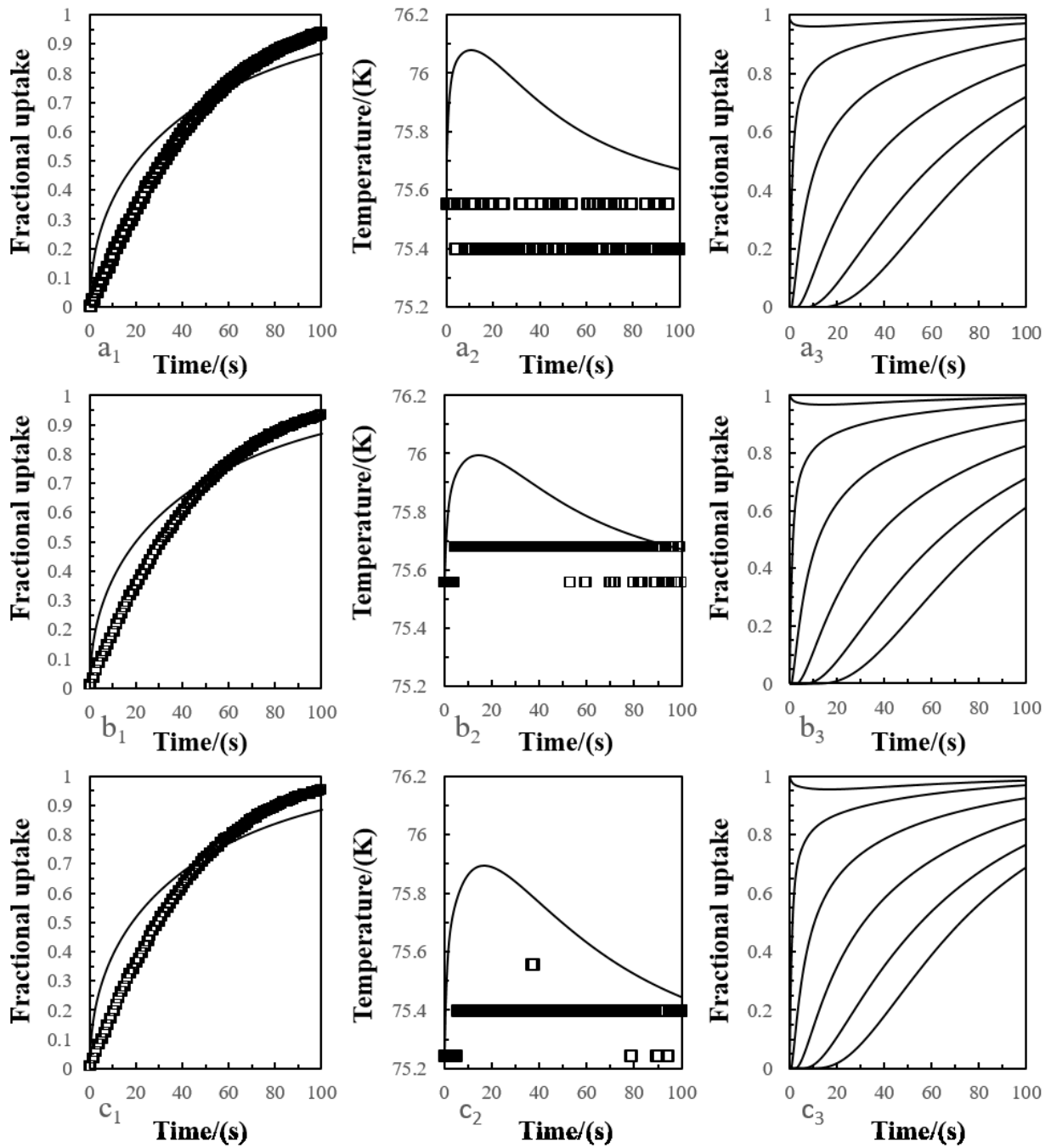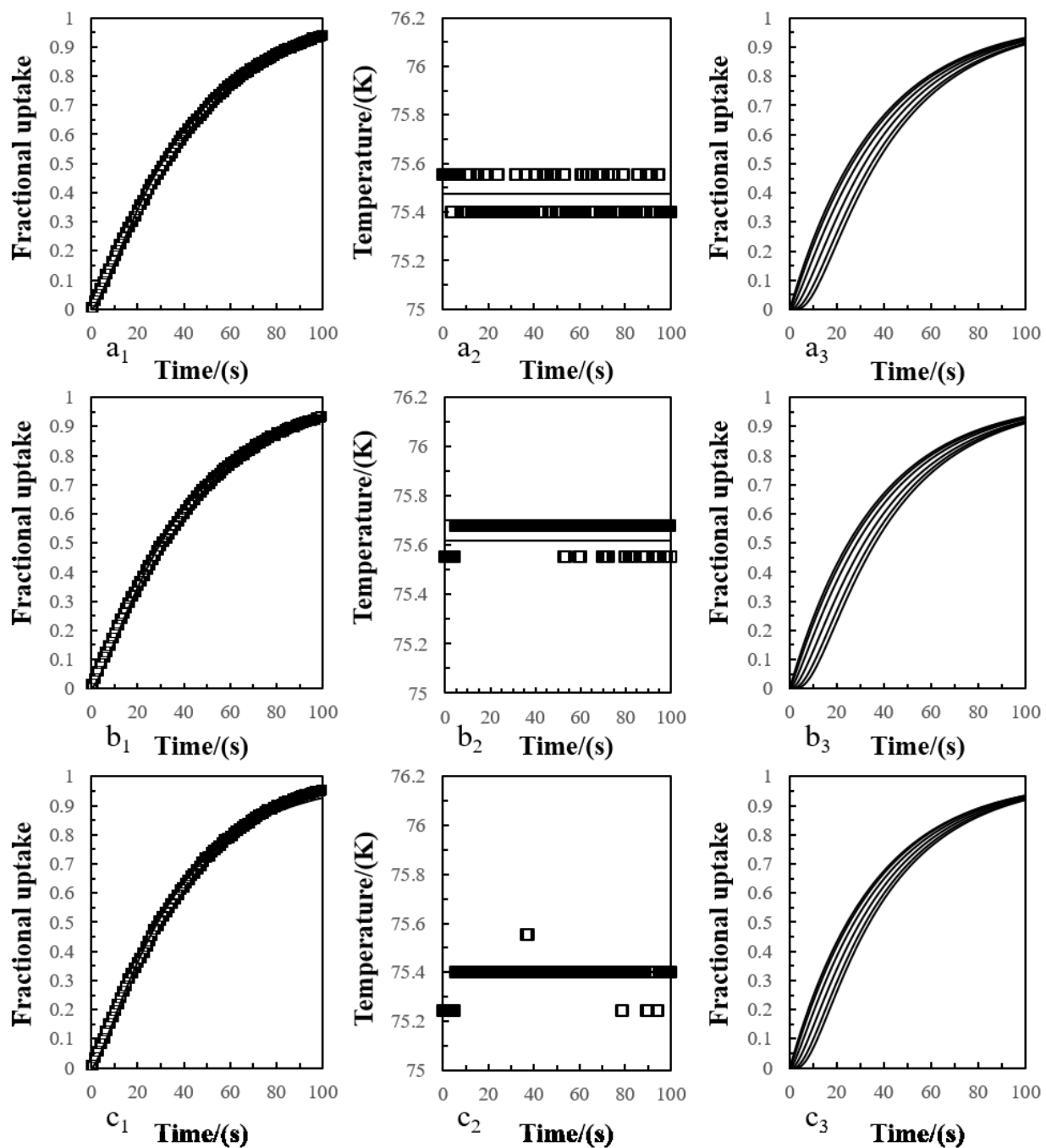
Figure 3.18: Adsorption kinetics: experimental results (black cube) and numerical modelling results (black line) for AC-MIL-101(Cr)-b (a), MIL-101(Cr)-a (b) and MIL-101(Cr)-b (c) respectively. Experiments are carried out at 0.2 bar. From left to right are adsorption kinetics profile (a_1, b_1, c_1), temperature profile (a_2, b_2, c_2) and adsorption kinetics profile modelled at different colocation points (a_3, b_3, c_3), respectively.
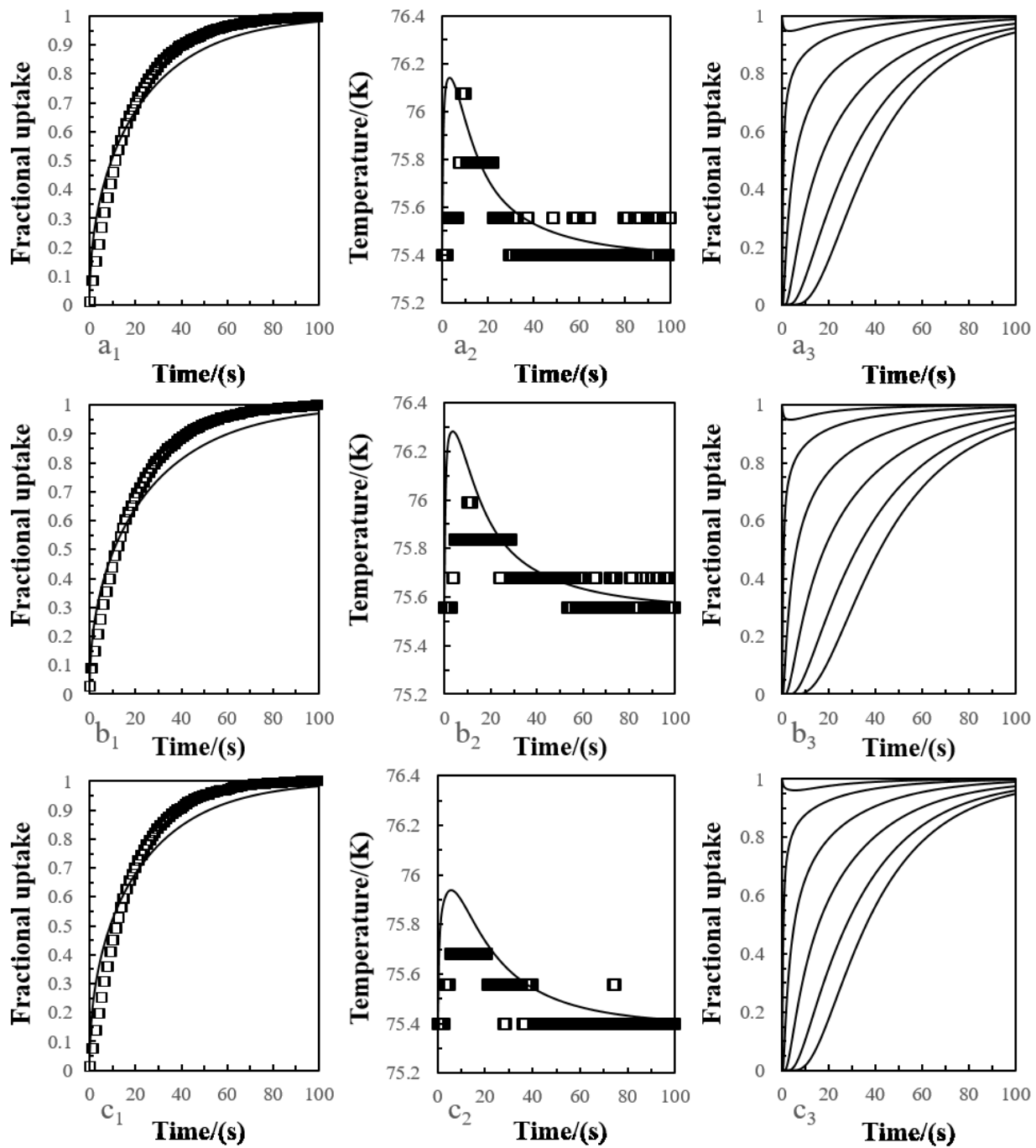
Figure 3.19: Adsorption kinetics: experimental results (black cube) and numerical modelling results (black line) for AC-MIL-101(Cr)-b (a), MIL-101(Cr)-a (b) and MIL-101(Cr)-b (c) respectively. Experiments are carried out at 0.5 bar. From left to right are adsorption kinetics profile (a₁, b₁, c₁), temperature profile (a₂, b₂, c₂) and adsorption kinetics profile modelled at different colocation points (a₃, b₃, c₃), respectively.
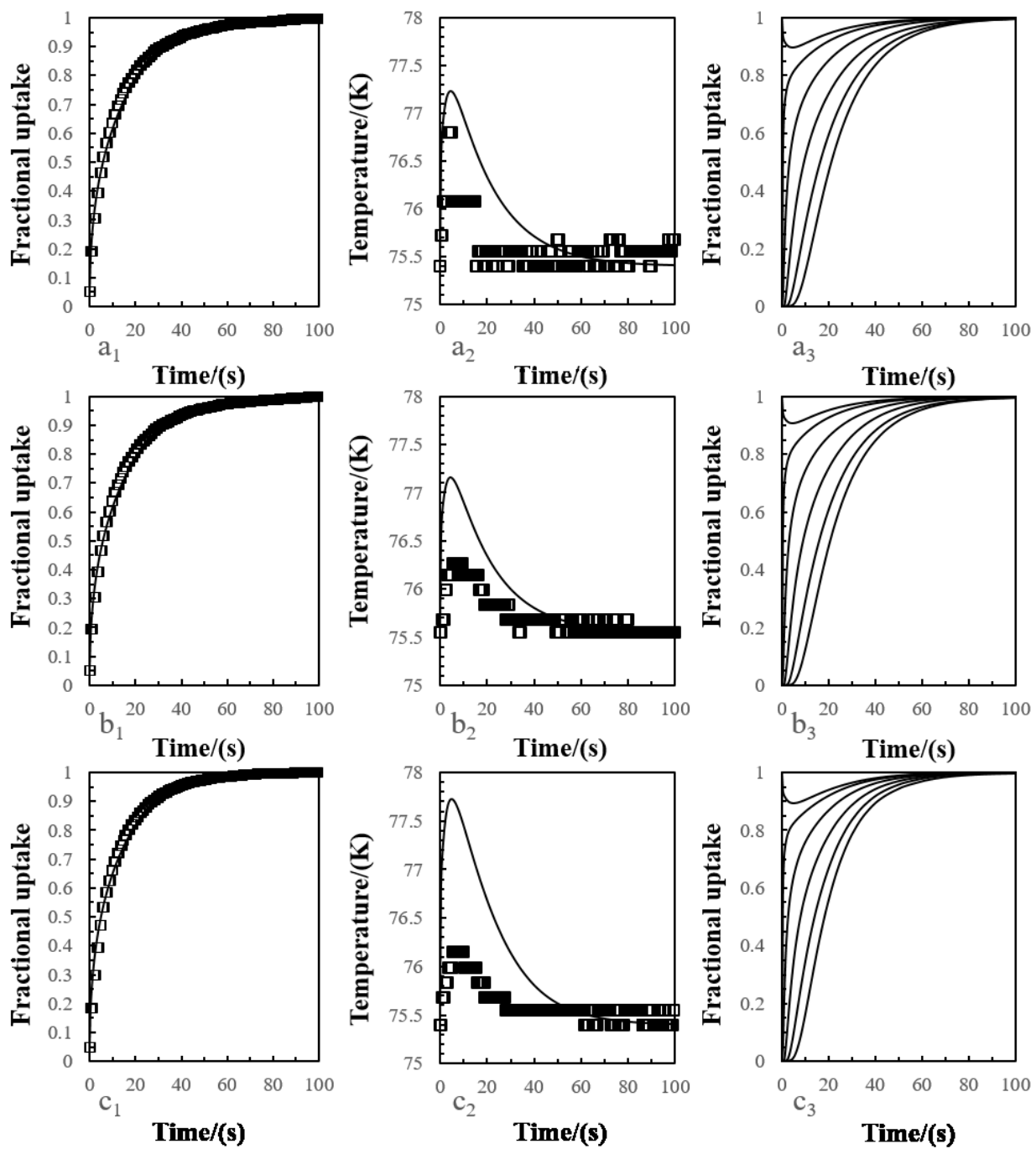
173

Figure 3.19: Adsorption kinetics: experimental results (black cube) and numerical modelling results (black line) for AC-MIL-101(Cr)-b (a), MIL-101(Cr)-a (b) and MIL-101(Cr)-b (c) respectively. Experiments are carried out at 0.5 bar. From left to right are adsorption kinetics profile (a_1, b_1, c_1), temperature profile (a_2, b_2, c_2) and adsorption kinetics profile modelled at different colocation points (a_3, b_3, c_3), respectively.
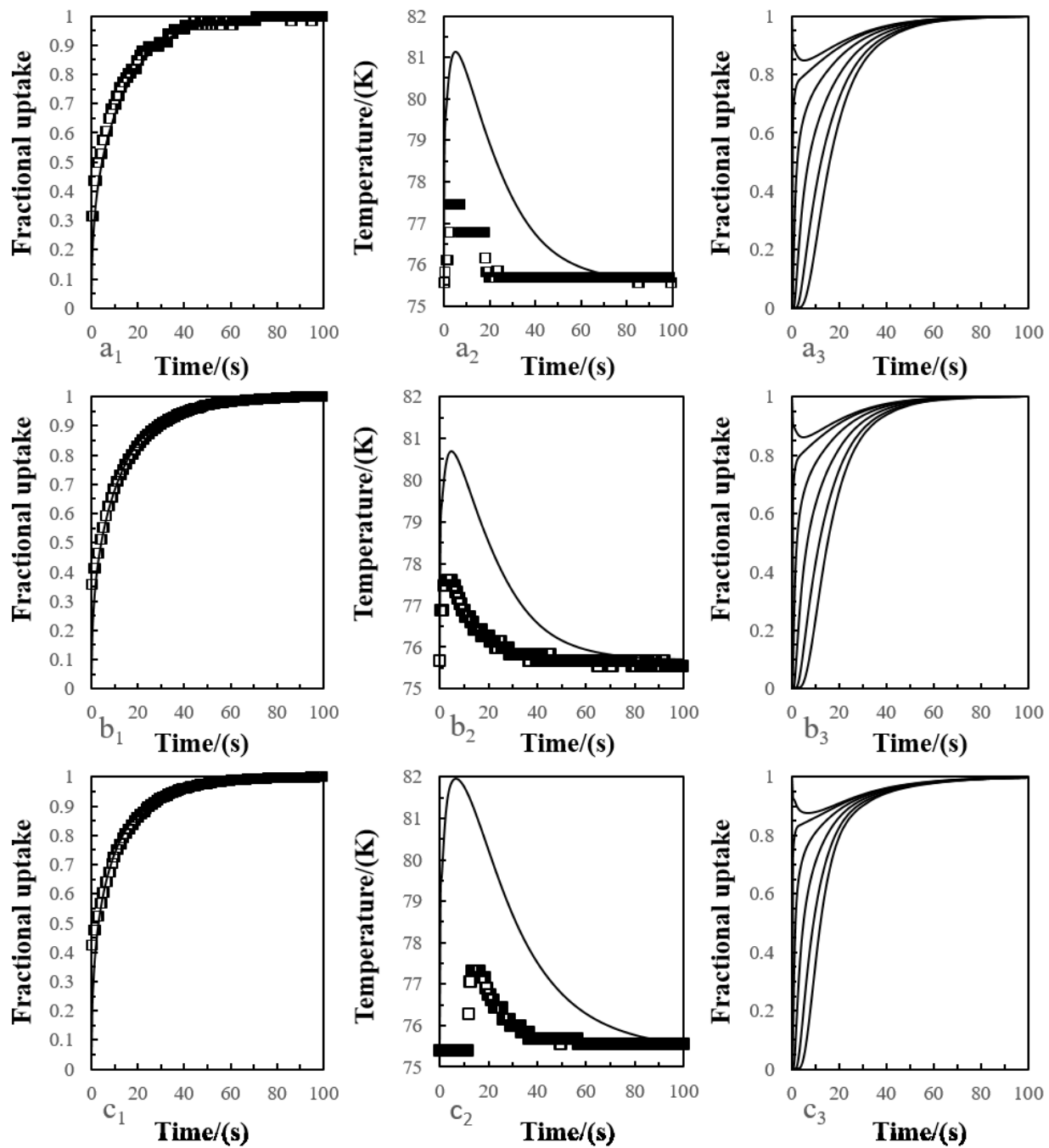
173

Figure 3.20: Adsorption kinetics: experimental results (black cube) and numerical modelling results (black line) for AC-MIL-101(Cr)-b (a), MIL-101(Cr)-a (b) and MIL-101(Cr)-b (c) respectively. Experiments are carried out at 1 bar. From left to right are adsorption kinetics profile (a₁, b₁, c₁), temperature profile (a₂, b₂, c₂) and adsorption kinetics profile modelled at different colocation points (a₃, b₃, c₃), respectively..

Figure 3.21: Adsorption kinetics: experimental results (black cube) and numerical modelling results (black line) for AC-MIL-101(Cr)-b (a), MIL-101(Cr)-a (b) and MIL-101(Cr)-b (c) respectively. Experiments are carried out at 5 bar. From left to right are adsorption kinetics profile (a$_1$, b$_1$, c$_1$), temperature profile (a$_2$, b$_2$, c$_2$) and adsorption kinetics profile modelled at different colocation points (a$_3$, b$_3$, c$_3$), respectively.

According to the imposed temperature model, the agreement obtained with the experimental curves is very good and notably improved compared with the non-isothermal adsorption model.

The values of both the two parameters, *i.e.* external mass transfer coefficient k_{ex} and reference diffusivity D_{s0}^0 fitted with the imposed temperature adsorption model are reported in Table 3.7 and Table 3.8, respectively.

Table 3.7: External mass transfer coefficients determined by the imposed temperature adsorption model.

Parameter	External mass transfer coefficient k_{ex} /(10^{-10} m.s^{-1})			
Equilibrium pressure/(bar)	0.2	0.5	1	5
MIL-101(Cr)-a	0.2	0.5	1.2	3.5
MIL-101(Cr)-b	0.4	1.2	5.9	10.8
AC-MIL-101(Cr)-b	0.3	1.1	3.8	8.1
Mean	0.3	0.9	3.7	7.4
Standard deviation	0.1	0.4	2.6	3.7

Table 3.8: Reference diffusivity data determined by the imposed temperature adsorption model

Parameter	Reference diffusivity D_{s0}^0 /(10^{-16} m^2.s^{-1})					
Equilibrium pressure/(bar)	0.2	0.5	1	5	Mean	Standard deviation
MIL-101(Cr)-a	1.51	1.54	1.6	1.62	1.57	0.05
MIL-101(Cr)-b	0.29	0.32	0.31	0.30	0.31	0.01
AC-MIL-101(Cr)-b	0.42	0.46	0.44	0.42	0.44	0.02

It can be observed from Figure 3.18 which shows the hydrogen kinetics uptake at low pressure (0.2 bar) that the differences between adsorbed concentration in different collocation points are small. This means that under this pressure, the diffusion process is governed by external mass transfer. The computed data for the external mass transfer coefficient k_{ex} vary from a material to another, and globally increase with pressure. According to the correlation of Petrovic and Thodos (1968), k_{ex} is proportional to $Re^{0.64}$ (see Table 3.1), so should increase with the gas velocity. The gas velocity effect well explains the influence of the setting equilibrium pressure on the external mass transfer coefficient increase. Moreover, k_{ex} is not dependent on the nature of the adsorbent but on the particle size, being proportional d_p^{-1}. Hence, k_{ex} for MIL-101(Cr)-a shows the largest particle size is the smallest among all three samples. k_{ex} for MIL-101(Cr)-b is the largest because the particle size of MIL-101(Cr)-b is the smallest.

Regarding the reference diffusivity data D_{s0}^0 reported in Table 3.8, a very good reproducibility (small standard deviations) is observed for all the adsorbent materials, confirming the non-dependence of this data with the setting pressure, as previously presented in Darken's surface diffusion model (see Section 3.2.2.4).

3.9. Hydrogen kinetics comparison

The kinetic performance of hydrogen diffusion in MIL-101(Cr), activated carbon incorporated MIL-101(Cr) and MOF-5 are compared to that of other materials studied in literature, *i.e.* MOFs

(Bimbo et al., 2015; Férey et al., 2003; Saha et al., 2009, 2008), activated carbon, zeolites (Lopes et al., 2009) and graphite (Purewal et al., 2012).

In order to compare hydrogen kinetic performance with other adsorbents of different particle size, or even for adsorbent that sometimes the particle size is hard to define, diffusion coefficient D_{s0}^0/r_p^2 (s^{-1}) is more convenient to be used. The calculated diffusion coefficients D_{s0}^0/r_p^2 in this work are presented and compared in Table 3.9.

Table 3.9: Diffusion coefficients D_{s0}^0/r_p^2 obtained for the studied adsorbents compared with the diffusion coefficients of different adsorbents from the literature.

Adsorbent	Experimental condition	Diffusion coefficient D_{s0}^0/r_p^2 /(s^{-1})	Reference
MIL-101(Cr)-a	0.2 bar, 77 K, LDF model	1.59×10^{-3}	This work
	0.2 bar, 77 K, non-isothermal model	1.46×10^{-3}	
	0.2 bar, 77 K, imposed temperature model	1.05×10^{-2}	
	0.5 bar, 77 K, LDF model	4.24×10^{-3}	
	0.5 bar, 77 K, non-isothermal model	3.13×10^{-3}	
	0.5 bar, 77 K, imposed temperature model	1.07×10^{-2}	
	1 bar, 77 K, non-isothermal model	5.35×10^{-3}	
	1 bar, 77 K, imposed temperature model	1.11×10^{-2}	
	5 bar, 77 K, non-isothermal model	5.14×10^{-3}	
	5 bar, 77 K, imposed temperature model	1.13×10^{-2}	
MIL-101(Cr)-b	0.2 bar, 77 K, LDF model	1.69×10^{-3}	
	0.2 bar, 77 K, non-isothermal model	1.67×10^{-3}	
	0.2 bar, 77 K, imposed temperature model	1.17×10^{-2}	
	0.5 bar, 77 K, LDF model	4.17×10^{-3}	
	0.5 bar, 77 K, non-isothermal model	3.33×10^{-3}	
	0.5 bar, 77 K, imposed temperature model	1.28×10^{-2}	
	1 bar, 77 K, non-isothermal model	5.56×10^{-3}	
	1 bar, 77 K, imposed temperature model	1.22×10^{-2}	
	5 bar, 77 K, non-isothermal model	5.83×10^{-3}	
	5 bar, 77 K, imposed temperature model	1.17×10^{-2}	
AC-MIL-101(Cr)-b	0.2 bar, 77 K, LDF model	1.72×10^{-3}	
	0.2 bar, 77 K, non-isothermal model	1.88×10^{-3}	
	0.2 bar, 77 K, imposed temperature model	1.25×10^{-2}	
	0.5 bar, 77 K, LDF model	4.22×10^{-3}	
	0.5 bar, 77 K, non-isothermal model	3.13×10^{-3}	
	0.5 bar, 77 K, imposed temperature model	1.20×10^{-2}	
	1 bar, 77 K, non-isothermal model	5.31×10^{-3}	
	1 bar, 77 K, imposed temperature model	1.18×10^{-2}	
	5 bar, 77 K, non-isothermal model	5.31×10^{-3}	
	5 bar, 77 K, imposed temperature model	1.16×10^{-2}	
MOF-5	0.2 bar, 77 K, LDF model	6.25×10^{-3}	
	0.5 bar, 77 K, LDF model	1.18×10^{-2}	

Adsorbent	Experimental condition	Diffusion coefficient D_{s0}^0/r_p^2 /(s^{-1})	Reference
MIL-101(Cr)	Up to 20 bar, 77 K	9.11×10^{-2}	(Bimbo et al., 2015)
	Up to 20 bar, 90 K	1.68×10^{-1}	
MOF-5	Up to 1 bar, 77 K	1.07×10^{-1}	(Saha et al., 2009)
	Up to 1 bar, 194.5 K	2.30×10^{-1}	
	Up to 1 bar, 298 K	2.67×10^{-1}	
MOF-177	0.38 bar, 77 K	8.91×10^{-2}	(Saha et al., 2008)
	0.65 bar, 77 K	9.61×10^{-2}	
	1 bar, 77 K	1.03×10^{-1}	
	Up to 1 bar, 194.5 K	2.14×10^{-1}	
	Up to 1 bar, 298 K	3.02×10^{-1}	
MIL-53(Cr)	15 bar, 77 K	$\sim 1.67 \times 10^{-2}$	(Férey et al., 2003)
Zeolite (extrudate)	1 bar, 303 K	9.32×10^{-2}	(Lopes et al., 2009)
	1 bar, 323 K	1.20×10^{-1}	
	1 bar, 343 K	1.60×10^{-1}	
Activated carbon (extrudate)	1 bar, 303 K	2.31×10^{-1}	
	1 bar, 323 K	3.17×10^{-1}	
	1 bar, 343 K	3.73×10^{-1}	
Graphite (potassium intercalated)	77 K	$\sim 1.38 \times 10^{-3}$	(Purewal et al., 2012)

For the purpose of comparing hydrogen kinetic uptake performance with hydrides, it is helpful to use the time required to reach equilibrium. This comparison is presented in Table 3.10.

Table 3.10: Hydrogen uptake kinetics compared with hydrides.

Material	Condition	Kinetics/(min)	Reference
MIL-101(Cr)-a	5 bar, 77 K	~1	This work
MIL-101(Cr)-b	5 bar, 77 K	~1	
AC-MIL-101(Cr)-b	5 bar, 77 K	~1	
MgH_2-5 mol% Fe_2O_3	2-15 bar, 573 K	20	(Jung et al., 2006)
MgH_2-5 mol% V_2O_3	15 bar, 523 K	1.6	
Mg-10 wt% CeO_2	11 bar, 573 K	60	(Song et al., 2002)
Mg-50 wt% $LaNi_5$	10-15 bar, 623-673 K	3.33	(Liang et al., 1998)
Mg-0.5 wt% Nb_2O_5	8,4 bar, 573 K	1	(Barkhordarian et al., 2004)
Mg_2Ni	1-15 bar, 553-603 K	1	(Shang and Guo, 2004)
Na_3AlH_6	1 bar, 473 K	150	(Zaluski et al., 1999)
$NaAlH_4$-2 mol% Ti	20-120 bar, 298-433 K	300-720	(Sun et al., 2003)
$NaAlH_4$-2 mol% $TiCl_3$	83-91 bar, 373-393 K	20	(Sandrock et al., 2002)
Li_2NH	7 bar, 373-403 K	10	(Hu and Ruckenstein, 2006)
$Li_3BN_2H_8$	1 bar, 523-641 K	228	(Pinkerton et al., 2005)
$LiBH_4$-0.5MgH_2-2 mol% $TiCl_3$	4.5-19 bar, 588-723 K	240	(Vajo et al., 2005)
$La_{1.8}Ca_{0.2}Mg_{14}N_{13}$	40 bar, 300-600 K	15	(Gao et al., 2005)
$La_{0.5}Ni_{1.5}Mg_{17}$	2.21-11.34 bar, 553-673 K	15	(Li et al., 2006)

From Table 3.9, it can be observed that the kinetic performance of hydrogen adsorption in different MIL-101(Cr) or AC doped MIL-101(Cr) adsorbents have relatively the same magnitude, which might imply that the hydrogen diffusion in these adsorbents does not correlate to the adsorbent particle size. Relative slow hydrogen kinetic properties of MIL-101(Cr) as well as AC doped MIL-101(Cr) are shown and compared with other MOFs at 77 K. The activated carbon doping does not affect as much as can be observed in the diffusion coefficient. Meanwhile, it is shown that the hydrogen kinetic uptake time to reach equilibrium in these materials are *ca* 1 minute, which achieves the ultimate DOE requirements.

Compared to hydrogen storage by chemical method (hydrides), which requires a longer time (several minutes to hours) (see Table 3.10), hydrogen storage by adsorption in porous materials is advantageous in its kinetic property.

3.10. Conclusion

Hydrogen adsorption kinetics were studied by using volumetric method for pristine MIL-101(Cr) and activated carbon doped MIL-101(Cr) as well as MOF-5 samples. The adsorption process in MIL-101(Cr) and AC doped MIL-101(Cr) can be completed within 2 minutes at 77K up to 5 bar while in MOF-5 the time required to complete adsorption is less than 40 seconds at 77 K up to 5 bar. The experimental results were firstly interpreted by using the LDF model for the purpose of hydrogen diffusivity calculation. However, it failed to give a satisfactory interpretation of hydrogen diffusion in porous adsorbents at high pressure and it was only applicable at 0.2 and 0.5 bar. The numerical resolution of the diffusion equation in a non-isothermal condition appeared to be another approach method. The results given by numerical modelling using non-isothermal condition were more satisfactory than LDF model and the diffusivities of hydrogen within different samples were in the magnitude of 10^{-16} $m^2.s^{-1}$. The results showed also that the diffusivity increases as a function of the applied pressure. Considering that the calculated uptakes did not correspond to the low pressure kinetic data, and the temperature profile curves calculated in the case of non-isothermal conditions over-estimated the effect of exothermicity of the adsorption process, an imposed temperature adsorption model was then proposed. In this model, an external resistance was applied and the temperature used during adsorption was the temperature experimentally measured. The results showed that the diffusion process of hydrogen in MIL-101(Cr) and AC doped MIL-101(Cr) can be accomplished within ~1 minute at 5 bar. This time, requirement fulfils the ultimate DOE target for hydrogen storage for mobile usage.

General conclusion and Perspectives

General conclusion and Perspectives

Hydrogen was proved to be a good candidate for future energy carrier. Its production, distribution and utilization are well developed while its storage remains challenging, especially for on-board usages. Different hydrogen storage methods were discussed and compared and it has been concluded that storage by adsorption in a Metal Organic Framework (MOF) type material could be promising.

This work concentrates the development of carbon-MOF composite for hydrogen storage and the study of the adsorbents' properties for future system scaling-up.

MOF type MIL-101(Cr) and Activated Carbon (AC) doped MIL-101(Cr) materials were synthesized using the hydrothermal method. Several mineralizing agents (hydrofluoric acid (HF), acetic acid (CH_3COOH) and sodium acetate (CH_3COONa)) and different heating methods (conventional oven and microwave) have been tested. For carbon-MOF composite synthesis, different concentrations of activated carbon (AC) from 2 to 10 wt% of the final yielded product were tested. The resulted as-synthesized products, MIL-101(Cr) and AC doped MIL-101(Cr) were washed with ethanol, dimethylformamide (DMF) or NH_4F solution to remove unreacted reactants from the pores of the framework. The synthesized products were characterized by using powder X-ray diffraction (PXRD), scanning electron microscopy (SEM), thermogravimetric analysis (TGA) and nitrogen (N_2) adsorption at 77 K techniques. It was found that MIL-101(Cr) synthesized by using acetic acid and conventional heating method exhibits high crystallinity compared to other synthesized products. Moreover, the crystal size is also influenced by the mineralizing agent effect and the concentration of doping agent positively affects the porosity of synthesized composites from 2 to 5 wt%. The microwave-assisted syntheses did not produce high-quality materials in terms of crystallinity and porosity.

The pore size distributions (PSDs) of different samples were analysed either by applying Barret-Joyner-Halenda (BJH) method or non-localized density functional theory (NLDFT) methods. The BJH method uses Kelvin equation to calculate the radius of the capillary which is directly used or corrected by using Faas and Kruk-Jaroniec-Sayari (KJS) corrections. Different adsorbate thickness equations were applied such as Harkins and Jura equation, Halsey equation, KJS equation and Broekhoff de Boer (BdB) equation. The results of analyses showed that in BJH method, the KJS correction and the KJS equation for adsorbate thickness calculation seems to correctly compute the pore size distribution In NLDFT method, a kernel developed by Tarazona was chosen and the latter provide the best fit of adsorption isotherm curve and a PSD close to theoretical one as well. A smaller pore size of 10 Å which can be attributed to the Super Tetrahedron structure (with 8.6 Å opening) was found in the framework. The total pore volumes of synthesized products were measured either by applying the Gurvich rule or by the integration of BJH PSD. It is interesting to observe that the doped MIL-101(Cr) show higher porosity than non-doped MIL-101(Cr) sample.

The hydrogen uptake capacities of these adsorbents were measured *via* both volumetric and gravimetric techniques by measuring the hydrogen adsorption isotherms at 77 K and 298 K up to 100 bar. An excess hydrogen uptake value of 13.5 wt%, which corresponds to an absolute uptake nearly 20 wt% and a volumetric storage capacity of 39 g.L^{-1}, has been measured at 77 K and 100 bar for the composite material which shows a great improvement of hydrogen capacity compared to the pristine MIL-101(Cr) (8.2 wt%).

The measured adsorption isotherms were fitted by applying the Langmuir monolayer adsorption model or the empirical Freundlich adsorption model which theoretically corresponds to a heterogeneous adsorption with an exponential distribution of energy of adsorption. The room temperature (298 K) hydrogen adsorption isotherms were measured using the gravimetric technique. The results showed that the maximum hydrogen uptake at 298 K up to 100 bar is about 0.5 wt%. All isotherms at room temperature followed the Henry's law and the Henry's constants were calculated.

The kinetics measurements of hydrogen adsorption were carried out at 77 K by using volumetric method under pressures between 0.2 and 5 bar. The obtained kinetic curves of pristine and doped MIL-101(Cr) did not show great difference of hydrogen adsorption kinetics. The kinetic curves showed that the hydrogen uptake at 0.2 bar was totally completed after a time of 2 minutes which decreases to 1 minute at 5 bar.

The Linear Driving Force (LDF) model was used to derive the effective hydrogen diffusivities within each compound. However, this model failed to give a satisfactory interpretation of hydrogen diffusion in porous adsorbents at high pressure and it was only applicable at 0.2 and 0.5 bar. The numerical resolution of the diffusion equation in a non-isothermal condition appeared to be another approach method. The results given by numerical modelling using non-isothermal condition were more acceptable and the diffusivities of hydrogen within different samples were in the magnitude of 10^{-16} m^2.s^{-1}. The results showed also that the diffusivity increases as a function of the applied pressure. Considering that the calculated uptakes did not correspond to the low pressure kinetic data, and the temperature profile curves calculated in the case of non-isothermal conditions over-estimated the effect of exothermicity of the adsorption process, an imposed temperature adsorption model was then proposed. In this model, an external resistance was applied and the temperature used during adsorption was the temperature experimentally measured. The results showed that the diffusion process of hydrogen in MIL-101(Cr) and AC doped MIL-101(Cr) can be accomplished within ~1 minute at 5 bar and this time requirement fulfils the ultimate DOE target for hydrogen storage for mobile usage.

Finally, this work constitutes a good investigation of the hydrogen storage media for mobile application, and the experimental measurements and the modelling have shown that activated carbon incorporated MIL-101(Cr) could be a good candidate for hydrogen storage. It has been shown also that a scaling up could be performed. However, the optimal performances of the materials appear only at a low temperature close to 77 K and these performances need to be

improved to reach an acceptable temperature of work. Moreover, the study has to be extended to consider a future utilization. According to these objectives, the following perspectives can be proposed:

- Improvement of the synthesis with other mineralizing agents such as nitric acid, sodium hydroxide, *etc.* in order to find the best way to produce high porous MIL-101(Cr).
- Different activated carbon materials could be tested for MIL-101(Cr) doping.
- The incorporation between activated carbon and MIL-101(Cr) can be studied either by numerical simulation or by further characterizations.
- An explanation of the doping effect at the microscopic level could be very helpful to understand and to improve the adsorption properties of the materials.
- Hydrogen adsorption/desorption cycling tests could be performed to evaluate the recyclability of the materials.
- Specific heat of adsorption measurements could provide useful information for the development at large scale.
- Industrial scale hydrogen adsorption-storage-desorption simulation could be achieved by using specific software such as ProSim.
- Test the other applications of adsorbent carbon-MOF such as methane and carbon dioxide storage and separation,

References

Aceves, S., Berry, G., Martinezfrias, J., Espinosaloza, F., 2006. *Vehicular storage of hydrogen in insulated pressure vessels*. Int. J. Hydrog. Energy 31, 2274–2283.

Ahluwalia, R., Hua, T., Peng, J.-K., Lasher, S., McKenney, K., Sinha, J., Gardiner, M., 2010. *Technical assessment of cryo-compressed hydrogen storage tank systems for automotive applications*. Int. J. Hydrog. Energy 35, 4171–4184.

Akiyama, G., Matsuda, R., Sato, H., Hori, A., Takata, M., Kitagawa, S., 2012. *Effect of functional groups in MIL-101 on water sorption behavior*. Microporous Mesoporous Mater. 157, 89–93.

Anbia, M., Hoseini, V., 2012. *Development of MWCNT@MIL-101 hybrid composite with enhanced adsorption capacity for carbon dioxide*. Chem. Eng. J. 191, 326–330.

Ascher, U.M., Petzold, L.R., 1998. *Computer methods for ordinary differential equations and differential-algebraic equations*. Society for Industrial and Applied Mathematics, Philadelphia.

Auerbach, S.M., Carrado, K.A., Dutta, P.K., 2003. *Handbook of Zeolite Science and Technology*. CRC Press.

Babarao, R., Jiang, J., 2008. *Diffusion and Separation of CO_2 and CH_4 in Silicalite, C_{168} Schwarzite, and IRMOF-1: A Comparative Study from Molecular Dynamics Simulation*. Langmuir 24, 5474–5484.

Barbir, F., 2012. *PEM fuel cells: theory and practice*. Academic Press.

Barkhordarian, G., Klassen, T., Bormann, R., 2004. *Effect of Nb_2O_5 content on hydrogen reaction kinetics of Mg*. J. Alloys Compd. 364, 242–246.

Barrett, E.P., Joyner, L.G., Halenda, P.P., 1951. *The Determination of Pore Volume and Area Distributions in Porous Substances. I. Computations from Nitrogen Isotherms*. J. Am. Chem. Soc. 73, 373–380.

Benard, P., Chahine, R., 2001. *Determination of the adsorption isotherms of hydrogen on activated carbons above the critical temperature of the adsorbate over wide temperature and pressure ranges*. Langmuir 17, 1950–1955.

Berdonosova, E.A., Kovalenko, K.A., Polyakova, E.V., Klyamkin, S.N., Fedin, V.P., 2015. *Influence of Anion Composition on Gas Sorption Features of Cr-MIL-101 Metal–Organic Framework*. J. Phys. Chem. C 119, 13098–13104.

Bhatia, S.K., Myers, A.L., 2006. *Optimum Conditions for Adsorptive Storage*. Langmuir 22, 1688–1700.

Biemmi, E., Christian, S., Stock, N., Bein, T., 2009. *High-throughput screening of synthesis parameters in the formation of the metal-organic frameworks MOF-5 and HKUST-1*. Microporous Mesoporous Mater. 117, 111–117.

Bimbo, N., Xu, W., Sharpe, J.E., Ting, V.P., Mays, T.J., 2015. *High-pressure adsorptive storage of hydrogen in MIL-101 (Cr) and AX-21 for mobile applications: Cryocharging and cryokinetics*. Mater. Des. doi:10.1016/j.matdes.2015.10.069

Biniwale, R.B., Kariya, N., Ichikawa, M., 2005. *Dehydrogenation of Cyclohexane Over Ni Based Catalysts Supported on Activated Carbon using Spray-pulsed Reactor and Enhancement in Activity by Addition of a Small Amount of Pt*. Catal. Lett. 105, 83–87.

Bird, R.B., Stewart, W.E., Lightfoot, E.N., 1960. *Transport Phenomena*, 780 pp. John Wiley Sons N. Y. 59, 67.

Birsa Čelič, T., Rangus, M., Lázár, K., Kaučič, V., Zabukovec Logar, N., 2012. *Spectroscopic Evidence for the Structure Directing Role of the Solvent in the Synthesis of Two Iron Carboxylates*. Angew. Chem. Int. Ed. 51, 12490–12494.

Board on Energy and Environmental Systems National Research Council, Division on Engineering and Physical Sciences National Research Council, Washington National Academy of Engineering, 2004. *The hydrogen economy: Opportunities, costs, barriers, and R&D needs*. National Academies Press.

Bobet, J.-L., Akiba, E., Darriet, B., 2001. *Study of Mg-M (M= Co, Ni and Fe) mixture elaborated by reactive mechanical alloying: hydrogen sorption properties*. Int. J. Hydrog. Energy 26, 493–501.

Bobet, J.-L., Akiba, E., Darriet, B., 2000. *Effect of substitution of Fe and Ni for Co in the synthesis of Mg 2 Co compound using the mechanical alloying method*. J. Alloys Compd. 297, 192–198.

Bordiga, S., Regli, L., Bonino, F., Groppo, E., Lamberti, C., Xiao, B., Wheatley, P., Morris, R., Zecchina, A., 2007. *Adsorption properties of HKUST-1 toward hydrogen and other small molecules monitored by IR*. Phys. Chem. Chem. Phys. 9, 2676–2685.

Bordiga, S., Vitillo, J.G., Ricchiardi, G., Regli, L., Cocina, D., Zecchina, A., Arstad, B., Bjørgen, M., Hafizovic, J., Lillerud, K.P., 2005. *Interaction of hydrogen with MOF-5*. J. Phys. Chem. B 109, 18237–18242.

Bromberg, L., Diao, Y., Wu, H., Speakman, S.A., Hatton, T.A., 2012. *Chromium(III) Terephthalate Metal Organic Framework (MIL-101): HF-Free Synthesis, Structure, Polyoxometalate Composites, and Catalytic Properties*. Chem. Mater. 24, 1664–1675.

Brunauer, S., Emmett, P.H., Teller, E., 1938. *Adsorption of Gases in Multimolecular Layers*. J. Am. Chem. Soc. 60, 309–319.

Butt, J.B., Reed, E.M., 1971. *Surface diffusion of single sorbates at low and intermediate surface coverage*. J. Phys. Chem. 75, 133–141.

Canepa, P., Nijem, N., Chabal, Y.J., Thonhauser, T., 2013. *Diffusion of Small Molecules in Metal Organic Framework Materials*. Phys. Rev. Lett. 110.

Cao, N., Su, J., Luo, W., Cheng, G., 2014. *Hydrolytic dehydrogenation of ammonia borane and methylamine borane catalyzed by graphene supported Ru@ Ni core–shell nanoparticles*. Int. J. Hydrog. Energy 39, 426–435.

Carslaw, H.S., Jaeger, J.C., 1959. *Conduction of heat in solids*. Oxf. Clarendon Press 1959 2nd Ed 1.

Cau, G., Cocco, D., Petrollese, M., Knudsen Kær, S., Milan, C., 2014. *Energy management strategy based on short-term generation scheduling for a renewable microgrid using a hydrogen storage system*. Energy Convers. Manag. 87, 820–831.

CEA, 2004. *De l'hydrogène à la production d'énergie*. Jounal CEA.

Chen, S.G., Yang, R.T., 1994. *Theoretical Basis for the Potential Theory Adsorption Isotherms. The Dubinin-Radushkevich and Dubinin-Astakhov Equations*. Langmuir 10, 4244–4249.

Chen, Y.D., Yang, R.T., 1991. *Concentration dependence of surface diffusion and zeolitic diffusion*. AIChE J. 37, 1579–1582.

Cheon, Y.E., Suh, M.P., 2009. *Enhanced Hydrogen Storage by Palladium Nanoparticles Fabricated in a Redox-Active Metal–Organic Framework*. Angew. Chem. Int. Ed. 48, 2899–2903.

Choi, H.J., Dinca, M., Long, J.R., 2008. *Broadly Hysteretic H_2 Adsorption in the Microporous Metal–Organic Framework Co (1, 4-benzenedipyrazolate)*. J. Am. Chem. Soc. 130, 7848–7850.

Chowdhury, P., Bikkina, C., Gumma, S., 2009. *Gas Adsorption Properties of the Chromium-Based Metal Organic Framework MIL-101*. J. Phys. Chem. C 113, 6616–6621.

Chui, S.S., 1999. *A Chemically Functionalizable Nanoporous Material $[Cu_3(TMA)_2(H_2O)_3]_n$*. Science 283, 1148–1150.

Cracknell, R.F., Gubbins, K.E., Maddox, M., Nicholson, D., 1995. *Modeling fluid behavior in well-characterized porous materials*. Acc. Chem. Res. 28, 281–288.

Cuevas, F., Joubert, J.-M., Latroche, M., Percheron-Guégan, A., 2001. *Intermetallic compounds as negative electrodes of Ni/MH batteries*. Appl. Phys. A 72, 225–238.

Cui, J., Wang, H., Liu, J., Ouyang, L., Zhang, Q., Sun, D., Yao, X., Zhu, M., 2013. *Remarkable enhancement in dehydrogenation of MgH_2 by a nano-coating of multi-valence Ti-based catalysts*. J. Mater. Chem. A 1, 5603–5611.

Czaja, A.U., Trukhan, N., Müller, U., 2009. *Industrial applications of metal–organic frameworks*. Chem. Soc. Rev. 38, 1284–1293.

Dantzer, P., 2002. *Properties of intermetallic compounds suitable for hydrogen storage applications*. Mater. Sci. Eng. A 329, 313–320.

Darken, L.S., 1948. *Diffusion, Mobility and Their Interrelation through Free Energy in Binary Metallic System*. Trans. AIME 175, 184–201.

Darriet, B., Pezat, M., Hbika, A., Hagenmuller, P., 1980. *Application of magnesium rich rare-earth alloys to hydrogen storage*. Int. J. Hydrog. Energy 5, 173–178.

De Boer, J., Lippens, B., Linsen, B., Broekhoff, J., Van den Heuvel, A., Osinga, T.J., 1966. *Thet-curve of multimolecular N_2-adsorption*. J. Colloid Interface Sci. 21, 405–414.

DeKock, R.L., Gray, H.B., 1989. *Chemical structure and bonding*. University Science Books.

Delage, F., Pré, P., Le Cloirec, P., 2000. *Mass Transfer and Warming during Adsorption of High Concentrations of VOCs on an Activated Carbon Bed: Experimental and Theoretical Analysis*. Environ. Sci. Technol. 34, 4816–4821.

Demessence, A., D'Alessandro, D.M., Foo, M.L., Long, J.R., 2009. *Strong CO_2 binding in a water-stable, triazolate-bridged metal– organic framework functionalized with ethylenediamine*. J. Am. Chem. Soc. 131, 8784–8786.

Department of Energy, 2015. Fuel Cell Technologies Office Multi-Year Research, Development, annd Demonstration Plan.

Deschamps, J., Paricaud, P., Catoire, L., 2015. *L'hydrogène, un atout pour la transition énertétique*. Industrie&Technologies 982-983, 57.

De Weireld, G., 2000. *Apport expérimental et théorique à la prédiction du comportement adsorbat/adsorbant dans une large gamme de température et de pression* (Thèse de doctorat). Faculté Polytechnique de Mons.

Diao, H.-Y., JIN, Z., Xun, F.-X., 2011. *Solvent Effect for the Synthesis of Metal organic Framework*. Chem. J. Chin. Univ. 590–594.

Didisheim, J., Zolliker, P., Yvon, K., Fischer, P., Schefer, J., Gubelmann, M., Williams, A., 1984. *Dimagnesium iron (II) hydride, Mg_2FeH_6, containing octahedral FeH_6^{4-}-anions*. Inorg. Chem. 23, 1953–1957.

Dincă, M., Dailly, A., Liu, Y., Brown, C.M., Neumann, D.A., Long, J.R., 2006. *Hydrogen Storage in a Microporous Metal−Organic Framework with Exposed Mn^{2+} Coordination Sites*. J. Am. Chem. Soc. 128, 16876–16883.

Diring, S., Furukawa, S., Takashima, Y., Tsuruoka, T., Kitagawa, S., 2010. *Controlled Multiscale Synthesis of Porous Coordination Polymer in Nano/Micro Regimes*. Chem. Mater. 22, 4531–4538.

Do, D.D., 1998. *Adsorption analysis: equilibria and kinetics*, Series on chemical engineering. Imperial College Press, London.

Dong, H., Huang, C., Moser, D., Noréus, D., Zhu, M., 2015. *Structure and stability of high pressure synthesized MgTM$_2$H$_6$ (TM= Zr, Nb) hydrides*. Acta Mater. 96, 237–248.

Dornheim, M., 2011. Thermodynamics of Metal Hydrides: Tailoring Reaction Enthalpies of Hydrogen Storage Materials, in: Moreno Pirajn, J.C. (Ed.), *Thermodynamics - Interaction Studies - Solids, Liquids and Gases*. InTech.

Dornheim, M., Doppiu, S., Barkhordarian, G., Boesenberg, U., Klassen, T., Gutfleisch, O., Bormann, R., 2007. *Hydrogen storage in magnesium-based hydrides and hydride composites*. Scr. Mater. 56, 841–846.

Dreisbach, F., Staudt, R., Tomalla, M., Keller, J.U., 1996. Measurement of Adsorption Equilibria of Pure and Mixed Corrosive Gases: The Magnetic Suspension Balance, in: LeVan, M.D. (Ed.), *Fundamentals of Adsorption*. Springer US, Boston, MA, pp. 259–268.

Dubinin, M.., 1967. *Adsorption in micropores*. J. Colloid Interface Sci. 23, 487–499.

Dubinin, M.M., Radushkevich, L.V., 1947. *The Equation of the Characteristic Curve of Activated Charcoal*. Proc. Acad. Sci., Physical Chemistry Section 55, 331.

Dumée, L., He, L., Hill, M., Zhu, B., Duke, M., Schütz, J., She, F., Wang, H., Gray, S., Hodgson, P., 2013. *Seeded growth of ZIF-8 on the surface of carbon nanotubes towards self-supporting gas separation membranes*. J. Mater. Chem. A 1, 9208–9214.

Dumont, E., Pré, P., Le Cloirec, P., 2006. *Hydrogen Storage by Adsorption Onto Different Activated Carbons*. Presented at The 2006 Annual Meeting.

Durbin, D.J., Malardier-Jugroot, C., 2013. *Review of hydrogen storage techniques for on board vehicle applications*. Int. J. Hydrog. Energy 38, 14595–14617.

Du, X., Wu, E., 2006. *Physisorption of Hydrogen in A, X and ZSM-5 Types of Zeolites at Moderately High Pressures*. Chin. J. Chem. Phys. 19, 457–462.

Eberle, U., Felderhoff, M., Schueth, F., 2009. *Chemical and physical solutions for hydrogen storage*. Angew. Chem. Int. Ed. 48, 6608–6630.

Eddaoudi, M., 2002. *Systematic Design of Pore Size and Functionality in Isoreticular MOFs and Their Application in Methane Storage*. Science 295, 469–472.

Eddaoudi, M., Moler, D.B., Li, H., Chen, B., Reineke, T.M., O'Keeffe, M., Yaghi, O.M., 2001. *Modular Chemistry: Secondary Building Units as a Basis for the Design of Highly Porous and Robust Metal−Organic Carboxylate Frameworks*. Acc. Chem. Res. 34, 319–330.

Eic, M., Ruthven, D.M., 1988. *A new experimental technique for measurement of intracrystalline diffusivity*. Zeolites 8, 40–45.

Ekins, P., Bellaby, P., 2008. *Hydrogen futures: emerging technologies for hydrogen storage and transport*. Solid-State Hydrog. Storage Mater. Chem. 18.

ENERTRAG, 2015. La Centrale Hybride | ENERTRAG [WWW Document]. URL https://www.enertrag.com/90_hybridkraftwerk.html?&L=2 (accessed 12.1.15).

Eurostat, 2015. *Renewable energy statistics*.

Faas, G.S., 1981. *Correlation of gas adsorption, mercury intrusion, and electron microscopy pore property data for porous glasses*. (Ph.D. Thesis) Georgia Institute of Technology

Farha, O.K., Eryazici, I., Jeong, N.C., Hauser, B.G., Wilmer, C.E., Sarjeant, A.A., Snurr, R.Q., Nguyen, S.T., Yazaydın, A.Ö., Hupp, J.T., 2012. *Metal–Organic Framework Materials with Ultrahigh Surface Areas: Is the Sky the Limit?* J. Am. Chem. Soc. 134, 15016–15021.

Farha, O.K., Özgür Yazaydın, A., Eryazici, I., Malliakas, C.D., Hauser, B.G., Kanatzidis, M.G., Nguyen, S.T., Snurr, R.Q., Hupp, J.T., 2010. *De novo synthesis of a metal–organic framework material featuring ultrahigh surface area and gas storage capacities*. Nat. Chem. 2, 944–948.

Feng, Z., 2006. *Hydrogen Permeability and Integrity of Hydrogen Transfer Pipelines* (FY 2006 Annual Progress Repport), III.A.1 DOE Hydrogen Program.

Férey, G., Latroche, M., Serre, C., Millange, F., Loiseau, T., Percheron-Guégan, A., 2003. *Hydrogen adsorption in the nanoporous metal-benzenedicarboxylate $M(OH)(O_2C–C_6H_4–CO_2)$ $(M= Al^{3+}, Cr^{3+})$, MIL-53*. Chem. Commun. 2976–2977.

Férey, G., Mellot-Draznieks, C., Serre, C., Millange, F., 2005a. *Crystallized Frameworks with Giant Pores: Are There Limits to the Possible?* Acc. Chem. Res. 38, 217–225.

Férey, G., Mellot-Draznieks, C., Serre, C., Millange, F., Dutour, J., Surblé, S., Margiolaki, I., 2005b. *A Chromium Terephthalate-Based Solid with Unusually Large Pore Volumes and Surface Area*. Science 309, 2040–2042.

Férey, G., Serre, C., Mellot-Draznieks, C., Millange, F., Surblé, S., Dutour, J., Margiolaki, I., 2004. *A Hybrid Solid with Giant Pores Prepared by a Combination of Targeted Chemistry, Simulation, and Powder Diffraction*. Angew. Chem. Int. Ed. 43, 6296–6301.

Filinchuk, Y., Cerny, R., Hagemann, H., 2009. *Insight into $Mg(BH_4)_2$ with synchrotron X-ray diffraction: structure revision, crystal chemistry, and anomalous thermal expansion*. Chem. Mater. 21, 925–933.

Filinchuk, Y., Richter, B., Jensen, T.R., Dmitriev, V., Chernyshov, D., Hagemann, H., 2011. *Porous and dense magnesium borohydride frameworks: synthesis, stability, and reversible absorption of guest species*. Angew. Chem. Int. Ed. 50, 11162–11166.

Fogler, H.S., 2006. *Elements of chemical reaction engineering*, 4th ed., 3.printing. ed, Prentice Hall PTR international series in the physical and chemical engineering sciences. Pearson Education International/Prentice Hall PTR, Upper Saddle River, NJ.

Foster, A.G., 1932. *The sorption of condensible vapours by porous solids. Part I. The applicability of the capillary theory*. Trans. Faraday Soc. 28, 645–657.

Frazer, R.A., Jones, W.N.P., Skan, S.W., Ministry, G.B.A., 1937. *Approximations to Functions and to the Solutions of Differential Equations*, A.R.C. technical report. HSMO.

Frost, H., Düren, T., Snurr, R.Q., 2006. *Effects of surface area, free volume, and heat of adsorption on hydrogen uptake in metal-organic frameworks*. J. Phys. Chem. B 110, 9565–9570.

Frost, H., Snurr, R.Q., 2007. *Design Requirements for Metal-Organic Frameworks as Hydrogen Storage Materials*. J. Phys. Chem. C 111, 18794–18803.

Furuhama, S., Hiruma, M., Enomoto, Y., 1978. *Development of a liquid hydrogen car*. Int. J. Hydrog. Energy 3, 61–81.

Furukawa, H., Ko, N., Go, Y.B., Aratani, N., Choi, S.B., Choi, E., Yazaydin, A.O., Snurr, R.Q., O'Keeffe, M., Kim, J., Yaghi, O.M., 2010. *Ultrahigh Porosity in Metal-Organic Frameworks*. Science 329, 424–428.

Furukawa, H., Miller, M.A., Yaghi, O.M., 2007. *Independent verification of the saturation hydrogen uptake in MOF-177 and establishment of a benchmark for hydrogen adsorption in metal–organic frameworks*. J. Mater. Chem. 17, 3197.

Gao, L., Chen, C., Chen, L., Wang, X., Zhang, J., Xiao, X., Wang, Q., 2005. *Hydriding/dehydriding behaviors of $La_{1.8}Ca_{0.2}Mg_{14}Ni_3$ alloy modified by mechanical ball-milling under argon*. J. Alloys Compd. 399, 178–182.

Gao, M., Krishnamurthy, R., 2008. Hydrogen Transmission in Pipelines and Storage in Pressurized and Cryogenic Tanks, in: *Hydrogen Fuel*. CRC Press, pp. 341–379.

GDF Suez, McPhy in French GRHYD project on methane, hydrogen, 2012. . Fuel Cells Bull. 2012, 10.

Geankoplis, C.J., 1983. *Transport Processes: Momentum, heat, and mass,* Allyn and Bacon series in engineering. Allyn and Bacon, Boston.

Ge, L., Wang, L., Rudolph, V., Zhu, Z., 2013. *Hierarchically structured metal–organic framework/vertically-aligned carbon nanotubes hybrids for CO_2 capture*. Rsc Adv. 3, 25360–25366.

Genma, R., Okada, N., Sobue, T., Uchida, H.-H., 2006. *Mechanically milled alanates as hydrogen storage materials*. Int. J. Hydrog. Energy 31, 309–311.

Ghoufi, A., Deschamps, J., Maurin, G., 2012. *Theoretical Hydrogen Cryostorage in Doped MIL-101(Cr) Metal–Organic Frameworks*. J. Phys. Chem. C 116, 10504–10509.

Gibbs, J.W., 1878. *On the equilibrium of heterogeneous substances*. Am. J. Sci. s3-16, 441–458.

Giraudet, S., Pré, P., Le Cloirec, P., 2009. *Modeling the Heat and Mass Transfers in Temperature-Swing Adsorption of Volatile Organic Compounds onto Activated Carbons*. Environ. Sci. Technol. 43, 1173–1179.

Glueckauf, E., 1955a. *Theory of chromatography. Part 10.Formulae for diffusion into spheres and their application to chromatography*. Trans. Faraday Soc. 51, 1540.

Glueckauf, E., 1955b. *Principles of operation of ion-exchange columns*. Ion Exch. Its Appl. 34–46.

Glueckauf, E., Coates, J., 1947. *Theory of chromatography. Part IV. The influence of incomplete equilibrium on the front boundary of chromatograms and on the effectiveness of separation*. J. Chem. Soc. Resumed 1315–1321.

Goesten, M.G., Stavitski, E., Juan-Alcañiz, J., Martiñez-Joaristi, A., Petukhov, A.V., Kapteijn, F., Gascon, J., 2013. *Small-angle X-ray scattering documents the growth of metal-organic frameworks*. Catal. Today 205, 120–127.

Gregg, S., Sing, K., 1982. *Adsorption, surface area and porosity*. Academic. N. Y. 242–245.

Groen, J.C., Peffer, L.A.., Pérez-Ramírez, J., 2003. *Pore size determination in modified micro- and mesoporous materials. Pitfalls and limitations in gas adsorption data analysis*. Microporous Mesoporous Mater. 60, 1–17.

Guo, J.T., Chen, Y., 2012. *Synthesis of Metal Organic Framework MIL-101 with Acetate as Mineralization Agent*. Chem. J. Chin. Univ. 33, 668–672.

Gupta, R., Pant, K., 2008. Fundamentals and Use of Hydrogen as a Fuel, in: Gupta, R. (Ed.), *Hydrogen Fuel*. CRC Press, pp. 2–32.

Hafizovic, J., Bjørgen, M., Olsbye, U., Dietzel, P.D., Bordiga, S., Prestipino, C., Lamberti, C., Lillerud, K.P., 2007. *The inconsistency in adsorption properties and powder XRD data of MOF-5 is rationalized by framework interpenetration and the presence of organic and inorganic species in the nanocavities*. J. Am. Chem. Soc. 129, 3612–3620.

Halsey, G., 1948. *Physical adsorption on non-uniform surfaces*. J. Chem. Phys. 16, 931–937.

Hamon, L., Chenoy, L., De Weireld, G., 2014. *Determination of absolute gas adsorption isotherms: simple method based on the potential theory for buoyancy effect correction of pure gas and gas mixtures adsorption*. Adsorption 20, 397–408.

Harkins, W.D., Jura, G., 1944. *Surfaces of solids. XIII. A vapor adsorption method for the determination of the area of a solid without the assumption of a molecular area, and the areas occupied by nitrogen and other molecules on the surface of a solid*. J. Am. Chem. Soc. 66, 1366–1373.

Harris, R., Book, D., Anderson, P., Edwards, P., 2004. *Hydrogen storage: the grand challenge*. Fuel Cell Rev. 1, 17–23.

Hemingway, B.S., Robie, R.A., 1984. *Thermodynamic properties of zeolites: low-temperature heat capacities and thermodynamic functions for phillipsite and clinoptilolite. Estimates of the thermochemical properties of zeolitic water at low temperature*. Am. Mineral. 69, 692–700.

Henry, W., 1803. *Experiments on the Quantity of Gases Absorbed by Water, at Different Temperatures, and under Different Pressures*. Philos. Trans. R. Soc. Lond. 93, 29–274.

Henschel, A., Gedrich, K., Kraehnert, R., Kaskel, S., 2008. *Catalytic properties of MIL-101*. Chem. Commun. 4192–4194.

Her, J.-H., Stephens, P.W., Gao, Y., Soloveichik, G.L., Rijssenbeek, J., Andrus, M., Zhao, J.-C., 2007. *Structure of unsolvated magnesium borohydride $Mg(BH_4)_2$*. Acta Crystallogr. B 63, 561–568.

Hess, W.T., Kurtz, A., Stanton, D., 1995. *Kirk-Othmer encyclopedia of chemical technology*. John Wiley Sons Ltd N. Y.

Hetland, J., Mulder, G., 2007. *In search of a sustainable hydrogen economy: How a large-scale transition to hydrogen may affect the primary energy demand and greenhouse gas emissions*. Int. J. Hydrog. Energy 32, 736–747.

He, Y., Chen, B., 2014. Metal-Organic Frameworks: Frameworks Containing Open Sites, in: Scott, R.A. (Ed.), *Encyclopedia of Inorganic and Bioinorganic Chemistry*. John Wiley & Sons, Ltd, Chichester, UK, pp. 1–23.

Higashi K., Ito H., Oishi J., 1963. *Surface Diffusion Phenomena in Gaseous Diffusion*, (I). J. At. Energy Soc. Jpn. At. Energy Soc. Jpn. 5, 846–853.

Hodoshima, S., Saito, Y., 2008. Hydrogen Storage in Organic Chemical Hydrides on the Basis of Superheated Liquid-Film Concept, in: Gupta, R. (Ed.), *Hydrogen Fuel*. CRC Press, pp. 437–474.

Holladay, J.D., Hu, J., King, D.L., Wang, Y., 2009. *An overview of hydrogen production technologies*. Catal. Today 139, 244–260.

Hong, D. -Y., Hwang, Y.K., Serre, C., Férey, G., Chang, J. -S., 2009. *Porous Chromium Terephthalate MIL -101 with Coordinatively Unsaturated Sites: Surface Functionalization, Encapsulation, Sorption and Catalysis*. Adv. Funct. Mater. 19, 1537–1552.

Huang, C.-Y., Song, M., Gu, Z.-Y., Wang, H.-F., Yan, X.-P., 2011. *Probing the Adsorption Characteristic of Metal–Organic Framework MIL-101 for Volatile Organic Compounds by Quartz Crystal Microbalance*. Environ. Sci. Technol. 45, 4490–4496.

Huo, S.-H., Yan, X.-P., 2012. *Facile magnetization of metal–organic framework MIL-101 for magnetic solid-phase extraction of polycyclic aromatic hydrocarbons in environmental water samples*. The Analyst 137, 3445.

Hu, Y.H., Ruckenstein, E., 2006. *Hydrogen storage of Li$_2$NH prepared by reacting Li with NH$_3$*. Ind. Eng. Chem. Res. 45, 182–186.

Hwang, Y.K., Hong, D., Chang, J., Jhung, S.H., Seo, Y., Kim, J., Vimont, A., Daturi, M., Serre, C., Férey, G., 2008. *Amine grafting on coordinatively unsaturated metal centers of MOFs: consequences for catalysis and metal encapsulation*. Angew. Chem. Int. Ed. 47, 4144–4148.

IEA, 2015a. *World Energy Outlook 2015*, World Energy Outlook. OECD Publishing.

IEA, 2015b. *IEA Energy Atlas*.

IEA, 2014. *World Energy Outlook 2014*, World Energy Outlook. IEA.

IEA, 2007. *IEA Energy Technology Essentials: Hydrogen production & Distribution*.

Jagiello, J., Bandosz, T.J., Putyera, K., Schwarz, J.A., 1994. *Adsorption energy and structural heterogeneity of activated carbons*. Stud. Surf. Sci. Catal. 87, 679–688.

Jagiello, J., Olivier, J.P., 2009. A simple two-dimensional NLDFT model of gas adsorption in finite carbon pores. Application to pore structure analysis. J. Phys. Chem. C 113, 19382–19385.

Jagiello, J., Schwarz, J.A., 1993. *Relationship between energetic and structural heterogeneity of microporous carbons determined on the basis of adsorption potentials in model micropores*. Langmuir 9, 2513–2517.

Jhung, S.H., Hwang, Y.K., Chang, J.-S., Park, S.-E., 2004. *Effect of acidity and anions on synthesis of AFI molecular sieves in wide pH range of 3–10*. Microporous Mesoporous Mater. 67, 151–157.

Jhung, S.H., Lee, J. -H., Yoon, J.W., Serre, C., Férey, G., Chang, J., 2007. *Microwave Synthesis of Chromium Terephthalate MIL-101 and Its Benzene Sorption Ability*. Adv. Mater. 19, 121–124.

Jiang, D., Burrows, A.D., Edler, K.J., 2011. *Size-controlled synthesis of MIL-101(Cr) nanoparticles with enhanced selectivity for CO$_2$ over N$_2$*. CrystEngComm 13, 6916–6919.

Jones, J.E., 1924. *On the Determination of Molecular Fields. II. From the Equation of State of a Gas*. Proc. R. Soc. Math. Phys. Eng. Sci. 106, 463–477.

Jordá-Beneyto, M., Suárez-García, F., Lozano-Castelló, D., Cazorla-Amorós, D., Linares-Solano, A., 2007. *Hydrogen storage on chemically activated carbons and carbon nanomaterials at high pressures*. Carbon 45, 293–303.

Jung, K., Lee, E., Lee, K., 2006. *Catalytic effects of metal oxide on hydrogen absorption of magnesium metal hydride*. J. Alloys Compd. 421, 179–184.

Kamegawa, A., Goto, Y., Kakuta, H., Takamura, H., Okada, M., 2006. *High-pressure synthesis of novel hydrides in Mg–RE–H systems (RE= Y, La, Ce, Pr, Sm, Gd, Tb, Dy)*. J. Alloys Compd. 408, 284–287.

Karikkethu Prabhakaran, P., Deschamps, J., 2015a. *Room temperature hydrogen uptake in single walled carbon nanotubes incorporated MIL-101 doped with lithium: effect of lithium doping*. J. Porous Mater. 22, 1635–1642.

191

Karikkethu Prabhakaran, P., Deschamps, J., 2015b. *Doping activated carbon incorporated composite MIL-101 using lithium: impact on hydrogen uptake*. J Mater Chem A 3, 7014–7021.

Karikkethu Prabhakaran, P., Rallapalli, P., Raj, M.C., Bajaj, H.C., Jasra, R.V., 2011. *Enhanced hydrogen sorption in single walled carbon nanotube incorporated MIL-101 composite metal–organic framework*. Int. J. Hydrog. Energy 36, 7594–7601.

Kaye, S.S., Dailly, A., Yaghi, O.M., Long, J.R., 2007. *Impact of Preparation and Handling on the Hydrogen Storage Properties of $Zn_4O(1,4$-benzenedicarboxylate$)_3$ (MOF-5)*. J. Am. Chem. Soc. 129, 14176–14177.

Keller, J.U., Staudt, R., 2005. *Gas adsorption equilibria: experimental methods and adsorptive isotherms*. Springer, New York, NY.

Kennard, E.H., 1938. *Kinetic theory of gases, with an introduction to statistical mechanics*.

Khan, N.A., Kang, I.J., Seok, H.Y., Jhung, S.H., 2011. *Facile synthesis of nano-sized metal-organic frameworks, chromium-benzenedicarboxylate, MIL-101*. Chem. Eng. J. 166, 1152–1157.

Khrussanova, M., Terzieva, M., Peshev, P., Konstanchuk, I., Ivanov, E., 1989. *Hydriding Kinetics of Mixtures Containing Some 3d-Transition Metal Oxides and Magnesium*. Z. Für Phys. Chem. 164, 1261–1266.

Khutia, A., Rammelberg, H.U., Schmidt, T., Henninger, S., Janiak, C., 2013. *Water sorption cycle measurements on functionalized MIL-101Cr for heat transformation application*. Chem. Mater. 25, 790–798.

Kim, S.-N., Yang, S.-T., Kim, J., Park, J.-E., Ahn, W.-S., 2012. *Post-synthesis functionalization of MIL-101 using diethylenetriamine: a study on adsorption and catalysis*. CrystEngComm 14, 4142–4147.

Kiselev, A.V., Yashin, Y.I., 1969. *Gas-Adsorption Chromatography*.

Kloutse, F.A., Zacharia, R., Cossement, D., Chahine, R., 2015. *Specific heat capacities of MOF-5, Cu-BTC, Fe-BTC, MOF-177 and MIL-53 (Al) over wide temperature ranges: Measurements and application of empirical group contribution method*. Microporous Mesoporous Mater. 217, 1–5.

Koh, K., Wong-Foy, A.G., Matzger, A.J., 2009. *A porous coordination copolymer with over 5000 m^2/g BET surface area*. J. Am. Chem. Soc. 131, 4184–4185.

Koh, K., Wong-Foy, A.G., Matzger, A.J., 2008. *A crystalline mesoporous coordination copolymer with high microporosity*. Angew. Chem. Int. Ed. 47, 677–680.

Kruk, M., Jaroniec, M., Sayari, A., 1997. *Application of large pore MCM-41 molecular sieves to improve pore size analysis using nitrogen adsorption measurements*. Langmuir 13, 6267–6273.

Kuchta, B., Firlej, L., Pfeifer, P., Wexler, C., 2010. *Numerical estimation of hydrogen storage limits in carbon-based nanospaces*. Carbon 48, 223–231.

Kyotani, T., Nagai, T., Inoue, S., Tomita, A., 1997. *Formation of new type of porous carbon by carbonization in zeolite nanochannels*. Chem. Mater. 9, 609–615.

Lamb, A.B., Coolidge, A.S., 1920. *The heat of absorption of vapors on charcoal*. J. Am. Chem. Soc. 42, 1146–1170.

Lange, R.S.A., Keizer, K., Burggraaf, A.J., 1995. *Analysis and theory of gas transport in microporous sol-gel derived ceramic membrane*s. J. Membr. Sci. 104, 81–100.

Langmi, H.W., Book, D., Walton, A., Johnson, S.R., Al-Mamouri, M.M., Speight, J.D., Edwards, P.P., Harris, I.R., Anderson, P.A., 2005. *Hydrogen storage in ion-exchanged zeolites*. J. Alloys Compd. 404-406, 637–642.

Langmuir, I., 1918. *The adsorption of gases on plane surface of glass, mica and platinum*. J. Am. Chem. Soc. 40,

Lastoskie, C., Gubbins, K.E., Quirke, N., 1993. *Pore size distribution analysis of microporous carbons: a density functional theory approach*. J. Phys. Chem. 97, 4786–4796.

Latroche, M., Surblé, S., Serre, C., Mellot-Draznieks, C., Llewellyn, P.L., Lee, J.-H., Chang, J.-S., Jhung, S.H., Férey, G., 2006. *Hydrogen Storage in the Giant-Pore Metal–Organic Frameworks MIL-100 and MIL-101*. Angew. Chem. Int. Ed. 45, 8227–8231.

Lebedev, O.I., Millange, F., Serre, C., Van Tendeloo, G., Férey, G., 2005. *First Direct Imaging of Giant Pores of the Metal−Organic Framework MIL-101*. Chem. Mater. 17, 6525–6527.

Lee, J., Farha, O.K., Roberts, J., Scheidt, K.A., Nguyen, S.T., Hupp, J.T., 2009. *Metal–organic framework materials as catalysts*. Chem. Soc. Rev. 38, 1450–1459.

Leighty, W., Holloway, J., Merer, R., Somerday, B., San Marchi, C., Keith, G., White, D., Economics, S.E., 2006. *Compressorless hydrogen transmission pipelines deliver large-scale stranded renewable energy at competitive cost*. Presented at the Proceedings of the 16th World Hydrogen Energy Conference, Lyon, FR, June, Citeseer.

Lemmon, E., Huber, M., McLinden, M., 2010. *NIST Standard Reference Database 23: Reference Fluid Thermodynamic and Transport Properties - REFPROP*.

Lewis, W.K., Gilliland, E.R., Chertow, B., Cadogan, W.P., 1950. *Adsorption Equilibria Hydrocarbon Gas Mixtures*. Ind. Eng. Chem. 42, 1319–1326.

Liang, G., Boily, S., Huot, J., Van Neste, A., Schulz, R., 1998. *Hydrogen absorption properties of a mechanically milled Mg–50 wt.% LaNi$_5$ composite*. J. Alloys Compd. 268, 302–307.

Liang, G., Huot, J., Boily, S., Van Neste, A., Schulz, R., 1999. *Catalytic effect of transition metals on hydrogen sorption in nanocrystalline ball milled MgH$_2$–Tm (Tm= Ti, V, Mn, Fe and Ni) systems*. J. Alloys Compd. 292, 247–252.

Li, J.-R., Kuppler, R.J., Zhou, H.-C., 2009. *Selective gas adsorption and separation in metal–organic frameworks*. Chem. Soc. Rev. 38, 1477.

Lim, D., Yoon, J.W., Ryu, K.Y., Suh, M.P., 2012. *Magnesium Nanocrystals Embedded in a Metal–Organic Framework: Hybrid Hydrogen Storage with Synergistic Effect on Physi-and Chemisorption*. Angew. Chem. 124, 9952–9955.

Lin, S.-Y., 2008. Hydrogen Production from Coal, in: Gupta, R. (Ed.), *Hydrogen Fuel*. CRC Press, pp. 103–125.

Lin, X., Jia, J., Zhao, X., Thomas, K.M., Blake, A.J., Walker, G.S., Champness, N.R., Hubberstey, P., Schröder, M., 2006. *High H$_2$ Adsorption by Coordination-Framework Materials*. Angew. Chem. Int. Ed. 45, 7358–7364.

Lin, Y., Lin, H., Wang, H., Suo, Y., Li, B., Kong, C., Chen, L., 2014. *Enhanced selective CO $_2$ adsorption on polyamine/MIL-101(Cr) composites*. J. Mater. Chem. A 2, 14658.

Li, Q., Chou, K., Jiang, L., Lin, Q., Lin, G., Lu, X., Zhang, J., 2006. *Hydrogen absorption and desorption characteristics in the La$_{0.5}$Ni$_{1.5}$Mg$_{17}$ prepared by hydriding combustion synthesis*. Int. J. Hydrog. Energy 31, 497–503.

Li, X., Ji, W., Zhao, J., Wang, S., Au, C., 2005. *Ammonia decomposition over Ru and Ni catalysts supported on fumed SiO2, MCM-41, and SBA-15*. J. Catal. 236, 181–189.

Li, Y., Yang, R.T., 2008. *Hydrogen storage in metal-organic and covalent-organic frameworks by spillover*. AIChE J. 54, 269–279.

Llewellyn, P.L., Bourrelly, S., Serre, C., Vimont, A., Daturi, M., Hamon, L., De Weireld, G., Chang, J.-S., Hong, D.-Y., Kyu Hwang, Y., Hwa Jhung, S., Férey, G., 2008. *High Uptakes of CO_2 and CH_4 in Mesoporous Metal-Organic Frameworks MIL-100 and MIL-101*. Langmuir 24, 7245–7250.

London, F., 1937. *The general theory of molecular forces*. Trans. Faraday Soc. 33, 8b.

Lopes, F.V.S., Grande, C.A., Ribeiro, A.M., Loureiro, J.M., Evaggelos, O., Nikolakis, V., Rodrigues, A.E., 2009. *Adsorption of H_2, CO_2, CH_4, CO, N_2 and H_2O in Activated Carbon and Zeolite for Hydrogen Production*. Sep. Sci. Technol. 44, 1045–1073.

McBain, J.W., Bakr, A.M., 1926. *A new sorption balance*. J. Am. Chem. Soc. 48, 690–695.

McDowall, W., Eames, M., 2006. *Forecasts, scenarios, visions, backcasts and roadmaps to the hydrogen economy: A review of the hydrogen futures literature*. Energy Policy 34, 1236–1250.

Mekhilef, S., Saidur, R., Safari, A., 2012. *Comparative study of different fuel cell technologies*. Renew. Sustain. Energy Rev. 16, 981–989.

Mellot-Draznieks, C., Férey, G., 2005. *Assembling molecular species into 3D frameworks: Computational design and structure solution of hybrid materials*. Prog. Solid State Chem. 33, 187–197.

Millet, P., 2012. Water Electrolysis for Hydrogen Generation, in: Liu, R.-S., Zhang, L., Sun, X., Liu, H., Zhang, J. (Eds.), *Electrochemical Technologies for Energy Storage and Conversion*. Wiley-VCH Verlag GmbH & Co. KGaA, Weinheim, Germany, pp. 383–423.

Mu, B., Walton, K.S., 2011. *Thermal Analysis and Heat Capacity Study of Metal–Organic Frameworks*. J. Phys. Chem. C 115, 22748–22754.

Muradov, N., 2008. Production of Hydrogen from Hydrocarbons, in: Gupta, R. (Ed.), *Hydrogen Fuel*. CRC Press, pp. 33–101.

Murata, K., Kaneko, K., Kokai, F., Takahashi, K., Yudasaka, M., Iijima, S., 2000. *Pore structure of single-wall carbon nanohorn aggregates*. Chem. Phys. Lett. 331, 14–20.

Murata, K., Miyawaki, J., Kaneko, K., 2002. *A simple determination method of the absolute adsorbed amount for high pressure gas adsorption*. Carbon 40, 425–428.

Murray, L.J., Dincă, M., Long, J.R., 2009. *Hydrogen storage in metal–organic frameworks*. Chem. Soc. Rev. 38, 1294.

MYRTE hydrogen energy storage test powers up in Corsica, 2014. . Fuel Cells Bull. 2014, 8.

Natarajan, S., Mahata, P., 2009. *Metal–organic framework structures–how closely are they related to classical inorganic structures?* Chem. Soc. Rev. 38, 2304–2318.

Neimark, A.V., Ravikovitch, P.I., Vishnyakov, A., 2003. *Bridging scales from molecular simulations to classical thermodynamics: density functional theory of capillary condensation in nanopores*. J. Phys. Condens. Matter 15, 347.

Nijkamp, M., Raaymakers, J., Van Dillen, A., De Jong, K., 2001. *Hydrogen storage using physisorption–materials demands*. Appl. Phys. A 72, 619–623.

O'Keeffe, M., 2009. *Design of MOFs and intellectual content in reticular chemistry: a personal view*. Chem. Soc. Rev. 38, 1215–1217.

O'Keeffe, M., Eddaoudi, M., Li, H., Reineke, T., Yaghi, O.M., 2000. *Frameworks for Extended Solids: Geometrical Design Principles*. J. Solid State Chem. 152, 3–20.

Orimo, S., Nakamori, Y., Kitahara, G., Miwa, K., Ohba, N., Towata, S., Züttel, A., 2005. *Dehydriding and rehydriding reactions of LiBH₄*. J. Alloys Compd. 404, 427–430.

Ouyang, L., Dong, H., Peng, C., Sun, L., Zhu, M., 2007. *A new type of Mg-based metal hydride with promising hydrogen storage properties*. Int. J. Hydrog. Energy 32, 3929–3935.

Paggiaro, R., Bénard, P., Polifke, W., 2010. *Cryo-adsorptive hydrogen storage on activated carbon. I: Thermodynamic analysis of adsorption vessels and comparison with liquid and compressed gas hydrogen storage*. Int. J. Hydrog. Energy 35, 638–647.

Panella, B., Hirscher, M., Pütter, H., Müller, U., 2006. *Hydrogen Adsorption in Metal–Organic Frameworks: Cu-MOFs and Zn-MOFs Compared*. Adv. Funct. Mater. 16, 520–524.

Pan, L., Sander, M.B., Huang, X., Li, J., Smith, M., Bittner, E., Bockrath, B., Johnson, J.K., 2004. *Microporous metal organic materials: promising candidates as sorbents for hydrogen storage*. J. Am. Chem. Soc. 126, 1308–1309.

Park, H.J., Suh, M.P., 2008. *Mixed-Ligand Metal–Organic Frameworks with Large Pores: Gas Sorption Properties and Single-Crystal-to-Single-Crystal Transformation on Guest Exchange*. Chem.- Eur. J. 14, 8812–8821.

Park, K.S., Ni, Z., Côté, A.P., Choi, J.Y., Huang, R., Uribe-Romo, F.J., Chae, H.K., O'Keeffe, M., Yaghi, O.M., 2006. *Exceptional chemical and thermal stability of zeolitic imidazolate frameworks*. Proc. Natl. Acad. Sci. 103, 10186–10191.

Payne, H.K., Sturdevant, G.A., Leland, T.W., 1968. *Improved Two-Dimensional Equation of State to Predict Adsorption of Pure and Mixed Hydrocarbons*. Ind. Eng. Chem. Fundam. 7, 363–374.

Perry, R.H., Green, D.W. (Eds.), 2008. *Perry's chemical engineers' handbook*, 8. ed. ed. McGraw-Hill, New York, NY.

Peterson, V.K., Liu, Y., Brown, C.M., Kepert, C.J., 2006. *Neutron powder diffraction study of D2 sorption in Cu₃ (1, 3, 5-benzenetricarboxylate)₂*. J. Am. Chem. Soc. 128, 15578–15579.

Petit, C., Bandosz, T.J., 2009. *MOF-Graphite Oxide Composites: Combining the Uniqueness of Graphene Layers and Metal-Organic Frameworks*. Adv. Mater. NA–NA.

Petit, C., Burress, J., Bandosz, T.J., 2011. *The synthesis and characterization of copper-based metal–organic framework/graphite oxide composites*. Carbon 49, 563–572.

Petrovic, L.J., Thodos, G., 1968. *Mass Transfer in Flow of Gases through Packed Beds. Low Reynolds Number Region*. Ind. Eng. Chem. Fundam. 7, 274–280.

Pezat, M., Darriet, B., Hagenmuller, P., 1980. *A comparative study of magnesium-rich rare-earth-based alloys for hydrogen storage*. J. Common Met. 74, 427–434.

Pinkerton, F.E., Meisner, G.P., Meyer, M.S., Balogh, M.P., Kundrat, M.D., 2005. *Hydrogen desorption exceeding ten weight percent from the new quaternary hydride Li₃BN₂H₈*. J. Phys. Chem. B 109, 6–8.

Pires, J., Pinto, M.L., Granadeiro, C.M., Barbosa, A.D., Cunha-Silva, L., Balula, S.S., Saini, V.K., 2014. *Effect on selective adsorption of ethane and ethylene of the polyoxometalates impregnation in the metal-organic framework MIL-101*. Adsorption 20, 533–543.

Polanyi, M., 1932. *Theories of the adsorption of gases. A general survey and some additional remarks. Introductory paper to section III*. Trans. Faraday Soc. 28, 316–333.

Polanyi, M., 1916. *Adsorption von Gasen (Dampfen) durch ein festes nichtfluchtiges Adsorbens*. Verhandlungen Dtsch. Physekalischen Ges. 18, 55–80.

Polanyi, M., 1914. *Adsorption from the point of view of the Third Law of Thermodynamics*. Verh Deut Phys Ges 16, 1012–1016.

Popov, V.N., 2004. *Carbon nanotubes: properties and application*. Mater. Sci. Eng. R Rep. 43, 61–102.

Pozzo, M., Alfe, D., 2009. *Hydrogen dissociation and diffusion on transition metal (= Ti, Zr, V, Fe, Ru, Co, Rh, Ni, Pd, Cu, Ag)-doped Mg (0001) surfaces*. Int. J. Hydrog. Energy 34, 1922–1930.

Pré, P., Huchet, G., Jeulin, D., Rouzaud, J.-N., Sennour, M., Thorel, A., 2013. *A new approach to characterize the nanostructure of activated carbons from mathematical morphology applied to high resolution transmission electron microscopy images*. Carbon 52, 239–258.

Pré, P., Shiryaev, A., Rouzaud, J.-N., Voloshchuk, A., 2013b. Chracterization of nanoporous carbons from X-ray scattering, transmission electron microscopy and (N2, CO2) adsorption. Presented at the Carbon 2013, Rio de Janeiro.

Proch, S., Herrmannsdörfer, J., Kempe, R., Kern, C., Jess, A., Seyfarth, L., Senker, J., 2008. *Pt@ MOF-177: Synthesis, Room-Temperature Hydrogen Storage and Oxidation Catalysis*. Chem.- Eur. J. 14, 8204–8212.

Purewal, J., Keith, J.B., Ahn, C.C., Brown, C.M., Tyagi, M., Fultz, B., 2012. *Hydrogen diffusion in potassium intercalated graphite studied by quasielastic neutron scattering*. J. Chem. Phys. 137, 224704.

Qian, D., Lei, C., Hao, G.-P., Li, W.-C., Lu, A.-H., 2012. *Synthesis of Hierarchical Porous Carbon Monoliths with Incorporated Metal–Organic Frameworks for Enhancing Volumetric Based CO2 Capture Capability*. ACS Appl. Mater. Interfaces 4, 6125–6132.

Quirke, N., Tennison, S.R.R., 1996. *The interpretation of pore size distributions of microporous carbons*. Carbon 34, 1281–1286.

Ranz, W., Marshall, W., 1952. *Evaporation from drops*. Chem Eng Prog 48, 141–146.

Rao, D., Lu, R., Xiao, C., Kan, E., Deng, K., 2011. *Lithium-doped MOF impregnated with lithium-coated fullerenes: A hydrogen storage route for high gravimetric and volumetric uptakes at ambient temperatures*. Chem. Commun. 47, 7698–7700.

Ravikovitch, P.I., Neimark, A.V., 2001a. *Characterization of nanoporous materials from adsorption and desorption isotherms*. Colloids Surf. Physicochem. Eng. Asp. 187, 11–21.

Ravikovitch, P.I., Neimark, A.V., 2001b. *Characterization of micro-and mesoporosity in SBA-15 materials from adsorption data by the NLDFT method*. J. Phys. Chem. B 105, 6817–6823.

Reich, R., Ziegler, W.T., Rogers, K.A., 1980. *Adsorption of Methane, Ethane, and Ethylene Gases and Their Binary and Ternary Mixtures and Carbon Dioxide on Activated Carbon at 212-301 K and Pressures to 35 Atmospheres*. Ind. Eng. Chem. Process Des. Dev. 19, 336–344.

Reilly, J.J., Sandrock, G.D., 1980. *Hydrogen storage in metal hydrides*. Sci AmUnited States 242.

Reilly, J.J., Wiswall, J.R.H., 1974. *Formation and properties of iron titanium hydride*. Inorg. Chem. 13, 218–222.

Reilly, J.J., Wiswall, J.R.H., 1968. *Reaction of hydrogen with alloys of magnesium and nickel and the formation of Mg_2NiH_4*. Inorg. Chem. 7, 2254–2256.

Ren, J., Musyoka, N.M., Langmi, H.W., Segakweng, T., North, B.C., Mathe, M., Kang, X., 2014. *Modulated synthesis of chromium-based metal-organic framework (MIL-101) with enhanced hydrogen uptake*. Int. J. Hydrog. Energy 39, 12018–12023.

Rosenbach, N., Jobic, H., Ghoufi, A., Salles, F., Maurin, G., Bourrelly, S., Llewellyn, P.L., Devic, T., Serre, C., Férey, G., 2008. *Quasi-Elastic Neutron Scattering and Molecular Dynamics Study of Methane Diffusion in Metal Organic Frameworks MIL-47(V) and MIL-53(Cr)*. Angew. Chem. Int. Ed. 47, 6611–6615.

Rouquerol, F., Rouquerol, J., Sing, K.S.W., 2014. Thermodynamics of Adsorption at the Gas/Solid Interface, in: *Adsorption by Powders and Porous Solids*. Elsevier, pp. 25–56.

Rouquerol, J., Avnir, D., Fairbridge, C.W., Everett, D.H., Haynes, J.M., Pernicone, N., Ramsay, J.D.F., Sing, K.S.W., Unger, K.K., 1994. *Recommendations for the characterization of porous solids (Technical Report)*. Pure Appl. Chem. 66.

Rouquerol, J., Llewellyn, P., Rouquerol, F., 2007. *Is the BET equation applicable to microporous adsorbents?* Stud. Surf. Sci. Catal. 49–56.

Rouquerol, J., Rouquerol, F., 2014. Methodology of Gas Adsorption, in: *Adsorption by Powders and Porous Solids*. Elsevier, pp. 57–104.

Rowsell, J.L.C., Yaghi, O.M., 2006. *Effects of Functionalization, Catenation, and Variation of the Metal Oxide and Organic Linking Units on the Low-Pressure Hydrogen Adsorption Properties of Metal–Organic Frameworks*. J. Am. Chem. Soc. 128, 1304–1315.

Rozain, C., Millet, P., 2014. *Electrochemical characterization of Polymer Electrolyte Membrane Water Electrolysis Cells*. Electrochimica Acta 131, 160–167.

RTE, 2013. *Bilan Electrique 2013.*

Rufford, T.E., Watson, G.C.Y., Saleman, T.L., Hofman, P.S., Jensen, N.K., May, E.F., 2013. *Adsorption Equilibria and Kinetics of Methane + Nitrogen Mixtures on the Activated Carbon Norit RB3*. Ind. Eng. Chem. Res. 52, 14270–14281.

Ruthven, D.M., 1984. *Principles of adsorption and adsorption processes*. Wiley, New York.

Sabo, M., Henschel, A., Fröde, H., Klemm, E., Kaskel, S., 2007. *Solution infiltration of palladium into MOF-5: synthesis, physisorption and catalytic properties*. J. Mater. Chem. 17, 3827–3832.

Saha, D., Wei, Z., Deng, S., 2009. *Hydrogen adsorption equilibrium and kinetics in metal–organic framework (MOF-5) synthesized with DEF approach*. Sep. Purif. Technol. 64, 280–287.

Saha, D., Wei, Z., Deng, S., 2008. *Equilibrium, kinetics and enthalpy of hydrogen adsorption in MOF-177*. Int. J. Hydrog. Energy 33, 7479–7488.

Sakintuna, B., Lamaridarkrim, F., Hirscher, M., 2007. *Metal hydride materials for solid hydrogen storage: A review*. Int. J. Hydrog. Energy 32, 1121–1140.

Salomon, W., Yazigi, F.-J., Roch-Marchal, C., Mialane, P., Horcajada, P., Serre, C., Haouas, M., Taulelle, F., Dolbecq, A., 2014. *Immobilization of Co-containing polyoxometalates in MIL-101 (Cr): structural integrity versus chemical transformation*. Dalton Trans. 43, 12698–12705.

Sandall, O.C., 1977. *Measurements in heat transfer*, second edition, E. R. G. Eckert and R. J. Goldstein(editors), McGraw-Hill Book Co., New York, 1976. 656 pages. AIChE J. 23, 772–773.

Sandrock, G., Gross, K., Thomas, G., Jensen, C., Meeker, D., Takara, S., 2002. *Engineering considerations in the use of catalyzed sodium alanates for hydrogen storage*. J. Alloys Compd. 330, 696–701.

Satyapal, S., Petrovic, J., Read, C., Thomas, G., Ordaz, G., 2007. *The US Department of Energy's National Hydrogen Storage Project: Progress towards meeting hydrogen-powered vehicle requirements*. Catal. Today 120, 246–256.

Schlapbach, L., 2009. *Technology: Hydrogen-fuelled vehicles*. Nature 460, 809–811.

Schlapbach, L., Züttel, A., 2001. *Hydrogen-storage materials for mobile applications*. Nature 414, 353–358.

Schmitz, B., Müller, U., Trukhan, N., Schubert, M., Férey, G., Hirscher, M., 2008. *Heat of Adsorption for Hydrogen in Microporous High-Surface-Area Materials*. ChemPhysChem 9, 2181–2184.

Schneider, P., Smith, J.M., 1968. *Chromatographic study of surface diffusion*. AIChE J. 14, 886–895.

Seaton, N., Walton, J., 1989. *A new analysis method for the determination of the pore size distribution of porous carbons from nitrogen adsorption measurements*. Carbon 27, 853–861.

Senkovska, I., Kaskel, S., 2008. *High pressure methane adsorption in the metal-organic frameworks $Cu_3(btc)_2$, $Zn_2(bdc)_2dabco$, and $Cr_3F(H_2O)_2O(bdc)_3$*. Microporous Mesoporous Mater. 112, 108–115.

Seo, Y.-K., Yoon, J.W., Lee, J.S., Lee, U.-H., Hwang, Y.K., Jun, C.-H., Horcajada, P., Serre, C., Chang, J.-S., 2012. *Large scale fluorine-free synthesis of hierarchically porous iron(III) trimesate MIL-100(Fe) with a zeolite MTN topology*. Microporous Mesoporous Mater. 157, 137–145.

Shampine, L.F., 1994. *Numerical solution of ordinary differential equations*, Mathematics. Chapman & Hall, New York.

Shang, C., Guo, Z., 2004. *Effect of carbon on hydrogen desorption and absorption of mechanically milled MgH_2*. J. Power Sources 129, 73–80.

Sieverts, A., 1929. *Die aufnahme von gasen durch metalle*. Z. Für Met. 37–46.

Sing, K.S.W., 1985. *Reporting physisorption data for gas/solid systems with special reference to the determination of surface area and porosity* (Recommendations 1984). Pure Appl. Chem. 57.

Sing, K.S.W., Rouquerol, F., Llewellyn, P., Rouquerol, J., 2014a. Assessment of Microporosity, in: *Adsorption by Powders and Porous Solids*. Elsevier, pp. 303–320.

Sing, K.S.W., Rouquerol, F., Rouquerol, J., 2014b. Classical Interpretation of Physisorption Isotherms at the Gas–Solid Interface, in: *Adsorption by Powders and Porous Solids*. Elsevier, pp. 159–189.

Sing, K.S.W., Rouquerol, F., Rouquerol, J., Llewellyn, P., 2014c. Assessment of Mesoporosity, in: *Adsorption by Powders and Porous Solids*. Elsevier, pp. 269–302.

Sips, R., 1948. *On the Structure of a Catalyst Surface*. J. Chem. Phys. 16, 490.

Si, T., Zhang, J., Liu, D., Zhang, Q., 2013. *A new reversible Mg_3Ag–H_2 system for hydrogen storage*. J. Alloys Compd. 581, 246–249.

Skripnyuk, V., Rabkin, E., 2012. *Mg_3Cd: a model alloy for studying the destabilization of magnesium hydride*. Int. J. Hydrog. Energy 37, 10724–10732.

Somayajulu Rallapalli, P.B., Raj, M.C., Patil, D.V., Karikkethu Prabhakaran, P., Somani, R.S., Bajaj, H.C., 2013. *Activated carbon @ MIL-101(Cr): a potential metal-organic framework*

composite material for hydrogen storage: A potential MOF composite material for hydrogen storage. Int. J. Energy Res. 37, 746–753.

Song, M., Bobet, J.-L., Darriet, B., 2002. *Improvement in hydrogen sorption properties of Mg by reactive mechanical grinding with Cr_2O_3, Al_2O_3 and CeO_2*. J. Alloys Compd. 340, 256–262.

Sonnauer, A., Hoffmann, F., Fröba, M., Kienle, L., Duppel, V., Thommes, M., Serre, C., Férey, G., Stock, N., 2009. *Giant Pores in a Chromium 2, 6-Naphthalenedicarboxylate Open-Framework Structure with MIL-101 Topology*. Angew. Chem. 121, 3849–3852.

Soulié, J.-P., Renaudin, G., Černý, R., Yvon, K., 2002. *Lithium boro-hydride $LiBH_4$: I. Crystal structure*. J. Alloys Compd. 346, 200–205.

Spath, P.L., Mann, M., Amos, W., 2000. *Update of hydrogen from biomass-determination of the delivered cost of hydrogen*. Natl. Renew. Energy Lab. Oper. US Dep Energy Midwest Res. Inst. Battelle Bechtel April Gold. Colo. USA.

Stampfer, J., Holley Jr, C., Suttle, J., 1960. *The magnesium-hydrogen system*. J. Am. Chem. Soc. 82, 3504–3508.

Stocker, T., Qin, D., Plattner, G., Tignor, M., Allen, S., Boschung, J., Nauels, A., Xia, Y., Bex, B., Midgley, B., 2013. *IPCC, 2013: climate change 2013: the physical science basis. Contribution of working group I to the fifth assessment report of the intergovernmental panel on climate change*.

Stock, N., Biswas, S., 2012. *Synthesis of Metal-Organic Frameworks (MOFs): Routes to Various MOF Topologies, Morphologies, and Composites*. Chem. Rev. 112, 933–969.

Suh, M.P., Park, H.J., Prasad, T.K., Lim, D.-W., 2012. *Hydrogen Storage in Metal–Organic Frameworks*. Chem. Rev. 112, 782–835.

Sumida, K., Brown, C.M., Herm, Z.R., Chavan, S., Bordiga, S., Long, J.R., 2011. *Hydrogen storage properties and neutron scattering studies of Mg_2(dobdc)—a metal–organic framework with open Mg^{2+} adsorption sites*. Chem. Commun. 47, 1157.

Sumida, K., Hill, M.R., Horike, S., Dailly, A., Long, J.R., 2009. *Synthesis and hydrogen storage properties of $Be_{12}(OH)_{12}$(1, 3, 5-benzenetribenzoate)$_4$*. J. Am. Chem. Soc. 131, 15120–15121.

Sun, D., Srinivasan, S.S., Kiyobayashi, T., Kuriyama, N., Jensen, C.M., 2003. *Rehydrogenation of dehydrogenated $NaAlH_4$ at low temperature and pressure*. J. Phys. Chem. B 107, 10176–10179.

Suzuki, M., Fujii, T., 1982. *Concentration dependence of surface diffusion coefficient of propionic acid in activated carbon particles*. AIChE J. 28, 380–385.

Szegö, G., 1939. *Orthogonal Polynomials*, American Mathematical Society colloquium publications. American mathematical society.

Szilágyi, P., Callini, E., Anastasopol, A., Kwakernaak, C., Sachdeva, S., van de Krol, R., Geerlings, H., Borgschulte, A., Züttel, A., Dam, B., 2014. *Probing hydrogen spillover in Pd@ MIL-101 (Cr) with a focus on hydrogen chemisorption*. Phys. Chem. Chem. Phys. 16, 5803–5809.

Takagi, H., Hatori, H., Soneda, Y., Yoshizawa, N., Yamada, Y., 2004. *Adsorptive hydrogen storage in carbon and porous materials*. Mater. Sci. Eng. B 108, 143–147.

Tarazona, P., 1985. *Free-energy density functional for hard spheres*. Phys. Rev. A 31, 2672–2679.

Tarazona, P., Marconi, U.M.B., Evans, R., 1987. *Phase equilibria of fluid interfaces and confined fluids: Non-local versus local density functionals*. Mol. Phys. 60, 573–595.

Texier-Mandoki, N., Dentzer, J., Piquero, T., Saadallah, S., David, P., Vix-Guterl, C., 2004. *Hydrogen storage in activated carbon materials: role of the nanoporous texture*. Carbon 42, 2744–2747.

The World Bank Databank, 2015. *Fossil fuel energy consumption (% of total)*.

Thommes, M., Kaneko, K., Neimark, A.V., Olivier, J.P., Rodriguez-Reinoso, F., Rouquerol, J., Sing, K.S.W., 2015. *Physisorption of gases, with special reference to the evaluation of surface area and pore size distribution (IUPAC Technical Report)*. Pure Appl. Chem. 87.

Thomson, W., 1871. *LX. On the equilibrium of vapour at a curved surface of liquid*. Philos. Mag. Ser. 4 42, 448–452.

Tromp, R., 2003. *Surface diffusion: Atoms go underground*. Nat. Mater. 2, 212–213.

Tsuruoka, T., Furukawa, S., Takashima, Y., Yoshida, K., Isoda, S., Kitagawa, S., 2009. *Nanoporous nanorods fabricated by coordination modulation and oriented attachment growth*. Angew. Chem. Int. Ed. 48, 4739–4743.

Umemura, A., Diring, S., Furukawa, S., Uehara, H., Tsuruoka, T., Kitagawa, S., 2011. *Morphology Design of Porous Coordination Polymer Crystals by Coordination Modulation*. J. Am. Chem. Soc. 133, 15506–15513.

Vajo, J.J., Skeith, S.L., Mertens, F., 2005. *Reversible storage of hydrogen in destabilized LiBH$_4$*. J. Phys. Chem. B 109, 3719–3722.

Valenti, G., 2016. Hydrogen liquefaction and liquid hydrogen storage, in: *Compendium of Hydrogen Energy*. Elsevier, pp. 27–51.

Van Vucht, J., Kuijpers, Fa., Bruning, H., 1970. *Reversible room-temperature absorption of large quantities of hydrogen by intermetallic compounds.* Philips Res Rep 25 133-40 Apr 1970.

Vilatela, J.J., Eder, D., 2012. *Nanocarbon composites and hybrids in sustainability: a review*. ChemSusChem 5, 456–478.

Villadsen, J., Michelsen, M.L., 1978. *Solution of differential equation models by polynomial approximation*, Prentice-Hall international series in the physical and chemical engineering sciences. Prentice-Hall, Englewood Cliffs, NJ.

Vitillo, J.G., Ricchiardi, G., Spoto, G., Zecchina, A., 2005. *Theoretical maximal storage of hydrogen in zeolitic frameworks*. Phys. Chem. Chem. Phys. 7, 3948–3954.

Wakao, N., Funazkri, T., 1978. *Effect of fluid dispersion coefficients on particle-to-fluid mass transfer coefficients in packed beds*. Chem. Eng. Sci. 33, 1375–1384.

Walker, G., 2008. *Solid-state hydrogen storage: materials and chemistry*, Woodhead publishing in materials. CRC Press, Boca Raton, Fla.

Wang, H., Lin, H.J., Cai, W.T., Ouyang, L.Z., Zhu, M., 2016. *Tuning kinetics and thermodynamics of hydrogen storage in light metal element based systems – A review of recent progress*. J. Alloys Compd. 658, 280–300.

Wee, L.H., Bonino, F., Lamberti, C., Bordiga, S., Martens, J.A., 2014. *Cr-MIL-101 encapsulated Keggin phosphotungstic acid as active nanomaterial for catalysing the alcoholysis of styrene oxide*. Green Chem. 16, 1351–1357.

Wicke, E., Kallenbach, R., 1941. *Die oberflächendiffusion von kohlendioxyd in aktiven kohlen*. Colloid Polym. Sci. 97, 135–151.

Wilson, E., Geankoplis, C., 1966. *Liquid mass transfer at very low Reynolds numbers in packed beds*. Ind. Eng. Chem. Fundam. 5, 9–14.

Wiswall, J.R.H., Reilly, J.J., 1972. *Inverse hydrogen isotope effects in some metal hydride systems*. Inorg. Chem. 11, 1691–1696.

Wong-Foy, A.G., Matzger, A.J., Yaghi, O.M., 2006. *Exceptional H2 Saturation Uptake in Microporous Metal–Organic Frameworks*. J. Am. Chem. Soc. 128, 3494–3495.

Wu, H., Chua, Y.S., Krungleviciute, V., Tyagi, M., Chen, P., Yildirim, T., Zhou, W., 2013. *Unusual and Highly Tunable Missing-Linker Defects in Zirconium Metal–Organic Framework UiO-66 and Their Important Effects on Gas Adsorption*. J. Am. Chem. Soc. 135, 10525–10532.

Wu, X., Chen, P., Lin, J., Tan, K.L., 2000. *Hydrogen uptake by carbon nanotubes*. Int. J. Hydrog. Energy 25, 261–265.

Xiang, Z., Hu, Z., Cao, D., Yang, W., Lu, J., Han, B., Wang, W., 2011. *Metal-Organic Frameworks with Incorporated Carbon Nanotubes: Improving Carbon Dioxide and Methane Storage Capacities by Lithium Doping*. Angew. Chem. Int. Ed. 50, 491–494.

Xiao, B., Wheatley, P.S., Zhao, X., Fletcher, A.J., Fox, S., Rossi, A.G., Megson, I.L., Bordiga, S., Regli, L., Thomas, K.M., 2007. *High-capacity hydrogen and nitric oxide adsorption and storage in a metal-organic framework.* J. Am. Chem. Soc. 129, 1203–1209.

Yamashita, M., Yamashita, M., Suzuki, M., Hirai, H., Kajigaya, H., 2001. *Iontophoretic delivery of calcium for experimental hydrofluoric acid burns*. Crit. Care Med. 29, 1575–1578.

Yang, J., Zhao, Q., Li, J., Dong, J., 2010. *Synthesis of metal–organic framework MIL-101 in TMAOH-Cr(NO3)3-H2BDC-H2O and its hydrogen-storage behavior*. Microporous Mesoporous Mater. 130, 174–179.

Yang, R.T., Fenn, J.B., Haller, G.L., 1973. *Modification to the Higashi model for surface diffusion*. AIChE J. 19, 1052–1053.

Yang, S.J., Choi, J.Y., Chae, H.K., Cho, J.H., Nahm, K.S., Park, C.R., 2009. *Preparation and enhanced hydrostability and hydrogen storage capacity of CNT@ MOF-5 hybrid composite*. Chem. Mater. 21, 1893–1897.

Yang, S.J., Cho, J.H., Nahm, K.S., Park, C.R., 2010. *Enhanced hydrogen storage capacity of Pt-loaded CNT@MOF-5 hybrid composites*. Int. J. Hydrog. Energy 35, 13062–13067.

Yang, Z., Xia, Y., Mokaya, R., 2007. *Enhanced hydrogen storage capacity of high surface area zeolite-like carbon materials*. J. Am. Chem. Soc. 129, 1673–1679.

Yan, Y., Lin, X., Yang, S., Blake, A.J., Dailly, A., Champness, N.R., Hubberstey, P., Schröder, M., 2009. *Exceptionally high H2 storage by a metal–organic polyhedral framework*. Chem. Commun. 9, 1025.

Ye, Y., Ahn, C.C., Witham, C., Fultz, B., Liu, J., Rinzler, A.G., Colbert, D., Smith, K.A., Smalley, R.E., 1999. *Hydrogen adsorption and cohesive energy of single-walled carbon nanotubes*. Appl. Phys. Lett. 74, 2307.

Young, K., Nei, J., 2013. *The current status of hydrogen storage alloy development for electrochemical applications*. Materials 6, 4574–4608.

Yushin, G., Dash, R., Jagiello, J., Fischer, J.E., Gogotsi, Y., 2006. *Carbide-Derived Carbons: Effect of Pore Size on Hydrogen Uptake and Heat of Adsorption*. Adv. Funct. Mater. 16, 2288–2293.

Zaluska, A., Zaluski, L., Ström-Olsen, J.O., 2000. *Sodium alanates for reversible hydrogen storage.* J. Alloys Compd. 298, 125–134.

Zaluski, L., Zaluska, A., Ström-Olsen, J., 1999. *Hydrogenation properties of complex alkali metal hydrides fabricated by mechano-chemical synthesis*. J. Alloys Compd. 290, 71–78.

Zaluski, L., Zaluska, A., Tessier, P., Ström-Olsen, J., Schulz, R., 1995. *Catalytic effect of Pd on hydrogen absorption in mechanically alloyed Mg$_2$Ni, LaNi$_5$ and FeTi*. J. Alloys Compd. 217, 295–300.

Zeldowitsch, J.B., 1935. *A response to the remarks of H. Zeise on my work "On the theory of the Freundlich adsorption isotherm."* ACTA PHYSICOCHIMICA URSS 3, 529–530.

Zervos, A., 2013. *Renewables 2013 global status report*. Renew. Energy Policy Netw. 21st Century Paris Fr.

Zhao, T., Jeremias, F., Boldog, I., Nguyen, B., Henninger, S.K., Janiak, C., 2015. *High-yield, fluoride-free and large-scale synthesis of MIL-101 (Cr)*. Dalton Trans. 44, 16791–16801.

Zhong, H., Wang, H., Liu, J., Sun, D., Zhu, M., 2011a. *Altered desorption enthalpy of MgH$_2$ by the reversible formation of Mg (In) solid solution*. Scr. Mater. 65, 285–287.

Zhong, H., Wang, H., Ouyang, L., Zhu, M., 2011b. *Microstructure and hydrogen storage properties of Mg–Sn nanocomposite by mechanical milling*. J. Alloys Compd. 509, 4268–4272.

Zhou, C., Fang, Z.Z., Lu, J., Zhang, X., 2013. *Thermodynamic and kinetic destabilization of magnesium hydride using Mg–In solid solution alloys*. J. Am. Chem. Soc. 135, 10982–10985.

Zhou, J.-J., Liu, K.-Y., Kong, C.-L., Chen, L., 2013. *Acetate-assisted Synthesis of Chromium(III) Terephthalate and Its Gas Adsorption Properties*. Bull. Korean Chem. Soc. 34, 1625–1631.

Zhou, X., Huang, W., Shi, J., Zhao, Z., Xia, Q., Li, Y., Wang, H., Li, Z., 2014. *A novel MOF/graphene oxide composite GrO@ MIL-101 with high adsorption capacity for acetone*. J. Mater. Chem. A 2, 4722–4730.

Zhu, Q.-L., Xu, Q., 2014. *Metal–organic framework composites*. Chem. Soc. Rev. 43, 5468–5512.

Zlotea, C., Campesi, R., Cuevas, F., Leroy, E., Dibandjo, P., Volkringer, C., Loiseau, T., Férey, G., Latroche, M., 2010. *Pd nanoparticles embedded into a metal-organic framework: synthesis, structural characteristics, and hydrogen sorption properties*. J. Am. Chem. Soc. 132, 2991–2997.

Züttel, A., 2004. *Hydrogen storage methods*. Naturwissenschaften 91, 157–172.

Züttel, A., 2003. *Materials for hydrogen storage*. Mater. Today 6, 24–33.

Thèse de Doctorat

YU Zhewei

Etudes à l'équilibre et cinétiques du stockage d'hydrogène sur adsorbants hybrides réseaux organo-métalliques-charbon actif produits par synthèses douces

Equilibrium and kinetics studies of hydrogen storage onto hybrid activated carbon-metal organic framework adsorbents produced by mild syntheses

Résumé

Depuis une quinzaine d'années, les matériaux poreux de type Metal Organic Frameworks (MOFs) offrent de nouvelles perspectives dans le cadre du stockage d'hydrogène par adsorption. Ces matériaux possèdent une structure et un réseau de pores particulièrement bien adaptés à l'adsorption des gaz. Ainsi, le téréphtalate de Chrome (III) (MIL-101(Cr)), composé chimiquement très stable, possède une grande capacité de stockage de l'hydrogène, du dioxyde de carbone et du méthane. Afin de renforcer sa capacité de stockage d'hydrogène, un dopage au charbon actif (AC) du matériau a été envisagé.

Les synthèses des matériaux dopés et non-dopés ont été réalisées et, pour cela, différents agents minéralisants (acide fluorhydrique, acide acétique et acétate de sodium) ont été testés. Les matériaux synthétisés furent caractérisés par diffraction des rayons X (DRX), par microscopie électronique à balayage (MEB), par analyses thermogravimétriques (ATG) et par adsorption d'azote à 77K.

Les capacités de stockage d'hydrogène de ces matériaux à 77 K et 100 bar ont été évaluées par mesures des isothermes d'adsorption d'hydrogène, réalisées par méthodes volumétrique et gravimétrique. Les résultats obtenus par ces deux méthodes sont en parfait accord et le matériau composite affiche une capacité d'adsorption de 13.5 wt%, qui est supérieure à celle du matériau non dopé (8.2 wt% dans les même conditions expérimentales).

Les cinétiques d'adsorption ont été mesurées à 77 K par méthode volumétrique. Les résultats obtenus ont été comparés au modèle de la force motrice linéaire, Linear Driving Force (LDF). Un modèle de diffusion dépendant de la température a été développé afin de tenir compte des variations de températures qui se produisent durant le processus d'adsorption.

Mots clés
MOF /MIL-101(Cr) /Charbon actif /Stockage d'hydrogène /Synthèse /Adsorption /Cinétique/ Expérimental /Modélisation

Abstract

Since the last 15 years, the porous solids such as Metal-Organic Frameworks (MOFs) have opened new perspectives for the development of adsorbents for hydrogen storage. The structure and the pore networks of these materials are especially adapted to the adsorption of gases. The chromium (III) terephthalate-based MIL-101(Cr) is a very stable material which exhibits good adsorption uptakes for hydrogen (H_2), carbon dioxide (CO_2) and methane (CH_4).

In this study, syntheses were carried out by different ways and several mineralizing agents such as hydrofluoric acid (HF), acetic acid (CH_3COOH) and sodium acetate (CH_3COONa) have been tested. Moreover, Activated Carbon (AC) has been introduced in the framework to create an AC incorporated composite material with an enhanced specific surface area. Conventional techniques such as powder X-ray diffraction (PXRD), scanning electron microscopy (SEM), thermogravimetric analysis (TGA) and nitrogen (N_2) adsorption isotherms at 77 K were used for materials characterizations.

In the aim to evaluate hydrogen storage capacities of these materials, hydrogen adsorption isotherms were measured at 77 K via both volumetric and gravimetric methods, and the obtained results are in good agreement. A hydrogen uptake value of 13.5 wt% has been measured at 77 K and 100 bar for the composite material which shows a great improvement of hydrogen capacity compared to the pristine MIL-101(Cr) (8.2 wt%).

Finally, hydrogen adsorption kinetics has been measured at 77 K using volumetric method. The obtained results were compared to the Linear Driving Force (LDF) and a temperature dependent diffusion model was also considered to take into account the temperature variations which occur during the adsorption process.

Keywords
MOF / MIL-101(Cr) / Activated carbon / Hydrogen storage / Synthesis / Adsorption / Kinetics / Experiment / Modelling

L'Université Nantes Angers Le Mans